Bacterial Response to Nanoparticles at the Molecular Level

A DISSERTATION
SUBMITTED TO THE FACULTY OF THE
UNIVERSITY OF MINNESOTA
BY

TIAN (AUTUMN) QIU

IN PARTIAL FULFILLMENT OF THE REQUIREMENTS
FOR THE DEGREE OF
DOCTOR OF PHILOSOPHY

Christy Haynes, Advisor

May 2018

Acknowledgements

I want to sincerely thank my thesis advisor, Prof. Dr. Christy Haynes, for her endless support during the past six years. I've probably said "thank you" a million times to her in person and in emails, but there is never enough. Her enthusiasm and optimism in science (it's contagious!) motivate me, and as a student from a different cultural background, her dedication to building a diverse and dynamic working environment makes the group a wonderful place for working and learning. It is my honor working with Christy, and I could not have imagined having a better advisor as passionate, professional and caring as she is.

I would like to thank the whole Haynes group, with whom I have had great pleasure working and being friends with. I am thankful to many Haynes people, including but not limited to: Dr. Ian Gunsolus, Dr. Melissa Maurer-Jones and Ben Meyer for guiding me when I firstly joined the group, Dr. Solaire Finkenstaedt-Quinn for colorful calendars and cat pictures, Dr. Katie Hurley, Dr. Victoria Szlag and Nathan Klein for being movie night buddies, Dr. Zhe Gao and Bo Zhi for hanging out together, Joe Buchman for always being there to help and have a laugh with, Natalie Hudson-Smith and Peter Clement for inspiring conversations, and everyone in lab for working, learning and having fun together. I would also like to thank all undergraduates that I've mentored for enduring me and giving me a chance to teach.

The people I've collaborated and been friends with in the Center for Sustainable Nanotechnology are amazing. I want to thank Dr. Jared Bozich and Nicholas Niemuth for hosting me in Milwaukee multiple times. Specifically, I am extremely thankful to Prof. Dr. Rebecca Klaper, who generously hosted me in her house and guided me into the area of toxicology; she is like my second advisor and it is my honor to work with her. I also want to give my special thanks to Prof. Vivian Feng, who is a mentor,

collaborator and great friend, and kudos to her wonderful undergraduate army. I would like to thank Dr. Marco Torelli, Dr. Ariane Vartanian, Prof. Robert Hamers and Prof. Cathy Murphy in the Center for Sustainable Nanotechnology, and Dr. Andrea Carrà and Prof. Silvia Balbo at Masonic Cancer Center at University of Minnesota, without whose guidance and collaboration I would not have been able to finish my thesis. Lastly, I would like to thank Christy, Prof. Silvia Balbo, Prof. Erin Carlson and Prof. Phil Buhlmann for being on my thesis committee.

Studying abroad is not easy. I want to thank my college professor and tutor, Prof. Jian Pei, for his continuous support that has started since college. I am truly grateful to all my friends who have been supporting me, especially to Yi Zhang, Xueyang Pan, Chao Li, and the girls in our SOTA a cappella group. Finally, I want to thank Minneapolis for its beautiful skyline, its (literally) breathtaking snow and its Minnesota nice. My special thanks to our tuxedo cat, Chaplin, who always surprises me with his endless energy, his big appetite and his persistence in distracting me every time I try to work from home.

This thesis is dedicated to my parents and my grandfather, who have been supporting me in pursuing a life and a career that I want and having faith in me.

I would also like to dedicate it to my fiancé, Liyang (Leon) Ma, for always standing by my side despite of the 6,286 miles and 13 (or 14) hours in between us.

Abstract

Nanotechnology has been an emerging field due to the promising properties of engineered nanomaterials, materials with at least one dimension less than 100 nanometers. With increasing application of NPs, the risk of these novel materials to environment requires thorough investigation to prevent negative impacts. NPs have enormous variety due to combinations of chemical compositions, sizes, shapes, structures and surface modifications. Building predictive models that link NP properties to biological outcomes is the key to proactive safer NP design.

High-throughput toxicity screening and investigating toxicity mechanisms are the common two strategies building towards predictive models of nanotoxicity. These two strategies work together: high-throughput assays facilitate preliminary screening of potentially toxic materials for further mechanistic studies to discover biomarkers and molecular pathways of interest, which will in turn be validated on multiple materials and organisms with high-throughput screening. My thesis work combines both strategies to develop high-throughput screening assays and mechanistic understanding at different molecular levels of how an environmental bacterium, *Shewanella oneidensis* MR-1, responds to various NP exposures.

In this work, Chapter 1 reviews recent advances in analytical nanotoxicology and identifies four key areas that would further bring the field to its maturity. Chapter 2 represents a comprehensive mechanistic study on bacteria responding to TiO_2 NPs with UVA illumination. Chapter 3 uses gene expression to explore molecular response among two organisms at different trophic levels to positively and negatively charged gold NPs. Chapter 4 identifies that purification method can be one neglected source of apparent NP toxicity. A high-throughput bacterial viability assay that is free of NP interference is presented in Chapter 5. Finally, in Chapter 6, DNA damage is revealed as a toxicity mechanism for nanoscale complex metal oxide nanomaterials to bacteria.

Table of Contents

List of Tables

List of Figures

List of Schemes

List of Abbreviations

AFM: atomic force microscopy
AGC: automatic gain control
ALP: alkaline phosphatase
ANOVA: analysis of variance
AO: adverse outcome
AOP: adverse outcome pathways
ATR-FTIR: Attenuated total reflectance Fourier transform infrared
AuNPs: gold nanoparticles
CFMA: carbon fiber microamperometry
CFU: colony forming unit
CNT: carbon nanotubes
CTAB: cetyltrimethylammonium bromide
DCF: dichlorofluorescin
$DCFH_2$: 2',7'-dichlorodihydrofluorescein
$DCFH_2$-DA: dichlorodihydrofluorescein diacetate
DLS: dynamic light scattering
DNA: deoxyribonucleic acid
DPBS: Dulbecco's phosphate-buffered saline
ENM: engineered nanomaterials
EPS: exopolysaccharide
FACS: fluorescence-activated cell sorting
FCS: fluorescence correlation spectroscopy
G6PD: glucose 6-phosphate dehydrogenase
GBV: growth-based viability assay
HCA: high-content analysis
HEPES: 4-(2-hydroxyethyl)-1-piperazineethanesulfonic acid
IBA: ion beam analysis
IPA: isopropanol
KE: key events
KER: key event relationships
LA-ICP-MS: laser ablation inductively coupled plasma mass spectrometry
LB: Luria-Bertani broth
LC-MS: liquid chromatography-mass spectrometry
LDI-MS(I): laser desorption/ionization mass spectrometry (imaging)
LIB: lithium-ion battery
LISNA: laser induced scattering around a nano-absorber
LIT: linear ion trap
LMA: low-melting agarose
LPS: lipopolysaccharides
LSPR: localized surface plasmon resonance
MALDI-MSI: matrix-assisted LDI-MSI

MEMS: microelectromechanical system
MHRW: moderately hard reconstituted water
MIC: minimal inhibitory concentration assay
MIE: molecular initiating event
MM: minimal medium
MPA: mercaptopropionic acid
MWCO: molecular weight cut-off
MWCNT: multi-wall carbon nanotubes
Nano-QSAR: NP quantitative structure-activity relationship
NL: neutral loss
NM: nanomaterial
NMR: nuclear magnetic resonance
NNI: National Nanotechnology Initiative
NP: nanoparticle
NPG-Ac: Newport Green DCF diacetate
NMC: lithium nickel manganese cobalt oxide
OD: optical density
PAA: poly(acrylic acid)
PAH: polyallylamine hydrochloride
PDE-1: Phospodiesterase-1
PE: polyelectrolyte
PEI: polyethyleneimine
PSS: poly(sodium 4-styrenesulfonate)
QCM-D: quartz crystal microbalance with dissipation monitoring
QD: quantum dots
qPCR: quantitative polymerase chain reactions
ROS: reactive oxygen species
RT: room temperature
RTCA: real-time cell analyzer
SALVI: System for Analysis at the Liquid Vacuum Interface
SDM: secondary derivative maximum
SEM: scanning electron microscopy
SERS: surface-enhanced Raman spectroscopy
SFG: sum-frequency generation
SIM: structural illumination microscopy
SIMS: secondary ion mass spectrometry
SLB: supported lipid bilayers
SSC: side scattering
STORM: stochastic optical reconstruction microscopy
TEM: transmission electron microscopy
TIR: total internal reflection
TOPO: trioctylphosphine oxide
XPS: x-ray photoelectron spectroscopy

Chapter 1

Linking nanomaterial properties to biological outcomes: analytical challenges in nanotoxicology for the next decade

Adapted from:

Qiu, T. A., Clement, P. L., Haynes, C. L., Linking nanomaterial properties to biological outcomes: analytical challenges in nanotoxicology for the next decade, ***Chemical Communication***, 2018, in preparation.

1.1 Introduction

The development of nanotechnology has enabled advances in far-ranging fields. Though the full extent to which nanomaterials (NMs) will revolutionize society remains to be seen, a conservative assessment of their impact to date would find that NMs have made significant and lasting contributions to a number of fields, especially medicine, computing, and energy storage and production.[1-4]

The explosion of nano-enabled products is made more impressive by the fact that the field is relatively new—arising in the second half of the twentieth century. At recent count, there are thousands of commercial products that contain NMs,[5] not to mention industrial processes that use ENMs.[6] To date, The Nanodatabase in Europe lists 3038 products containing NMs, and The Project on Emerging Nanotechnologies has documented 1827 NM-containing consumer products.[7,8] The rapid advance in nanotechnology over the past half-century is due in no small part to the National Nanotechnology Initiative funded by the government of the United States of America, championed by Mihail Roco and brought to fruition in 2000. In 2004, Roco outlined four generations of NMs: 1) passive materials that don't differ too significantly from bulk materials but enhance bulk properties; 2) active nanomaterials which a comprise materials that are the active participants in processes; 3) 3-D nanosystems and systems of nanosystems; and 4) heterogenous nanostystems in which different individual components play roles in the performance of the whole.[1] Over the past decades, as predicted, the complexity of NMs and related nanosystems has remarkably increased and will not stop expanding in the future.

From the early days of the National Nanotechnology Initiative (NNI) it was clear that NMs would interact with living systems in engineered (e.g. medicine, agriculture, etc.) and incidental capacities.[1,9] In light of this, wide-spread calls were made for understanding the environmental health and safety of NMs, and specifically for

understanding mechanisms of nanotoxicity at the molecular level.[9,10] The study of the environmental health and safety of NMs has made great strides in recent years and provided key insights into chemical interactions between NMs and organisms of varying complexity.

Pre-dating the NNI, a large community was interested in the human health implications of ultrafine particles and aerosols.[10,11] This "zeroth generation" of nanotoxicologists was largely concerned with either natural NMs (e.g. asbestos) or unintentionally synthesized NMs (e.g. carbonaceous materials from combustion) and used language that may be unfamiliar to the current field, but their questions were the same: By what chemical mechanisms do nanoscale materials impact organisms? Are these interactions fundamentally different than those of small molecules?

The first generation of nanotoxicologists heeded the call from the NNI and looked to answer how engineered NMs may impact cell lines and organisms. These groups studied the interactions between a wide range of NMs and organisms. In the process, those in the first generation of nanotoxicology identified some of the primary mechanisms of nanotoxicity and built foundational knowledge that current scientists rely upon when testing hypotheses, such as generation of reactive oxygen species (ROS). However, in this wide-open field, the NMs studied were often chosen for ease of access, either synthetically or commercially, rather than to systematically test hypotheses. Similarly, testing was performed on a number of cell lines and living systems, but the choices of biological systems were often arbitrary. Most limiting, groups, including our own, often used off-the-shelf tools developed for small molecule toxicology. It has now been well-documented that established tools, such as the MTT viability assay or fluorescence assays can suffer from false-positive or -negative due to properties of nanomaterials.[12,13]

We contend that the field of nanotoxicology is currently in its second generation. Choices of NMs and organisms used for exposures are more systematic, enabling analysis of trends across organisms or between types of nanomaterial.[14-16] During the second generation of nanotoxicology, it has also been realized that there was huge discrepancy in nanotoxicity data acquired on similar materials, creating confusion and hindering accurate risk assessment of nanomaterials to both human health and environment.[17,18] Unlike small molecules which are the objects of study in traditional toxicology, the unique properties of NPs could affect accurate measurement of nanotoxicity. For instance, the status of nanomaterials under different testing conditions, such as aggregation state and surface-adsorbed molecules ("corona"), could vary drastically from one testing medium to another and result in changes in observed toxicity.[19] In addition, nanotoxicity assays are subject to the optical, catalytic and other properties that are specific for each kind of NM and lead to under- or over-estimation of toxicity.[18] Solving these discrepancies has been a challenge to analytical chemists and toxicologists. Off-the-shelf tools started to be validated and new tools were developed.[18,20] Methodologies for characterization of NM transformation in complex biological and environmental matrices and the nano-bio interface when NMs encounter biological system have been developed and will continue to grow in the future.[21]

As nanotoxicology approaches the end of its second decade, the strong foundation built in the zeroth, first, and second generations has provided a launching point for chemists to better understand molecular mechanisms of nanotoxicity. A critical challenge that was started by the second generation of nanotoxicologists is to build predictive models that link nanoparticle physiochemical properties to the biological outcome of NM exposure in a quantitative manner. As we are entering the third decade of nanotoxicology, NMs are being designed and produced fast, and with increasing complexity, as predicted.[1] Proactive establishment of safe NP design rules has never been as critical as it is right now. Ideally, a powerful predictive model can provide

information on potential toxicity and preliminary risk assessment of a theoretically designed NM, when the relevant parameters of this designed NM are input into the model. This grand challenge has motivated the field to explore various approaches to link the physiochemical properties of NMs to biological outcomes and build the desired predictive model.

To build predictive models for the biological outcome of NP exposure, two general approaches can be taken: either creating libraries to test a significant amount of different exposure scenarios or exploring underlying mechanisms that potentially play roles across different scenarios and can be attributed to certain NM characteristics. The former approach relies on large-scale data generation and analysis usually through construction of NM or cell libraries, high-throughput assays, and statistical modeling. The mechanistic approach depends on bioanalytical techniques to characterize biological processes as thoroughly as possible. Such approaches can be either hypothesis- or discovery-driven. The two approaches contribute to predictive models in different ways. The data-demanding approach will provide a large amount of data points to better reveal the trends, while mechanistic information helps to reduce omitted variable bias and improve predictive power. Together, the two approaches give the foundation of predictive models.

In this chapter, we have identified four analytical challenges that should be addressed in the third generation of nanotoxicity to better elucidate mechanisms of nanotoxicity and build predictive models that link NM/nanoparticle (NP) properties to biological outcomes. Here NMs and NPs are used interchangeably. The four challenges are: 1) shifting the paradigm of the mechanistic approach from correlation to causation, 2) overcoming NM interferences in *in vitro* toxicity assays, 3) connecting NP interaction to biological responses at the single-cell level, and 4) measuring the nano-bio interface in real-time and *in situ* with chemical information. The sections below detail the

motivations for each of these foci and discuss current work and methods that show promise in addressing these challenges.

1.2 From correlation to causation: shifting paradigm of mechanistic approach

Understanding mechanisms of NP toxicity means knowing the causal relationship among NP exposure, affected biochemical processes, and final biological outcomes (**Figure 1.1**). NPs for exposure can vary in their physiochemical properties, such as composition, size, charge, and surface modification/adsorption. Biochemical processes, the events on the cellular and molecular levels involving species such as protein and RNA, can be affected differently depending on the NP traits. Final biological outcomes, depending on the scope of the study, can be cytotoxicity for *in vitro* tests or whole-organism outcomes such as survival and reproduction for *in vivo* studies. The causal relationships among these three variables are key to understanding how NPs affect biological organisms and furthermore, impact human health and environment.

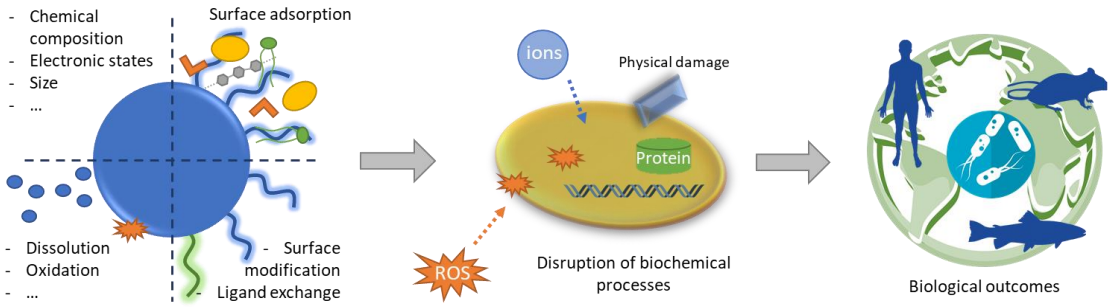

Figure 1.1 Causal relationships among NP properties, affected biochemical processes, and final biological outcomes**.**

A common practice to reveal causal relationships is to control the properties of NPs, followed by measurements of NP-affected biochemical processes and whole-organism endpoints. In some early work from the Haynes lab, researchers synthesized and characterized either mesoporous silica nanospheres or graphene oxides varying in size,

pore character, composition, and/or surface modification, and found correlations among NP characteristics, their hemolytic activities, and cytotoxicity.[22,23] With such studies, however, there are two things that may result in revealing only a correlative, rather than causal, relationship.

When varying one NP property, it is extremely hard not to affect other traits as many physiochemical properties are interconnected, as stated extensively in a review.[24] For example, to change size, it is likely that the coverage of surface modification and the capability of surface adsorption will change as well. These unintended and interlinked changes could act as confounding variables, meaning omitted factors that actually contribute to the causation and lead to inaccurate conclusions. Efforts to fill the gap include construction of NP libraries to systematically represent various combinations of NP properties,[14,25,26] thorough characterization of NPs,[24,27] and development of accurate descriptors that account for interconnected NP characteristics. Burello et al. extensively reviewed both theoretically and experimentally driven descriptors to portray NP properties that can be applied to establish NP quantitative structure-activity relationship (nano-QSAR) models.[28] Using descriptors of NP characteristics, Singh et al. built nano-QSAR models that outperform previous studies with a robust, reliable ensemble learning approach.[29] Lynch et al. further suggest mapping interlinked physicochemical properties into three principle components as overarching descriptors.[30] Advances in NP synthesis, characterization, and statistical modeling will help nano-QSAR to move forward.

Another limitation of the common practice lies in the lack of seeing the whole picture when measuring biochemical processes. Like an old Chinese proverb says, one cannot picture the whole leopard by peeking into a tube and only seeing a spot. Often in practice, due to the limited resources and time, several individual biochemical tests are done to probe toxicity mechanisms, mostly driven by specific hypotheses. Detection of

intracellular reactive oxygen species and metabolites, assays for various enzyme activities and membrane integrity, and measurement of changes in certain biomarkers such as DNA lesions and gene expression are all among popular assays for probing biochemical processes. However, performing individual functional tests is like looking at a leopard through a narrow tube. Spots are observed, and we may conclude correlations among several observations; however, with thousands of other events happening at the same time, we are likely to omit other important variables and thus cannot conclude causal relationships with limited observations. Failure to conclude causal relationships among biochemical processes and final biological outcomes may mislead efforts in future mechanistic studies and diminish the power of predictive models for nanotoxicity.

One obvious way to gain a whole picture is application of –omics methods, part of system toxicology approaches.[31] By definition, -omics refer to measurements on the whole collection of events in biological organisms. An -omics approach can be applied at different molecular levels including DNA (genomics, DNA adductomics), epigenetics (DNA methylation and histone modification), gene expression (transcriptomics), proteins (proteomics, redox and affinity proteomics), metabolites (metabolomics) and other molecules (lipidomics, glycomics). Various recent reviews have covered the application of -omics in analytical nanotoxicology and suggested that, combined with bioinformatic approaches like pathway analysis, -omics can help to identify perturbed pathways, discover new biomarkers, and form new hypotheses.[32-35] Schnackenberg et al. and Matysiak et al. outlined the application of metabolomic and proteomic approaches in nanotoxicology with an emphasis on human health risk assessment.[36,37] In ecotoxicology, Revel et al. recently presented -omics as powerful tools in aquatic nanotoxicology.[38] Integration of -omics at different molecular levels further adds the power of these system biology approaches. Pillai et al. revealed dynamic toxicity response of algae to silver NP exposure by integrating transcriptomics,

proteomics, and phenotype data.[39] A recent review by Shin et al. discussed the integration of metabolomics and transcriptomics ("metabotranscriptomics") in nanotoxicology.[40] In the future, we expect increasing application of diverse -omics in nanotoxicology on both human health and ecological systems, especially integrated -omics across different levels, to depict whole pictures of molecular mechanisms of NP toxicity.

However, due to limitation of resources and complexity in performing -omics experiments, biochemical assays will most likely keep being methods of first choice when testing nanotoxicity. Thus, it is important to incorporate such individual assays in a framework that emphasizes the causal relationships among biological events. Adverse outcome pathways (AOP), a recently developed conceptual framework that links existing toxicological knowledge on biological events between a molecular initiating event (MIE) to an adverse outcome (AO) that is relevant to risk assessment, depict a series of causally related key events (KE) that span multiple biological levels (**Figure 1.2**).[41] The causal relationships between key events are defined as key event relationships (KERs). The AOP framework provides possibilities to integrate existing knowledge on different biological levels, predict toxicity pathways of new chemicals, and guide discovery of biomarkers, and is considered a promising way to reduce animal testing as it facilitates the extrapolation of chemical effects across species.[42]

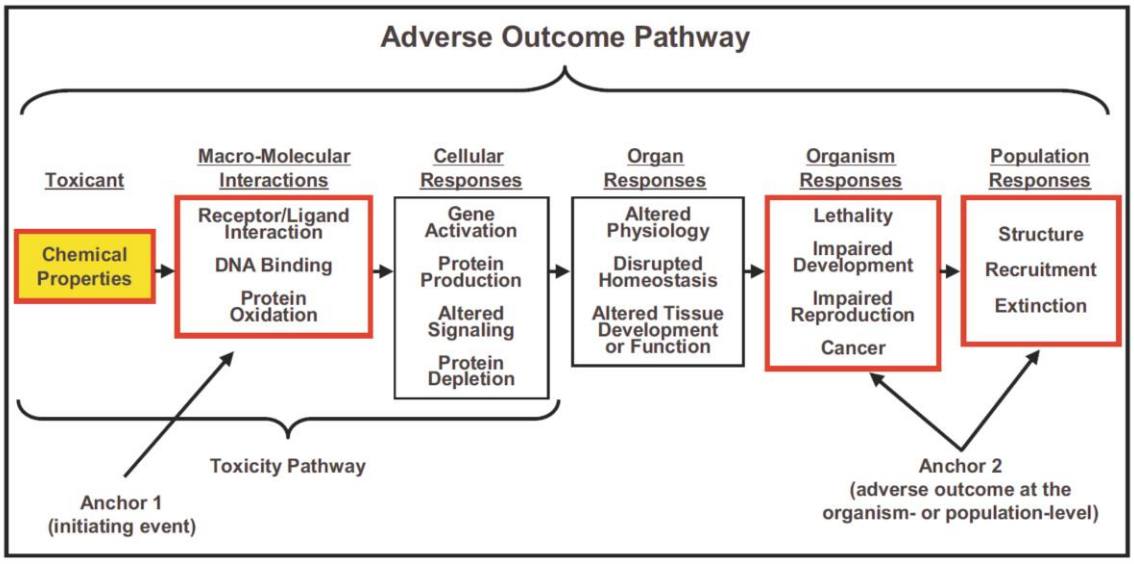

Figure 1.2 Illustration of Adverse Outcome Pathway (AOP). (Reprinted with permission from **Ref 41**. Copyright 2010 Wiley InterScience.)

Establishment of AOPs is fed by studies on toxicity mechanisms, including both individual toxicity tests and system toxicology approaches. Many efforts have been made to build AOPs for chemicals, and multiple databases have been developed, such as AOP wiki, AOP knowledge base, and Effectopedia. Using existing, but mostly fragmented, knowledge on nanotoxicity mechanisms, researchers have recently started developing AOPs for nanotoxicity. Vietti et al. reviewed toxicity literature of lung fibrosis induced by carbon nanotubes to draft an AOP on the fibrotic potential of CNTs.[43] Knowledge gaps in toxicity mechanisms were identified while developing the AOP for CNTs. Instead of reviewing literature, Labib et al. developed an AOP for lung fibrosis upon MWCNT exposure based on *in vivo* transcriptomic data, showing the potential of -omics data being used to reveal causal relationships among events.[44] Two challenges in building AOPs for nanotoxicity were pointed out by Gerloff et al.[45] The first one is to identify characteristics of NPs that can initiate a molecular event. A great example is relating the oxidative potential of NPs to ROS generation as an MIE. As oxidative stress is proven to be an important mechanism for nanotoxicity, NP characteristics that lead to potential oxidative stress, such as bandgap and hydration energy, have been identified as predictors for nanotoxicity both experimentally and

theoretically.[25,46-49] However, other traits that could potentially be related to MIEs are still vague and lacking sufficient evidence, leaving plenty of room for future research. The second challenge is that the nature of MIEs for nanotoxicity can be different from chemicals. While the molecular interactions at the nano-bio interface inform potential MIEs that initiate an AOP, the nano-bio interaction might be physical or mechanical, thus not necessarily a "molecular event". The authors suggested that instead of using MIEs, the first key event following MIE, called initial KE, might be used instead as the first event in a nano-specific AOP. In their recent work, Gerloff et al. reviewed the liver toxicity induced by both chemicals and metal oxide NPs, and most importantly, suggested that establishment of an AOP should not be limited to nano-specific toxicology literature but also expand to established knowledge on chemical AOPs, as they may share downstream key events despite differences in MIEs and early KEs.[45] In conclusion, when designing experiments, we encourage consideration of incorporating individual analytical tests in the framework of potential AOPs, which can help researchers to form reasonable hypotheses and integrate future new knowledge into the existing database of nanotoxicity.

As mentioned at the very beginning of this section, a common practice for mechanistic study is to expose organism of interest with NPs of various properties and measure their toxicity response upon exposure. Uncommon for analytical chemists and toxicologists, manipulation of biological processes and components is a less used yet powerful approach to infer causal relationships between exposure and biological outcomes. As a great example, Jacobson and Gunsolus et al. revealed that lipopolysaccharides (LPS) on Gram-negative bacterial membranes are the primary binding site for AuNPs wrapped with positively charged polymers.[50] To confirm that LPS is the binding site, researchers chemically depleted a fraction of LPS on the bacterial cell outer membrane. A significant decrease in NP-cell association was observed in LPS-depleted cells compared to normal cells. Combined with experiments on solid-supported LPS-

containing lipid bilayers interacting with NPs, strong evidence showed that positively charged NPs interact with bacterial cells through LPS. Another example is to use a library of *E. coli* knockout mutants for toxicity screening; the mutants that are more sensitive than the wild type can inform important cellular functions and pathways in responding to nanomaterials.[51,52] Similar to the concerns about controlling NP characteristics via synthesis, manipulating one biological variable might be accompanied by undesirable, yet inevitable, changes in other variables. Therefore, thorough characterization of manipulated processes and potentially affected processes is desired. Nevertheless, using tools from biochemistry, chemical biology, and molecular biology, biological processes and components can be controlled or blocked, providing evidence of toxicity mechanisms from another angle different from simply measuring responses upon exposure. Thus, we encourage analytical chemists and toxicologists to consider implementation of these available tools outside analytical chemistry through broader collaboration across chemistry and biology to gain complementary information to complete the picture of toxicity mechanisms.

1.3 Overcoming NP interferences in in vitro toxicity assays

There are many ways that NPs can interfere with an *in vitro* toxicity assay on biological endpoints. The intrinsic optical properties of NPs can interfere with many assays that rely on measuring changes in absorbance or fluorescence of molecular indicators for cellular activities. Due to their high surface reactivity, NPs can adsorb[53] or react with assay reagents[54] or release chemical species[55] in testing media, altering the behavior of dyes and enzymes in assays. In some cases, catalytic NPs can cause side reactions such as ROS production. All these interferences contribute to discrepancies observed in nanotoxicity studies and has been extensively discussed.[18,56-58] One analytical challenge in the field of nanotoxicology has been and will continue to be the development of toxicity assays that are free of NP interference and improvement of well-established toxicity protocols where interference cannot be avoided and neglected.

The optical interference, including absorbance and fluorescence, can be possibly corrected via proper control and background subtraction. Many well-established toxicity protocols have been re-validated on NPs, and optical interference from NPs in *in vitro* assays have been checked and taken into account in data analysis.[59-64] However, background subtraction does not always work, especially when reagents (converted or not) react with NPs or side products from catalytic reaction of NPs. More well-considered and complicated controls need to be done in this case. For instance, Semisch et al. found that copper ion released from CuO NPs caused the reduction of tetrazolium salt, the dye for the WST cytotoxicity assay.[55] In this case, the WST assay is not proper to test the toxicity of CuO NPs, unless NP concentration for exposure is low enough that the interference from released copper ion can be neglected. Interference from catalytic properties can potentially be mitigated by controlling experimental conditions, such as avoidance of UV illumination for TiO_2 NPs in the presence of assay reagents.[65]

Studies have pointed out that NP interference cannot be predicted as it is highly specific to different assays and type and concentration of NP exposure.[13,66] Thus, it is critical to include proper controls when designing each set of specific experiments. Rosslein et al. have provided a good example by using cause-and-effect analysis to design a well-controlled MTS assay layout on 96-well plates, taking NP interference into account.[67] Drasler et al. discussed different controls that should be added for *in vitro* nanotoxicity studies, including measurement on (1) NPs alone dispersed in testing medium for background correction, (2) untreated cells with NPs being added at the end of the actual exposure to test if NPs interfere with converted reagents (such as formazan in the MTT assay), and (3) centrifuged supernatants from NM-exposed cells to remove NP agglomerates.[17] In addition to the above controls, it is also beneficial to test if the reagents themselves will react with NPs without the presence of cells.[54] Another factor that contributes to inaccurate conclusions in nanotoxicity is insufficient purification of

colloid suspensions. Apparent toxicity measured in an assay is thus not only due to nanoparticles but also leftover reagents in the colloidal suspension. Studies have shown that impurities from insufficient purification can dominate the observed apparent toxicity in standard assays, leading to over-estimation of nanoparticle toxicity.[68-70] We thus suggest that the supernatant from NP suspensions following proper ultracentrifugation should always be included as a control in nanotoxicity assays.

Besides implementation of adequate controls, researchers have been seeking analytical methods that are free of or less sensitive to NP interference. For mammalian cell lines, visualization of cell morphology under microscopy is considered a technique that complements cytotoxicity assays, but it is not sufficient to quantitatively measure toxicity endpoints. Colony counting assay for microbial cells is widely accepted as a standard microbial toxicity assay that is not affected by NP interference.[17] Microbial cells are treated with NPs and spread onto solid medium; after overnight incubation, colonies grown from individual viable cells are counted as colony forming units (CFUs). As the biological endpoint is the number of visible colonies, it is unlikely that NPs will play a role in colony forming and counting beyond any bacterial toxicity that they display. However, both cell visualization and colony counting assays suffer from very low throughput and high labor demand. Haynes and coworkers recently developed a simple but effective assay for high-throughput bacterial nanotoxicity screening.[20] After exposure, bacterial suspension is largely diluted into fresh medium to allow re-growth. Optical interference from NPs is negligible due to the large dilution, and the re-growth profiles are quantitatively related to the relative number of viable cells, thus viability. This assay is done on 96-well plates, allowing fast and robust bacterial toxicity screening. Respirometry, where oxygen consumption by a microbial population or other organisms is measured to reflect growth and viability, is another NP interference-free test, and the Haynes lab has frequently used it to perform reliable toxicity measurement on bacterial cells.[71,72]

Impedance-based measurements are promising in terms of overcoming NP interference with fast speed and high throughput.[73-75] Impedance spectroscopy measures the resistance at electrode surfaces. Cells can attach to electrodes, and any change in the cell-electrode interface will result in changes in electrode capacity and resistance. Thus, impedance spectroscopy can be used to monitor changes in cell morphology, cell density, viability, and extent of cell adhesion. Otero-Gonzalez et al. developed a real-time cell analyzer (RTCA) based on impedance spectroscopy and measured the response of human bronchial epithelial cells upon exposure of 11 different inorganic nanomaterials.[76] Besides being interference-free, impedance spectroscopy is label-free, non-invasive, high-throughput and real-time. However, it should be noted that the biological meaning of impedance measurement is not as clear as other well-established cytotoxicity assays, making results hard to interpret and to compare with other biological endpoints. In addition, the versatility of impedance assays is limited as adhesion of cells onto the electrode surface is required to perform this assay.

Researchers have also been expanding on using "biomarkers" instead of apical biological endpoints. In toxicology, a biomarker is a characteristic that can be measured that is indicative of the level of exposure, the extent of biological response, and toxic effect or susceptibility.[77] Measurements on biomarkers are intrinsically at the molecular level and provide information on toxicity mechanisms.

Genotoxicity assays that measure toxic effects on DNA have been used to evaluate the risk of nanoparticles, especially nanomedicines, and whether current genotoxicity assays are suitable for nanotoxicology has also been discussed.[18,65,78] The Comet assay is a genotoxicity assay that measures DNA strand breakage using single-cell electrophoresis. After treatment of NPs, cells are embedded in agarose, lysed *in situ*, and released DNA is imaged after electrophoresis. Concerns about NPs directly reacting

with either naked DNA released from cells or lesion-specific endonucleases as reagents have been examined, and it is generally believed that Comet assay is adequate for NP genotoxicity, though caution still needs to be taken due to possible interferences.[79-84] The Ames test, chromosome aberration, and micronucleus assays were tested on AuNP genotoxicity, and authors concluded that the latter two assays are more suitable for NP genotoxicity test as chances are low for reagents to directly interact with DNA.[85] Further tests need to be done to validate genotoxicity assays, focusing on understanding interference and expanding genotoxicity assays from mammalian cells to microbes.

Measurements at the mechanistic level beyond genotoxicity, such as gene expression, metabolite secretion, immunotoxicity, and changes in epigenetics have been explored and discussed recently as alternative ways to evaluate the toxicity of NPs.[86] These measurements, while more complicated, are always free of NP interference because NPs are usually excluded during sample preparation and not present at the point of measurement. One challenge for these assays is to validate proposed biomarkers and relate the measurement at the molecular level to organism- or cell-level biological endpoints such as population survival. Elucidation of all biological processes related to one specific biomarker is also desired for biomarker validation.

In conclusion of the aforementioned factors, toxicity evaluation of NPs should avoid relying on one single assay, especially when the assay might be subjected to NP interferences. Multiple assays on the same, similar, or related endpoints should be performed to confirm a certain effect. An example mentioned earlier is investigating AuNP genotoxicity using four different assays.[85] While a fluorescence assay for ROS might suffer from NP interference, examining gene expression changes on ROS-related genes can be used to complement fluorescence assays.[87] Even for cytotoxicity assays, it is good practice to use multiple assays to reach a more solid conclusion. In addition, standardized operating procedures across labs is also desired to minimize the

discrepancies in studies reported from different labs. Toxicity response is, to an extent that is not fully realized by the nanotoxicology community, surprisingly dependent on plenty of factors other than NP dosage, including cell density, cell status, assay background, reagent concentration, etc.[24] Measurement on NP toxicity adds another layer of complexity in terms of dosimetry, as NPs can be quantified in different ways (e.g. mass/particle/surface area concentration).[24] Piret et al. reported an inter-laboratory study on a series of *in vitro* cytotoxicity and pro-inflammation assays to test NP toxicity and examined potential sources of variation in these protocols.[88] Standardized procedures among labs, plus as many details as possible being reported in publications, will help to find the source of discrepancy among different labs.

1.4. Connecting NP interaction to biological responses at single-cell level

In the first and second generations of studying nano-bio interactions, one dominant focus has been on the response of cell populations to NM exposure. Such ensemble approaches have been used widely in cell viability and functional assays. Easy-to-perform, ensemble measurements have established strong foundational knowledge of the types of interactions between NMs and cells and the biological response by populations of cells to NMs.

As we are approaching a new decade for nanotoxicology, many researchers have realized the importance of studies at the single cell level, due to the heterogeneity of both cell and nanoparticle populations. Xia et al. outlined that cell populations can vary cell-to-cell depending on genetic variations, different cell cycle phase, biochemical state (namely protein concentrations/bursts), and microchemical environments.[89] Nanomaterials, different than traditional molecular toxicants, could vary from one particle to another within a population in terms of size and structure; thus, the load of NPs within individual cells within a population can vary. Assessing NP effect on population level biological systems risks averaging out the real effect of NP exposure,

and results in difficulty distinguishing a bimodal response, where some cells respond weakly and others respond strongly, from a unimodal response in which all cells exhibit similar responses. The averaging of biological responses may hamper the development of molecular level insights into mechanisms of interactions and likely contributes to the high level of disparate data in nanotoxicology studies. Thus, it is critical to push past the limitation of population measurements towards single-cell level analysis.

Two general categories of analytical methods are available to study NPs interacting with single cells: imaging-based and cytometry-based techniques. Imaging-based, i.e. microscopic, methods are frequently used to study NP uptake, co-localization and trafficking in cells, as they can resolve fine details of NPs interacting with sub-cellular components and monitor kinetics of NP-single cell interaction over time. While lacking structural and temporal information, flow cytometry and mass cytometry provides much higher throughput, better quantification, and possibilities to separate cells into sub-populations for subsequent studies. To correlate cellular responses to effective NP loads at a single-cell level, measurements of both NP uptake/localization and biological response needs to be achieved simultaneously on the same single cell. This represents one big challenge for analytical nanotoxicologists, and current single-cell techniques need to be expanded and integrated to achieve this goal. In this section, we highlight three recent studies that correlate cellular NP load to response on a single-cell level and discuss related recent analytical advances toward this goal.

Case study: high-content imaging to correlate cellular NP load to single-cell response. Starting very early in the field of nanotoxicology, microscopy has been a powerful tool to study NP-cell interactions. Depending on the purpose of the study (co-localization, trafficking or quantification), the nature of biological samples (fixed or living cells) and the size of NPs (small or large), a whole collection of microscopy methods ranging from electron to optical microscopy can be potentially useful. Amongst all,

fluorescence microscopy is the most widely used based on its versatility and simplicity. Combined with a wide range of fluorescent dyes available to label cellular components and indicate cellular activity, fluorescence microscopy can co-localize NPs in fixed cells or track single particles dynamically in living cells, both at single-cell resolution.[90-94]

Recent work from Manshian et al. made the first attempt to correlate the concentration of QDs at the single-cell level using high-content imaging with confocal microscopy.[95] High-content analysis (HCA) is a multi-color imaging-based technique frequently used for drug discovery.[96] Using different fluorescent tags, multiple cellular phenotypes can be monitored with simultaneous readout, thus named as "high-content". HCA has been applied to nanotoxicity studies. Jan et al. stained neural cells with four fluorescent dyes: Hoeschst for nuclei, TMRM for mitochondrial membrane potential, Fluor-4 for free calcium concentration, and propidium iodide for membrane integrity, to evaluate if a single cell is healthy, impaired or dying upon QD exposure.[97] Other work using zebrafish embryos,[98] fibroblast cell lines,[99] and various other cell lines[100] has demonstrated that HCA is a powerful tool to study cellular response at a single-cell level. Pushing it further, Manshian et al. simultaneously quantified the relative QD load of individual cells based on QD intensity and area in cells, and binned data on single cell biological responses into categories based on NP load (**Figure 1.3**). As a result, they found conflicting mechanisms such as apoptosis and autophagy in cell subpopulations with medium to high QD load at apparent sub-cytotoxic concentrations. Together with other work, this study revealed that cell populations do not respond to NPs uniformly, and the distribution of single-cell response is correlated to NP load per cell.

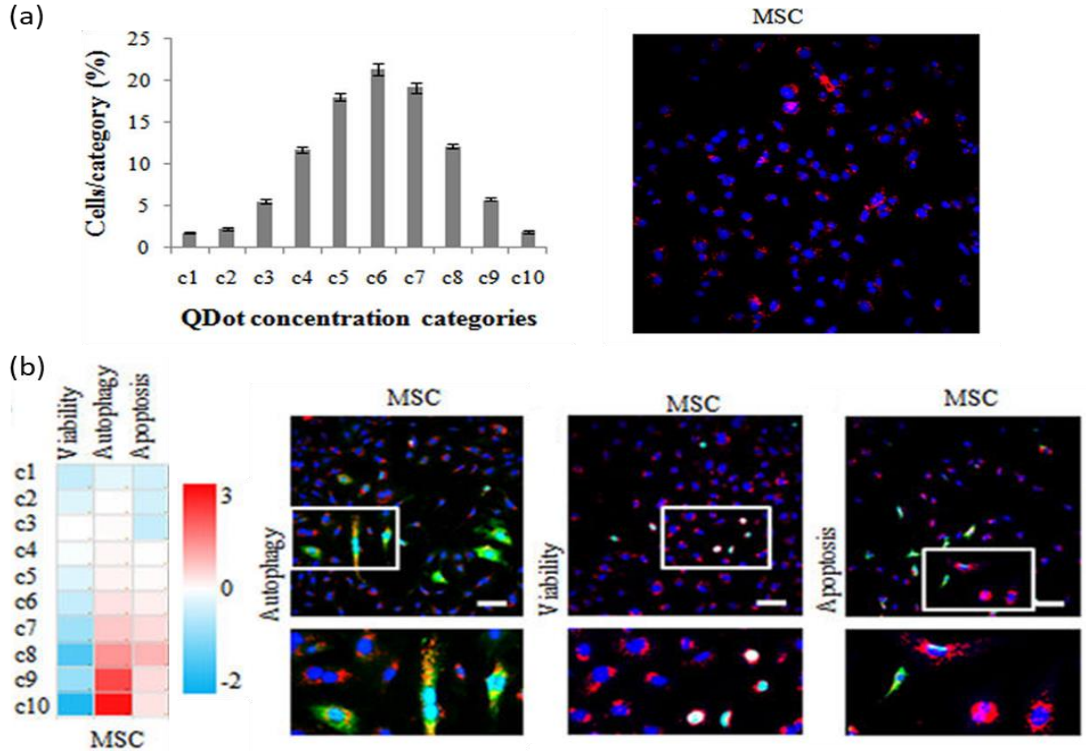

Figure 1. 3 (a) Histograms indicating the number of MSC cells per QD-load category and a representative image of MSCs exposed to 10 nM QDs. The population was divided into 10 categories spanning the range of determined QD load for individual cells. (b) Heatmap showing cell response in viability, autophagy and apoptosis clustered for each categories of NP load and representative HSC images for each kind of response. (Adapted from **Ref 95** under the Creative Commons license.)

The work highlighted above by Manshian et al. used microscopy to obtain data to correlate NP load to cell response at the single-cell level. Such microscopic studies can benefit from (1) **precise quantification and dynamic tracking of NPs** and (2) **visualization of cellular processes with high resolution**; both rely on the development of state-of-the-art microscopic techniques and the integration of multiple imaging techniques to obtain data about NP load and cell response simultaneously. Recently, Vanhecke et al. discussed in a review the most recent advances in quantifying NPs at single-cell levels,[101] and Ivask et al. presented a comprehensive review on methodologies for NP-cell interactions.[21] Generally, conventional optical microscopy is semi-quantitative for NP quantification, due to the diffraction limit, fluorophore quenching, optical interference from samples, etc. Confocal fluorescence microscopy

has been extensively used to visualize NPs with limited capability for NP quantification. Label-free optical methods have also been applied to image non-fluorescent NPs, such as hyperspectral imaging for QDs and AuNPs[102,103] and Raman spectroscopy for carbon nanotubes and TiO_2 NPs.[104,105] Lasne et al. presented a home-built imaging system to track individual 5-nm gold NPs in living cells by detecting the laser induced scattering around a nanoabsorber (LISNA).[106]

Beyond the optical diffraction limit, electron microscopy achieves resolution better than the size of NPs. Traditional biological transmission electron microscopy (bio-TEM) requires sample preparation including fixation and slicing into ultrathin sections, making quantification difficult unless 3D imaging can be re-constructed from 2D stacks, and even then, the small sampling volume presents challenges to quantitation. Advances in liquid cell TEM have enabled whole-cell imaging in aqueous medium, though its resolution still needs improvement.[107] In addition, conventional bio-TEM is not able to clearly differentiate between high mass contrast stained cellular components and exogenous NPs.[108] Dark-field TEM, applied for nanotoxicology in our group, helps to solve this problem by looking for the unique diffraction patterns from crystalline nanoparticles but not stained biological components.[109] Besides electron microscopy, super-resolution imaging, a collection of optical imaging techniques that overcome the diffraction limit, has also been employed to acquire fine details on NP localization and trafficking in cells. A direct comparison was made between confocal fluorescence microscopy, stochastic optical reconstruction microscopy (STORM), and electron microscopy to co-localize NPs with organelles in HeLa cells, showing that previously unknown details at nanoscale resolution can be revealed by super-resolution microscopy.[110] Using structural illumination microscopy (SIM), Gunsolus et al. revealed co-colocalization of QDs on the cell membrane of Gram-positive and Gram-negative bacterial cells.[111] Compared to electron microscopy, super-resolution microscopy provides possibilities to image live cells and multiple cellular components

along with NPs simultaneously, though requirements for particular fluorophore characteristics (e.g. photoswitchable dye for STORM) still limit universal application.

Mass spectrometry imaging provides chemical information that is not available through optical imaging. Using a laser to ablate and vaporize surface materials of a sample, laser ablation inductively coupled plasma mass spectrometry (LA-ICP-MS) uses ICP-MS for elemental analysis. LA-ICP-MS has been used for bioimaging of metals.[112] As an example of its application in nanotoxicology, Elci et al. applied this technique to characterize the biodistribution of AuNPs in mice organs.[113] However, LA-ICP-MS cannot differentiate (1) NPs and biomolecules if they contain the same element (e.g. carbon nanotubes), and (2) elements in different forms, e.g. AgNPs from Ag ions. Laser desorption/ionization mass spectrometry imaging (LDI-MSI) applies laser irradiation to ionize molecules on a sample surface and analyzes the generated ions with a mass analyzer. With the assistance of a solvent ("matrix"), matrix-assisted LDI-MSI (MALDI-MSI) allows detection of a wide range of biomolecules.[114] Chen et al. mapped a carbon cluster fingerprint with MALDI-MSI to reveal the distribution of carbon nanomaterials in mice organs and tissues.[115] By tuning laser fluency, LDI-MS was used to differentiate cell surface-bound and internalized AuNPs.[116] Higher resolution MS imaging can be achieved by secondary ion mass spectrometry (SIMS), a surface analysis technique achieved by sputtering the surface of sample using highly focused primary ion beams and analyzing the ejected secondary ions. SIMS has been used to examine metabolites and nanoparticle distribution in single cells.[117-120] Overall, mass spectrometry imaging provides good quantification of NPs and simultaneous determination of biological matrices through elemental and mass analysis.

The power of correlative microscopy has been underutilized for NP-single cell interaction studies. Le Trequesser et al. assessed uptake of TiO_2 NPs into individual primary human foreskin keratinocytes cells by using multimodal correlative

microscopy: fluorescence microscopy for sub-cellular compartments, scanning electron microscopy (SEM) for surface analysis, and ion beam analysis (IBA) for in-depth elemental analysis and *in situ* quantification of TiO_2 NPs.[121] Similarly, quantification of ZnO NP uptake, distribution, and dissolution was done by combination of ion beam milling, X-ray fluorescence microscopy, and SEM.[122] A more complicated system where mass spectrometry imaging and super-resolution microscopy were integrated into a home-built microreactor called the "system for analysis at the liquid vacuum interface (SALVI)" was used to perform time-of-flight SIMS (ToF-SIMS) and structural illumination microscopy (SIM) on the same sample.[118] SIM was used to characterize cells and guide subsequent ToF-SIMS analysis. ToF-SIMS identified lipid fragments and ion transport upon NP exposure and showed direct evidence of ZnO NP uptake as well. Multi-modal correlative microscopies provide details that complement each other from the same sample, showing numerous possibilities for studies on correlating the status of NPs in cells to biological responses at the single-cell level. A great example is from Liu et al., who used a combination of bright field microscopy, fluorescence microscopy, and AFM for estimation of NP load, cytoskeleton and ROS production, and single-cell mechanics, respectively.[123] The level of NP uptake was related to changes in cell stiffness, ROS production, and damage to the actin network. Multimodal correlative microscopy, combined with other assays, provides information at multiple dimensions and thus helps to understand causal relationships between NP exposure and biological consequences. The power of multimodal correlative microscopy is yet to be fully exploited in nanotoxicology studies.

Microscopy can also be combined with single-cell electrochemical analysis, whose application in nanotoxicity has been reviewed.[73] The Haynes lab pioneered using carbon fiber microamperometry (CFMA) to monitor exocytosis from single mast cells and other cell types upon AuNP, AgNP and TiO_2 NP exposure.[124-128] Exocytosis is a highly conserved cell function across cell types and plays important roles in chemical

communication among cells. By using microelectrodes, the Haynes group was able to monitor the process of single-cell exocytosis and correlate changes in single-cell exocytosis to bulk measurements of NP uptake and cytotoxicity. Using a microelectromechanical system (MEMS)-based sensing array that can trap cells, Shah et al. presented a platform for electrochemical impedance spectroscopy of single cells and small cell populations upon metal oxide NP exposure.[75] As slow speed might be one drawback of single-cell electrochemical measurements, MEMS systems with cell capturing capability and sensing arrays present a future direction for the integration of single-cell microscopic and electrochemical measurements with fast speed and relatively high throughput.[129,130]

Case study: flow cytometry, and single-cell RNA-Seq for cells with varied QD loads. There are two circumstances beyond reach of imaging techniques despite their versatility: when analysis of millions of cells is desired or when single cells need to be separated first for subsequent analysis. Flow-based single-cell techniques, including flow cytometry, mass cytometry, and cell sorting have provided solutions for both research needs. Cells and particles are suspended in a fluid and pass through laser(s) in a fluid stream as separated single cells. Using different detectors, multiparametric detection of each individual cell's optical characteristics such as light scattering and fluorescence can be achieved simultaneously. Coupled with ICP-MS, cytometry can perform elemental analysis on single cells, called mass cytometry. Originally, mass cytometry specifically referred to the detection of metal ion labelled antibodies in single cells[131] but now researchers have adapted this technique for NP quantification in cells.[132] Cell sorting techniques further allow the separation of single cells based on their characteristics, such as the amount of associated NPs and further analysis like single-cell -omics.

Here, we highlight two studies to demonstrate the power of flow-based single-cell

techniques. The first study is from Toduka et al. where flow cytometry was used to correlate NP association and cellular response at the single cell level.[133] Compared to microscopy, flow cytometry provided orders of magnitude higher throughput. Side scattering (SSC) was developed to evaluate NP association with mammalian cells[134,135] and bacteria[71,136] and combined with fluorescence staining to determine cellular states. Pan et al. used SSC to gate a NP-loaded cell subpopulation and evaluate the states of these gated cells as healthy, apoptotic, or necrotic based on fluorescence staining on the same cell population.[137] Pushing it further, Toduka et al. plotted SSC versus fluorescence induced by intracellular ROS after their simultaneous detection with flow cytometry upon metal oxide and Ag NP exposure. Results showed clear correlation between NP association and ROS production in single cells (**Figure 1.4**). With analysis of millions of cells, flow cytometry provides richer information than bulk experiments. Recent development of imaging flow cytometry further enables analysis of cell morphology and particle tracking.[138] Such combination of microscopic and flow cytometry analysis makes it a powerful tool for future high-throughput and high-content single-cell analysis for nanotoxicology, as it has been applied.[139]

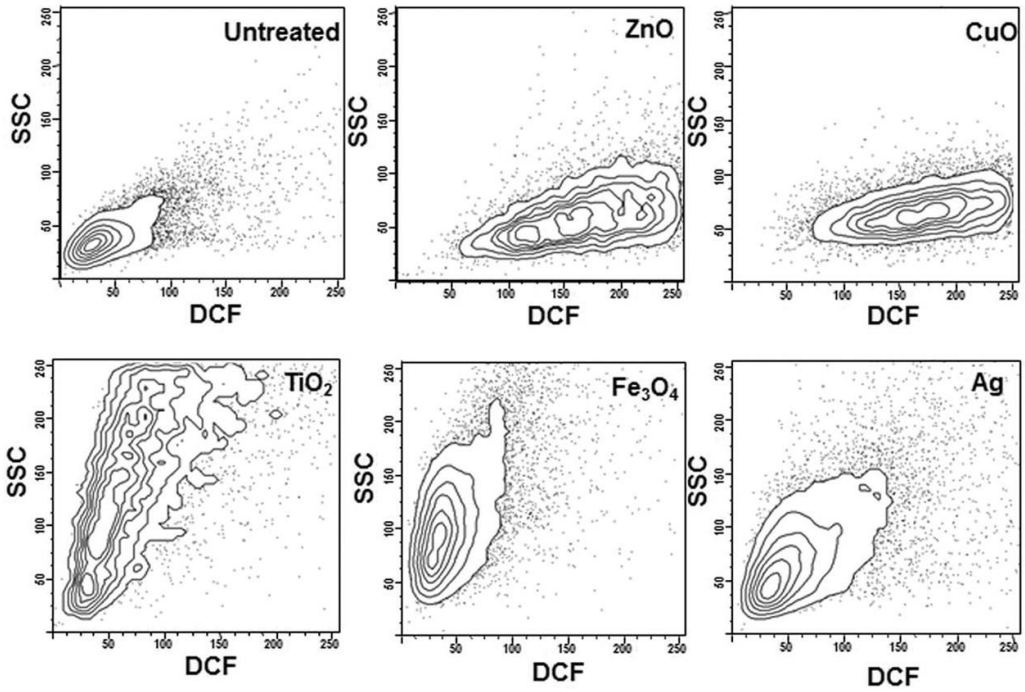

Figure 1. 4 Contour plot patterns of SSC and DCF intensity showed correlation between NP association and ROS production in single cells. Reprinted with permission from **Ref 133**. Copyright © 2012 American Chemical Society.

For more accurate quantification of NP association, as stated earlier, Yang et al. adapted mass cytometry for high-throughput quantification of AuNPs in single cells.[132] Compared to flow cytometry, mass cytometry showed higher sensitivity and lower limits of detection for measuring NP load. Combined with metal-chelated antibodies, cell types and NP load per cell were determined simultaneously for each individual cell. While achieving precise quantification and high sensitivity, mass cytometry removes information on the chemical status of elements, e.g. dissolved ions vs. NPs. In the future, integration of flow cytometry and mass cytometry on one platform is promising for giving precise and comprehensive information on NP-single cell interactions.

Flow-based cell sorting techniques provide capability to separate and collect sub-populations of cells for subsequent analysis. In fluorescence-activated cell sorting (FACS), individual cells in the fluid stream are given different electrostatic charges based on detected fluorescence and deflected to containers at different sides by passing

between two charged plates.[140] Other optical characteristics can be used for cell sorting as well. As an example, Jacobson et al. used both fluorescence and side light scattering to sort live cells with AuNP association, and dark-field microscopy plus hyperspectral imaging was subsequently used to confirm that the sorted cells were associated with AuNPs.[50] Another recent study by Mitchell et al. combined cell sorting techniques and single-cell -omics.[141] Gene expression and transcriptomics have been extensively used in nanotoxicology on both prokaryotic and eukaryotic cell lines to reveal NP toxicity mechanisms, while studies on single-cell levels are scarce. In this study, a fluorescence-activated cell sorter determined the level of QD load to each single cell based on QD fluorescence intensity and harvested the portions of cells associated with high or low level of QD load. Individual cells were then analyzed by single-cell RNA-Seq, an -omics technique allowing global gene expression profiling in one single cell. Results showed that cells carrying lower QD loads responded with multiple strategies that are different for each QD type, while high loads of QD induced more uniformly, mostly down-regulated processes shared across QD types. This study clearly linked cellular NP association to gene expression profile, which would have been averaged and likely not observed in bulk experiments. As single-cell -omics are emerging in all -omics areas, including transcriptomics, proteomics, metabolomics, genomics and epigenomics,[142,143] it is promising to combine them with flow cytometry and advanced cell sorting platforms[130] and reveal otherwise unavailable details on the molecular level.

1.5 Real-time and *in situ* measurements with chemical information at nano-bio interface

The interface between NPs and biological systems is dynamic. The NP surface, the solid-liquid interface when NPs interact with surrounding medium, and the contact zone where the solid-liquid interface encounters a biological system are closely interconnected and constantly undergoing changes.[19] Upon entering a new matrix, pristine NPs instantly gain new "identities" via interacting with surrounding molecules,

including chemical reactions and dissolution, biological transformation and physical adsorption of surrounding molecules, both in biological and environmental media.[144,145] NPs with the new "identity" then interact with biological systems like cell membranes. Such interactions can induce cellular responses, change the behaviors of cell membranes in contact with NPs, and further alter NP characteristics in turn. The dynamic nature of nano-bio interactions thus requires powerful physical and analytical tools for real-time and *in situ* measurements to resolve the kinetics of nano-bio interactions without disturbance. Depending on NPs' pristine surface, surrounding environment, and biological systems, nano-bio interactions can be loose or tight, as non-specific as electrostatic interactions or as specific to certain binding sites as antigen-antibody binding.[144] Understanding the chemical nature of nano-bio interactions will greatly contribute to the establishment of nano-QSAR and other predictive models. With all this in mind, an ideal technique to monitor the nano-bio interface should be both real-time and *in situ*, and the capability to provide chemical information would be a significant advantage. Here, we discuss techniques used for capturing the kinetics at the nano-bio interface on the two aforementioned interfaces: interactions between NPs and surrounding molecules in the medium and interaction of NPs with model membranes or biological systems.

Measurement on NPs interacting with surrounding molecules. The new "identity" of NPs when entering a new matrix is decided by their pristine surface features, chemical reactions, physical adsorption, and biological transformation. Chemical transformation of NPs in aqueous medium includes dissolution, oxidation, ligand exchange, surface coating degradation, photocatalytic reactions, etc.[145] Although not necessarily a "nano-bio" interaction, chemical reaction accompanies bio-mediated reactions and physical adsorption and is an integral part of the process to form NPs' new identity. Mechanisms of chemical reactions on NP surfaces, especially dissolution, photochemistry and catalysis, have been extensively studied.[145-147]

Attachment of surrounding molecules through physical adsorption ranges from ions to small molecules to biomacromolecules via forces including hydrodynamic, van der Walls, electrostatic and static interactions, plus hydrophobic effects.[19] Physical adsorption has been widely studied in the context of human health[144] and the environment,[148] and is believed to be the main source of NPs' identity in biological and environmental matrices. As a prominent example, the protein "corona", referring to layers of tightly or loosely bound proteins on NP surfaces, has undergone extensive investigation in the past decade.[149] A common practice to study the protein corona is separating NPs from aqueous matrices via centrifugation and stripping off the NP-bound proteins for further analysis using methods such as gel electrophoresis and mass spectrometry. Such separation-based techniques have been used to study protein corona evolution at the time scales of minutes to hours.[150-152] To study protein adsorption kinetics at a much shorter time scale, correlation spectroscopy has been used. Vilanova et al. used fluorescence correlation spectroscopy (FCS), a sensitive fluorescence technique to measure concentration and size of particles by monitoring fluorescence fluctuation in solution to estimate the fraction of protein binding to the NP surface and adsorption kinetics.[153] Scattering correlation spectroscopy and surface plasmon resonance were also used for *in situ* measurement of protein interaction with gold NPs[154,155] and del Pino et al. gave an extensive review on how kinetic parameters can be extracted from spectroscopic data.[156]

While techniques based on absorbance, fluorescence, scattering (e.g. dynamic light scattering) and surface plasmon resonance can be used to determine kinetic parameters, chemical information is not available from these studies. Attenuated total reflectance Fourier transform infrared (ATR-FTIR) spectroscopy is a surface analysis technique capable of real-time and *in situ* characterization of surface dynamics with chemical information. ATR-FTIR utilizes the evanescent field of the total internal reflection (TIR)

of infrared radiation at the solid-liquid interface, and the surface sensitivity stems from the short penetration depth (at the magnitude of 1 micrometer) of the evanescent field. NPs are typically immobilized on the ATR crystal, and adsorption of molecules onto NP surfaces is monitored over time; specific functional groups in adsorbed molecules can be thus identified by examining detected IR absorption bands. Mudunkotuwa et al. has given a detailed review on the application of ATR-FTIR spectroscopy to investigate nanoparticle surface adsorption,[157] and numerous studies have shown the application on probing NP surface adsorption of proteins[158-160] and small molecules such as surfactants[161] and phosphate.[162] A vibrational spectroscopy, Raman spectroscopy also provides chemical information at the nano-bio interface. By using plasmonic NPs as substrates, surface-enhanced Raman spectroscopy (SERS) amplifies Raman signals near metallic substrates, thus it's a great platform for probing nano-bio interactions. Bonifacio et al. systematically studied the SERS spectra of Ag and AuNPs in blood plasma and serum to fingerprint biological fluid composition.[163] In another study, SERS spectra of serum albumin protein and cysteine adsorption onto AgNPs were acquired and compared with Raman spectra of free protein and cysteine, showing a strong decrease in S-S bond signal in the adsorbed protein.[164] Micro Raman spectroscopy is also used to study NP interactions with small molecules such as ATP.[165] Overall, the capability of both ATR-FTIR and Raman/SERS is yet to be explored for dynamicly probing NP surface adsorption of surrounding molecules, especially in complex matrices that contain multiple species.

Solution nuclear magnetic resonance (NMR) has been a tool to examine protein and ligand adsorption onto NP surfaces. Binding and exchange of ligands on NP surfaces from small molecules to polymers and proteins can be characterized and quantified using ^{1}H NMR, while NPs usually needs to be centrifuged or dried followed by re-suspension for ^{1}H NMR analysis. [166,167] Wang et al. achieved *in situ* measurement on protein adsorbing to 15-nm AuNP surfaces using solution ^{1}H NMR and two-

dimensional TROSY NMR with ^{15}N labeled proteins.[168] No centrifugation was needed prior to NMR measurement, and the measurement time was reduced to as little as 10 min. Combined with data from a binding competition assay and results from other work, the authors concluded a three-step model for protein adsorption onto AuNP surface: reversible association at first, followed with rearrangement/reorientation, and finally irreversible binding via cysteine to AuNP surface. Using relaxation-based solution NMR, Ceccon et al. revealed the global motions and exchange kinetics on the microsecond scale for a model protein, ubiquitin, binding to negatively charged lipid nanoparticles (liposomes).[169] Another NMR technique, solid-state NMR, has also been used to characterize the interactions between ligands and NP surfaces.[170,171] Together with other spectroscopic methods, NMR represents a powerful technique to study the kinetics of molecule adsorption onto NP surface with chemical information.

Measurement on nano-bio interaction with model membranes and cells. When NPs reach a biological organism, the first interface they will likely to encounter is a cell membrane.[19] Thus, the interaction between NPs and membranes has been a focus for researchers interested in nano-bio interactions. The characteristics of the cell membrane can vary drastically among different organisms. For example, Gram-negative bacterial cell membrane features a large coverage of lipopolysaccharides (LPS), while the Gram-positive bacterial cell membrane is covered with a thick peptidoglycan layer and teichoic acids. Membranes of most eukaryotic cells contain proteins, glycolipids and components other than phospholipids. Nevertheless, phospholipids compose the main structure of a cell membrane. Model membrane systems are manually constructed lipid bilayers to mimic real cell membranes. By tailoring the composition (e.g. ratio of different phospholipids and other components) and architecture (e.g. vesicle, planar supported bilayer, etc.), model membrane systems have been an effective approach to study cell membrane functions, the role of different membrane components, and membrane interactions.[172] Naturally, this approach has been widely applied to

understand the interaction between NPs and membranes. A recent review by Rascol et al. has discussed in detail the application of model membrane systems for investigating nano-bio interactions.[173]

Depending on the hypothesis of interest, three architectures are among the most commonly used model membrane systems: lipid bilayer vesicles, planar lipid bilayers, or supported lipid bilayers. Lipid vesicles, i.e. liposomes, are structurally the closest to real cells and range from tens of nanometers to hundreds of micrometers. Microscopy and dye leakage assays, in which vesicle-encapsulated dye molecules are released upon membrane disruption, can be used to assess lipid bilayer permeation upon NP exposure and NP association and colocalization with vesicles.[174-177] Planar lipid bilayers can be tethered between two bridges to separate two chambers filled with electrolytic solution for capacitance measurements. Changes in planar lipid bilayers upon NP interaction can be probed via measuring changes in their capacitance.[178] While these measurements on vesicle and planar bilayers provide visualization and dynamics of NP-membrane interactions, they are not quantitative in determining the extent of NP binding to model membranes and also lack chemical information.

In contrast to free-floating lipid vesicles and tethered planar lipid bilayers, supported lipid bilayers (SLB) are formed on planar solid surfaces. The solid surface helps to stabilize the SLB, providing high flexibilities in tuning composition, architecture and fluidity of model membranes. Quartz crystal microbalance with dissipation monitoring (QCM-D) has been extensively used to quantify the extent of NP binding and membrane disruption as well.[173,179,180] When mass is added to or removed from a piezoelectric crystalline quartz, changes in the quartz's mechanical resonance frequency is proportional to the mass change. Using QCM-D, the deposition kinetics of graphene oxides on SLBs were determined.[179] Combined with atomic force microscopy (AFM) and structured illumination microscopy (SIM), Melby et al.

explored the interaction of 4-nm AuNPs on model membranes that contained segregated domains.[181] Besides QCM-D, AFM and other microscopies as well as electrochemical techniques are used for real-time and *in situ* measurement of membrane changes. Lu et al. showed fabrication and application of microfluidic lipid bilayer arrays for high-throughput electrochemical measurements on NP-membrane interactions.[182]

As mentioned at the beginning of this section, the capability to provide chemical information on nano-bio interactions would be enlightening. While QCM-D and microscopic techniques complement each other as quantitative and qualitative measurements, sum-frequency generation (SFG) spectroscopy is a surface-/interface-sensitive technique that performs real-time and *in situ* measurement on molecular symmetry. In two recent studies, the dynamics of inner and outer leaflets of lipid bilayers upon interacting with AuNPs[183] or chitosan NPs[184] were determined by collecting a time series of SFG spectra. Combined with ATR-FTIR, Hu et al. concluded that SLBs undergo a flip-flop movement upon AuNP interaction.[183] A comprehensive study performed by Troiano et al. using SFG along with a series of other techniques determined the dynamics of positively or negatively charged AuNPs interacting with SLBs with different lipid compositions.[185]

Currently, most model membrane systems are quite simple, consisting of a few phospholipids and occasionally incorporating other membrane components. Increasing the complexity of model membranes by adding more components such as lipopolysaccharides (LPS)[50] and membrane proteins and exploring different composition ratios will bring the system closer to real cell membranes. Extracted cell membranes might also be used and compared with model membrane systems of controlled composition. In addition, spectroscopic methods that provide chemical information, such as SFG, ATR-FTIR, SERS and NMR, used in combination with

microscopy will further facilitate *in situ* measurement of the NP-membrane interface. As evidence from model membrane experiments has been used to complement both experimental data on cell-NP interaction[186] and computational simulation,[175,187] studies on NP-membrane interaction will continue to serve as a bridge that connects nano-bio interaction systems at different levels of complexity.

1.6 Conclusion

Analytical chemistry plays a big role in nanotoxicology, ranging from characterization of NP properties to measurement of biological response upon NP exposure. As we are entering the third decade of nanotoxicology, building predictive models between NP properties and biological outcomes for safe NP design is more critical than ever, as confusion and discrepancies prevent accurate assessment of NP toxicity due to the unique characteristics of nanomaterials. Herein, we identified four analytical challenges in nanotoxicology for the next decade, including shifting studies on nanotoxicity mechanisms from correlative to causative, overcoming NP interferences for accurate *in vitro* nanotoxicity assays, connecting NP interaction to cellular response at the single-cell level, and developing a kinetic understanding of various nano-bio interfaces with chemical information. With these challenges in mind, analytical chemists will continue to contribute to solving puzzles in nanotoxicology and build predictive models together with wide collaboration with researchers in biology, materials science, and computational chemistry.

Chapter 2

A mechanistic study of TiO_2 nanoparticle toxicity on *Shewanella oneidensis* MR-1 with UVA illumination: bacterial growth, riboflavin secretion, and gene expression

Adapted from:

Qiu, T. A., Meyer, B. M., Christenson, K. G., Klaper, R. D., Haynes, C. L., A mechanistic study of TiO_2 nanoparticle toxicity on *Shewanella oneidensis* MR-1 with UV-containing simulated solar irradiation: Bacterial growth, riboflavin secretion, and gene expression, ***Chemosphere***, 2017, **168**, 1158-1168.

2.1 Introduction

The biocidal effect of titanium dioxide (TiO_2) nanoparticles (NPs) has resulted in extensive development of TiO_2-NP-based anti-microbial materials,[1-3] but also generated rising concern about the adverse effects of TiO_2 NPs on non-target species in ecological systems. Previous studies have revealed toxicity of TiO_2 NPs to ecologically relevant organisms, including algae, zebrafish, water fleas, and fish.[4-7] The intended biocidal effects of TiO_2 NPs, combined with the potential release of TiO_2 NPs into the environment[8,9] with anticipated increase in the usage of TiO_2 NPs,[10,11] generates an emerging need to assess the ecological risk of TiO_2 NPs on relevant organisms.[12-14]

Although released NPs can potentially affect all organisms within the food web, low trophic level organisms like bacteria are most likely to interact with released NPs due to their wide distribution and their localization in microenvironments where nanoparticles may accumulate. Quite a few studies have addressed the influence of TiO_2 NPs on bacteria species, but most of these studies focus on *E. coli* and other pathogenic bacteria.[15-18] *Shewanella oneidensis* MR-1, an environmentally beneficial Gram-negative bacterium of genus *Shewanellae*, has a unique dissimilatory metal-reducing capability to respire heavy metals, including Mn(III), Mn(IV), Fe(III), and Cr(VI).[19,20] With this capability, *S. oneidensis* MR-1 plays an important role in solubilizing metal salts for species throughout the food web as well as having a potential role in bioremediation of toxic elements in the ecosystem. Because of these environmental implications, *S. oneidensis* MR-1 has been employed to study toxicological response to environmental factors like pH, heavy metals and electron acceptors.[21-24] Though to a very limited extent, it also has been employed as an environmentally relevant bacterial model in nanotoxicity studies as is done here.[25-27]

Mechanistic studies of the adverse effects of toxic agents can provide important implications for the assessment of ecological risk and the prediction of toxicity. One of

the most studied mechanisms of TiO_2 NP impact on biological systems is the generation of reactive oxygen species (ROS), which could potentially be a molecular initiating event in damage to cells by nanoparticles.[4,18,28-30] As a photocatalyst, TiO_2 NPs absorb photons and generate electron-hole pairs, and these charge carriers move to the NP surface; ROS can be generated during the reaction between the TiO_2 NP surface and the surrounding aqueous medium.[31] Previous work has shown that UV-illuminated TiO_2 NPs exhibited higher toxicity across species than TiO_2 NPs alone, and ROS generated by TiO_2 NPs are believed to be the means by which TiO_2 NPs kill bacteria.[15-17] Li et al. built a linear correlation between the total ROS generation by metal oxide NPs, including TiO_2 NPs, and the toxicity of these NPs to *E. coli*.[18] The production of intracellular ROS could result in subsequent cellular response including lipid peroxidation or DNA damage, either of which could be measured as endpoints.[32] In *S. oneidensis* MR-1, the secretion of riboflavin is one important cellular endpoint that can be monitored. Riboflavin is a redox molecule that acts as an electron shuttle between the cell surface and external acceptors like metal oxide surfaces and plays a critical in cell-mediated metal reduction.[33,34] The presence of riboflavin is also important in its role as a photosensitizer as it was found to generate ROS in a light-dependent manner.[35] In fact, previous research has demonstrated that the amount of *S. oneidensis*-secreted riboflavin increased as a cellular response upon TiO_2 NP exposure.[25]

Efforts have been made to elucidate the molecular responses upon TiO_2 NP exposure by monitoring changes in gene expression levels.[36-39] Nanoparticles have been shown to cause changes in RNA expression levels in organisms varying from human cells to bacteria. Using gene expression levels to assess nanotoxicity can provide direct information on mechanisms of nanotoxicity and help identify biomarkers for future high-throughput nanotoxicity assessments.[40,41] Although oxidative stress has been identified as one of the major toxicity mechanisms in other bacterial models with various nanoparticles,[42,43] other modes of action have been revealed via gene expression

studies.[36,44-47] Kubacka et al. revealed changes in the level of gene expression related to various pathways other than oxidative stress, including the activation of detoxification and repair pathways and a decrease in a pathway related to cell-cell communication, in a pathogenic bacterium upon TiO_2-UV treatment.[36] Ideally, gene expression data, measured and correlated with other cellular responses and changes in cell population growth, could enable the construction of a sequential series of biological responses that can be used in the identification of adverse outcome pathways for nanoparticles and assist in risk assessment for TiO_2 NPs.

Herein, we used an integrated toxicology approach, from cellular responses on molecular levels to cell population change, to comprehensively explore the mechanisms of nanoparticle interaction with bacterial cells, using *Shewanella oneidensis* MR-1 as a model organism exposed to TiO_2 NPs and concurrent UVA illumination. The impact of TiO_2 NPs and UVA illumination on bacterial cell viability and population growth were monitored, followed by assessments of intracellular ROS generation and riboflavin secretion. Gene expression changes upon continuous nanoparticle and UVA exposure were also monitored at different time points. By combining several analytical methodologies to probe impacts from cell viability to gene expression, this work enables a mechanistic understanding of nanoparticle-bacterial cell interaction and brings an integrative scheme to assess the risk of nanoparticle exposure to the environment.

2.2 Materials and methods

2.2.1 Bacteria preparation

LB broth (BD Difco, BD Diagnostics, Franklin Lakes, NJ), made by dissolving 25 grams of pre-mixed LB broth powder (consisting of 10 g tryptone, 5 g yeast extract and 10 g NaCl) in 1 liter of Milli-Q water followed by autoclaving, was used in this work

as the bacteria cell culture medium. *S. oneidensis* MR-1 was a kind gift from Professor Jeffery Gralnick, University of Minnesota Department of Microbiology and was stored at -80°C before use. Bacteria were inoculated onto a LB broth agar plate and incubated at 30°C for 24 hours or until visible colonies formed. Colonies were inoculated into 5-15 mL of autoclaved LB broth in sterile culture tubes and grown overnight.

2.2.2 Monitoring cell growth over time

Bacterial growth curves were monitored by measuring the optical density (OD) of a bacterial suspension over time with different nanoparticle doses. After the bacterial suspension reached stationary phase, 200 μL of suspension was diluted with fresh autoclaved LB broth to a total volume of 5 mL to reach a diluted cell density of approximately 107 cells/mL. The diluted bacteria suspension was grown in a 30-32°C orbital shaker at 300 rpm for 6 hours either in the dark or under UV illumination with continuous exposure to 0, 1, 5, 10, 25, or 100 mg/L TiO2 nanoparticles. 200 μL aliquots were transferred periodically to a Costar® 96-well assay plate (Corning Incorporated, NY), and measurements of OD at λ = 600 nm (OD600) were recorded with a Synergy 2 Multi-Mode Microplate Reader (BioTek, VT). Background due to nanoparticle extinction and assay plate wall absorbance was subtracted to generate normalized data, which was plotted and analyzed by Prism (GraphPad Software, CA).

2.2.3 Monitoring cell oxygen uptake

Cell growth was also characterized by measuring oxygen uptake by the cell suspension over time. A PF-8000 aerobic/anaerobic respirometer system (Respirometer Systems and Applications, LLC, Arkansas) was used to monitor oxygen uptake. This instrument consists of biological reaction vessels, a stirring base for mixing samples, and a control module that contains the pneumatic and electronic controls for oxygen or gas flow measurement. Bacteria were grown in LB broth to stationary phase and diluted 1:10 into fresh autoclaved LB broth in reaction vessels to reach a total volume of 100 mL.

TiO_2 nanoaprticles were added into the reaction vessels to a final concentration of 25 mg/L or 100 mg/L. A tube filled with 1 mL 30% potassium hydroxide solution was inserted into each reaction vessel to absorb carbon dioxide released by bacteria aerobic respiration. The negative pressure created by oxygen consumption of bacteria was compensated by oxygen injection continuously to keep a constant pressure in the headspace of reaction vessel. Oxygen uptake was recorded automatically by the instrument, and each measurement was done in duplicate.

2.2.4 G6PD cytotoxicity assay for cell viability

Cell viability was measured using a commercial cytotoxicity assay, the Vybrant™ Cytotoxicity Assay Kit (Molecular Probes, OR), which uses an enzymatic fluorescence reaction to measure the glucose 6-phosphate dehydrogenase (G6PD) released from dead cells. Bacteria were first grown in LB broth overnight to stationary phase (OD_{600} = 1.5-1.7) and then exposed to 100 mg/L TiO_2 nanoparticles for 30 minutes, either in the dark or under UV illumination. The TiO_2 NPs were sonicated for 30-45 minutes prior to exposure (same for all exposures in this study). Following exposure, 1 mL of bacterial suspension was centrifuged at 17,000 × g for 2 minutes, and the supernatant was collected for measurement. A resazurin/reaction 2X mixture was prepared following the kit's protocol, and 50 µL of the mixture was added into 50 µL supernatant on a 96 well plate. The microplate was incubated at 37°C for 30 minutes in the dark before fluorescence readings were taken with excitation at 530 nm and emission at 590 nm. Cell death was proportional to the intensity of fluorescence signal. The background fluorescence signal was obtained from a control group that only contained LB broth and the resazurin/reaction mixture, and this signal was subtracted from experimental fluorescence signals.

2.2.5 Intracellular ROS generation measurement

Dichlorodihydrofluorescein diacetate ($DCFH_2$-DA), which can be deacetylated by cellular esterases to a non-fluorescent intermediate that is later oxidized to fluorescent 2', 7'-dichlorofluorescin (DCF) upon reaction with ROS, was used as an indicator of ROS. $DCFH_2$-DA was diluted to a 10 μM working solution using fresh LB medium. Then, 100 mL of bacterial suspension was grown to the stationary phase (OD_{600} = 1.5-1.7) followed by centrifugation for 10 minutes at 1,500 ×g. After decanting the supernatant, the bacteria cell pellet was resuspended with 40 mL $DCFH_2$-DA 10 μM working solution. The resulting suspension was then incubated at 30°C for 1 hour in the dark to avoid photo-oxidization of the ROS indicator. The bacteria suspension was centrifuged again at 1,500 ×g for 10 minutes, and the supernatant was removed. 8 mL of fresh LB broth was applied to wash the pellet three times and the cell pellet was diluted with 60 mL of fresh LB broth.

TiO_2 NP suspension was added to 2.94 mL of the final bacteria suspension to reach a NP concentration of 100 mg/L. 360 μL of bleach was used as a positive control as it can generate an excessive amount of ROS. The bacterial suspension was incubated in the dark for 15 minutes after TiO_2 nanoparticle exposure, transferred to a 96 well flat bottom polystyrene reading plate (Corning Incorporated, NY) and then either exposed to UV illumination or kept in the dark for another 15 minutes. The fluorescent signal from the ROS indicator was excited at 488 nm and measured at 515 nm by a Synergy 2 Multi-Mode Microplate Reader (BioTek, VT).

A control experiment was done to explore the interference of TiO_2 NPs on the detection of fluorescence of DCF, the fluorescent molecule converted from $DCFH_2$-DA in cells. 92.5 nM and 481 nM of DCF was diluted in fresh LB broth to generate fluorescence signals that are comparable to what were detected in bacterial suspension in the dark and under UV illumination, respectively. 100 mg/L TiO_2 NPs were added to DCF

solution and mixed well, and the fluorescence signals were read using the same method as stated above. Five material replicates were done in this control experiment.

2.2.6 HPLC measurement of riboflavin secretion

Flavin secretion, an important function of *S. oneidensis*, was measured by HPLC analysis of bacterial suspension supernatant. First, bacterial suspensions were exposed to 100 mg/L TiO_2 nanoparticles in the dark or under UV illumination. Then, 1 mL of bacterial suspension was collected from same tube after 30 min, 1 hour, or 6 hours, and centrifuged for 15 min at 5000 ×g. Exposure was done in triplicate. 200 μL of the supernatant was transferred to an amber HPLC vial with a 250 μL glass insert and placed on the autosampler of an Agilent 1200 HPLC (Agilent Technologies, CA). A Zorbax Eclipse XDB-C_{18} 4.6 × 150 mm, 5 μm analytical column was washed with acetonitrile and equilibrated using mobile phase, a 70:30 mixture of 20 mM citric acid buffer (pH 3.3)/methanol. The injection volume was 30 μL, and isocratic elution was performed with a flow rate of 1 mL/min. Riboflavin was detected by a fluorescence detector after flowing through an Eclipse XDB-C_{18} 4.6 × 12.5 mm, 5 μm analytical guard column, with excitation at 450 nm and emission at 530 nm. Riboflavin elution was achieved after approximately 6.7 min.

2.2.7 RNA extraction

RNA was extracted from bacteria cells exposed 25 mg/L of TiO_2 nanoparticles and sent to the University of Minnesota Genomics Center (UMGC) at the University of Minnesota for quantitative real-time PCR analysis. A Direct-zol™ RNA MiniPrep kit (Zymo Research, CA), allowing quick and high-quality DNA-free RNA extraction and purification using spin columns, was used according to the manufacturer's recommendations for total RNA extraction. Bacteria were grown in LB broth to stationary phase and exposed to 25 mg/L of TiO_2 nanoparticles in the dark or under UV illumination in triplicates. At 0, 0.5, 1, and 6 hours after nanoparticle exposure and/or

UV illumination, 1 mL of bacteria suspension was centrifuged at 1500 ×g for 10 minutes. The supernatant was removed, and the cell pellet was sufficiently resuspended in 800 µL of RNAzol®RT (Molecular Research Center, Inc., OH). The extraction kit protocol was followed using a centrifugation speed of 12,000 ×g with an on-column DNase I treatment at 30°C for 15 minutes. RNA was finally eluted from the column using 25 µL of DNase/RNase-free water at 16,000 ×g for 1 minute. The total RNA solution was normalized to 200 ng/µL and submitted for quantitative real-time PCR analysis.

2.2.8 qPCR and data analysis

Quantitative real-time PCR (qPCR) was done by the University of Minnesota Genomics Center using the same protocol and instrument described earlier [25]. For each gene of interest, three sets of primers were designed using Universal ProbeLibrary ProbeFinder software, followed by validation of amplification efficiency. The primer pairs with the highest amplification efficiency for each gene were chosen for subsequent qPCR experiments. **Table 2.1** shows a full list of genes investigated along with their corresponding functions and their primers used in qPCR experiments. The raw data was processed using the qPCR data analysis program, Miner,[48] which applies an objective method to determine efficiency and the fractional cycle number (Ct) at threshold of individual PCR reactions. Ct values were determined using Miner program, and relative fold change was calculated based on the ΔΔCt method.[49] Among two candidates, *gyrB* and *recA*, *recA* was chosen as the housekeeping gene due to a lower standard deviation in expression level.

Table 2. 1 Target genes, corresponding functions, and their primers for qPCR experiment.

Target gene	Forward primer (5′–3′)	Reverse primer (5′–3′)	Probe number	Function	Accession number

Fe/Mn superoxide dismutase (*sodB*)	GCA ATG TTC GCC CTG ACT AC	CCT GCG AAG TTT TGG TTC AC	#95	Superoxide dismutase activity	NP_718453 .1
Diguanylate cyclase-like protein (*mxdA*)	CAT TTC GCA AGT TGA ACA CC	CCA CAC CAA TAT GAC GCA AA	#44	Indirectly modulate cyclic di-GMP (ref 68)	NP_719709 .1
Phage shock protein B (*pspB*)	TTG ATT GCG AAA GCC GAT A	ATC AAG AAT CGC CTC TAA GGT TT	#46	Phage shock response	NP_717416 .1
Double-stranded DNA translocase (*ftsK*)	GAT AGT CGA TGG CAT TGT GGT	TAG GCT TAG TCG GCA CAG GT	#142	Cytokinesis	NP_717901 .1
Catalase HPII (*katB*)	GGC ATT GAT CCT GAT TCT TCT C	TCC AAC GAG GGA AGT TAC CA	#157	Catalase activity, oxidative stress	NP_716697 .1
Extracellular iron oxide respiratory system surface decaheme cytochrome c component (*omcA*)	TCG ATT ATG GCA AAG TGC AT	CGT GAC AGG CTG CAC AAT	#28	Electron carrier activity	NP_717388 .1
DNA gyrase B subunit (*gyrB*)	AGA ATG GAT CGA CGC CTT TA	ATA CAG TAC GCC GCT GTT TTC	#31	DNA replication	NP_715653 .1
Recombinase A (*recA*)	GGT GAC TCA CAC ATG GGC TTA	CCG CTA ACT TAC GCA TTG CT	#136	DNA-dependent ATPase activity	NP_718983 .1

2.3 Results

2.3.1 TiO_2 nanoparticle characterization

Synthesis of acid-catalyzed TiO_2 NPs followed by a 48-hour hydrothermal treatment was performed using a sol-gel method developed by Isley and Penn.[50] Details can be found in the Supporting Information. The dynamic light scattering (DLS)- based size and ζ-potential of synthesized nanoparticles were measured in both Milli-Q water and LB broth before toxicity tests, and the results are summarized in **Figure A.1.1**. It was noted that upon re-suspension in LB broth, the hydrodynamic diameter increased drastically, with a significant peak shift in size distribution, indicating that TiO_2 NPs

aggregated in LB broth. The large aggregation was also confirmed by hyperspectral microscopic images (**Figure A.1.2)**; more information on hyperspectral imaging can be found in Supporting Information). Meanwhile, the absolute size of the primary TiO_2 NPs, determined from TEM images, did not change. This aggregation is expected based on the high concentration of salts and nutrients in LB broth.[51] Changes in ζ-potential from positive to almost neutral in LB broth may result from both pH change (from 6.05 of Milli-Q water to 7.30 of LB broth) and peptide adsorption onto the TiO_2 NP surface, as LB broth contains high concentration of peptides. Stability results show that, once re-dispersed in LB broth, the aggregation status of TiO_2 remains quite stable for 6 hours, the experimental time frame in this study.

2.3.2 Effect of TiO_2 NPs and UV illumination on cell growth

Bacterial cell density (OD_{600}) was monitored hourly upon 1, 5, 10, 25, or 100 mg/L TiO_2 NP exposure, either in the dark or under continuous UV illumination. TiO_2 NP extinction and LB broth background at 600 nm were subtracted from the original readings to obtain background-subtracted OD_{600} values, as plotted in **Figure 2.1(a)(b)**. Data from 1 and 10 mg/L exposure followed the same trend but are not shown in the figure for clarity. Data from 3-hour time point were identified as outliers (ROUT method, Q=1.0%, GraphPad Prism)[52] and excluded from further statistical analyses. In both cell growth curves in the dark and under UV illumination in **Figure 2.1(a)** and **2.1(b)**, there appeared to be a dose-dependent negative effect of TiO_2 NP treatment, a trend that was also supported upon analysis of the final cell density after 6 hours; this finding is consistent with precedent work.[25] However, it should be noted that the optical density change, even with the highest nanoparticle dose (100 mg/L), was less than 10%. Thus, the effect of TiO_2 exposure under these conditions can be considered minor. For the most part, no additional effect of UV illumination and TiO_2 nanoparticle treatment was observed, with the exception of a few trials were the interaction of TiO_2 and UV illumination was determined to be significant when testing final OD_{600} values using a

two-way ANOVA. Given the fact that (1) the significance was not repeated for all trials and (2) the difference in OD_{600} change was at most 14%, it is concluded that, overall, UV illumination and TiO_2 nanoparticle treatment shows no interactive effect.

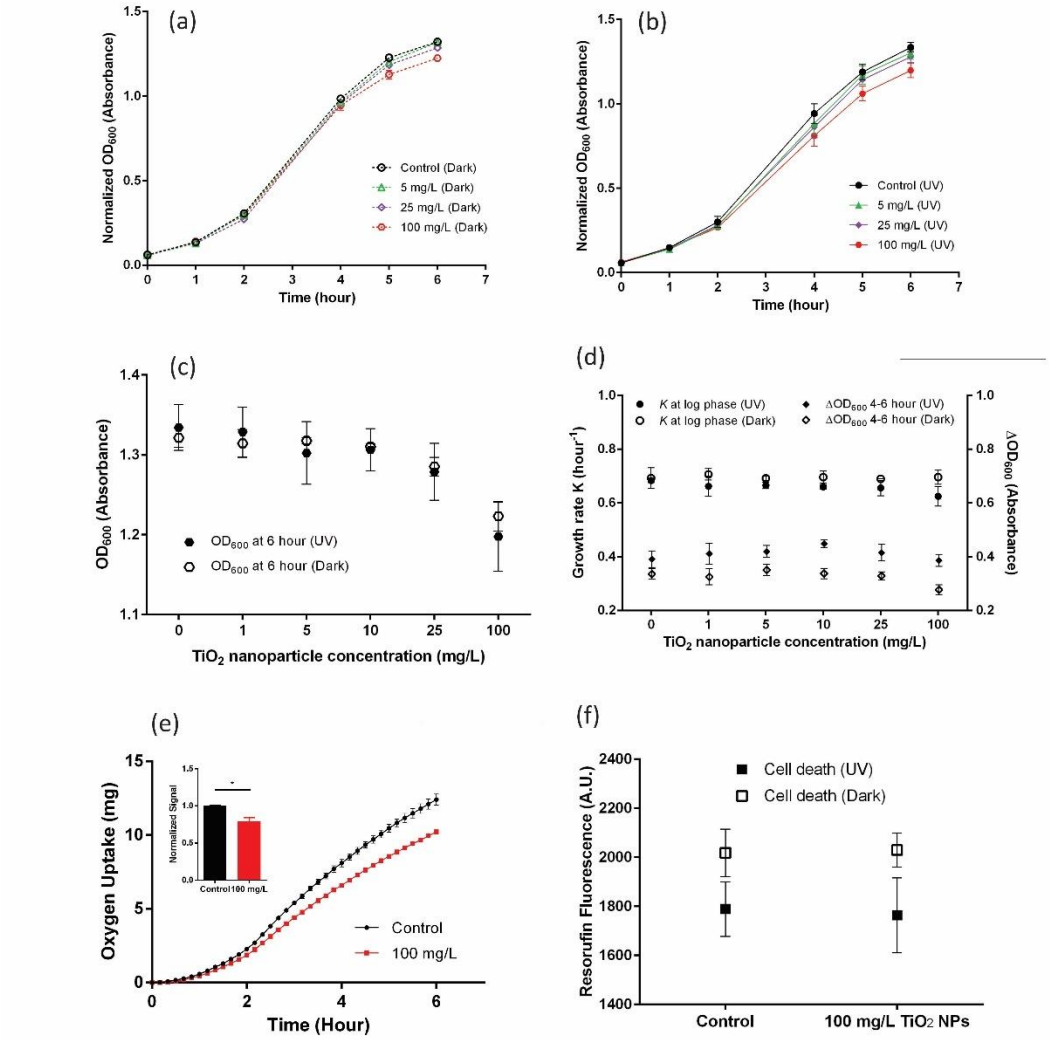

Figure 2. 1 (a) (b) High concentrations of TiO_2 nanoparticles (100 mg/L) inhibit *Shewanella oneidensis* growth in LB to a small extent both in the dark and under UV illumination. (c) TiO_2 NP treatment has a dose-dependent negative effect on final cell density (two-way ANOVA, $F(5, 24)=16.85$, $p<0.0001$) though UV illumination did not show a significant effect. (d) Detailed analysis of the effect of UV and TiO_2 exposure on the growth rate (K) at log phase and the increase in cell growth (ΔOD_{600}) between 4 and 6 hours. (e) Cell respiration was inhibited during 100 mg/L TiO_2 nanoparticle exposure in the dark (Student's t-test, $p=0.0314$). (f) Cytotoxicity assays following TiO_2 and UV exposure on S. oneidensis showed TiO_2 nanoparticles, even at 100 mg/L, did

not kill cells compared to control groups.

The first 4-hour of bacterial growth was identified as the log/exponential growth phase by fitting the logarithmic transformed cell number values using linear regression, and the growth rate *K* was calculated from the following equations:

$$N = N_0 e^{Kt}$$

$$\log N = (K \log e)t + \log N_0$$

$$K = \ln 10 \times slope = 2.303 \times slope$$

where *N* is the cell number, calculated from optical density (1 Abs = 10^9 cells/mL), and N_0 is the cell number at the beginning (0 hour). *K* ($hour^{-1}$) refers to the growth rate in the log phase, and *e* is the natural logarithm. Two-way ANOVA revealed a statistically significant difference in the growth rate, *K*, between dark and UV illumination ($F(1,24)=20.87$, $p=0.0001$); a Tukey post-hoc test showed that at 100 mg/L TiO_2 dose, the growth rate *K* at log phase under UV illumination is statistically significantly lower than that in the dark (Tukey's multiple comparison, $p=0.0087$). TiO_2 exposure did not have any effect on bacterial growth rate in the log phase.

After 4 hours, bacterial growth slowed as it entered the stationary phase; thus, the growth rate cannot be determined by the equations above. To explore the bacteria growth at this transition stage, the differences in OD_{600} values between the 4- and 6-hour time points were calculated and used to represent the bacteria growth in this period (**Figure 2.1(d)**). Two-way ANOVA revealed that both UV illumination ($F(1,24)=107.9$, $p<0.0001$) and TiO_2 concentration ($F(5,24)=4.471$, $p=0.0051$) have statistically significant effects on the bacterial growth at 4 and 6 hours. The positive effect of UV illumination on cell growth during 4-6 hours compensated for the slowed growth during the log phase induced by UV exposure, resulting in no significant effect of UV illumination on the final OD at 6-hour (**Figure 2.1(c)**, two-way ANOVA, $F(1,24)=0.2968$, $p=0.5909$). Meanwhile, TiO_2 treatment has a significant effect on the

final OD reading at 6-hour (two-way ANOVA, $F(5,24)=18.13$, $p<0.0001$), and a Tukey post-hoc test showed that 100 mg/L TiO_2 NP treatment statistically significantly decreased the OD reading at 6-hours compared to control and other lower concentrations (Tukey's multiple comparison, $p<0.05$).

Oxygen uptake by the bacterial populations was also measured over time by monitoring oxygen uptake with either 25 mg/L (data not shown) or 100 mg/L TiO_2 nanoparticle exposure. It should be noted that the respiration measurement was only performed in the dark due to the limitations of the instrument. Using the first derivative of the oxygen uptake curve, the maximum oxygen uptake rate (k_{max}) and the time point when the maximum rate was reached (t_{max}) were calculated. The quotient of k_{max} divided by t_{max} was calculated to represent bacterial oxygen uptake, as shown in the inset of **Figure 2.1(e)**. A decrease in the value indicates inhibition of bacterial oxygen uptake. A two-tailed, unpaired student t-test showed that upon 100 mg/L TiO_2 NP exposure, bacterial respiration was inhibited ($p=0.0314$), consistent with the growth curve results.

2.3.3 Effect of TiO_2 NPs and UV illumination on cell death

A cytotoxicity assay was also applied to test bacterial cell viability upon TiO_2 NP exposure and/or UV illumination for a short time period (30 min). Cells are known to release the cytosolic enzyme glucose 6-phosphate dehydrogenase (G6PD) upon cell damage. In the Vybrant cytotoxicity assay, G6PD is measured by a two-step enzymatic reaction that generates a red-fluorescent probe, resorufin. The results show that TiO_2 NP treatment, even at the highest dose considered herein (100 mg/L), did not increase cell death. Interestingly, two-way ANOVA indicated a significant effect of UV illumination on increasing cell viability ($F(1,8)=14.70$, $p=0.005$) after the 30-minute exposure. Considering the short time frame, this effect can be explained by an increased growth rate upon UV illumination in the first hour of bacterial growth (two-way ANOVA, $F(1,24)=7.698$, $p=0.01$, data not shown). No additional effect between

nanoparticles and UV illumination was observed on cell viability in the cytotoxicity assay.

2.3.4 ROS generation affected by TiO_2 NPs and UV illumination

Bacterial cells were loaded with $DCFH_2$-DA, a probe which can be converted to fluorescent DCF upon reaction with cellular esterases and ROS, to indicate the amount of intracellular ROS, followed by exposure of 100 mg/L TiO_2 NPs and/or UV illumination. It was hypothesized that with the presence of TiO_2 NPs, an increase of intracellular ROS level would be observed due to the photocatalytic properties of TiO_2 NPs. Surprisingly, the results (**Figure 2.2(a)**) showed that TiO_2 NPs decreased the fluorescent signals, indicating that the amount of intracellular ROS had a minor, but statistically significant, decrease. To explore the source of this minor decrease in fluorescent signals, a control experiment was done to see if TiO_2 NPs interfered with the DCF fluorescence. Results showed that it was very likely that the decrease in fluorescent signals was attributed to the optical interference of TiO_2 NPs in suspension (**Figure 2.2(b)**). Thus, it was concluded that the treatment of TiO_2 NPs, even at the highest dose here, did not induce changes in intracellular ROS level. The dramatic increase in ROS levels upon UV illumination was probably due to the photo-induced transformation of $DCFH_2$-DA to fluorescent DCF,[53] as their magnitude was comparable to the positive control (data not shown).

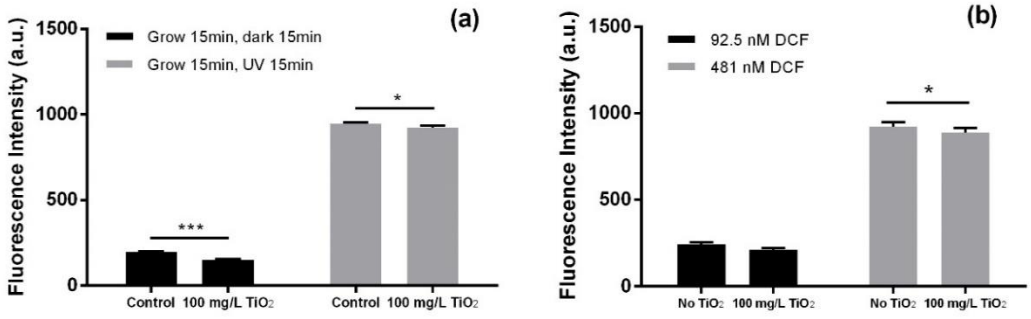

Figure 2. 2 (a) A minor decrease in fluorescence intensity was detected upon TiO_2 exposure both in dark and under UV illumination (Tukey's multiple comparison test, $p<0.05$). (b) The presence of TiO_2 NPs resulted in a minor, but statistically significant, decrease in the fluorescence of DCF (two-way ANOVA, $F(1,16)=11.99$, $p=0.0032$).

Star denotes the statistical significance between groups (Tukey's multiple comparison test, $p<0.05$).

2.3.5 Riboflavin secretion affected by TiO_2 NPs and UV illumination

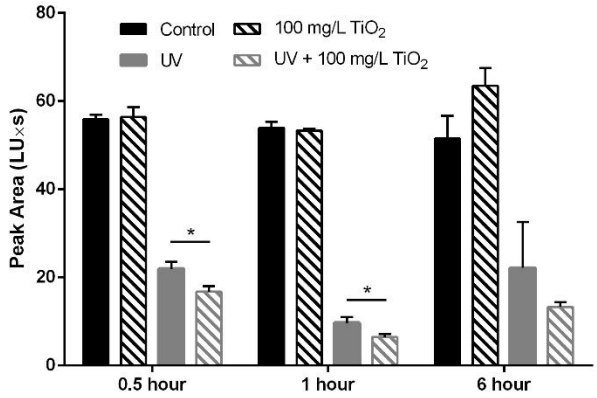

Figure 2.3 Riboflavin secretion was affected by UV illumination at all time points (statistical significance not shown) and further decreased in the presence of TiO_2 NPs after 0.5- and 1-hour exposure (two-way ANOVA and post-hoc Tukey's test within one time point, $p<0.05$). Asterisks denote statistical significance.

Riboflavin secretion upon TiO_2 NPs and/or UV light exposure was examined at different time points (30 min, 1 hour and 6 hour) using HPLC. For all three time points, no change was observed in riboflavin secretion upon TiO_2 NP exposure in the dark, even with the highest TiO_2 nanoparticle dose in this study (100 mg/L). UV illumination significantly decreased the amount of riboflavin detected in the supernatant, mostly attributed to the photodegradation of riboflavin under UV light; it was confirmed by a control experiment that no riboflavin peaks were observed for a 4 μM solution of riboflavin after a 6-hour UV illumination (data not shown). Interestingly, there was a statistically significant interaction between the effects of TiO_2 and UV on riboflavin secretion upon 0.5- and 6-hour exposure (two-way ANOVA, $F(1,8)=9.694$ and 8.633, $p=0.0144$ and 0.0188, respectively), indicating that the presence of TiO_2 NPs further reduced the amount of riboflavin in the supernatant of the bacterial suspension.

2.3.6 Effect of TiO_2 NPs and UV illumination of gene expression

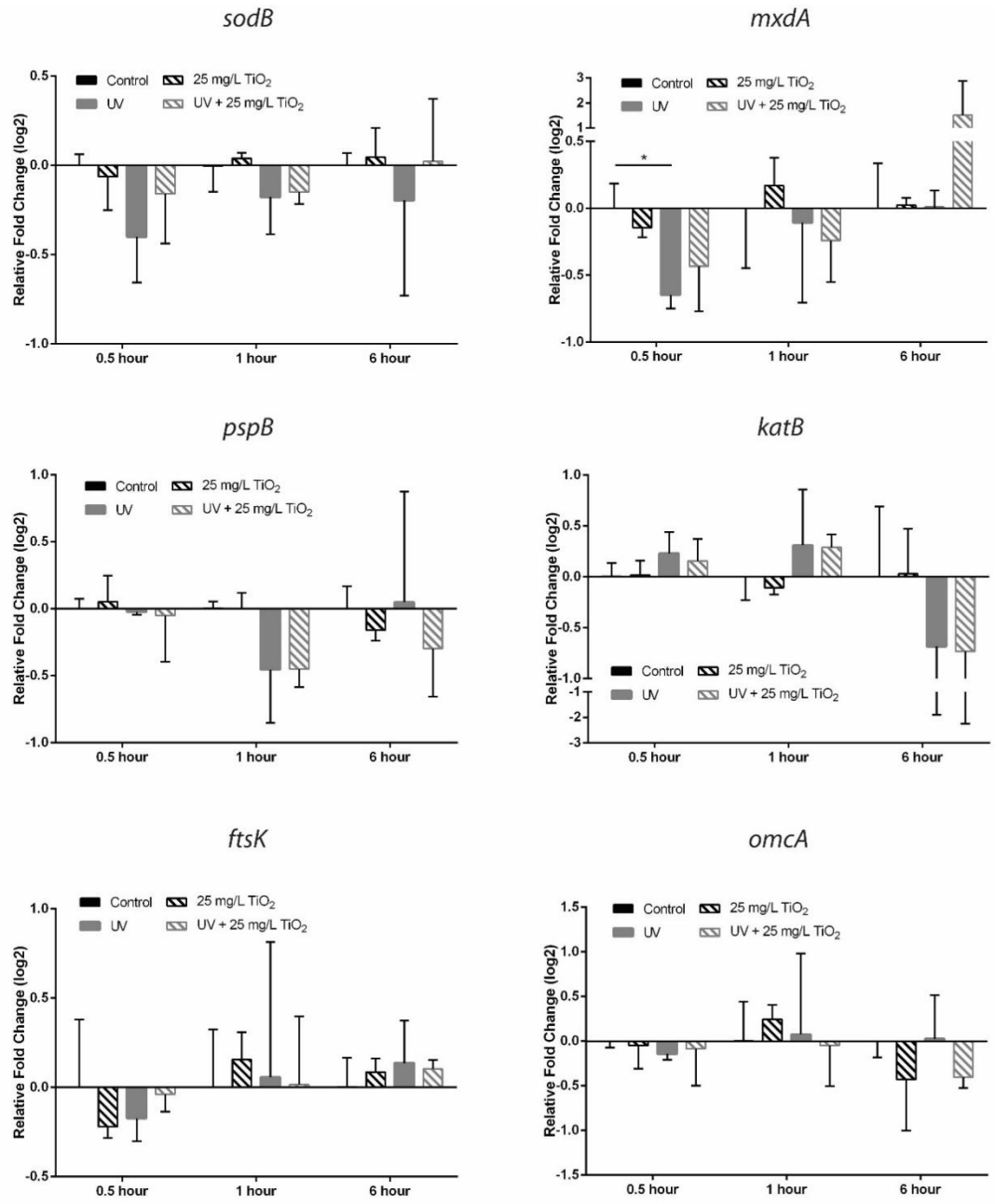

Figure 2. 4 Gene expression pattern of 6 different genes in *S. oneidensis* MR-1 upon TiO_2 nanoparticle (25 mg/L) and/or UV exposure for different time periods. TiO_2 NPs did not affect gene expression at this dose, and UV illumination induced minor effects. Asterisks denote statistical significance in post-hoc Tukey's test ($p<0.05$).

In the gene expression studies, 25 mg/L was used as the TiO_2 NP dose as it was found to be the highest dose that did not induce inhibition in bacterial growth. Two-way

ANOVA and a post-hoc Tukey's multiple comparison test was applied to log2-transformed relative fold change values. *gyrB* and *recA* were included as candidates for housekeeping genes, and *recA* was finally chosen as the housekeeping gene after comparing the variation of the expression levels of these two genes. Results showed that TiO_2 nanoparticle (25 mg/L) and UV exposure induced almost no effect on *S. oneidensis* MR-1 gene expression. Two-way ANOVA showed statistically significant effects of UV illumination on *sodB* expression at 0.5 hour ($F(1,8)=5.367$, $p=0.0492$) and 1 hour ($F(1,8)=5.630$, $p=0.0451$), *mxdA* expression at 0.5 hour ($F(1,8)=10.05$, $p=0.0132$), and *pspB* expression at 1 hour ($F(1,8)=24.12$, $p=0.0012$). In a post-hoc Tukey's test ($p<0.05$), there was a statistically significant decrease in the expression level of the *pspB* gene in UV-illuminated samples when compared to either control or TiO_2-treated samples in the dark. Overall, TiO_2 NPs did not affect gene expression at the dose of 25 mg/L.

2.4 Discussion

2.4.1 Minimal inhibition of TiO_2 NPs and UV illumination on *S. oneidensis* growth

Measurements of cell growth, oxygen uptake, cell death, and intracellular ROS generation collectively indicated that UV illumination, even at high intensity, does not enhance the toxicity of TiO_2 nanoparticles; this result forces us to reject our initial hypothesis that UV illumination would enhance the toxicity of TiO_2 NPs by generating excess reactive oxygen species (ROS). This finding is also not consistent with previous research on other gram-negative bacteria species.[15] Considering the fact that a very nutrient-rich medium, LB broth, was used in this study, it is possible that the ROS generated from TiO_2 NPs are readily quenched by components in LB medium, such as peptides, making the external ROS level too low to damage the cell membrane and further impact intracellular ROS; this was further proved by the gene expression results (see below). In addition, as TiO_2 NPs are not internalized by but are in close proximity

to the bacterial cells (**Figure A.1.2**), TiO_2 NPs simply have no chance to directly generate ROS within the cell plasma. While TiO_2 NPs, either in the dark or under UV illumination, still induced inhibition of bacterial growth at high dosage, we postulate that the inhibition of growth is mostly caused by adsorption of nutrients to TiO_2 NP surfaces rather than ROS generation from TiO_2 NPs, due to the fact that (1) UV illumination did not enhance the inhibition; (2) the inhibition began after log phase, when the growth started to be limited by the availability of nutrients in media; and (3) cell viability after short exposure was not decreased by the combination of TiO_2 exposure and UV illumination. Thus, in future research, a minimal medium will be more desirable than LB broth and might reveal toxicity in viability/growth that was not observed in this study. However, it is still possible that TiO_2 NPs and UV illumination caused subtle effects that cannot be observed by only viability/growth measurements; this possibility was addressed by cellular function assessment and gene expression studies subsequently.

2.4.2 Riboflavin level change upon TiO_2 NP and UV exposure

Riboflavin, a redox molecule secreted by *S. oneidensis* MR-1 cells, acts as an electron shuttle between the cell surface and external acceptors, like metal oxide surfaces.[33,34] However, the redox potential of TiO_2 conduction band at pH 7 (-0.7 V vs. SHE[54]) is considered too low for reduction by flavins (with a midpoint potential of -0.2 to -0.25 V[34]). Thus, we were not expecting riboflavin level to increase upon TiO_2 exposure; on the contrary, considering that fact that bacterial growth was inhibited by TiO_2 NPs, the hypothesis was that riboflavin secretion would be somewhat inhibited, correlating with growth results. However, for all three time points, no change was observed in riboflavin secretion upon only TiO_2 NP exposure, even with the highest TiO_2 nanoparticle dose in this study (100 mg/L). This indicated that riboflavin secretion does not correlate with bacterial growth. A previous study showed that riboflavin secretion increased upon 24-

hour TiO_2 NP exposure in a dose-dependent manner;[25] this was not observed in this study, possibly due to the different time frame of these two studies.

As expected, UV illumination induced a decrease in riboflavin amount in cell suspension drastically, probably due to the photodegradation of riboflavin upon UV exposure, as shown in control experiments and previous work;[55,56] control experiments showed that no riboflavin peaks were observed after 6 hours under UV illumination for a 4 μM solution of riboflavin (data not shown). The degradation was not likely due to ROS as adding antioxidants, including N-acetylcysteine or glutathione, did not recover the riboflavin level in cell suspension (**Figure A.1.3**). Considering the fact that all riboflavin was degraded after a 6-hour exposure in control experiments, it seems that bacterial cells in suspension "re-establish" riboflavin levels to counteract depletion of riboflavin from UV illumination. In a previous study, electrochemical activities were observed in a mediator-less microbial fuel cell using *Shewanella putrefaciens* cells, indicating that cells established a level of mediators for electron shuttling.[57] Interestingly, TiO_2 NPs further reduced the riboflavin level in addition to UV exposure, indicating some additive effect between UV illumination and TiO_2 NPs on the amount of riboflavin outside cells. This additional effect may be due to changes in either cell riboflavin secretion or photodegradation of riboflavin outside bacterial cells. Studies have shown that riboflavin can be adsorbed on TiO_2 surfaces, likely via the phenolic group, and photo-excited flavin can transfer electrons into the conduction band of TiO_2.[58,59] Thus, it is possible that TiO_2 NPs act as a mediator/catalyst in riboflavin photodegradation.

2.4.3 Gene expression change upon TiO_2 NP and UV exposure

To further investigate subtle effects that cannot be observed by only viability/growth measurements, 6 genes related to oxidative stress, exopolysaccharide (EPS) synthesis, extracytoplasmic stress, cell division and metal-reducing pathways were included in

this gene expression study to test the hypothesized mechanisms of how bacterial cells respond to TiO_2 NPs. Different mechanisms of bacterial stress response were addressed by these 6 genes. TiO_2 NPs were hypothesized to kill bacteria via generating ROS under UV illumination,[16] while previous transcriptional analysis displayed that a series of ROS-scavenging related genes were up-regulated upon UVA illumination.[60] Thus, the *katB* gene, one of the peroxide response-inducible genes controlled by the redox-sensitive transcriptional activator OxyR,[61] and the *sodB* gene, a gene coding for Fe-containing superoxide dismutase,[62] were chosen to represent the cell responses to oxidative stress from excessive ROS potentially generated by TiO_2 NPs and UV illumination. Analysis of the results using two-way ANOVA showed that the *katB* gene was not influenced by TiO_2 NP and/or UV light exposure while UV illumination had a statistically significant effect on the expression level of the *sodB* gene after 30-min and 1-hour exposure, but TiO_2 NPs did not show any effect. This correlated with the observation from the intracellular ROS assay, where TiO_2 NPs did not induce any increase in ROS level within bacterial cells. However, though the expression level of the *katB* gene did not change, it does not necessarily indicate a lack of oxidative stress, as other ROS-scavenging related genes may respond instead of the *katB* gene based on observations from previous work.[60] Interestingly, the expression level of superoxide dismutase decreased instead of the up-regulation that we expected; this may indicate a decrease of oxidative stress from superoxide ions upon UV illumination, but the expression level change was very minor. Overall, the response from the *katB* and *sodB* genes did not implicate a role for oxidative stress as a result of TiO_2 NP exposure.

Cyclic di-GMP is an intracellular signaling molecule in a lot of bacterial species.[63] Biofilm formation, an important function of *S. oneidensis* that is related with bacterial interaction with mineral surface and electron transfer,[64,65] was postulated to be controlled by cyclic di-GMP via production of EPS.[63] In the same work, a Δ*mxdA* mutant exhibited strong defect in biofilm formation, followed by a further discovery

that the intracellular cyclic di-GMP level was indirectly modulated by MxdA in *S. oneidensis* MR-1.[66] Based on these precedent studies, the *mxdA* gene, coding for a diguanylate cyclase-like protein, was chosen to indicate potential changes in biofilm formation. Two-way ANOVA analysis showed that after a 30-minute exposure, UV illumination had a statistically significant effect on the expression level of the *mxdA* gene, while no impact was observed upon TiO_2 NP exposure. No effect was observed at longer time points. These results indicate the potential modulation of cyclic di-GMP within the cells, but this effect vanished as the exposure time lengthened with a time frame of 6-hour. Previous work indicated that the TiO_2-exposed bacteria had slower biofilm growth with no change in the amount of EPS observed, and the *mxdA* gene showed no difference in expression level upon 1-hour and 6-hour TiO_2 exposure.[25]

Filamentous phage infection, osmotic shock, and ethanol treatment have been shown to induce the response of phage-shock-protein (Psp) genes in bacterial cells.[67-69] It was postulated that extracytoplasmic stress disrupts the membrane potential by dissipating the proton-motive force on cell membranes.[67] As precedent work[25] and microscopic images (**Figure A.1.2**) showed that TiO_2 NPs were not internalized by but in proximity to the bacterial cells, it was reasonable to hypothesize that TiO_2 NPs exert membrane stress to bacterial cells by associating with the bacterial membrane; thus, as part of the Psp response system, the *pspB* gene was chosen to reveal potential extracytoplasmic stress.[67] Results show that *pspB* gene expression was down-regulated after 1 hour upon UV illumination, but no change was observed at other time points or upon TiO_2 exposure. Considering the role of PspB protein in Psp response, acting largely as a signal detector/transducer that detects extracytoplasmic signals and initiates the Psp response by binding to PspA protein, *pspB* gene expression might not be directly regulated upon membrane stress. Further experiments can be done using *pspA* or *pspG* as genes of interest, as they are the two genes that are regulated by PspF regulon following PspA protein binding to the PspB/C complex during the Psp response.[69] The

down-regulation of *pspB* expression upon UV illumination is hard to interpret without additional information; no precedent work has reported change of *pspB* expression level upon UV illumination. Further experiments might include a membrane potential measurement upon TiO_2 NP exposure and UV illumination to obtain more information on membrane stress.

The other two genes of interest, *ftsK* and *omcA*, did not show any statistically significant changes upon TiO_2 NP or UVA exposure. The FtsK protein actively pushes DNA through the closing division septum during bacterial chromosome segregation in cell division,[70] so we expected the *ftsK* gene expression level to be a biomarker for bacterial growth. However, though *S. oneidensis* MR-1 displayed a growth inhibition upon TiO_2 NP exposure, the expression level of *ftsK* gene did not change. The OmcA protein is a part of the metal-reducing pathway of *S. oneidensis* MR-1, which is important for the bacterial respiration of oxidized metals like Fe(III) and Mn (IV). It is located on the outer membrane, and previous research shows that this protein is required for electron transfer from the inner membrane to the electron terminal acceptors via electron shuttles like flavins.[71] Based on this information, we expected the expression level of the *omcA* gene to be indicative of riboflavin secretion. However, *omcA* gene expression level did not change upon exposure, and was not correlated with riboflavin secretion measured by HPLC. A better candidate for riboflavin biomarker might be a gene directly related with riboflavin biosynthesis (e.g. *ribA*/*B*, *ushA*).[33,72]

It should also be noted that though there were some statistically significant changes in gene expression levels, the degree of change was relatively small in a biological context (smaller than 2). With a higher dose of 100 mg/L, one might see more change, but in a previous study, 100 mg/L of TiO_2 nanoparticles also did not show any relative fold change larger than 2.[25] Based on the result of this study, none of the genes can be considered as biomarkers for the inhibition of growth. For future work, the *nqrF* gene,

coding for Na-translocating NADH-quinone reductase, might be a candidate as a biomarker of cell respiration and growth.[73,74]

2.5 Conclusions

In this study, we showed that TiO_2 nanoparticles inhibited the growth on *Shewanella oneidensis* MR-1 at high dosage but had no effect on cell viability, while concomitant UV-A illumination did not induce extra inhibition in growth. It is likely that the minimal impacts are due to the nutrient-rich medium used in this study. Because environmental systems are not likely to be nutrient rich, future work will examine effects in minimal medium that only contains minimal amount of salts.[75] Further assessments on reactive oxygen species and riboflavin secretion indicated that TiO_2 NPs induced neither intracellular ROS accumulation nor riboflavin secretion but had additive effect with UV-A illumination to further reduce the amount of riboflavin outside cells. Finally, we demonstrated that gene expression is a tool to explore NP toxicity mechanisms in combination with cell function, thus providing more information on how cells respond to NPs and understanding the subtle influences of NPs to the ecological systems.

Chapter 3

Gene expression response of the Gram-negative bacterium *Shewanella oneidensis* and the water flea *Daphnia magna* exposed to functionalized gold nanoparticles

Adapted from:

Qiu, T. A.*, Bozich, J. S.*, Lohse, S. E., Vartanian, A. M., Jacob, L. M., Meyer, B. M., Gunsolus, I. L., Niemuth, N. J., Murphy, C. J., Haynes, C. L., Klaper, R. D., Gene expression as an indicator of the molecular response and toxicity in the bacterium *Shewanella oneidensis* and the water flea *Daphnia magna* exposed to functionalized gold nanoparticles, ***Environmental Science: Nano***, 2015, **2**, 615-629.

*T.A.Q. and J.S.B. contributed equally to this work. T.A.Q. contributed to all work regarding bacteria.

3.1 Introduction

Engineered nanoparticles (NPs) are being produced to enhance a wide range of societally beneficial applications, from energy storage capacities and material durability to medical therapeutics and water treatment devices.[1-3] These applications are possible because of the novel physiochemical properties NPs display, such as high surface area and reactivity as well as distinct surface chemistries, composition, and size distributions. It is, however, these same size-dependent physiochemical properties that may influence their biocompatibility.[4-8] For example, size, shape, and core composition have been thought to mediate receptor-ligand binding rates, cellular phagocytosis, exocytosis, and cytotoxicity.[9-12] Other studies suggest that NP surface charge is the main determinant of biological interactions, with positively charged particles being more toxic than negatively or neutrally charged particles.[13-18]

These classifications of critical features that determine biological impact all focus on the NPs themselves. The differences in response across organisms or cell types is less often considered despite the fact that toxicological evaluations of the biological impacts caused by engineered NPs have revealed a wide range in responses across cell types or organisms considered.[19-23] For example, Sohaebuddin et al. (2010)[24] demonstrated that cell type determines the extent of response to nanomaterials with different composition and size. In another study using ZnO NPs, the EC_{50} differed by orders of magnitude for *V. fischeri*, *D. magna* and *T. platyurus*.[25] Variation across cell systems and organisms makes it difficult to develop a common understanding of the properties of nanomaterials that may determine toxicity. Even for well-studied chemicals, such as pesticides, models that use general acute endpoint data to predict impacts often inaccurately estimate concentrations that cause effects across similar chemicals, and rarely are applicable across organisms.[26,27] These studies have shown that a more mechanistic understanding of the impacts of chemicals at sublethal doses provides a more accurate description of impacts and better data for modeling these effects across

species. The goal of this study is to achieve a more mechanistic understanding of NP/organism interactions to facilitate efficient prediction of the impact nanotechnology will have on environmental health. Linking specific molecular mechanisms that are impacted by NPs across organisms will not only greatly aid in assessing the potential environmental impact of these materials but is also crucial to informing NP design for safe and sustainable development of nanotechnologies.

Currently, the major proposed molecular mechanism for NP toxicity is oxidative stress.[4,28-31] However, the exposures that produce oxidative stress in many studies are well above what is estimated to be the current or future environmental concentrations; long-term low dose exposures are the more likely scenario.[32,33] In addition, the molecular mechanisms responsible for coping with oxidative stress are triggered upon exposure to a wide range of chemical species[34,35] and are a natural biological response that does not necessarily lead to an adverse outcome.[36] The focus on oxidative stress and lethal dose exposures makes it difficult to uncover other mechanisms that may have a greater predictive power for the environmental impact of NPs. Sublethal concentration-based exposures allow the cell to have a more natural perturbation by the contaminant that triggers subtle, but potentially specific, molecular responses.[37,38] It is these more realistic exposure scenarios that will uncover more mechanism-based information to predict meaningful impacts across species.

Molecular biomarkers provide a sensitive indicator of the response of an organism to stressors such as exposure to a toxicant in addition to providing information on the mechanisms that are impacted by exposure.[37,38]. Mechanistic information that can be tied to larger impacts on reproduction for example enhance the possibility of predicting negative outcomes where standardized toxicological tests, although valuable, have limited the ability to accurately predict the impact of emerging contaminants. Overreliance on these methods has led to risk assessment failures.[39] Developing such

candidates for molecular biomarkers for NP toxicity will greatly aid in the rapid assessment and impact prediction for current and emerging nanomaterials across a wide range of organisms. Previously developed biomarkers, for example, vitellogenin, have been used for the successful determination of adverse outcomes of some classes of endocrine disruptors and their impacts on vertebrate reproduction.[40-42] Metallothioneins are biomarkers used in organisms to detect toxic metal ion exposure, and they are known to respond to a wide range of metal-based contaminants associated with environmental pollution.[43] Heat shock proteins, indicative of proteotoxic stressors, indicate sublethal cellular damage and respond in a dose-dependent manner to environmental stressors.[44] Molecular biomarkers that provide mechanistic insight for grouping nanomaterials by their molecular level interactions, especially if they apply to effects seen across species, would provide insight for grouping nanomaterials by their molecular level interactions. Furthermore, they may indicate both nonspecific and specific modes of action as well as underlying mechanisms for toxicity of NPs with particular physiochemical properties.

In this study, we examined several candidate biomarkers in two model species, the bacterium *Shewanella oneidensis* and the invertebrate Daphnia magna, that are associated with pathways of importance in these two species and determined how their expression related to the biological impacts of exposure to gold NPs (AuNPs) with positively or negatively charged surfaces. *Shewanella oneidensis* MR-1 is an environmentally beneficial Gram-negative bacterium with a unique metal-reducing capability to respire heavy metals; *S. oneidensis* plays an important role in the cycling of metal elements in the ecosystem as well as the bioremediation of toxic elements.[45] *Daphnia magna* is a designated toxicology and toxicogenomics model organism by multiple agencies (OECD, NIH and EPA), and is an environmentally relevant freshwater invertebrate that composes an integral part of freshwater food webs.[46] AuNPs were chosen as a model NP in this study due to the chemical inertness of the

gold core and our ability to readily control size,[47] shape,[48] and surface functionalization.[49] Two ligands were used for AuNP functionalization, positively charged polyallylamine hydrochloride (PAH) and negatively charged mercaptopropionic acid (MPA).

We explored genes in various molecular pathways in our two model organisms. Pairs of genes selected from each organism were selected to represent pathways encoding for similar cellular functions in two organisms, including oxidative stress, xenobiotic detoxification, protein folding, cellular electron transport, and cellular maintenance. In addition, genes in pathways related to reproduction in *D. magna* and to cell division, DNA repair and extracytoplasmic stress in *S. oneidensis* were also investigated. The goal was to determine 1) how the exposure to NPs with differing surface properties impacted each organism and how this differed from their respective ligand controls 2) if gene expression for these pathways were an indication of impacts seen in each organism 3) if exposure duration altered effects and gene expression measurements and if acute measurements of gene expression would provide an indication of chronic impacts 4) if gene expression for similar pathways across organisms would provide biomarkers that were predictive across species. The NPs used in this study were quantitatively and qualitatively characterized prior to and after exposure to assay media to aid us in understanding how alterations in NP physical properties may impact molecular pathways. Overall, this work aims to link molecular pathways to NP characteristics in two distinct environmentally relevant organisms.

3.2 Experimental

3.2.1 Functionalized AuNP synthesis and characterization

All materials were used as received, unless otherwise noted. Gold tetrachloroaurate trihydrate ($HAuCl_4 \cdot 3H_2O$), sodium borohydride ($NaBH_4$), trisodium citrate, 3-mercaptopropionic acid (MPA), and polyallylamine hydrochloride (PAH; Mw 15, 000

g/mol) were obtained from Sigma Aldrich. Ultrapure deionized water was prepared using a Barnstead NANOPURE water filtration system. PALL Minimate tangential flow filtration capsules for AuNP purification with 50 kD pore size was obtained from VWR. Transmission electron microscopy grids were obtained from PELCO (SiO on copper mesh).

The 4.7 (± 1.5)-nm-diameter PAH-AuNPs were prepared by polyelectrolyte wrapping of ~4-nm-diameter citrate-coated AuNPs. The (4.3 ± 1.3)-nm-diameter MPA-AuNPs were prepared by direct synthesis. After synthesis, measuring and counting using TEM images determined size distributions. Detailed descriptions of the AuNP syntheses are given below.

PAH-AuNPs *(4.7 ± 1.5 nm).* As a first step in synthesis of PAH-AuNPs citrate AuNPs were synthesized using previously reported procedures.[47] In an *aqua regia*-cleaned round-bottomed flask, 5.0 mL of aqueous gold tetrachloraurate hydrate ($HAuCl_4 \bullet 3H_2O$, 10.0 mM) was combined with 1.5 mL of aqueous 0.1M sodium citrate and diluted to a final volume of 400 mL with ultrapure deionized water. The reaction mixture was stirred vigorously for 10 min. An aqueous solution of ice-cold 10.0 mM sodium borohydride (30.0 mL) was then added to the reaction mixture, while stirring continued. Following borohydride addition, the solution rapidly changed color to a deep brown, and then red-orange over the course of the first 10 minutes of stirring. The resulting AuNP solution was then stirred for a further 3.0 hours. The crude 4 nm Cit-AuNPs were then concentrated using a diafiltration apparatus, prior to polyelectrolyte wrapping.[50] Cit-AuNPs were then wrapped with polyallylamine hydrochloride (PAH) to prepare 4 nm PAH- AuNPs, as previously described.[51] Briefly, the concentrated Cit-AuNP solution was dispersed in 20.0 mL of a 1.0 mM aqueous sodium chloride solution to give a final AuNP concentration of approximately 20.0 nM. To each 20.0 mL of polyelectrolyte wrapping solution, 500 µL of 15 000 Mw PAH (10.0 mg/mL) dissolved

in 1.0 mM NaCl was then added. The wrapping solution was briefly mixed at vortex briefly and left to stand for 16 h. The PAH-AuNPs were subsequently purified by centrifugation and washing (55 min. at 18,894 × g), in ultrapure deionized water. The purified PAH-AuNPs were then concentrated in a diafiltration membrane.[50]

MPA-AuNPs *(4.3 ± 1.3 nm).* MPA-stabilized AuNPs were prepared by direct synthesis with sodium borohydride according to previously reported methods.[52] Briefly, a 500 mL aqueous solution of HAuCl4 (1.5 mM) and MPA (3.0 mM) was prepared using ultrapure deionized water in aqua regia-cleaned round-bottomed flask. The pH of the growth solution was adjusted to approximately 8.5 by the addition of dilute aqueous sodium hydroxide and stirred at vortex for 10 min. 10.0 mL of a 0.1 M aqueous sodium borohydride solution was then added to the reaction mixture. The combined solutions rapidly changed color to a deep orange-brown, and the reaction mixture was stirred for a further 3 hours. The thiol-stabilized AuNPs were then concentrated and purified by diafiltration (40.0 volume equivalents of ultrapure deionized water in a 50 kD membrane).

3.2.2 AuNP characterization and analysis

Synthesized functionalized AuNPs were characterized in Milli-Q water, bacteria growth medium, and Daphnia medium using various analytical techniques, including TEM for absolute sizes (JEOL 2100 Cryo TEM), dynamic light scattering for hydrodynamic diameter (Brookhaven ZetaPALS), zeta-potential for surface charge (Brookhaven ZetaPALS), and UV-Vis localized surface plasmon resonance (LSPR) spectroscopy for particle concentration and aggregation (Mikropack DH-2000 UV-vis-NIR Spectrometer).

3.2.3 Free ligand suspensions

Free ligands, MPA and PAH (M_w 15, 000 g/mol), were obtained from Sigma Aldrich.

MPA and PAH ligands are readily soluble in water and do not require a co-solvent for dispersion. The ligands were dissolved into Milli-Q water at a maximum concentration of 50 mg/L and diluted accordingly for free ligand toxicity control experiments.

3.2.4 *Shewanella oneidensis* MR-1 cultivation and cell respiration assay

S. oneidensis MR-1 cultivation. *S. oneidensis* MR-1 was obtained from Professor Jeffery Gralnick, University of Minnesota Department of Microbiology and was stored at -80°C before use. Bacteria were inoculated onto a LB broth agar plate and incubated at 30°C for 24 hours or until visible colonies formed. A minimal medium consisting of salts and buffering agent was used in this study. 0.68 g NaCl, 0.3 g KCl, 0.285 g $MgCl_2 \cdot 6H_2O$, 0.3975 g Na_2SO_4, 0.15 g NH_4Cl, and 2.383 g HEPES (4-(2-hydroxyethyl) piperazine-1-ethanesulfonic acid) were dissolved in 1 liter of Milli-Q water. After autoclaving and cooling down, 0.0125 g Na_2HPO_4 and 0.0056 g $CaCl_2$ were added per liter. Right before use, 1.86 mL sodium DL-lactate syrup (60% w/w, Sigma-Aldrich) was mixed with the minimal medium to make 100 mL of the final growth medium containing 129 mM sodium DL-lactate. Lactate was used as an additional carbon source to promote bacterial growth. Colonies formed on agar plates were inoculated into the minimal medium with lactate in sterile culture tubes and grown in a 32 °C orbital shaker at 300 rpm until OD_{600} ~0.25, the maximal optical density that *Shewanella oneidensis* MR-1 can reach in the minimal medium with lactate.

Monitoring *S. oneidensis* oxygen uptake. The oxygen uptake of the bacteria population over time was monitored using a PF-8000 aerobic/anaerobic respirometer system (Respirometer Systems and Applications, LLC). Bacteria were grown in minimal medium with lactate until it reached OD_{600} ~0.25 and diluted 1:10 into that growth medium supplied with NP/ligands in reaction vessels that were kept in a 32 °C water bath. Exposures of PAH-NPs were conducted at 30, 100, and 5000 μg/L, and exposures of PAH ligand were 30, 100, 300, 600, 1000, 2000 and 5000 μg/L. In all

subsequent experiments and comparisons, a ten-fold mass concentration of PAH free ligand and an equivalent mass concentration of MPA free ligand were used as ligand controls, which was calculated to be an overestimate of possible total free ligand present in the suspension (See Appendix A.2.1 and A.2.2).[53] A tube filled with 1 mL 30% (w/w) KOH solution was inserted into each reaction vessel to absorb carbon dioxide generated from cell respiration. The consumption of oxygen was compensated by continuous oxygen injection to keep the pressure constant in the headspace of the reaction vessels. Oxygen uptake was recorded every 10 minutes automatically for 24-48 hours by the instrument. The first derivative of oxygen uptake was plotted to identify the maximal oxygen uptake rate and the time of that maximum. To represent each cell oxygen uptake trace with a single value, the ratio of maximal oxygen uptake rate to the time when it reached maximal rate was calculated following the equation below:

$$Ratio = \frac{Maximal\ rate\ (\frac{mg}{h})}{Time\ to\ reach\ maximal\ rate\ (h)}$$

The ratio was then normalized to the average of control groups and represented as a percentage, where 100% indicates no inhibition of cell oxygen uptake.

3.2.5 *Daphnia magna* cultivation and biological assays

***D. magna* cultivation.** Populations used in this experiment were cultivated at the UW-Milwaukee School of Freshwater Sciences in the R. Klaper laboratory. *Daphnia* neonates used for the gene expression assays were collected from populations maintained in moderately hard reconstituted water (MHRW) incubated at 20°C on a 16:8 light/dark cycle as designated by EPA protocols.[54] *Daphnia* breeding populations were held at a concentration of 14 adult *Daphnia* per 1 L of media in glass beakers and were discarded once adults reached 28 days old. *Daphnia* were fed 50 mL freshwater algae (*Pseudokirchneriella subcapitata*) at an algal density of 400,000 algal cells/mL and 15 mL of dissolved alfalfa (*Medicago sativa*). Alfalfa stock was prepared by

suspending 405 mg of Alfalfa in 50 mL milli-Q water after 15 minutes of stirring and 5 minutes of centrifugation at 3,829 × g.

***D. magna* acute assay.** Acute survival assays were carried out in a 48-hr static exposure. All exposures used 5 *Daphnia* neonates (24-48 hours old) per 100 mL of MHRW (control), NPs, or free ligands suspended in MHRW, bringing the total volume to 100 mL. A minimum of three replicates was carried out for each treatment, and survival was determined as percentage alive at 48 hrs. Exposures were carried out to determine sublethal concentrations of NPs and free ligands. Concentrations tested for NPs and free ligands are: 1, 5, 10, 50, 100 μg/L for PAH-AuNPs and PAH free ligand and 1, 5, 10 and 25 mg/L for MPA-AuNPs and MPA free ligand.

***D. magna* chronic assay.** *Daphnia* chronic exposures used 5 *Daphnia* neonates (24 - 48 hours old) exposed to NPs or ligands for 21 days in a static renewal exposure, and triplicate assays were performed for each condition. A total of 5 neonates were placed in 94 mL of MHRW (control) or NPs/ligands where full media change out occurred three times per week. In chronic exposures, daphnids are supplemented with 4 mL of algae (*Selenastrum capricornitum*) and 2 mL of alfalfa (*Medicago sativa*) at each media exchange to bring the total volume to 100 mL. Concentrations tested in the chronic assay were: 1 and 5 μg/L for PAH-AuNPs and PAH free ligand and 5 and 25 mg/L for MPA-AuNPs and MPA free ligand. Reproduction and mortality were measured at each media exchange, and body size was recorded at the end of the exposure.

Reproductive exposures adhered to the mortality and reproduction guidelines designated by the OECD (OECD guidelines 1998). Daphnids were kept at a concentration of 5 daphnids per 100 mL, and results were normalized to controls (i.e. daphnia exposed to only MHRW) to account for changes in reproduction and body size as these replicate exposures took place over a period of several months.

3.2.6 Gene expression exposures and RNA preservation

Gene expression exposures were performed in parallel with bacterial oxygen uptake and *D. magna* survival and reproduction assays.

S. oneidensis. Colonies from agar plates were inoculated in minimal medium supplied with 129 mM lactate until the bacterial suspension reached OD_{600} ~0.25. The bacterial suspension was adjusted to OD_{600} = 0.2 before AuNPs were added. The sublethal dosages, 30 µg/L of PAH-AuNPs and 300 µg/L of PAH ligand, and 5 mg/L of MPA-AuNPs/ligands, were primarily used for gene expression studies; in addition, a 100 µg/L dose of PAH-AuNPs was used to investigate two biomarker candidates, in order to provide further evidence to link molecular pathways to inhibition of bacterial oxygen uptake. After exposure, the bacterial suspension was incubated on a 32°C orbital shaker at 300 rpm for 1 hour or 6 hours. Cells were harvested by centrifuging at 1,500 × g for 10 minutes, and then the pellets were sufficiently re-suspended into either 200 µL (PAH-AuNP/ligand) or 1 mL (MPA-AuNP/ligand) of RNAzol®RT (Molecular Research Center, Inc.) for cell lysis and RNA preservation.

D. magna. *Daphnia* neonates (24-48 hours old) were exposed to NPs and free ligands in an acute exposure lasting 24 hours. All exposures used 10 neonates per 100 mL of MHRW (control) or NPs or free ligands suspended in MHRW (treatment) bringing the total volume to 100 mL. Exposures were carried out at sublethal concentrations of NPs/free ligands between 5-1000 µg/L depending on the NP/free ligand being considered. Sublethal concentrations for acute exposures were chosen based on previous study.[13] Greater than three replicates were carried out for each treatment and concentration tested. At the end of the exposure duration, daphnids were collected and put in a 1.5 mL RNase-free eppendorf tube corresponding to their replicate number. Excess liquid was removed and daphnids were immediately flash frozen in liquid

nitrogen and stored at -80°C to await further processing. For *D. magna* chronic exposures, exposures were carried out at sublethal concentrations of NPs/free ligands between 5-5000 µg/L, and daphnids were collected at the end of the 21-day exposure period and preserved using the same method as the acute exposure samples. For all samples, RNA was extracted using TRIzol® for cell lysis and RNA preservation.

3.2.7 RNA extraction, reverse transcription and real-time quantitative PCR

A Direct-zol™ RNA MiniPrep kit (Zymo Research) was used for total RNA isolation and purification by spin columns. The manufacturer's recommended protocol was followed using a centrifugation speed of 12,000 × g with an on-column DNase I treatment at 30°C for 15 minutes. RNA was finally eluted from the column at 16,000 ×g for 1 minute. Total RNA was characterized using a Thermo Scientific NanoDrop 8000 and an Agilent 2100 Bioanalyzer for quality control.

Total RNA was reverse transcribed into cDNA following the manufacturer's protocols. Briefly, 100 ng of total RNA were incubated in the presence of either random primers (Promega) for *S. oneidensis* or oligo(dT)$_{15}$ primer (Promega) for *D. magna* at 65°C for 5 minutes. After cooling on ice for 1 minute, the SuperScript III reverse transcriptase, DTT, and RNaseOUT™ recombinant ribonuclease inhibitor (Life Technologies) were added into the mixture followed by incubation at 25°C for 5 minutes (this step was only for random primers), 50°C for 60 minutes, and 70°C for 15 minutes for primer extension. Once synthesized, cDNA samples were stored at -20°C.

Target genes were chosen for both *S. oneidensis* and *D. magna*. Four pairs of genes in similar pathways related to stress response in the two organisms were selected, including *gst* (*S. oneidensis*)/*gst* (*D. magna*, same order for the following pairs) for xenobiotic detoxification, *nqrF*/*nadh* for electron transport, *katB* and *sodB*/*cat* for oxidative stress attenuation, and *ibpA*/*hsp70* for heat shock response. To link to apical

endpoints, the *vtg* gene for *D. magna* reproduction and *ftsK* for bacterial cell division were also examined. Genes for actin (*act*) in *D. magna* and for 16S ribosomal RNA (16S) and RNA polymerase (*rpoA*) in *S. oneidensis* were monitored to consider NP/ligand impacts on basic organism machinery. In addition, stress response genes including *pspB* for extracytoplasmic stress, *sodB* for oxidative stress, and *radA* for DNA repair were also examined in *S. oneidensis*. **Table 3.1** shows a full list of genes along with their corresponding functions.

Primers for real-time quantitative PCR were designed by the PrimerQuest Tool (Integrated DNA Technologies). Two sets of primers were designed for each gene, and the one with efficiency closest to 1 was chosen to be the primer for subsequent real-time PCR. Table 3.1 includes a full list of primers used in this study.

Real-time quantitative PCR (qPCR) was performed on a StepOnePlus™ Real-Time PCR System (Life Technologies) using SYBR Green as the fluorescent intercalating dye (iTaq™ Universal SYBR® Green Supermix, Bio-Rad). For each qPCR reaction, cDNA and primers were mixed with the fluorescence dye following the manufacturer's protocol. Starting with an initial 10 min denaturation at 95°C, real-time PCR repeated 40 cycles of amplification, each of which was 15 s at 95°C followed by 30 s at 60°C. Fluorescence of SYBR Green was detected at the end of each cycle. All qPCR experiments were done in technical duplicates.

Table 3. 1 Target genes, corresponding functions, and their primers for qPCR.

***Shewanella oneidensis* MR-1**				
Target Gene	**Forward primer (5'-3')**	**Reverse primer (5'-3')**	**Function**	**Accession Number**
Glutathione S-transferase (*gst*)	GCA AAG CAT TCC AGC AAT TT	GAC CTT CTT GCG TTT TGA GC	Xenobiotic detoxification	NP_720213.1
Na-translocating NADH-quinone reductase subunit F (*nqrF*)	CGC TTA CTC GAT GGC TAA CTA C	GCA AGG CAG CGT CAA ATT AC	Mitochondrial electron transport NADH to ubiquinone	NP_716734.1
Double-stranded DNA translocase (*ftsK*)	TAC GAG TCG TGT TGC GAT AAA	AAG GGC TGA CAC TGG AAT AAA	Cell division	NP_717901.1
Catalase HPII (*katB*)	GGC ATT GAT CCT GAT TCT TCT C	TCC AAC GAG GGA AGT TAC CA	Catalase activity; response to oxidative stress	NP_716697.1
16 kDa heat shock protein A (*ibpA*)	GCA ACT CAG GTT ATC CTC CAT AC	CGC TAC TGA TCT CAA GCT CTT C	Response to heat; chaperone activity	NP_717873.1
16S ribosomal RNA (16S)	TCA AGT CAT CAT GGC CCT TAC	TAC GAC GAG CTT TGT GAG ATT AG	Component of prokaryotic ribosomes	NR_074798.1
RNA polymerase alpha subunit (*rpoA*)	TCG CAT CCT ATT GTC GTC TAT G	CTT CTT GTA CGC CTT CCT TAC T	DNA-directed RNA polymerase activity	NP_715896.1
ATP-dependent protease (*radA*)	TTC GGC AAT TTT CCT CTC C	ACA CCA CCA TGA CCA AGG AT	DNA repair	NP_716849.1
Phage shock protein B (*pspB*)	TTG ATT GCG AAA GCC GAT A	ATC AAG AAT CGC CTC TAA GGT TT	Extracytoplasmic stress	NP_717416.1
Fe/Mn superoxide dismutase (*sodB*)	GCA ATG TTC GCC CTG ACT AC	CCT GCG AAG TTT TGG TTC AC	Removal of superoxide radicals	NP_718453.1

Daphnia magna				
Target Gene	**Forward primer (5'-3')**	**Reverse primer (5'-3')**	**Function**	
Glutathione S-transferase (*gst*)	CAA CGC GTA TGG CAA AGA TG	CTA GAC CGA AAC GGT GGT AAA	Xenobiotic detoxification	AF448500.1
Dehydrogenase (*nadh*)	GCA GGA AAC AAT AAG GCA AAC C	GGT GGC ACA GAC CAT TTC TTA	Mitochondrial electron transport and energy production	ABD19473.1
Vitellogenin (*vtg*)	CTG TTC CTC GCT CTG TCT TG	CCA GAG AAG GAA GCG TTG TAG	Reproduction, sexual maturation and general stress	BAE94323.1
Catalase (*cat*)	CAG GAT CAT CGG CAG TTA GTT	CTG AAG GCA AAC CTG TCT ACT	Oxidative stress attenuation	ACU81116.1
Heat shock protein 70 (*hsp70)*	CCT TAG TCA TGG CTC GTT CTC	TCA AGC GGA ACA CCA CTA TC	Response to heat; protein folding	ACB11340.1
β-Actin (*act*)	CCA CAC TGT CCC CAT TTA TGA A	CGC GAC CAG CCA AAT CC	Cytoskeleton production and cell maintenance	CAB99474.1

3.2.8 NORMA-Gene analysis of qPCR data

Real-time quantitative PCR data were processed by the Miner[55] program and NORMA-Gene algorithm.[56] Miner applies an objective analysis scheme to obtain the dynamic fluorescence threshold (R), threshold cycle number (C_t), and efficiency (E) for each qPCR reaction, instead of using the same threshold for all reactions. Data of normalized reporter signal (Rn) versus cycle number were extracted from amplification data exported from the StepOnePlus™ software as the input to the Miner program to obtain R, C_t, and E values for each reaction. R_0, the initial fluorescent reporter signal, was calculated based on the equation below:

$$R_0 = R \times (1 + E)^{-C_t}$$

Due to the change in housekeeping genes throughout experiments, NORMA-Gene, a qPCR normalization method based on target gene data, was applied to normalize the gene expression data and reduce the variation among replicates rather than using a single housekeeping gene. Using this technique, the geometric means of R_0 values of technical duplicates were calculated as the average and were put into the NORMA-Gene workbook generously provided by Dr. Yuya Hayashi. Normalized R_0 values, which were the output of NORMA-Gene algorithm, were then further normalized to control groups by dividing the normalized R_0 of treated groups by the geometric mean of normalized R_0 values of control groups to obtain the relative fold change.

3.2.9 Statistical analysis

The normalized ratios from oxygen uptake traces were further subjected to statistical analysis. No normality and outliers were considered within this data set due to the limited sample size ($N<5$). The two-tailed Student's t-test was performed on treated samples versus their respective control group with $\alpha = 0.05$. GraphPad Prism (GraphPad Software, Inc.) was used for statistical analysis.

Data from *Daphnia* acute studies failed to meet the assumptions of normality. Therefore,

the effects of NP and free ligand exposures on *Daphnia* survival, were compared to controls using the Student's t-test for two-independent samples (N<3). Impacts on daphnid reproduction and body size were assessed using one-way ANOVA with Tukey's multiple comparison tests after normality and variance homogeneity were determined (N>3). One round of statistically determined outliers was removed, and treatments were deemed significantly different than controls at probability value < 0.05. SPSS (IBM 2013).

The relative fold change values of *S. oneidensis* gene expression were $\log_2$-transformed followed by the combination of control groups. Outliers were identified and excluded from the data set (ROUT algorithm, Q = 1.0%, Prism GraphPad), and post-hoc Tukey's tests after ANOVA were performed to determine statistical significance among different treatments at one time point and one gene of interest. For the 16S and *sodB* genes upon 100 µg/L PAH-AuNP exposure, as there was only one treatment, an unpaired t-test was used instead of ANOVA. Again, normality was not tested due to the limited sample size (N < 6). GraphPad Prism was used to perform statistical analysis.

The relative gene expression data from *Daphnia* short-term and long-term gene exposures were normalized to controls and $\log_2$ transformed to fit a normal distribution. Outliers were removed prior to statistical analysis. Significant differences in relative expression were determined using one-way ANOVA with Tukey's multiple comparison tests after normality and variance homogeneity were determined ($p < 0.05$) (N>3). SPSS (IBM 2013) was used to interpret data.

3.3 Results

3.3.1 Nanoparticle characterization

TEM analysis of absolute size showed that the two AuNPs had very similar core size, while the hydrodynamic diameter of PAH-AuNPs in water was larger than MPA-

AuNPs, possibly due to the polyelectrolyte wrapping (**Table 3.2**). It was notable that MPA-AuNPs showed increased hydrodynamic diameter and a peak shift in UV-vis extinction upon resuspension in growth medium, indicating the aggregation of MPA-AuNPs, though the MPA-AuNPs still retained a negative surface charge in the growth medium (**Table 3.2**). The aggregation may result from elevated ionic strength in the growth medium or the pH change from slightly acidic Milli-Q water (pH ~6.3) to neutral growth medium (pH ~7.2). This aggregation might lead to altered NP toxicity, as previous studies have revealed.[19,57] Similar behavior was not observed on PAH-AuNPs, indicating more stability of PAH-AuNPs in growth medium than MPA-AuNPs (**Table 3.2**).

Table 3. 2 Nanoparticle characterization.

	PAH-AuNPs		MPA-AuNPs	
	S. oneidensis Media	*D. magna* Media	*S. oneidensis* Media	*D. magna* Media
[b]LSPR λ_{max} (nm) (in H_2O)	528		515	
LSPR λ_{max} (nm) (in medium)	530	530	555	575
d_{core} (nm) *	4.7 ± 1.5 (N ≥ 250)		4.3 ± 1.3 nm (N = 501)	
D_h (nm) (in H_2O)	[a]200.2 ± 3.5		126.4 ± 3.7	
D_h (nm) (in medium)	[a]159.5 ± 0.6	[a]79.43 ± 1.9	339.6 ± 21.9	364 ± 34.2
ζ-Potential (mV) (in H_2O)	+68.5 ± 1.6		-17.3 ± 0.6	
ζ-Potential (mV) (in medium)	+24.57 ± 5.6	+10.5 ± 4.8	-24.28 ± 3.2	-29.8 ± 1.3

*Based on TEM analysis. See Figure A.2.1 for TEM images.

[a] For polyelectrolyte wrapped particles, hydrodynamic diameter (D_h) determined by dynamic light scattering is not accurate. [b] Localized surface plasmon resonance (LSPR) wavelength of maximum peak value (λ_{max}).

3.3.2 *Shewanella oneidensis* oxygen uptake

PAH-AuNPs significantly affected bacterial oxygen uptake at 100 μg/L (unpaired t-test, $t=9.895$, $df=5$, $p < 0.05$) while its corresponding free ligand control, 1 mg/L of PAH free ligand elicited similar inhibition compared to control groups (unpaired t-test, $t=4.222$, $df=6$, $p < 0.05$) (**Figure 3.1(c)**). A concentration of 30 μg/L of PAH-AuNPs was chosen as the sublethal dose as this concentration produced no inhibition; this NP dose was paired with the 10-fold dose, 300 μg/L, as the corresponding PAH free ligand control. MPA-AuNPs did not inhibit bacterial oxygen uptake at the highest dose tested (5 mg/L), while the respective 5 mg/L of MPA free ligand demonstrated oxygen uptake inhibition ($t=9.713$, $df=2$, $p < 0.05$) (**Figure A.2.2**).

As the oxygen uptake reflects bacterial population growth, the doubling time of bacterial growth at the exponential phase was calculated based on oxygen uptake traces (See Appendix A.2.3). Results showed that *S. oneidensis* had an average doubling time between 2 and 3 hours in the growth medium used in this study; thus, 1 hour was chosen as a time point for short-term exposure and 6 hours for long-term exposure in the subsequent gene expression studies.

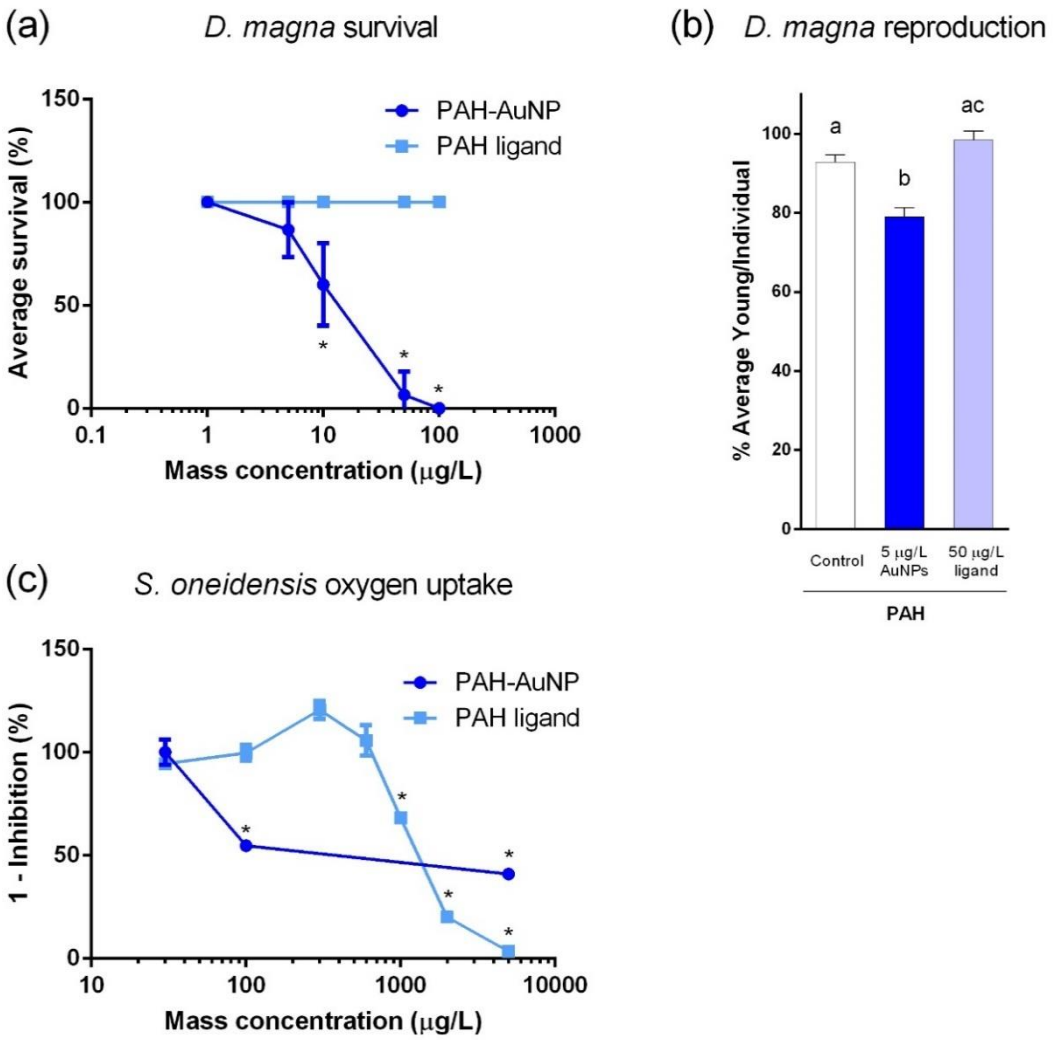

Figure 3. 1 Impact of PAH-AuNPs and PAH ligand on (a) *D. magna* survival (%), (b) *D. magna* reproduction and (c) *S. oneidensis* oxygen uptake. Error bars represent standard error of the mean. Stars indicate significant difference compared to corresponding control groups (*S. oneidensis*, unpaired t-test, α=0.05, n≥2; *D. magna*, unpaired t-test, α=0.05, n≥3). Different letter designations in (b) indicate significant difference between groups (Tukey's test, α=0.05).

3.3.3 *S. oneidensis* gene expression response

At the sublethal exposure dosages, differential expression levels of ten genes in *S. oneidensis* were observed at both 1-hour and 6-hour time points when comparing treatment and control. The general pattern of gene expression is summarized in the heat map (**Figure 3.2(a)**).

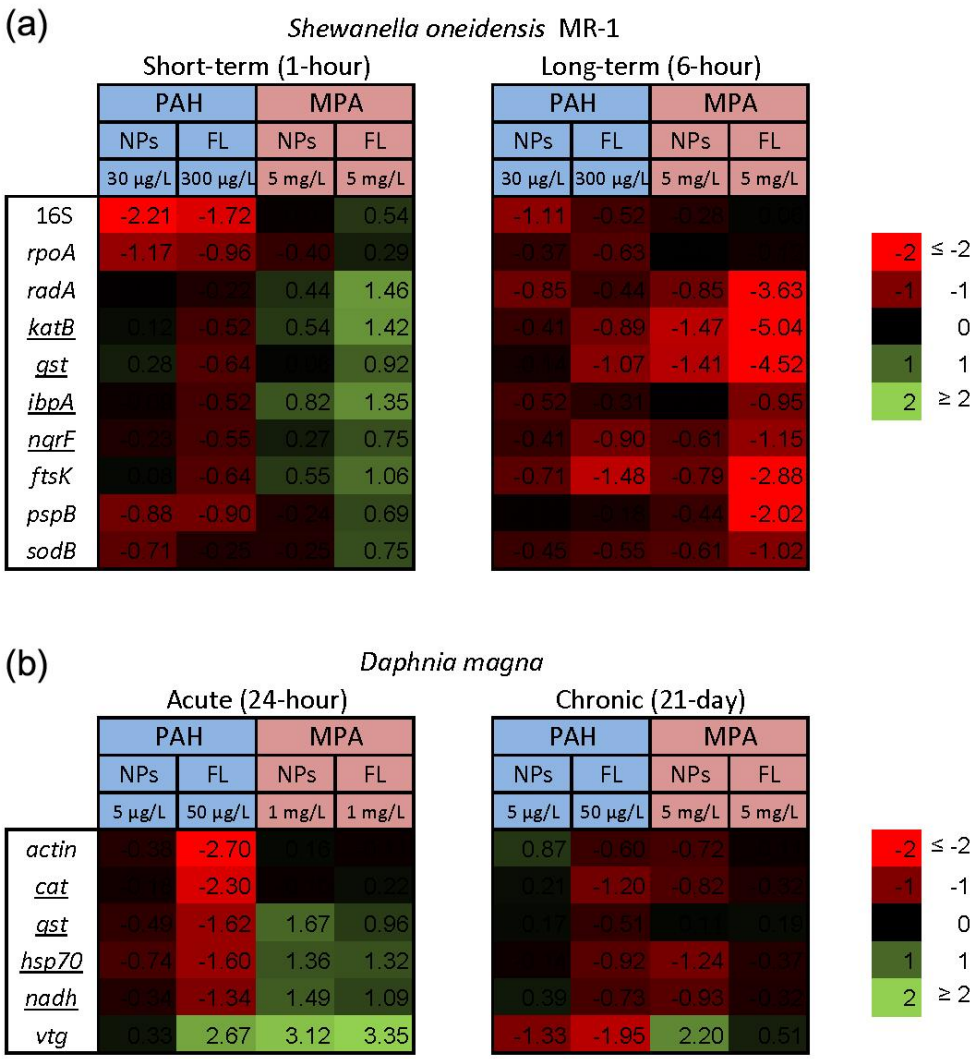

Figure 3. 2 Heat map of (a) *S. oneidensis* and (b) *D. magna* gene expression response. Sublethal dosages of AuNPs and their respective ligand control were used in the gene expression study, as shown in the figure. Genes encoding for similar cellular functions in two model organisms were underlined.

In all cases, the differences in gene expression appear to be dominated by ligand rather than NP exposure. All changes in gene expression induced by ligand-NP combination were accompanied by the changes in their respective free ligand control, including 16S

(PAH, F = 18.33, df = 22, p < 0.0001), *rpoA* (PAH, F = 8.177, df = 31, p = 0.0001), *pspB* (PAH, F = 8.198, df = 22, p < 0.0003), and *ibpA* (MPA, F = 36.92, df = 22, p < 0.0001) at 1-hour exposure (**Figure 3.3(a)**), and *sodB* (PAH and MPA, F = 10.06, df = 22, p < 0.0001) at 6-hour exposure (**Figure 3.3(b)**). Exceptions are two NP-specific effects that were observed in *sodB* (PAH, F = 7.543, df = 22, p < 0.05) at 1-hour exposure and 16S (PAH, F = 3.238, df = 22, p < 0.05) at 6-hour exposure, where the free ligand control did not elicit similar effects as NPs when compared to control. For these two genes, *S. oneidensis* was exposed to a higher dosage (100 µg/L) of PAH-AuNPs to explore the link to inhibition of oxygen uptake (**Figure 3.4**). The 16S gene expression decreased upon 100 µg/L PAH-AuNP exposure at 6-hour exposure (unpaired t-test, t=38.67, df=7, p<0.0001), while *sodB* gene expression did not show a significant difference compared to the control group at 1-hour exposure.

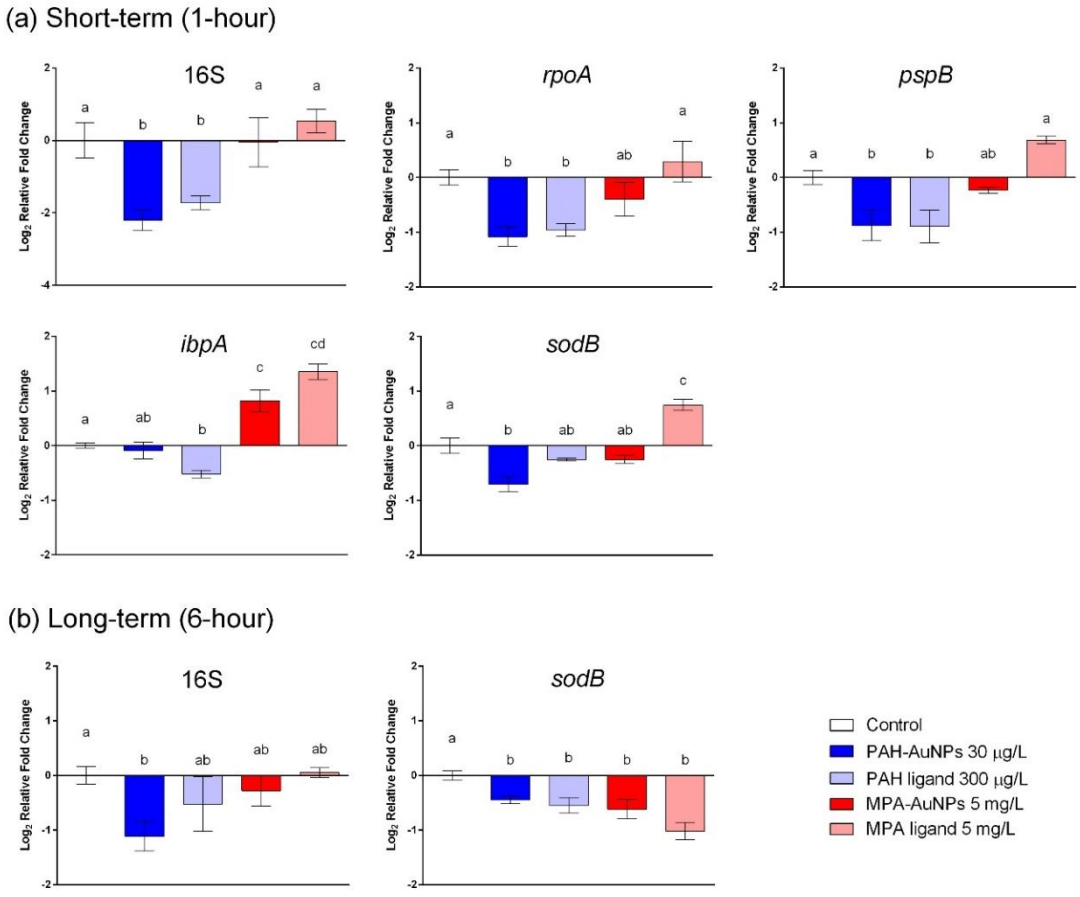

Figure 3. 3 Selected gene responses in *S. oneidensis* upon AuNP/ligand exposure. Error bars showed standard error of the mean (PAH-AuNP, n=5; PAH ligand, n=4; MPA-

AuNP/ligand, n=3). All figures follow the same legend, and the first bar in every figure indicates control group. Different letter designations between different groups indicate significant difference (Tukey's test, α=0.05).

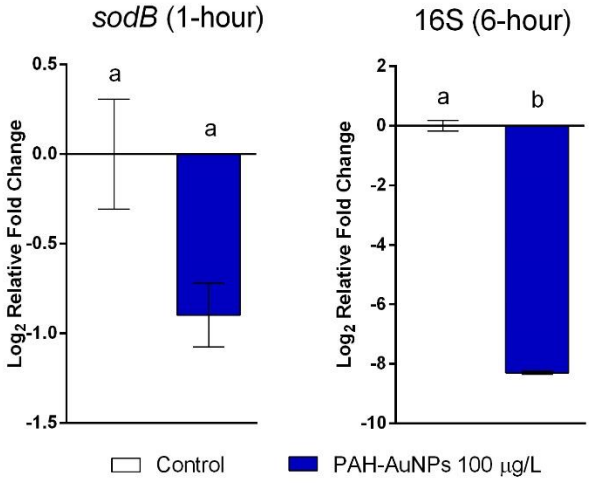

Figure 3. 4 In *S. oneidensis*, 16S gene expression decreased upon 100 μg/L PAH-AuNP exposure at long-term exposure (6-hour), while *sodB* gene expression did not show significant difference compared to control group. Error bars showed standard error of the mean (n≥4). Both figures follow the same legend. Different letter designations indicate significant difference between groups (unpaired t-test, α=0.05).

The difference in ligand-NP combination appears to be important in determining the differential gene expression pattern at 1-hour exposure, as only down-regulation was observed in PAH-AuNP exposure but only up-regulation was observed in MPA-AuNP exposure (**Figure 3.2(a)**). However, upon 6-hour exposure, the ligand-NP combination did not determine the gene expression pattern, as only down-regulation was observed for all treatments, regardless of the type of ligand (**Figure 3.2(a)**).

Time frame is also an important factor in terms of gene expression response, as differential gene expression responses were observed at different time points. In the response to PAH-AuNP/ligand exposure, effects that were observed in the *rpoA* and *pspB* genes at 1-hour exposure diminished by the 6-hour exposure timepoint. More interestingly, for MPA-AuNP/ligand exposure, the expression level compared to control

at 6-hour exposure appeared to be opposite of the responses in 1-hour exposure, especially for MPA ligand exposure.

3.3.4 *Daphnia magna* acute toxicity

NP surface functionalization played an important role in acute toxicity in the form of daphnid survival, with positively charged PAH-AuNPs being orders of magnitude more toxic than the negatively charged MPA–AuNPs (**Figure 3.2(a)**). PAH–AuNPs significantly affected daphnid mortality, eliciting 40% mortality at 10 μg/L ($U = 0$, $p < 0.05$).[13] MPA–AuNPs did not significantly affect daphnid survival at the highest concentration tested, 25 mg/L (data not shown) ($p > 0.05$).[13] The free ligands used in NP functionalization had no impact on daphnid survival at any concentration tested.

3.3.5 *Daphnia magna* chronic toxicity

Ligand-NP combination is also important in governing the chronic impacts on daphnid reproduction. Of the two NPs tested, PAH-AuNPs significantly decreased daphnid reproduction over the 21-day chronic exposure (**Figure 3.2(b)**) while MPA-AuNPs did not (data not shown). PAH–AuNPs significantly decreased daphnid reproduction by 15% at the highest concentration tested, 5 μg/L ($F= 14.751$, $df= 23$, $p < 0.05$). In comparison, PAH free ligand caused a statistically insignificant increase in daphnid reproduction at 50 μg/L. As previously reported, 5 mg/L MPA free ligand increased daphnid reproduction by 14% ($U = 4$, $p < 0.05$, data not shown).[13]

3.3.6 *Daphnia magna* acute gene expression response

After a 24-h acute exposure, NP functionalization is also an important factor in determining *Daphnia* response at the gene level when exposed to PAH and MPA-AuNPs, resulting in different gene expression patterns for *cat, nadh*, *vtg, gst* and *hsp70* (**Figure 3.2**). For *Daphnia* exposed to PAH-AuNPs, there was a significant 0.74 fold

decrease in the relative expression of *hsp70* (F= 31.799, df= 49, P<0.05) compared to controls. *Daphnia* exposed to MPA-AuNPs caused a statistically significant 1.36 fold increase for *hsp70* (F= 31.799, df= 49, P<0.05), 1.49 fold increase for *nadh* (F=29.066, df=55, p<0.05), 1.67 fold increase for *gst* (F=23.116, df=53, p<0.05) and 3.12 fold increase for *vtg* (F=11.556, df=47, p<0.05) over controls. MPA-AuNP-exposed *Daphnia* had significantly different gene expression patterns than *Daphnia* exposed to PAH-AuNPs for *nadh, vtg, gst* and *hsp70* (**Figure 3.2 and 3.5**). Notably, PAH-AuNPs caused a 0.33 fold increase in relative expression of *vtg* while MPA-AuNPs elicited a 3.12 fold increase in relative expression of *vtg* (F=11.556, df=47, p<0.05).

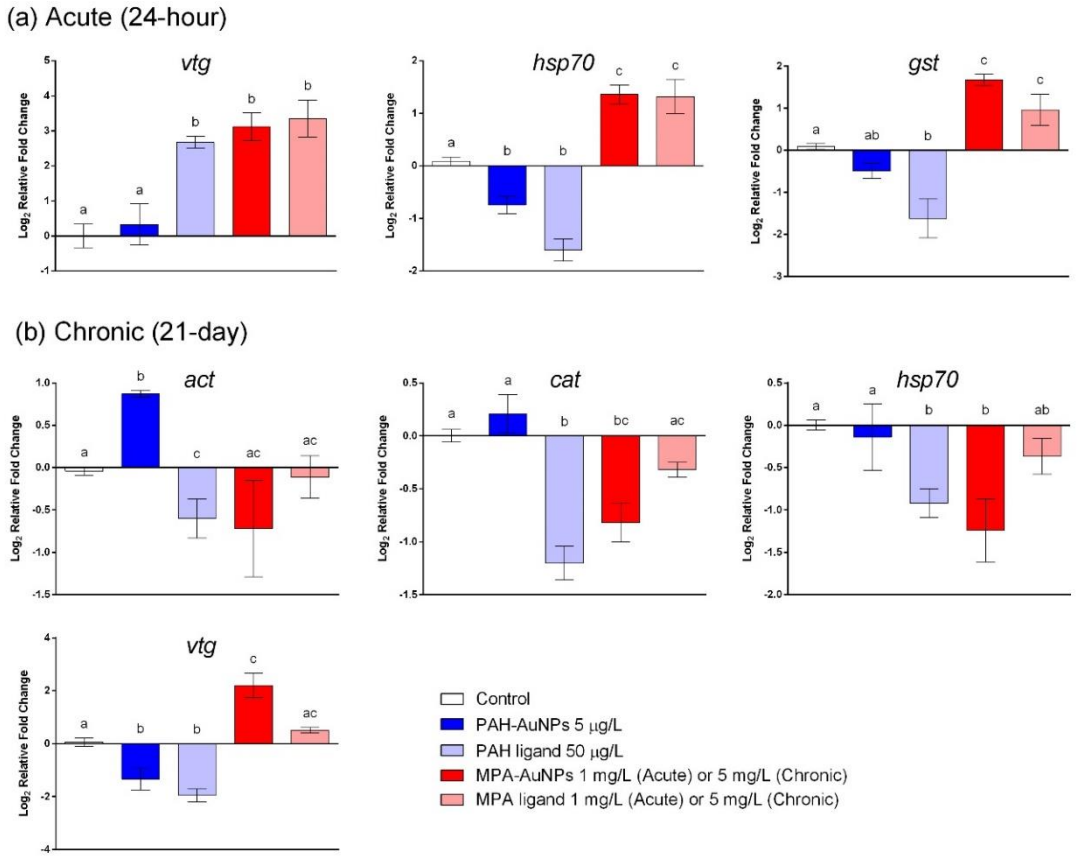

Figure 3. 5 Selected gene responses in *D. magna* upon AuNP/ligand exposure. Error bars showed standard error of the mean (n≥6 for all exposure). All figures follow the same legend. Different letter designations between different groups indicate significant difference (Tukey's test, α=0.05).

The impacts of free ligands used in particle functionalization closely follow the gene expression patterns observed for their respective functionalized NPs at 24-hour exposure (**Figure 3.2**). *Daphnia* exposed to the PAH ligand showed no statistical difference compared to *Daphnia* exposed to PAH-AuNPs for all genes tested except *cat* ($F= 8.640$, $df=55$, $p<0.05$) and *vtg* ($F=11.556$, $df=47$, $p<0.05$). Each gene that showed a significant positive fold change in relative expression for *Daphnia* exposed to MPA-AuNPs also showed a significant fold change in relative expression for the MPA free ligand treatment and did not significantly differ between the two.

3.3.7 *Daphnia magna* chronic gene expression response

Similar to the 24-hr acute exposure, AuNP surface functionalization played an important role in determining gene expression levels in *Daphnia* chronically exposed to AuNPs (**Figure 3.2 and 3.5**). For *Daphnia* exposed to PAH-AuNPs, there was a significant 1.33 fold decrease in the relative expression of *vtg* ($F=16.592$, $df=42$, $p<0.05$) and a significant 0.87 fold increase in the relative expression of *act* ($F=9.68$, $df=42$, $p<0.05$) over controls (**Figure 3.5**). MPA-AuNPs elicited a significant 1.24, 0.82 and 0.93 fold decreases in the relative expression of *hsp70* ($F=9.294$, $df=42$, $p<0.05$), *cat* ($F=18.128$, $df=44$, $p<0.05$) and *nadh* ($F=14.9$, $df=44$, $p<0.05$), respectively, compared to controls (**Figure 3.2 and 3.5**). Notably, for this treatment, there was a significant 2.2 fold increase in the relative expression of *vtg* ($F=16.592$, $df=42$, $p<0.05$) over controls (**Figure 3.2**). A significantly different gene expression response was observed for several genes when AuNP treatments were compared. PAH-AuNP treatment elicited a positive fold change in the relative expression of *cat*, *nadh* and *act* while MPA-AuNP elicited a negative fold for these same genes. The greatest difference between these two treatments was observed for *vtg*.

NP-specific impacts were observed in *Daphnia* chronically exposed functionalized AuNPs versus their respective PAH and MPA ligands as reflected in the gene expression

patterns (**Figure 3.2 and 3.5**). PAH-AuNP and PAH ligand caused a similar relative expression pattern in *Daphnia* for genes *gst*, *hsp70*, *vtg* and *nadh*, as no significant difference was observed among these conditions (**Figure 3.2**). However, PAH ligand caused 0.6-fold decrease in relative expression for *act* compared with the PAH-AuNP treatment that elicited a 0.98-fold increase in relative expression for *act* ($F=9.68$, $df=42$, $p<0.05$) (**Figure 3.5**). There were no significant differences between MPA ligand and MPA-AuNP treatments on *Daphnia* relative expression for all genes tested.

3.4 Discussion

Ligand-NP combinations differed in the extent of organismal apical endpoint impacts. Both model organisms were impacted to a greater extent by positively charged ligand-NP combinations with differential sensitivities. PAH-AuNPs were determined to be 2-3 orders of magnitude more toxic than the MPA-AuNPs for both *S. oneidensis* and *D. magna*. MPA-AuNPs caused no acute mortality in *D. magna* or inhibition on *S. oneidensis* oxygen uptake at the highest concentration tested (25 mg/L for daphnids and 5 mg/L for bacteria (**Figure A.2.2**).[13] PAH-AuNPs elicited mortality in *D. magna* at concentrations as low as 10 μg/L and decreases in reproduction at 5 μg/L (**Figure 3.1(a)**),[13] while *S. oneidensis* started to show respiratory inhibition at 100 μg/L (**Figure 3.1(c)**). Electrostatic interactions could largely drive the differences in sensitivity to the differently charged particles, as both eukaryotes and prokaryotes have cell surfaces that are negatively charged.[58,59] It is thought that, due to electrostatic interactions, positively charged NPs are more likely to interact with cell surfaces than negatively charged NPs. Goodman et al. observed similar differences in the toxicity of AuNPs functionalized with cationic and anionic side chains when exposed to mammalian cell lines and bacterial cells, [60] and Feng et al. demonstrated a similar correlation between toxicity and NP-cell association where increased NP-cell association was found for positively charged NPs compared to negatively charged NPs in bacteria. [61] In addition to electrostatic interactions, the low toxicity of MPA-AuNPs may be potentially explained

by the high degree of aggregation of MPA-AuNPs experienced in both organisms' exposure media, thus reducing bioavailability (**Table 3.2**). Overall, similar differential toxicity of the two functionalized NPs was observed in our study in both model organisms, indicating these organisms may follow the same electrostatic mechanism for interacting with NPs despite having distinct membrane surface chemistry, and that the general response of whole organism may be extrapolated from the response of cell lines, although they differ in sensitivity.

In some cases, the toxicity of select NPs may not be determined by their respective ligand alone, which demonstrates NP-specific organismal impacts. However, this nanoparticle specific effect was only true for *D. magna*, where the impacts to *S. oneidensis* could largely be attributed to the ligand itself and only at much higher concentrations. The differences in sensitivity observed for these two model organisms exposed to PAH-AuNPs may be due to the distinct differences in the cell surface chemistry of Gram-negative bacteria and the aquatic eukaryotes. Besides the cytoplasmic membrane, which are found in both bacterial and *Daphnia* cells, the Gram-negative *S. oneidensis* bacterial cell also has an envelope that consists of a peptidoglycan-lipoprotein complex, periplasmic zone, and an outer membrane layer.[58] The outer membrane layer is the first barrier that NPs would encounter, and this lipid bilayer retains various amounts of embedded lipopolysaccharides (LPS).[58] LPS are high molecular weight molecules with a basal lipid anchored in the lipid bilayer and a long negatively charged chain of polysaccharide. Recent work using *S. oneidensis* demonstrated that LPS is an important binding site for AuNPs.[62] Compared to the animal cell membrane, the complex structure of the cell envelope in *S. oneidensis* may provide extra protection when NPs are in proximity to the cells, thus desensitizing bacterial cells to NP exposures. In addition, studies demonstrate that eukaryote cells have many more mechanisms for supramolecular and colloidal particle internalization (e.g. receptor mediated endocytosis, pinocytosis and phagocytosis) for both nano- and

macro-sized particles, while very few studies show plausible evidence of internalization of nanomaterials into bacterial cells.[63-65] Furthermore, the manner by which multi and single-cellular organisms interact with NPs may also contribute to the difference in sensitivity. *Daphnia* actively accumulate NPs internally while bacteria only passively interact with NPs through random encounters on the surface. The difference in how NP interact and accumulate in two organisms may also result in the NP-specific effect observed in *D. magna* but not in *S. oneidensis*. PAH-AuNPs resulted in a decrease in *Daphnia* survival (10 μg/L) while the respective PAH free ligand control (100 μg/L) did not show any mortality (**Figure 3.1(a)**). However, when PAH-AuNPs elicited inhibition to bacterial oxygen uptake at 100 μg/L, the respective ligand control (1 mg/L) displayed a similar inhibition (**Figure 3.1(c)**). These biological differences and impacts of NP surface functionalization and free ligand type are further addressed by the presented gene expression study.

Gene expression revealed insight into potentially unique molecular pathways that may be impacted upon exposure to NPs and may explain the differences in toxicity across different ligand-NP combinations and supported the mortality and respiration results indicating a particle-specific impact in *Daphnia* versus *Shewanella*. In both acute and chronic assays, *Daphnia* exposed to PAH-AuNPs elicited a significantly different gene expression pattern compared with *Daphnia* exposed to MPA-AuNPs, despite the two NPs having the same gold core. These differences were notable in the 24-hr acute exposure for *hsp70, gst, vtg* and *nadh* and in the 21-day chronic assay for *hsp70, vtg, nadh, cat* and *act*. Amongst the genes that responded, a positive relative fold change for *act* was unique to the PAH-AuNP treatment in the 21-day assay with respect to the ligand control. Actin (*act*) encodes for a protein important to cytoskeleton and muscle fibril production as well as other cell functions. Studies have linked an increase in protein concentration of actin as a compensatory mechanism to maintain muscular and cellular performance in times of environmental stress.[66] In addition, studies have

indicated a high binding affinity of microparticles for actin[67] and have shown that multiple NP types damage actin filaments *in vitro*.[68-70] PAH-AuNPs could be potentially damaging muscle fibrils and cellular structure over long-term exposures in *Daphnia* and may be used as an indicator for stress to positively charged NPs, however, the relationship of this gene with apical endpoints impacted in *Daphnia* within this study remains unclear. *Daphnia* exposed to MPA-AuNPs only uniquely responded to the treatment with an increase in the relative fold change of *gst* at 24 hrs. This gene encodes for an enzyme glutathione S-transferase and is an important enzyme in xenobiotic detoxification as it conjugates compounds with glutathione and may be elevated in times of oxidative stress. Our previous studies observed *gst* induction in *Daphnia* dependent upon NP functionalization for fullerenes but only at concentrations that elicited significant mortality (> 5 mg/L).[9] Like MPA-AuNPs, these NPs exhibited a high degree of aggregation and exhibited low toxicity in *Daphnia*. This may demonstrate an acute whole organismal response to a high amount of negatively charged NPs. Our more recent previous study examined adult daphnid guts exposed to 4 nm PAH and MPA-AuNPs and their ligands at low concentrations (< 0.05 mg/L).[18] Here, we showed that significant amounts of ROS were produced for both MPA and PAH AuNPs and their respective ligands at the same concentrations. This leads us to believe that ROS production does not fully explain the adverse outcomes observed in our acute and chronic studies. Therefore, other mechanisms may be responsible for the observed impacts as *Daphnia* responded differently to MPA and PAH AuNPs but had similar amounts of ROS detected upon exposure to these treatments at the same concentrations. However, in our current study and the previous, gene expression patterns were different for the two ligand-NP combinations. These results suggest that pathways affected by NPs are strongly dependent upon NP surface properties.

For *S. oneidensis* gene expression assays were again indicative of the observed apical endpoint impacts. Most of the gene expression responses for *S. oneidensis* were

provoked equally by the free ligand exposure and ligand-NP combination at both time points. While MPA-AuNPs did not show any impact that was specific to NPs, the decrease in expression of 16S at 6-hour exposure and *sodB* gene at 1-hour exposure were unique to the PAH-AuNP but not to PAH free ligand. The *sodB* gene encodes for one of the superoxide dismutase (SODs) that protect cells from deleterious reactions of reactive oxygen species;[71] it has been previously reported that the *sodB* gene was up-regulated upon *S. oneidensis* exposure to chromium (VI).[72] More related, a previous study using 60-nm amino-functionalized polystyrene nanomaterial (PS-NH_2-NPs) on *E. coli* single-gene deletion mutants showed that the Δ*sodB* mutant was more sensitive to the exposure of PS-NH_2-NPs compared to the parent strain.[73] As PAH-AuNPs have a similar surface-functionalization of amine groups with PS-NH_2-NPs, these results suggest that the *sodB* gene plays an essential role in bacterial cell response to amine-functionalized nanomaterials, making it possible to use *sodB* as a biomarker for this specific NP surface functionalization. 16S ribosomal RNA (rRNA) is one of the three rRNAs, which are components of prokaryotic ribosomes. The rRNA transcription is the rate-limiting step in ribosome synthesis, and thus, directly correlates to protein synthesis and cell growth.[74] Previous research has reported that rRNA degradation occurs during environmental stress, including oxidative stress and starvation.[75-77] Notably, it was also reported that rRNA is degraded due to a change in cell membrane permeability, potentially leading to the entry of RNase I, an endoribonuclease, from the periplasmic space into the cytoplasm.[78,79] Extensive cell membrane damage can also result in the efflux of RNA due to the loss of plasma membrane integrity.[80] Previous research has shown the disruption of membrane integrity in *S. oneidensis* cells upon PAH-AuNP exposure,[61] correlating with the decrease in the expression of 16S. It should be noted that at 1-hour exposure, the respective PAH ligand control also elicited decrease in 16S expression, while at 6-hour exposure only PAH-AuNPs showed the effect; thus, the potential of 16S to be used as a biomarker that is specific for PAH-AuNPs is limited to long-term exposures. In effort to link 16S and *sodB* gene response

to the apical biological endpoints, the gene expression level of these two genes was examined at a higher dosage (100 µg/L) that also caused inhibition in bacterial oxygen uptake (**Figure 3.1(c)**). While the *sodB* gene at 1-hour exposure did not elicit change in gene expression, 16S at 6-hour exposure showed a similar decrease upon 100 µg/L PAH-AuNP exposure (**Figure 3.4**), proving that 16S can be potentially used as a biomarker for the impact of PAH-AuNPs on bacterial oxygen uptake; future work will explore the adverse outcome pathway from the decrease in 16S rRNA expression to the inhibition of bacterial oxygen uptake, and we postulated the inhibition is mediated via reduced activity in protein synthesis. MPA-AuNPs did not induce a similar response of 16S rRNA expression, or any other NP-specific response, indicating a distinction between the same AuNP cores functionalized with different surface ligands.

Length of exposure had an impact on the effects seen in both species and on both gene expression and apical endpoints measured. Short-term exposures for both *D. magna* and *S. oneidensis* revealed that functionalized NP impacts on certain molecular pathways might be predicted by their respective ligand alone**.** Out of all *S. oneidensis* regulated genes, three genes stand out as potential predictors of NP impacts based on the ligand alone. These genes are *pspB* and *rpoA* for PAH-AuNP/ligand and *ibpA* for MPA-AuNP/ligand at 1-hour exposure, as they were influenced similarly upon exposure to both the ligand-bound AuNPs and the respective free ligand. For *D. magna*, three genes were most notable; these genes were *hsp70 and vtg* for PAH-AuNP/ligand and *hsp70*, *vtg* and *nadh* for MPA-AuNP/ligand. These results suggest that NP impacts on specific molecular pathways may be predicted based on response to the ligand alone. This finding is especially important for ligands or functional groups that are commonly used to achieve desired physiochemical properties for NPs. However, as demonstrated with our study, ligand-NP combinations did alter several genes that the ligand alone did not, and the concentrations of NPs that impacted apical endpoints, in particular PAH-AuNPs, differed from that of the ligand. This diminishes the potential ability to use

ligand information alone as a predictor for NP toxicity; rather, the overall NP characteristics, including charge or size, may be more informative.

Our study revealed that gene expression in acute exposures was not predictive of long-term impacts or differences among treatments with respect to ligand versus nanoparticle-ligand combinations. In addition, long-term exposure to NPs resulted in gene expression patterns that could not be predicted based on gene expression patterns from short-term exposures. Upon exposure to MPA-AuNP/ligand, both *S. oneidensis* and *D. magna* showed decreases in gene expression during short-term exposure and that this response flipped to mostly an increase in gene expression upon long-term exposure. Exceptions to this finding are observed in the decrease of 16S and *sodB* expression upon PAH-AuNP exposure in S. *oneidensis* and the increase of *vtg* gene expression upon MPA-AuNP exposure in *D. magna*, which show similar response in gene expression levels at both time points. Our results indicate that, although it is possible to predict long-term gene expression impacts based on short-term impacts, it is limited to select genes, which may downplay the significance of this finding.

Gene expression responses across organisms provide an indication of how organisms are similar or different in their response to NP exposures. A notable signature shared across two organisms was the up-regulation of *ibpA*/*hsp70* induced by MPA-AuNP and ligand for short-term exposures. Both *ibpA* and *hsp70* encode for heat shock protein in *S. oneidensis* and *D. magna*, respectively. Heat shock proteins (Hsp) are a large family of proteins that help unfolded or misfolded proteins to fold correctly in vivo and are widely considered to be good indicators of proteotoxic stress.[81,82] The up-regulation of heat shock protein induced by MPA-AuNPs and ligands potentially indicate the disruption of membrane proteins, provoking pathways that help adapt to change in chemical environment caused by introduction of NPs or ligands. This feature, shared by both organisms, potentially indicates a universal stress-response to negatively

charged NPs, making the genes encoding for heat shock protein a good candidate for predicting the effect of NPs based on the response to their respective ligands. However, MPA-AuNPs did not lead to any adverse outcomes at the concentrations we tested, which makes understanding the importance of this pathway within the context of our study difficult.

3.5 Conclusion

Molecular studies can tease out distinct modes of action for NP toxicity and help to develop biomarkers for assessing NP impacts on environmentally relevant endpoints. Using standard toxicological and gene expression assays, we revealed that: 1) the ligand-NP combinations determine the extent of impacts on organismal endpoints and the toxicity of select NPs may not be determined by their respective ligand alone; 2) depending on the organism considered, exposure to ligand-NP combinations may impact unique molecular pathways that differ from the ligand alone; 3) short-term exposures reveal that ligand-NP impacts on certain molecular pathways might be predicted by their respective ligand alone but the ability to predict long-term impacts may be minimal; and 4) examining gene expression responses across organisms may provide an indication of how organisms are similar or different in their response to NP exposures. Lastly, this study reveals that there are mechanisms other than oxidative stress for NP toxicity and that these may be elucidated using molecular level experiments and exposures that consider sublethal concentrations.

Chapter 4

Quantification of free polyelectrolytes present in colloidal suspension reveals source of toxic responses for polyelectrolyte-wrapped gold nanoparticles

Adapted from:

Qiu, T. A., Torelli, M. D., Vartanian, A. M., Rackstraw, N. B., Buchman, J. T., Jacob, L. M., Murphy, C. J., Hamers, R. J., Haynes, C. L., Quantification of free polyelectrolytes present in colloidal suspension, revealing source of toxic responses for polyelectrolyte-wrapped gold nanoparticles, ***Analytical Chemistry***, 2017, **89**, 1823–1830.

4.1 Introduction

Polyelectrolyte (PE) coating is an easily accessible method used to control the surface properties of both planar substrates and colloidal particles due to its simplicity and versatility and is of interest across many technological sectors.[1-4] A standard PE coating process takes advantage of attractive electrostatics between opposing charges of the PE coating and substrate to create nanoscale PE layers on surfaces, which may be repeated for layer-by-layer assembly. Polyelectrolyte-wrapped nanoparticles (NPs) have been used for a variety of applications including drug delivery,[5] Raman tags,[6] and fuel cell catalysts.[7] Because colloidal nanoparticles are often difficult to sediment due to their small sizes, immersive *in situ* presentation of the polyelectrolyte to the particle is the most widely used method to achieve colloid modification. In this technique, an excess amount of polyelectrolyte is usually introduced for each step of polymer deposition and then rinsed in an effort to remove excess polyelectrolyte.[3]

An efficient purification step is necessary after polymer deposition, because leftover polyelectrolytes could disrupt the formation of subsequent PE layers for a traditional layer-by-layer assembly scheme or could act as problematic impurities in a final nanoparticle suspension product. Specifically, if colloidal nanoparticles are used in humans (e.g. for photothermal therapy)[8] or released into the environment (e.g. for pollutant remediation),[9] impurities may compromise nanoparticle functionality or cause unintentional biological effects. Indeed, numerous studies have shown that the apparent toxicity of nanomaterials can be traced to excess surface capping agents. For example, Alkilany et al. showed that the unbound capping agent, cetyltrimethylammonium bromide (CTAB), was responsible for the toxicological response caused by CTAB-capped gold nanorod solutions,[10] and Harper et al. demonstrated improved biocompatibility of gold NPs (AuNPs) functionalized with small peptides in zebrafish embryos by adding extra purification steps.[11] Similarly, an extra purification step using anion exchange chromatography improved the performance of silica-coated AuNPs as

surface-enhanced Raman scattering substrates.[12]

The most common purification method in polyelectrolyte wrapping of colloidal nanoparticles is centrifugation.[3] After polyelectrolyte wrapping, the colloidal suspension is centrifuged, followed by the removal of supernatant and re-dispersion of the pellet. Pellets are usually rinsed several times to ensure the removal of excess polymers from the surface modification. However, centrifugation is labor-intensive, hard to automate, and not scalable; moreover, centrifugation can potentially induce particle aggregation and is not always achievable for particles with excellent colloidal stability. Diafiltration- or tangential flow filtration-based purification overcomes these shortcomings and has become a popular choice to purify nanoparticle dispersions from excess reagents, including small molecules and large polymers.[13-15] A continuous filtration setup is used in such filtration devices (**Scheme 4.1**); the colloidal suspension continuously flows through a tube of dialysis membrane with a molecular weight cut-off (MWCO) selected to elute small impurities while retaining the desired particle suspension. In a continuous flow reactor, diafiltration allows for scale-up and automation of purification steps, while following greener practices than centrifugation.[16] Additionally, for nanoparticles with diameters of 5 nm or less, diafiltration provides a more practical purification strategy than centrifugation due to the high centrifugation speed needed to sediment small-diameter nanoparticles.

Herein, we evaluated both centrifugation and diafiltration as purification strategies after polyelectrolyte wrapping of 4-nm-diameter gold nanoparticles using poly(allylamine hydrochloride) (PAH), a common polyelectrolyte used for colloidal stabilization as well as applications in cell encapsulation,[17] nanofiltration membranes,[1] and drug delivery.[18] PAH-AuNPs have been used for bacterial exposure in Chapter 3. In this chapter, we measured the amount of free PAH polymers that are unbound from the AuNP surface in PAH-AuNP suspensions; these measurements were motivated by unexpected levels of AuNP toxicity to bacteria in preliminary experiments. The toxicological response to

the PAH-AuNP suspension was examined using the bacterium *Shewanella oneidensis* MR-1 (*S. oneidensis*), a beneficial Gram-negative bacterium critical in geochemical nutrient cycling in ecological systems.[19] The origin of distinct toxicological effects from PAH-AuNPs purified using different methods was revealed to be due to unbound PAH polymers, in spite of a properly sized MWCO of the dialysis membrane. Finally, we demonstrated that, by choosing a dialysis membrane with a higher MWCO or adding an extra ultra-centrifugation step, the PAH impurities can be minimized to increase the biocompatibility of PAH-AuNPs.

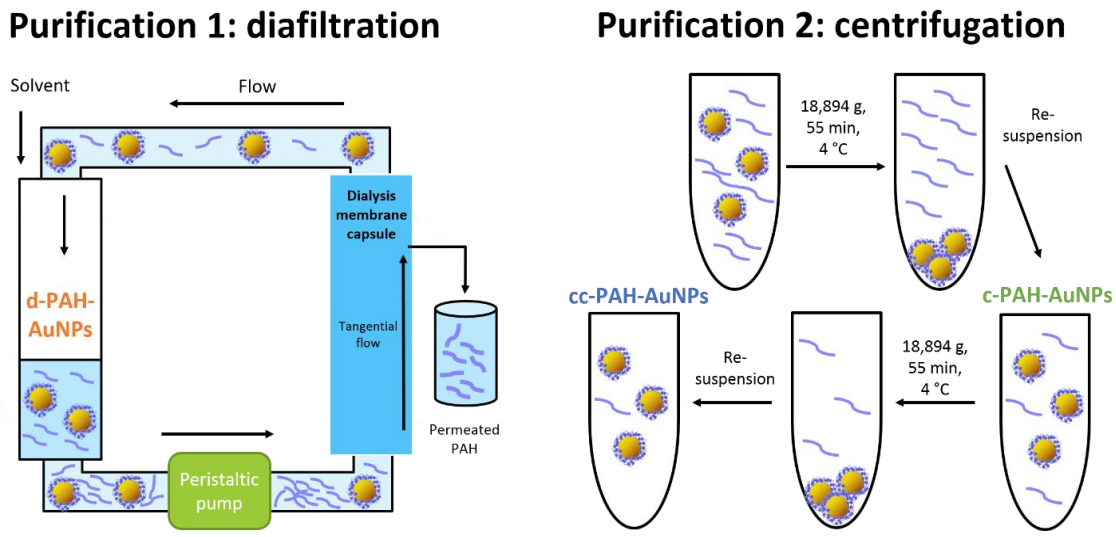

Scheme 4. 1 Illustration of the two purification strategies used in this study and the three differently-purified PAH-AuNP samples.

4.2 Experimental section

4.2.1 Materials

All materials were used as received, unless otherwise indicated. Poly(allylamine hydrochloride) (PAH; M_w 15,000 g/mol) was obtained from Sigma Aldrich. PAH (M_w 3,000 g/mol) was obtained from Nittobo (catalog #PAA-03). All water used for NP synthesis, diafiltration, NMR, XPS and dialysis experiments was ultrapure deionized water collected from Barnstead NANOPURE water filtration systems (Resistance at least 17.8 MΩ·cm). All water used for nanoparticle characterization and bacterial

toxicity assays was Milli-Q water (Resistance 18.2 MΩ·cm) or autoclaved Milli-Q water. PallALL Minimate tangential flow filtration capsules with 50 kDa molecular weight cutoff (MWCO) were obtained from VWR. Dialysis tubing (50 and 300 kDa MWCO) for dialysis experiments was obtained from Biotech CE, SpectrumLabs (catalog #131384/131456).

4.2.2 PAH-AuNP synthesis and purification

PAH-AuNPs were synthesized by polyelectrolyte-wrapping of 4-nm-diameter citrate-AuNPs using a typical flow reactor synthesis as described before (see Supporting Information for more details).[14] After synthesis, the 3.2 L of as-synthesized PAH-AuNP nanoparticle solution was concentrated by tangential flow filtration through a 50 kDa MWCO capsule to a final volume of 25 mL (**Scheme 4.1**, left). The concentrated solution was washed by diafiltration with 2 L NaCl (1 mM), followed by 500 mL water, generating diafiltered PAH-AuNPs (d-PAH-AuNPs).

To purify NPs via centrifugation, the as-synthesized PAH-AuNP solution was firstly concentrated by tangential flow filtration through a 50 kDa MWCO capsule to 100 mL. The concentrated PAH-AuNPs were centrifuged at 18,894 × g for 55 min at 4 °C, and the pellet was re-suspended in equal amount of nanopure water. The product at this stage was regarded as centrifuged PAH-AuNPs (c-PAH-AuNPs). After that, c-PAH-AuNPs were purified by centrifugation a second time (18,894 × g for 55 min at 4 °C), and the pellet was re-suspended in an equal amount of autoclaved Milli-Q water, generating the double-centrifuged PAH-AuNPs (cc-PAH-AuNPs).

4.2.3 Nanoparticle characterization

All nanoparticles were characterized using UV-vis spectroscopy, transmission electron microscopy (TEM), dynamic light scattering (DLS) and ζ-potential measurement (see SI for details). The mass concentration of the AuNP suspensions was calculated based

on the UV-vis spectrum (see SI).[20] For DLS, the intensity-weighted average diameter was reported as "Z-average", and the mean diameter from the multimodal distribution was also reported.

4.2.4 Drop plate counting for bacterial toxicity assay

An adapted drop plate counting from the traditional plate-counting method was used to measure the bacterial toxicity of PAH-AuNPs and PAH polymer to *Shewanella oneidensis* MR-1 (see Appendix A.3 for more details).[21]

4.2.5 Dose-response curve

Dose-response curves for the three different types of PAH-AuNP as well as the PAH polymer-only sample were collected using the drop plate counting method described above. PAH polymer was weighed, dissolved in Milli-Q water, and diluted accordingly to prepare working solutions, and suspensions of the three different PAH-AuNP samples were also diluted in Milli-Q water from stock suspension. The bacterial suspension was exposed to 0, 0.3, 0.6, 1, 2.13, 4.3, 10 or 13.8 mg/L PAH polymer, 0, 0.3, 1, 2.13, 4.60 or 30 μg Au/L d-PAH-AuNPs, 0, 30, 78.6, 131, 250, 300 or 600 μg Au/L c-PAH-AuNPs, and 0, 0.3, 0.6, 1.2 or 2.0 mg Au/L cc-PAH-AuNPs.

4.2.6. Nuclear magnetic resonance (NMR) spectroscopy

NMR samples were prepared from aqueous nanoparticle solutions in D_2O (10 nM particle concentration for d-PAH-AuNP, c-PAH-AuNP, and cc-PAH-AuNP samples; 130 μM for the free PAH sample). ^1H NMR spectra were acquired using a Varian Unity Inova 500 MHz narrow-bore spectrometer. For aqueous nanoparticle samples prepared in D_2O containing residual water, the large water peak was suppressed using presaturation. The presaturation delay for aqueous samples was 2 s and the acquisition time was 1 s, with a 2- or 4-step purge. Chemical shifts are reported in parts per million (ppm) and are referenced to the residual proton solvent peak. All NMR spectra were

processed using MNova.

4.2.7 X-ray photoelectron spectroscopy (XPS)

Particles were analyzed by XPS using a custom-built, ultrahigh-vacuum Phi XPS system with a base pressure of <2 x 10^{-10} Torr. X-rays were produced by an Al Kα source with quartz-crystal monochromator. Measurements were taken with pass energies of 46 eV (effective resolution 0.64 eV) and an electron collection angle of 45° with respect to surface normal. For analysis, nanoparticles were pelleted by centrifugation at 14,100 × g, and pellets were suspended in minimal nanopure water, drop-cast onto conductive silicon (P-doped, <0.004 Ω-cm resistivity), and dried at thickness such that signal from the underlying silicon was attenuated. Peak areas were determined in IgorPro by fitting to Voigt profiles.

4.2.8 Quantification of unbound PAH in AuNP suspensions

The amount of unbound PAH polymer was determined using a fluorescence assay. Fluorescamine fluoresces after binding to primary amines, and this dye has been previously used for primary amine quantification.[22,23] A solution of fluorescamine was prepared by dissolving 0.01 g of fluorescamine (Sigma-Aldrich) in 10 mL acetonitrile to reach a concentration of 0.1% (w/v). A 0.05 M sodium borate buffer was prepared by dissolving 5.03 g $Na_2B_4O_7$ in 500 mL Milli-Q water followed by pH adjustment to approximately 8 using 12 M HCl. To prepare samples for measurement, 20 µL of borate buffer was added for all measurements first, and 120 µL of the aqueous samples were mixed with borate buffer in a 96-well plate. Lastly, 60 µL of fluorescamine solution was added to the mixture. Negative controls were done on all plates where 120 µL Milli-Q water was added instead of samples. The reaction was incubated at room temperature for 5 minutes, and the fluorescence intensity was measured by a plate reader with E_{ex}/E_{em} = 425 nm/480 nm.

A calibration curve was made for every experimental run. Three PAH stock solutions were made by dissolving weighed PAH polymer solid in Milli-Q water, and then diluting to 148.3 mg/L as three standard solutions. Aliquots of standard solutions from 0 to 40 μL were mixed with Milli-Q water in the 96-well plate to reach a total sample volume of 120 μL. Calibration curves from three standard solutions were finally averaged to make a master calibration curve for all assays in the experimental run.

To obtain unbound PAH polymer sample in AuNP suspension, PAH-AuNP suspension was diluted in Milli-Q water and ultra-centrifuged at 66,000 × g for 45 minutes at 4 °C to pellet all AuNPs. A PAH polymer solution in Milli-Q water of 350 mg/L was also ultra-centrifuged together with PAH-AuNP samples as a control. The supernatant was removed from the centrifuge tubes and then supernatants from c-PAH-AuNPs and cc-PAH-AuNPs were concentrated using a Savant SpeedVac Concentrator. An aliquot of each sample was then subjected to the fluorescence assay, and the concentration of samples were determined based on the linear fitting results from the calibration curve. Only fluorescence readings that were lower than the upper limit of calibration curve and higher than the limit of quantification (defined as ten times the standard deviation of readings from the negative control) were used for quantification.

4.2.9 Determining the source of differential toxicity

To determine if the unbound PAH polymer contributed to the differential toxicity, the aforementioned drop plate counting method was performed to assess the toxicity comparing a pair of nanoparticles purified by two different methods near the concentration where the more toxic nanoparticle killed a large population of bacterial cells and the less toxic nanoparticle showed no compromised bacterial viability. The amount of excess PAH polymer present in each pair was determined by fluorescence assay. This excess in polymer (ΔPAH concentration) was then added to the less toxic particle to identify the critical factors contributing to bacterial toxicity. At least 7

biological replicates were collected for each treatment. Normalized viability values were tested for normality using the Shapiro-Wilk normality test,[24] and the Grubbs' test was performed on data sets that passed the normality test to identify outliers. In cases where data sets did not pass the normality test, nonparametric Kruskal-Wallis test with Dunn's multiple comparisons test was used to test statistical significance using GraphPad Prism.

4.2.10 Dialysis of different PAH polymers

To experimentally estimate the amount of PAH polymer remaining after dialysis, 0.5 mg/mL 15 kDa PAH (Sigma) in 0.5 mM NaCl was dialyzed using 50 kDa dialysis membrane without the presence of gold nanoparticles. To test if increasing pore size of dialysis membrane and decreasing the molecular weight of polymer can improve the PAH removal efficiency, PAH of 3 kDa was obtained from Nittobo, and was dialyzed in 0.5 mM NaCl using 300 kDa dialysis membrane. Both solutions were then dialyzed through 12 L of water over 3 water exchanges. The resulting solution represented the retentate. The concentration of PAH polymer remaining after dialysis was determined using the aforementioned fluorescamine assay (see Appendix A.3.8 for details).

4.3 Results and discussion

4.3.1 Characterization of three PAH-AuNPs

As-synthesized PAH-AuNPs were purified in three different ways: (1) *via* diafiltration (d-PAH-AuNPs), (2) by single centrifugation (c-PAH-AuNPs), or (3) by double centrifugation (cc-PAH-AuNPs), as shown in **Scheme 4.1**. These three differently purified PAH-AuNPs were characterized by commonly used NP characterization techniques, including TEM, UV-vis spectroscopy, DLS, and ζ-potential measurement. TEM sizing showed that they have similar absolute sizes (**Figure 4.1(a-c)**). A loss of AuNPs during centrifugation was observed by comparing the heights of plasmon bands in the UV-vis spectra of c- and cc-PAH-AuNPs (**Figure 4.1(d)**). Slight shifts in the

plasmon bands towards longer wavelengths were observed in extinction spectra from d-PAH-AuNPs (~531 nm) to c-PAH-AuNPs (~535 nm) to cc-PAH-AuNPs (~537 nm) (**Figure 4.1(d)**). The longer peak wavelength might indicate either a more compacted (higher refractive index) PAH layer or a slight aggregation of PAH-AuNPs purified by centrifugation[25] compared to those purified by diafiltration; however, the Z-average (intensity-weighed) determined by DLS showed a slightly larger hydrodynamic size of PAH-AuNPs purified by diafiltration than by either method of centrifugation (**Figure 4.1(e)**). The mean diameters determined from the DLS multimodal size distribution were much smaller than the Z-average; with the polydispersity values as large as ~0.2, these data indicate that there might be a small population of heavily aggregated PAH-AuNPs in all three AuNP suspensions. Overall, c-PAH-AuNPs and cc-PAH-AuNPs were not differentiable with these characterization techniques, and d-PAH-AuNPs had slight but noticeable differences from PAH-AuNPs purified by centrifugation.

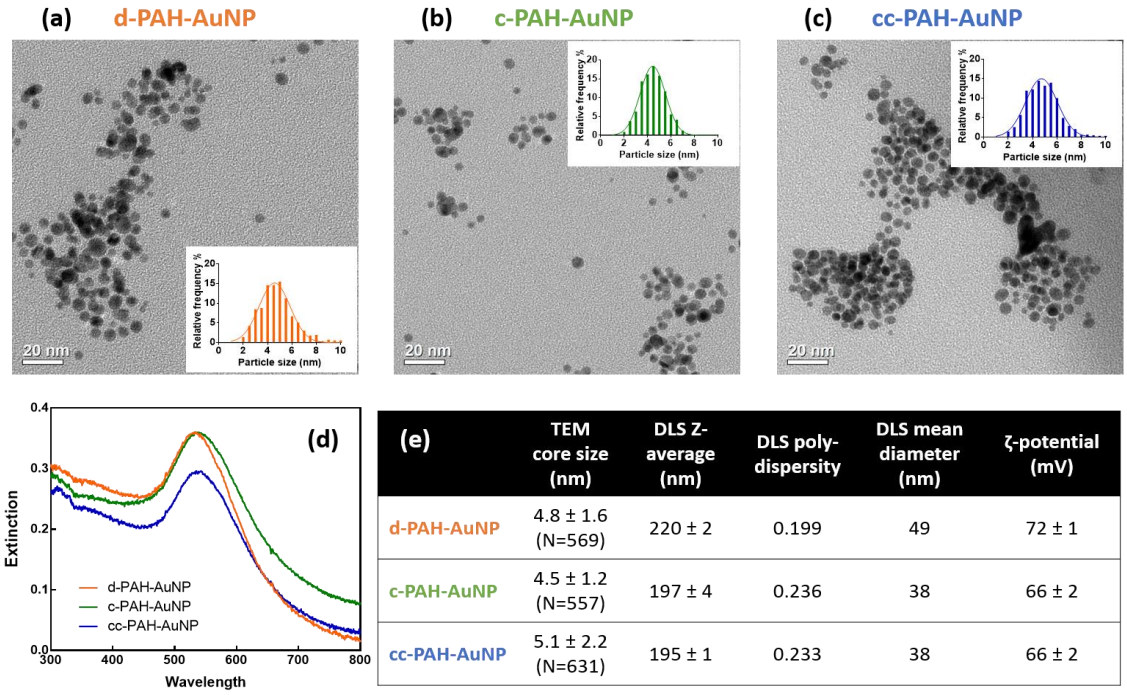

(e)	TEM core size (nm)	DLS Z-average (nm)	DLS poly-dispersity	DLS mean diameter (nm)	ζ-potential (mV)
d-PAH-AuNP	4.8 ± 1.6 (N=569)	220 ± 2	0.199	49	72 ± 1
c-PAH-AuNP	4.5 ± 1.2 (N=557)	197 ± 4	0.236	38	66 ± 2
cc-PAH-AuNP	5.1 ± 2.2 (N=631)	195 ± 1	0.233	38	66 ± 2

Figure 4. 1 PAH-AuNP characterization. (a-c) TEM image and size distribution of three PAH-AuNPs; (d) Extinction spectra of the three PAH-AuNP suspensions; (e) TEM core sizes, DLS, and ζ-potential of the three PAH-AuNPs. DLS Z-average is an average diameter which is weighted by the intensity of light scattered by each particle, and the DLS mean diameter is acquired from the multimodal size distribution.

4.3.2 Bacterial toxicity responses differ for the three PAH-AuNP samples

The bacterium *Shewanella oneidensis* MR-1 was used to assess the toxicity response of three differently purified PAH-AuNPs. **Figure 4.2(a)** clearly shows that the three PAH-AuNPs had orders of magnitude different toxicity towards *S. oneidensis*. Due to the unusual shape of the dose-response curves, sigmoid fitting was not successful on all plots, and LC_{50} (lethal concentration for 50% of the bacterial population) values were estimated by visual observation. Diafiltered-PAH-AuNPs showed the highest toxicity with an LC_{50} value near 4.6 μg Au/L, followed by c-PAH-AuNPs with an LC_{50} near 250 μg Au/L. Double-centrifuged PAH-AuNPs showed the least toxicity towards *S. oneidensis* with an LC_{50} between 1200 and 2000 μg Au/L. PAH polymer without AuNPs showed an LC_{50} between 1000 and 2000 μg/L. It is notable that the shape of the dose-response curve of the free PAH polymer (without AuNPs, **Figure 4.2(b)**) was similar to those of d-PAH-AuNPs and c-PAH-AuNPs (note that the scales on x-axis for AuNPs and PAH polymers are different). Although particle size and potential aggregation could result in different toxicity response to nanoparticles,[26] the orders of magnitude of difference in the toxicity response to these three differently purified PAH-AuNPs cannot be fully explained by particle size or aggregation, especially as the characterization of NPs showed minimal differences among the three types of PAH-AuNPs. Harper et al. demonstrated that surface-modified AuNPs with more centrifugation steps in purification induced lower toxicity to zebrafish embryos;[11] this observation complements our results on c- and cc-PAH-AuNPs. Thus, it was suspected that distinct amounts of impurities from different purification methods were responsible for differing toxic responses.

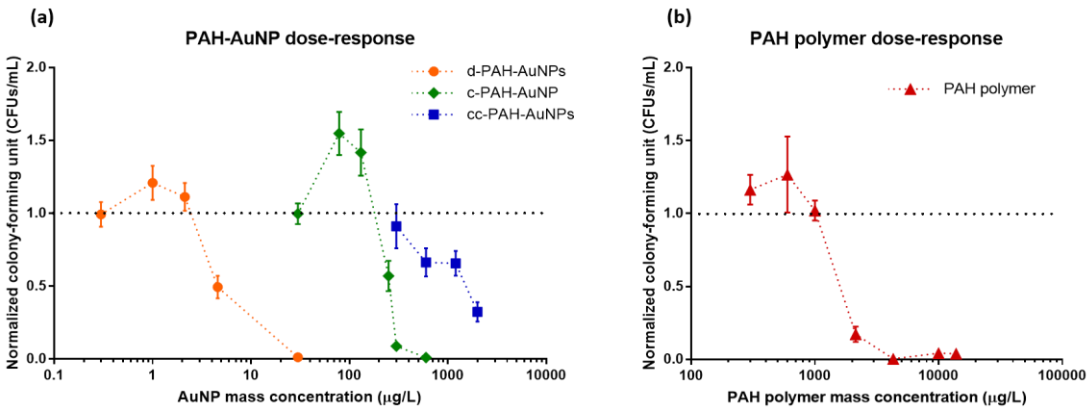

Figure 4. 2 Dose-response curves of *Shewanella oneidensis* MR-1 to (a) the three types of PAH-AuNPs and (b) free PAH polymer. Error bars indicate standard error of the mean.

4.3.3 NMR and XPS indicate unbound PAH polymer

To understand why the observed differences in toxicity arise, NMR spectroscopy and XPS experiments were performed on the three different PAH-AuNP and free PAH polymers without AuNPs. ^{1}H NMR experiments were carried out on 10 nmol/L d-PAH-AuNPs, c-PAH-AuNPs, and cc-PAH-AuNPs, as well as 130 μmol/L of free PAH (**Figure 4.3(a)**). The spectra suggest that the purification methods differ dramatically in efficacy, influencing the final concentration of PAH in the nanoparticle solution. Free PAH polymer gave rise to three distinct resonances corresponding to its chain group methylene protons (-R_2-C**H**$_2$, 1.43 ppm), chain group methine proton (-R_3-C**H**, bimodal: 1.87 and 1.96 ppm), and side group methylene protons (-N-C**H**$_2$, 2.95 ppm). The sharp doublet of doublets at 2.4 ppm arises from citrate molecules that are likely bound as counter-ions far from the core of the PAH-AuNPs; citrate molecules immobilized between the gold surface and the PAH are expected to be far broader.[27] PAH resonances were clearly present for d-PAH-AuNPs and c-PAH-AuNPs; the approximate integration was much larger for the d-PAH-AuNPs than the c-PAH-AuNPs, suggesting that the d-PAH-AuNP sample contained qualitatively more PAH (accurate quantification by NMR is challenging with polymers and nanoparticles, partly a consequence of line broadening). No obvious resonances indicating the presence of

PAH were observed in the cc-PAH-AuNP spectrum. As the positive ζ-potential confirms successful wrapping of PAH on the surface of cc-PAH-AuNPs, the absence of PAH resonances indicates that the PAH bound to the surface of AuNPs was below the NMR detection limit (~10^{16}-10^{18} nuclei or ~10^{-5} mol/L). This result reveals that the PAH resonances observed in the d- and c-PAH-AuNP spectra do not arise from PAH bound to AuNPs, but likely from unbound PAH in suspension.

XPS characterization comparing c-PAH-AuNPs and d-PAH-AuNPs shows two peaks for N(1s) at 400 and 402 eV, representing an amine and protonated amine, respectively (**Figure 4.3(b)**).[28] The peak areas associated with N and Au, however, differ between particles purified by different methods. We quantified these differences through the ratio of areas of the N(1s) peak to the Au(4f). The peak area ratio $A_{N(1s)}/A_{Au(4f)}$ varies from 0.68 ± 0.03 for single-centrifuged particles to 2.2 ± 0.4 for diafiltered particles, indicating a greater amount of PAH present in diafiltered samples, even after being pelleted and cleaned *via* centrifugation (details in the experimental section). Additionally, deconvolution of the N(1s) peak gives information about the relative protonation states of the PAH amine between the particles. The $A_{NH_3^+(402eV)}/A_{NH_2(400eV)}$ ratio of the d-PAH-AuNPs resembles that expected of an aliphatic amine, dominated primarily by contribution from 402 eV of the protonated state.[28,29] Interestingly, for the c-PAH-AuNPs, the $A_{NH_3^+(402eV)}/A_{NH_2(400eV)}$ ratio becomes almost equal, decreasing from 5.2 for d-PAH-AuNPs to 1.2 for c-PAH-AuNPs. This change suggests an alteration in the local chemical environment of the amines where a higher percentage of the amines on the polymer are in their more reduced (unprotonated) form. This change likely arises from binding of the PAH polymer to the negative, citrate-coated gold surface, as the negative, electron-rich environment near the gold surface can donate density to the amines on PAH molecules near the surface. Given that the spectrum for the d-PAH-AuNP resembles an ensemble of amines from solution, the greater amount of N(1s) detected is likely to arise from unbound PAH polymer in the

aqueous solution, while the N(1s) detected in c-PAH-AuNP samples is mainly from PAH polymer bound to the negative, citrate-coated gold surface.

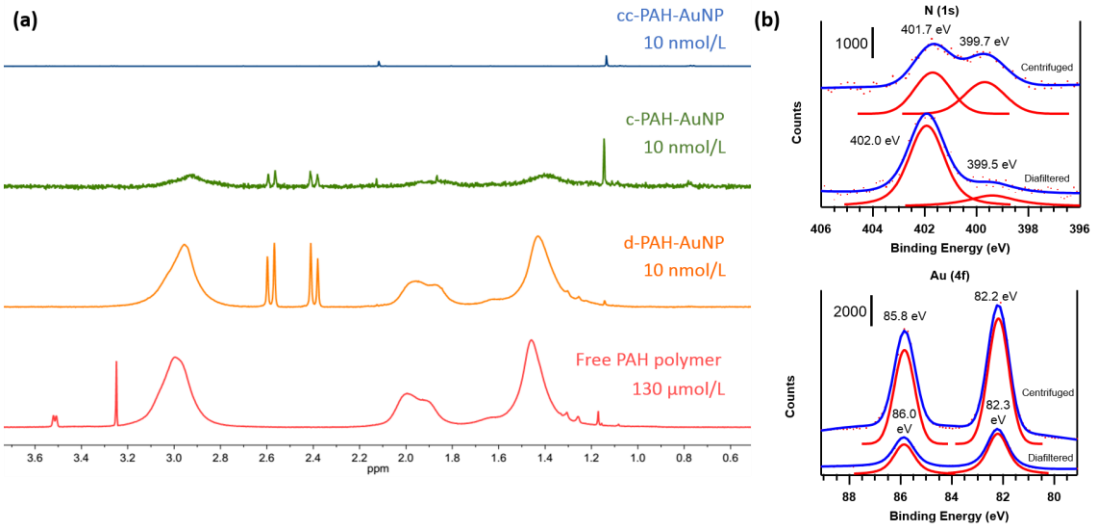

Figure 4. 3 (a) NMR spectra of 10 nmol/L PAH-AuNPs and 130 µmol/L free PAH polymer, showing that a large amount of PAH polymer is present in d-PAH-AuNPs compared to c- and cc-PAH-AuNPs. (b) XPS analysis of washed c- and d-PAH-AuNPs show that a relatively larger amount of protonated amine exists in d-PAH-AuNPs compared to c-PAH-AuNPs.

4.3.4 Unbound PAH polymer is responsible for differing toxicity responses

The amounts of unbound PAH polymer in the three PAH-AuNP suspensions were determined using a fluorescence assay using fluorescamine, a dye that reacts with primary amine. PAH-AuNPs were pelleted *via* centrifugation, and the clear supernatants were carefully pulled out and subjected to the assay, where the primary amines on PAH react with fluorescamine to generate a fluorescent product. We normalized the experimentally determined concentration of unbound PAH (mg/L PAH in supernatant) by the mass concentration of AuNPs (mg Au/L), yielding a ratio that enables a direct comparison among three AuNP suspensions. After normalization, results showed that for per mg Au/L of AuNPs, d-PAH-AuNP, c-PAH-AuNP and cc-PAH-AuNP suspensions contained 463 ± 27, 7.53 ± 0.20 and 0.49 (0.47-0.51) mg/L of

unbound PAH, respectively (**Figure 4.4(a)**). A similar amount of PAH was detected in another batch of PAH-AuNPs purified in the same way, showing the unbound PAH amount was consistent across batches (**Table A.3.1**). Considering the orders of magnitude difference in toxicity responses (**Figure 4.4(a)**), these data suggest that the unbound PAH polymer potentially dominates the differential toxicity among the three PAH-AuNP preparations.

A bacterial toxicity assay was applied to test this hypothesis. Aliquots of bacterial suspension were treated with 30 μg/L d- and c-PAH-AuNPs and revealed that 30 μg/L d-PAH-AuNPs killed almost the whole bacterial population while the same concentration of c-PAH-AuNPs did not have an observable effect (**Figure 4.4(b)**). Based on the PAH quantification results, the 30 μg/L d-PAH-AuNP suspension contained 13.9 ± 0.8 mg/L unbound PAH, and same concentration of c-PAH-AuNP suspension contained 0.226 ± 0.006 mg/L; the difference in the amount of unbound PAH was 13.7 ± 0.8 mg/L (**Figure 4.4(a)**, Row 2). Thus, if unbound PAH dominates the toxicity response, addition of 13.7 ± 0.8 mg/L of PAH into 30 μg Au/L of c-PAH-AuNPs should show the same toxicity to bacteria as d-PAH-AuNPs. The results were as expected: the mixture of 13.8 mg/L PAH (within the range of 13.7 ± 0.8 mg/L determined), which is equivalent to the difference in the amount of unbound PAH in 30 μg/L d- and c-PAH-AuNP suspension, and 30 μg/L c-PAH-AuNP suspension, as well as 13.8 mg/L PAH without AuNPs, resulted in the same drastic toxicity response as 30 μg/L d-PAH-AuNPs (**Figure 4.4(b)**).

Similar experiments were performed on the pair of c- and cc-PAH-AuNPs. After the additional round of centrifugation, the amount of unbound PAH polymer reduced one order of magnitude (7.53 *versus* 0.49, mg/L per mg Au/L of AuNPs) (**Figure 4.4(a)**). Using a similar setup (**Figure 4.4(a)**, Row 3), bacterial viability was tested upon exposure of 300 μg/L c- and cc-PAH-AuNPs, 2.13 mg/L PAH, and 300 μg/L cc-PAH-

AuNP supplemented with 2.13 mg/L PAH polymer (**Figure 4.4(c)**). Results were similar to those of d- and c-PAH-AuNPs. After the cc-PAH-AuNP suspension was supplemented with the extra PAH polymer to match the c-PAH-AuNP batch, the AuNP suspension showed the same toxicity as the c-PAH-AuNP suspension. Together, these results clearly demonstrate that the differential toxicity between d-, c-, and cc-PAH-AuNPs can be attributed to the unbound PAH polymer remaining in the PAH-AuNP suspensions.

(a)	d-PAH-AuNP	c-PAH-AuNP	cc-PAH-AuNP	Δ(PAH concentration)
Unbound PAH in AuNP suspension (mg/L PAH per mg Au/L of AuNPs)	463 ± 27	7.53 ± 0.20	0.49 (0.47-0.51)	--
Unbound PAH in 30 µg/L AuNP suspension (mg/L)	13.9 ± 0.8	0.226 ± 0.006	--	**13.7 ± 0.8**
Unbound PAH in 300 µg/L AuNP suspension (mg/L)	--	2.26 ± 0.06	0.15 (0.14-0.16)	**2.11 ± 0.06**

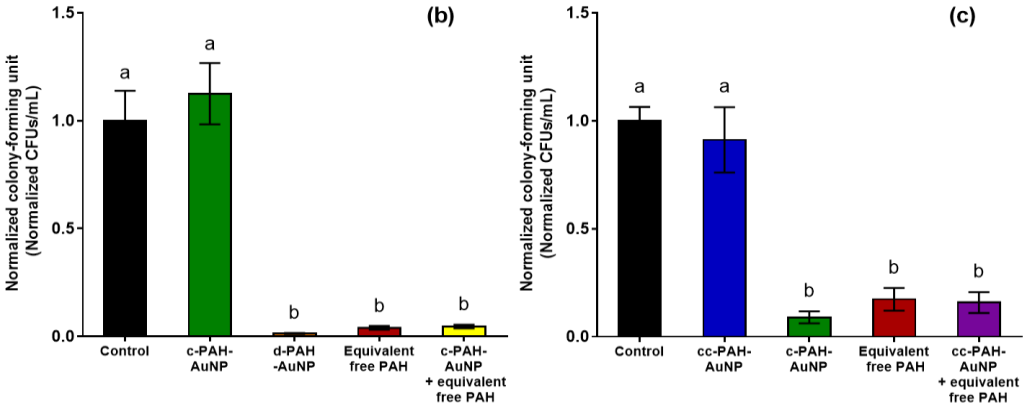

Figure 4. 4 (a) Amount of unbound PAH polymer measured in PAH-AuNP suspensions. The differences in unbound PAH amount between 30 µg/L d- and c-PAH-AuNPs and 300 µg/L c- and cc-PAH-AuNPs were calculated. Standard deviations are calculated for all values except for the values of cc-PAH-AuNPs, as less than three replicates were done due to the limited amount of available materials; ranges are shown instead. Toxicity results revealed that unbound PAH polymer is responsible for the differences in toxicity between (b) 30 µg/L d- and c-PAH-AuNPs and (c) 300 µg/L c- and cc-PAH-AuNPs. Equivalent free PAH refers to 13.8 mg/L free PAH in (b) and 2.13 mg/L free PAH in (c). Different letters designate statistically significant differences (Dunn's multiple comparisons test, post-hoc Kruskal-Wallis test, $p<0.05$). Error bars indicate standard error of the mean.

4.3.5 Dialysis membrane is not sufficient in removing unbound PAH

The large amount of unbound PAH polymer in the d-PAH-AuNP suspensions was clearly due to insufficient purification during diafiltration. As the MWCO for the dialysis membrane used in diafiltration was 50 kDa, the 15 kDa PAH polymer should be able to permeate the dialysis membrane, and unbound polyelectrolyte remaining in the as-synthesized AuNP suspension should be removed. A dialysis experiment using a 500 mg/L solution of PAH polymer with 0.5 mM NaCl without nanoparticles was performed using a 50 kDa dialysis membrane, and the concentration of PAH polymer in the dialysis tube was quantified using the aforementioned fluorescence assay. Unexpectedly, only 29% of the PAH passed through the dialysis membrane (**Table 4.1**). In previous work, Dalwadi et al. used polyethersulfone ultrafiltration membranes with 100 and 300 kDa MWCO to filter 9-10 kDa polyvinyl alcohol (PVA), and they demonstrated that the dialysis membrane with the 100 kDa MWCO removed less than 20% of the PVA.[30] Membrane fouling by polyelectrolytes has long been known,[31] so polyelectrolytes like PAH and PVA could potentially cause membrane fouling during early stages of dialysis and may result in insufficient permeation of polyelectrolytes later in the dialysis time. More importantly, as the dialysis membranes are generally intended for proteins that exist in a folded state, an equivalent molecular weight of a charged polymer like PAH may be more extended than a protein, resulting in a larger hydrodynamic diameter. For example, the 65 kDa protein hemoglobin A has a hydrodynamic radius of 3.18 nm.[32] By contrast, the hydrodynamic radius of 15 kDa PAH polymer was determined to be at least 4.5 nm.[33] Thus, a dialysis membrane that rejects a protein larger than 50 kDa should also reject PAH of 15 kDa. Additionally, because the polymer is polydisperse it is possible that a small portion of polymer with shorter length may pass through the dialysis membrane as expected, while the majority of polymer molecules with an actual MW at and above 15 kDa are likely retained.

Increasing the ionic strength is believed to screen the charges on polyelectrolyte chains and encourage long chains to fold.[34] In our nanoparticle synthesis, 1 mM of NaCl was

used to facilitate the wrapping of PAH onto small AuNPs according to previous research.[35] More importantly, adding salt was aimed to assist the permeation of PAH polymers through the dialysis membrane, by increasing the flexibility of the polymer chains. However, in this work, adding salt did not seem to promote PAH transport, and Jachimsak et al. also showed that the hydrodynamic radius of 15 kDa PAH actually increased with higher ionic strength.[33]

A potential solution to remove free polymer is to increase the MWCO of the dialysis membrane and/or decrease the molecular weight of the polymer. With this in mind, we tested a dialysis membrane with a 300 kDa MWCO on a 3 kDa PAH polymer. The resulting data show that this setup removed 92% of the PAH polymer (**Table 4.1**), indicating that increasing membrane MWCO and decreasing polymer size could be a strategy for better post-synthesis purification. However, it should be noted that with an increasing dialysis membrane pore size, very small nanoparticles could also pass through the membrane. Based on the DLS data for the three PAH-AuNPs considered herein (**Figure 4.1(e)**), the 300 kDa membrane with about 20-nm pore size has the potential for a good separation between 15 kDa PAH and the 4-nm-diameter PAH-wrapped AuNPs. Overall, while diafiltration is a good strategy for automation and easy scale-up of post-synthesis purification, optimal choices of dialysis membrane and other experimental conditions need to be carefully considered. In layer-by-layer techniques, many other alternative polyelectrolytes can be used for particle-wrapping, such as PEI (polyethyleneimine), PAA (poly(acrylic acid)), PSS (poly(sodium 4-styrenesulfonate)),[36] and because all of these are charged polymers like PAH, they are likely to experience similar issues in dialysis. As purification strategies can significantly affect the residual amount of polyelectrolytes, it is important to carefully evaluate these processes to reveal the source of colloid toxicity and thus minimize adverse biological effects.

Table 4. 1 The concentrations of remaining PAH polymers after dialysis was determined and confirmed that the 50 kDa dialysis membrane used in PAH-AuNP purification process was not efficient in removing excess unbound 15 kDa PAH polymers.

	15 kDa PAH (Sigma) 50 kDa dialysis membrane	**3 kDa PAH (Nittobo) 300 kDa dialysis membrane**
Starting PAH concentration before dialysis (mg/L)	500	500
PAH concentration detected after dialysis (mg/L)	355 ± 22	40.5 (39.1-41.8) [a)]
Leftover %	71.0%	8.10%

a) Range is shown instead of standard deviation as results from less than three replicates were obtained.

4.4 Conclusion

The results presented herein demonstrate that the method chosen for post-synthesis purification of nanoparticles has a significant effect on the composition and toxicity of the final product. 4-nm-diameter PAH-AuNPs purified by three different methods were hard to differentiate *via* common NP characterization techniques, but surprisingly contained different amounts of unbound PAH, left over from the stabilizing polyelectrolyte-wrapping process. Diafiltration was the least efficient for PAH removal, due to insufficient permeation of the PAH polymer across the 50 kDa MWCO dialysis membrane; increasing the MWCO of the dialysis membrane and/or decreasing polymer molecular weight greatly improved the removal efficiency. One round of centrifugation significantly reduced the amount of PAH leftover compared to diafiltration, and an extra round of centrifugation, although it reduced the yield of recovered PAH-AuNPs, eliminated most of the unbound PAH. Diafiltered-PAH-AuNPs showed the highest toxicity to the bacterium *Shewanella oneidensis* MR-1, followed by centrifuged- and then double-centrifuged-PAH-AuNPs. The differential toxicity correlates quantitatively with the different amounts of unbound PAH in these three PAH-AuNP suspensions.

Thus, by decreasing the amount of PAH left from synthesis, one can make the PAH-AuNPs more benign, which is desirable considering the wide application of PAH in polyelectrolyte wrapping. These results can be potentially extrapolated to other polyelectrolyte-wrapped nanoparticles with careful evaluation of both polyelectrolyte toxicity and purification processes. Together, this work shows the importance of choosing a proper post-synthetic purification method for nanoparticles to avoid undesirable biological effects, and the analytical scheme presented in this study can be adapted to investigate various polyelectrolyte-wrapping procedures in colloids.

Chapter 5

A growth-based bacterial viability assay for interference-free and high-throughput toxicity screening of nanomaterials

Adapted from:

Qiu, T. A., Nguyen, T. H. T., Hudson-Smith, N. V., Clement, P. L., Forester, D-C., Frew, H., Hang, M. N., Murphy, C. J., Hamers, R. J., Feng, Z. V., Haynes, C. L., Growth-based bacterial viability assay for interference-free and high-throughput toxicity screening of nanomaterials, ***Analytical Chemistry***, 2017, **89**, 2057–2064.

5.1 Introduction

Understanding how exposure to nanoparticles influences the growth and development of microorganisms is of great concern to communities studying both antimicrobial[1] and toxicological[2,3] properties of these materials. The increasing complexity of engineered micro- and nano-materials is driving the need for efficient toxicity screening with minimal interference. A number of biological and chemical assays have been developed previously to assess the toxicity of particles towards microbes.[3] Among these, cultivation-based[4] and optical[5] assays are two of the most widely used methods to assess bacterial viability, together with some less common methods such as nucleic acid-based assays.[6]

Among all viability assays, optical methods have the highest potential to be adapted into high-throughput formats as they can be performed on standard plate readers. Indeed, most of the high-throughput toxicological assays are luminescence-based.[7] One widely used fluorescence-based bacterial viability assay is the LIVE/DEAD® BacLight viability staining, wherein all cells are stained with a green fluorophore, SYTO9, and cells with damaged membranes are also stained with a red fluorophore, propidium iodide.[8] Assays harnessing the bioluminescence of marine bacterium *Vibrio fischeri* have also been engineered into high-throughput format and used for both traditional chemical and nanomaterial toxicity screening.[9,10]

While luminescence-based viability assays are amenable to high-throughput screening formats, interference due to the presence of nanoparticles (NPs) is not always negligible. Properties such as high surface adsorption capacity, optical absorption, scattering and fluorescence of nanomaterials interfere with toxicity assays as was discussed earlier in Chapter 1,[11,12] and have resulted in conflicting nanoparticle toxicity conclusions in mammalian cell lines.[13,14] Interference mostly due to the optical properties of various nanomaterials was demonstrated using several commonly used mammalian cell

viability assays.[15] In another example, NPs were shown to enhance or decrease optical response in optical assays, depending on the NP/assay combination.[16] Since it is almost impossible to separate nanoparticles from biological samples without disturbing cell viability, nanoparticles often remain in the sample during assays. Thus, the use of optical-based viability assays for high-throughput nanotoxicity screening is currently limited by potential interference from nanoparticles, and careful control experiments are necessary to correctly interpret the results.

Cultivation-based bacterial viability assays include conventional colony counting and related methods.[5] Cultivability remains the gold standard in microbiology to demonstrate bacterial viability. While cultivation-based assays, especially plate-based colony counting, are unlikely to suffer from optical interference by nanoparticles, they are hard to adapt into a high-throughput format. Efforts have been made to automate image analysis in colony counting methods,[17] but the experimental procedure remains labor-intensive. The minimal inhibitory concentration assay (MIC) has been adapted for nanotoxicity screening.[18-20] However, growth assays of this type need to be carried out in nutrient-rich medium, in which nanoparticles could aggregate and adsorb surrounding molecules, thus potentially changing the subsequent effect in exposure.[7] An assay that allows any medium to be used during nanoparticle exposure is desirable.

Herein, we developed a growth-based viability assay that is free of optical interference from nanomaterials and is performed in 96-well plates to achieve efficient assessment. After exposing bacterial cells to materials, a small portion of exposure mixture that contained viable cells and exposure materials was transferred into a large portion of fresh growth medium to dilute the mixture and minimize any optical interference by nanomaterials. The bacterial growth curves from the fraction of viable cells were analyzed, and the viability of bacterial cells after exposure was quantified by the delay in the bacterial growth curve. This analysis method was inspired by quantitative

polymerase chain reactions (qPCR), wherein the amount of starting material is correlated with a delay in the amplification curve. Automated data analysis was achieved here by developing algorithms to analyze individual growth curves in R code. We tested this assay using both a molecular toxicant (an antibiotic, kanamycin) and a variety of NPs with potential for significant optical interference, including gold nanoparticles with plasmonic extinction and emerging nanoscale battery materials with a rich brown color in solution. Since Gram-negative and Gram-positive are the major two categories of bacteria, we tested the assay on both Gram-negative bacterium *Shewanella oneidensis* MR-1 and Gram-positive bacterium *Bacillus subtilis* SB 491 along with two *B. subtilis* mutants. Together, this manuscript demonstrates that this interference-free assay is ideal for high-throughput bacterial toxicity screening of micro- and nano-sized particles and any other materials that may interfere with optical detection.

5.2 Experimental section

5.2.1 Materials and reagents

Shewanella oneidensis MR-1 was obtained from the laboratory of Professor Jeffrey A. Gralnick at University of Minnesota. *Bacillus subtilis* strains (SB 491, *ΔdltA* and *ΔtagE*) were purchased from the Bacillus Genetic Stock Center. Kanamycin sulfate solution (10 mg/mL) was purchased from ThermoFisher Scientific (Catalog #15160054).

5.2.2 Growth-based viability assay

The objective of the growth-based viability assay is to quantify the relative amount of viable bacterial cells after NP exposure using the delay in growth after samples are diluted into fresh growth medium as a metric (**Scheme 5.1(a)**). A similar setup has been used before, where bacterial growth curve ODs were compared at an arbitrary time point and only semi-quantitative analysis was performed.[21] In this work, prepared

bacterial suspensions (see Appendix A.4.3 for more details) were exposed to NPs or antibiotics in a desired exposure medium in parallel with negative controls. This negative control (lacking in NP or antibiotic addition) was regarded as 100% viability. After the incubation period, the 100%-viable sample was serially diluted to generate bacterial suspensions with a range of cell densities that would be used to produce a calibration curve. Equal small volumes of all samples were individually transferred and diluted 20- to 40-fold into fresh LB medium on a 96-well plate to yield a total volume of 200 μL in each well; at least two technical replicates were included on the well plate for each condition. The plate was covered with its lid and incubated in a plate reader (Synergy 2 Multi-Mode Microplate Reader, BioTek, VT) with or without its edge being parafilmed (as will be described later) at 30 °C for *S. oneidensis* and 37 °C for *B. subtilis*. The plate was shaken for 30 seconds before reading OD_{600} every 20 minutes over a period of 12 hours. As an example, a detailed experimental layout is described in the following sections and in **Scheme 5.1**.

5.2.3 Experimental layout for high-throughput screening

The experimental layout for a 96-well plate to determine dose-response curves usually consists of two sections: one for establishing a calibration curve and a second for the high-throughput screening. In some cases, a third section is included that is dedicated to residue controls, as shown in **Scheme 5.1(b)**. The layout shown in **Scheme 5.1(b)** is also referred to later as the "original layout". The whole plate with the "original layout" is an experimental run of one biological replicate. Details on other layouts for experimental optimization, including the randomized layout and the water evaporation control, can be found in Appendix A.4.5 and A.4.6.

***Calibration Curve Section*.** To quantitatively determine cell viability, the calibration curve, showing OD as a function of time, was required for every experimental trial (grey part of **Scheme 5.1(b)**). The bacterial suspension regarded as 100% viability was

the same as the negative control (i.e. no added NPs or antibiotics). After the same period of incubation as those exposed to NPs or antibiotics, the 100%-viability suspension was serially diluted, and using a multi-channel pipet, equal volumes of bacterial suspension were transferred into pre-added fresh LB medium for growth.

Screening Section. The screening section of the well plate was set up to expose bacterial suspensions to chemicals or NPs of interest and obtain viability after exposure (yellow part of **Scheme 5.1(b)**). Concentrated working solutions/suspensions of kanamycin or nanomaterials were prepared via serial dilution in a designated well-plate column and were then transferred to another column for exposure to bacteria as shown in **Scheme 5.1(b)**. After incubation, equal volumes of the antibiotic or NP exposure mixtures were transferred into pre-added fresh LB medium for growth using a multi-channel pipet.

Residue Control Section. When transferring exposed bacterial suspension to fresh LB medium, it is not possible to completely separate the bacterial cells from other components, such as nanomaterials, that are present. Consequently, a residual amount, called "residue" here, will accompany bacterial growth in fresh medium. To examine the effect of such residue on bacterial growth, a *residue control* (green part in **Scheme 5.1(b)**) was used. In *residue control* section, the two exposure components (bacterial suspensions and NPs/antibiotics) were "separated" before being diluted into fresh medium so that the impacts of bacterial residue and NP/antibiotic residue could be delineated. The working solution was exposed to sterile autoclaved Milli-Q water instead of to a bacterial suspension, and at the same time, the prepared bacterial suspensions were incubated with sterile autoclaved Milli-Q water instead of NP/antibiotic working solutions. Once the incubation was complete, the same volume as used in other two sections was transferred to fresh LB broth to make up the same total volume in each well. The *residue control* section was done to validate the results

from the screening section of the well plate, and it was done either on the same plate with the other 2 sections (**Scheme 5.1(b)**) or a separate customized plate. When it is run separately, a calibration curve may not be necessary.

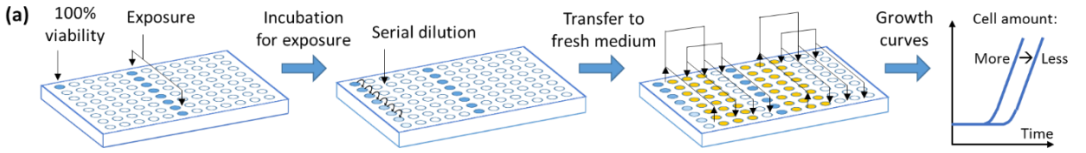

(b)

	Calibration curve				Screening				Residue control*			
	1	2	3	4	5	6	7	8	9	10	11	12
	Bacteria serial dilution	**Growth****			**10X working solution (WS)**	**Exposure**	**Growth****		**Diluted working solution**	**Bacteria**	**Growth****	
A	• 180 µL bacteria • 20 µL ddH_2O	All wells: • 195 µL LB • 5 µL diluted bacteria series parallel transferred from Column 1 **Technical replicates**			Working solution of the highest concentration	All wells: • 180 µL bacteria • 20 µL 10X working solution parallel transferred from Column 5	All wells: • 195 µL LB • 5 µL exposed bacteria parallel transferred from Column 6 **Technical replicates**		• 180 µL ddH_2O • 20 µL A5	All wells: • 180 µL bacteria • 20 µL ddH_2O	All wells: • 190 µL LB • 5 µL diluted working solution parallel transferred from Column 9 • 5 µL bacteria parallel transferred from Column 10 **Technical replicates**	
B C D E F G	1:1 serial dilution from well A1 using exposure buffer				1:1 serial dilution from well A5 using ddH_2O				1:1 serial dilution from the well above using ddH_2O			
H	Exposure buffer only				ddH_2O only				ddH_2O only			

* Residue control can be run on the same or a separate plate. ** Both dilution fold of 40 (majority) and 20 were used in this study.

Scheme 5. 1 Experimental design of the growth-based viability assay. (a) Illustration of growth-based viability assay set-up. (b) A detailed experimental layout for high-throughput screening.

5.2.4 Nanomaterial and antibiotic toxicity screening

Using user-adapted experimental layouts listed in **Table 5.1**, this growth-based viability assay has been tested on four bacterial strains exposed to various nanomaterials or a traditional molecular antibiotic. Characterization of nanomaterials can be found in the **Table A.4.1** and **Figure A.4.1**.

5.2.5 Data analysis

The hypothesis and data analysis of the growth-based viability assay are inspired by data analysis in qPCR reactions.[25-27] The key principle is that the time needed for a population of bacteria to reach a specified cell density at exponential phase is correlated with the number of culturable and viable cells at the beginning of bacterial growth. This

specified cell density is a threshold (*th*) that needs to be defined to determine the time needed to reach the "threshold" of cell density; the time at this crossing point is referred to as a fractional cycle number (Ct) (**Figure 5.1(a)**). Here, a cycle number is a user-defined unit to replace the unit "time" and simplify data analysis. For simplicity, each reading of the plate reader is counted as one cycle number. With a calibration curve between Ct numbers and log-transformed viability, one can obtain the viability of an unknown sample by fitting a Ct number calculated from a growth curve onto the calibration curve.

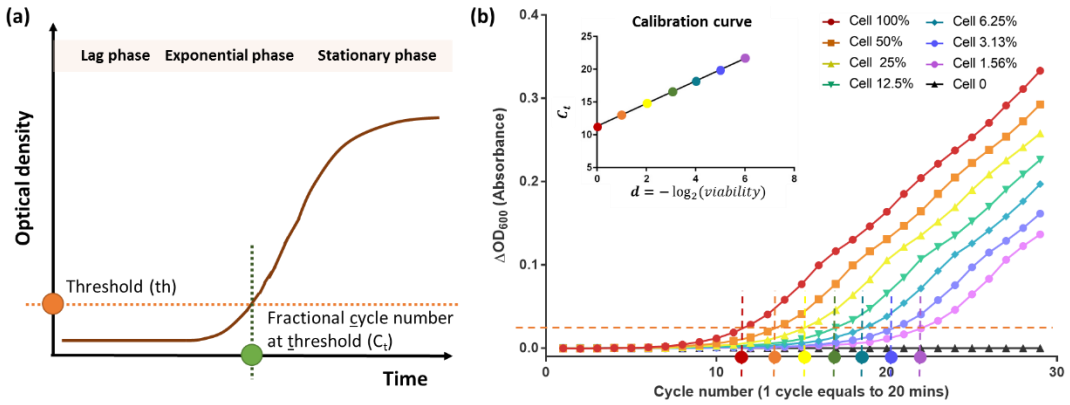

Figure 5. 1 Data analysis of the growth-based viability assay. (a) Setting up a threshold value to obtain fractional cycle number (Ct) for a single growth curve. (b) Constructing calibration curves from the growth curves of the dilution series. The growth curves are plotted on a linear scale for better illustration despite the calculation of Ct values being done on a log scale as described in the method section.

Table 5. 1 Experimental layouts and conditions of toxicity screening on different bacterial strains and various materials.

Material	Source	Experimental layout	Exposure medium	Exposure time	Dosages	Bacterial strain
Kanamycin	Purchased	Original layout (**Scheme 5.1(b)**) Randomized layout (**Scheme A.4.1**) Original layout with water evaporation control (**Scheme A.4.2**)	HEPES buffer (d)	15-min	20, 10, 5, 2.5, 1.25, 0.625 and 0.312 mg/L	*Shewanella oneidensis* MR-1
PAH-AuNPs (a)	Synthesized[22]	Original layout (**Scheme 5.1(b)**)	HEPES buffer	15-min	2800, 1400, 700, 350, 175, 87.5, 43.8 μg/L	*Shewanella oneidensis* MR-1
NMC (b)	Synthesized[23]	Customized layout with water evaporation control	Minimal medium with sodium lactate (e)	3-hour	100, 50, 25, 12.5, 6.25 mg/L	*Shewanella oneidensis* MR-1
MPNH$_2$-AuNPs (c)	Synthesized[24]	Customized layout	HEPES buffer	15-min	0.50, 5.00, 10.00 mg/L	*Bacillus subtilis* SB491 (wild type), Δ*dltA*, Δ*tagE*

a) 4-nm-diameter poly(allylamine hydrochloride)-wrapped gold NPs; (b) Two different nanoscale lithium nickel manganese cobalt oxide copositions: $Li_{0.61}Ni_{0.23}Mn_{0.55}Co_{0.22}O_2$ and $Li_{0.52}Ni_{0.14}Mn_{0.72}Co_{0.14}O_2$; (c) 9-nm-diameter mercaptopropylamine-capped gold NPs; (d)-(e): see SI for the composition of exposure buffers.

Manual analysis of single growth curves. The exponential growth phase of the bacteria needs to be located to set a threshold value to obtain Ct numbers for further data analysis. In this study, a growth curve was first plotted as optical density *versus* cycle number, with each optical density reading regarded as one cycle. This cycle length was 20 minutes, and the first reading at $t = 0$ was regarded as cycle 1. The optical density background signal was calculated as the average of the initial optical density readings across the bacterial wells and was subtracted from each growth curve. The background-corrected growth curve was then plotted on a log scale, which facilitated visualization of the linear range of the log-transformed plot and the location of the exponential growth window. Linear regression was then performed on the log-transformed data points within the exponential growth. A threshold value of $\log_{10}(0.02)$, which was within the linear range, was used, and the cycle number at the crossing point of the fit line was calculated as the Ct value of the analyzed growth curve.

Automatic analysis of single growth curves. To achieve faster and more robust Ct determination, algorithms were developed and written in R to automate data analysis of individual growth curves. Threshold and exponential growth windows were determined by algorithms instead of by visual inspection (see Appendix A.4.12 for more detail). With the code, users can obtain the Ct values of all growth curves across the plate by simply inputting raw data sets from the plate reader.

Constructing calibration curves. The construction of a calibration curve is demonstrated in **Figure 5.1(b)**. A threshold value was set for all growth curves, and the crossing points were calculated to obtain Ct values as described earlier. Ct values from technical replicates were averaged to represent the biological replicate. The averaged Ct values were plotted against $-\log_2(viability)$, named as d (named from "dilution fold" in serial dilution), followed by a linear regression to obtain a calibration curve.

***Quantifying viability of unknown samples*.** Similarly, Ct values of the growth curves obtained from the screening section were calculated using the same threshold as used for the calibration curve, and Ct values from technical replicates were averaged to represent the biological replicate. The Ct number was then plugged into the calibration curve to calculate *d*, and the equation:

$$v = viability = 2^{-d}$$

was used to transform *d* to viability.

5.3 Results and discussion

5.3.1 Correlating the delay of growth curve to cell viability

The hypothesis behind the development of this growth-based viability assay was that the delay of the exponential phase of bacterial growth, for both Gram-negative and Gram-positive bacteria, is correlated with the relative amount of bacterial cells at the beginning of growth. Mathematical modeling reveals that, with several assumptions regarding bacterial growth, there is a linear relationship between Ct values and negative log2-transformed viability ($d = -\log_2 viability$) (**Equation 5.1**):

$$C_t = \frac{1}{k} \cdot d + \left[\frac{T_{OD} - \log(P) - \log\left(N_{0,0}\right)}{k \cdot \log(2)} + L \right] \qquad (5.1)$$

Ct: fractional cycle number; *k*: growth rate (Ct^{-1}); *d*, negative log2-transformed viability; T_{OD}, threshold; $N_{0,0}$, the absolute number of viable cells in the 100% viability reference at the $t = 0$; *L*, length of lag phase; *P*: a constant. See Appendix A.4.11 for more details of the mathematical modeling.

The results from calibration curves show clear linear correlations ($R^2 > 0.99$) between Ct values and negative log2-transformed viability in all four bacterial strains tested (**Figure 5.2**), and these calibration curves are reproducible across different experimental runs. This result shows the promise of this assay for application to a wide variety of culturable bacteria. For *S. oneidensis* MR-1, the calibration curve was tested

from 100% viability (d = 0) to 0.006% (d = 14), and the linearity held (**Figure A.4.2**). This demonstrates that the linear range is quite wide and would be sufficient for most toxicity tests.

According to the mathematical model, the slope of the calibration curve is the reciprocal of bacterial replication rate at exponential growth (k). The slower a bacterium grows (smaller k), the larger the slope of calibration curve is, indicating higher sensitivity of Ct values in responding to changes in viability. Results show that among all 4 strains, *S. oneidensis* MR-1 have the highest sensitivity with an average of slope of 1.7 ± 0.2 *Ct*. It is possible to tune the sensitivity of the calibration curve by slowing or accelerating bacterial growth through adjustments in the growth conditions (e.g. composition of growth medium, temperature).

Calibration curves were also obtained for bacterial suspensions of *S. oneidensis* MR-1 harvested at mid-log phase and stationary phase (**Figure A.4.3**). Results show the same slope and different intercept for the two calibration curves. The same slope indicates the same replication rate of viable bacterial cells in the same medium, agreeing with **Assumption 1** in the mathematical model (Appendix A.4.11). As **Equation 5.1** shows, the y-intercept of the fit line depends upon several variables, including the number of viable cells in the 100% viability reference at t = 0 ($\log(N_{0,0})$). The larger intercept in the calibration curve from stationary phase-harvested bacteria is likely due to the decreased proportion of viable cells at stationary phase. It is known that bacterial cells start to become non-viable in the stationary phase, and the optical density measurement cannot differentiate between viable and dead cells. Thus, using bacteria harvested before entering stationary phase, especially at mid-log phase, is recommended.

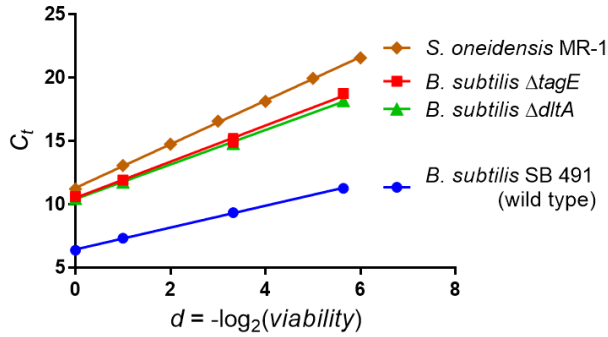

Figure 5. 2 Representative calibration curves for four bacterial strains used in this study (brown is *S.oneidensis* MR-1, red is *B. subtilis* Δ*tagE*, green is *B. subtilis* Δ*dltA*, and blue is *B. subtilis* SB 491). The abscissa refers to the negative log2-transformed viability, and ordinate indicates the Ct number calculated from growth curves. Solid lines indicate the linear regression of data points ($R^2 > 0.99$).

5.3.2 High-throughput toxicity screening of antibiotics and nanomaterials

Dose-response curves were acquired from the GBV assay as described earlier using different exposure conditions (**Table 5.1**, **Figure 5.3**). The dose-response curves for kanamycin, an antibiotic, and PAH-AuNPs are compared to those obtained using a conventional plate colony counting method (**Figure 5.3(a) and 5.3(b)**). Results show that the dose-response curves from the two assays are similar, but do not perfectly overlap. The dose-response curves from the GBV are shifted slightly to the right compared to those from the plate colony counting assay, indicating slightly higher viabilities determined using the GBV assay compared to those from colony counting under the same dosages. This may be due to different growth conditions of the exposed bacteria (solid nutrient plate *versus* liquid medium); previous reports show that liquid media performs better than solid media for the recovery of stress-injured cells,[28] and bacterial cells could be stressed during transfer from liquid medium to solid medium-filled plates for plate colony counting.[29] Of note, the GBV shows similar or less data variation than plate colony counting, reflected by error bars, with fewer biological replicates performed.

Figure 5.3(c) shows the results of using the GBV assay for toxicity screening of NMC nanomaterials on *S. oneidensis* MR-1, and **Figure 5.3(d)** shows a screening of $MPNH_2$-AuNP toxicity towards 3 *B. subtilis* strains. It should be noted that the exposure time and medium for NMC toxicity screening were different from those for kanamycin and PAH-AuNPs on *S. oneidensis* MR-1. Additionally, both NMC and $MPNH_2$-AuNP screening were done using slight variations on the aforementioned experimental layouts (to meet user requirements and experimental limitations). The ability to easily vary the medium and experimental layout demonstrate the versatility of this GBV assay platform, and the assay worked equally well for both the Gram-positive and Gram-negative bacterial strains we chose.

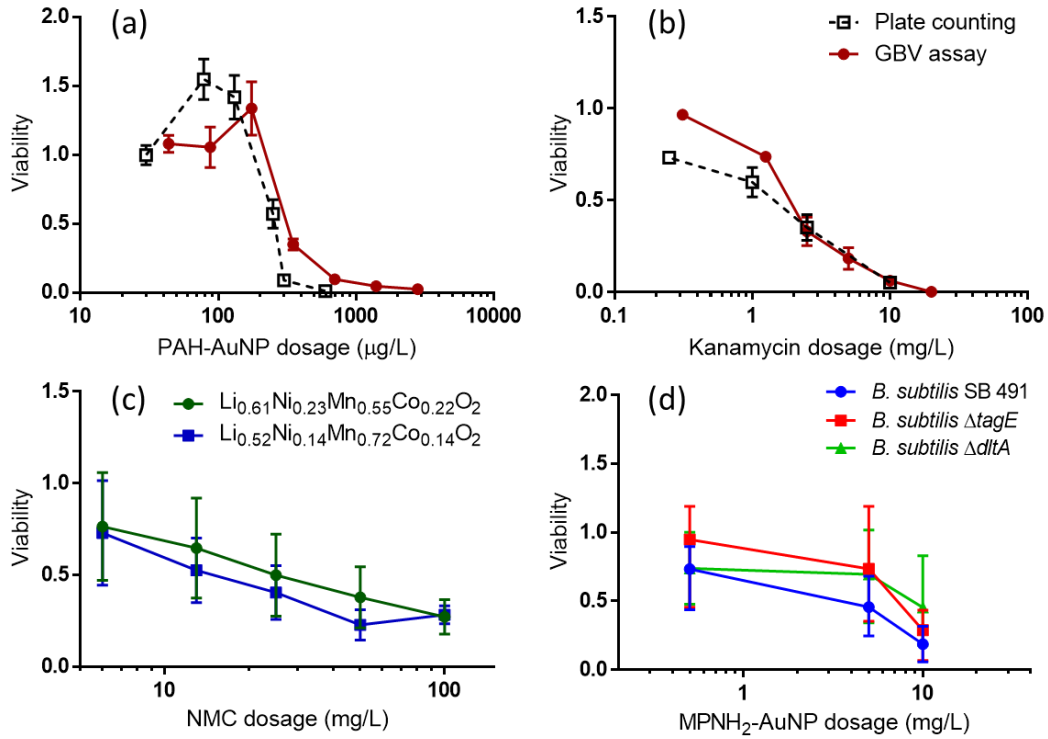

Figure 5. 3 Dose-response curves for *S. oneidensis* MR-1 responding to (a) PAH-AuNPs, (b) kanamycin and (c) two different composition NMC nanomaterials ($Li_{0.61}Ni_{0.23}Mn_{0.55}Co_{0.22}O_2$ and $Li_{0.52}Ni_{0.14}Mn_{0.72}Co_{0.14}O_2$)[23] and (d) *B. subtilis* SB491, Δ*dltA* mutant, and Δ*tagE* mutant responding to $MPNH_2$-AuNPs. Solid symbols with solid lines indicate data from GBV assays while hollow symbols with dashed lines indicate comparative data from plate counting. Error bars indicate standard error of the mean in (a)-(c) and range in (d). In all experiments, ≥ 6 biological replicates were

collected for plate colony counting assays, and ≥ 3 replicates, except for (d), were collected for GBV assays.

5.3.3 Negligible interference from antibiotic or NP residue

In an exposure of planktonic bacterial cells in liquid medium with soluble small molecules or dispersible colloids, it is almost impossible to separate bacterial cells from exposure materials. Thus, in most high-throughput assays, materials stay in the exposure mixture for later steps, potentially resulting in interference with the assay read-out. For example, the 4-nm-daimeter PAH-AuNPs used in this study have strong plasmonic extinction with a peak at approximately 530 nm. As optical density is usually measured as the extinction at 600 nm, the plasmonic extinction of AuNPs can be a significant source of optical interference. A 2.8 mg/L PAH-AuNP suspension shows extinction of about 0.5. With optical density readings usually less than 2, the optical interference from 2.8 mg/L AuNPs is not negligible.

In the GBV assay, the exposure mixture is diluted into fresh growth medium, thus minimizing both optical and toxic interference from exposure materials. After a 20-fold dilution of 2.8 mg/L AuNPs, the residual AuNP concentration in fresh growth medium is 140 μg/L, which has an OD_{600} of approximately 0.02. To further eliminate any optical interference from NPs, the baseline OD of each individual growth curve is subtracted from the raw optical density reading to create a normalized growth curve in further analysis.

It is still possible that the residue after dilution can impact bacterial growth after dilution into the fresh growth medium. This concern is addressed by the *residue control section* described in the rationale of the GBV experimental design. **Figure 5.4** shows results from the GBV assay residue control section for PAH-AuNPs and kanamycin exposure to *S. oneidensis*. The relative percentage change of residue-exposed samples compared to the corresponding control were calculated as:

$$Relative\ difference\ (\%) = \frac{C_{t,exposed} - C_{t,sample}}{C_{t,sample}} \times 100$$

and one-way ANOVA plus post-hoc Tukey's test were performed. No statistically significant difference is revealed, indicating that the residues of neither PAH-AuNPs nor kanamycin impact bacterial growth. A stricter control experiment (referred as "orthogonal residue control", more details in Appendix A.4.10) further showed that the residues do not affect bacterial growth starting at different cell densities (**Figure A.4.4**). In a scenario where the effect of residue is detected, two strategies can be implemented to minimize the interference: 1) larger dilution fold can be used (e.g. switching 20-fold dilution to 40-fold) to reduce the amount of residue in the fresh growth medium, and/or 2) the dosage can be reduced below toxic levels.

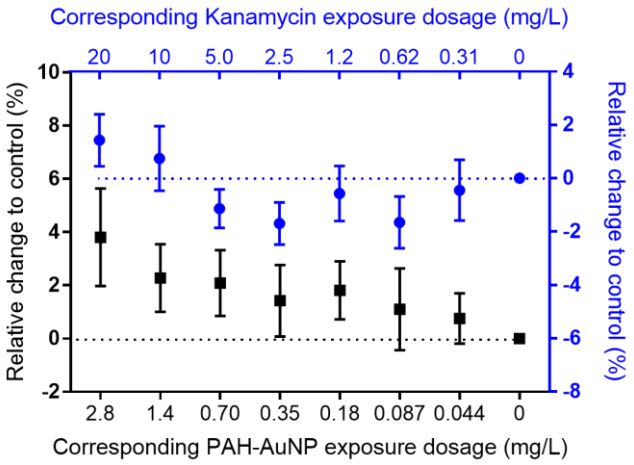

Figure 5. 4 Residue from PAH-AuNP (black square) or antibiotic (blue dot) exposure did not affect the growth of *S. oneidensis* after dilution into fresh medium. Error bars represent standard error of the mean of 3 (PAH-AuNP) and 7 (kanamycin) biological replicates. No statistical significance was found among the growth controls that correspond to negative control and various exposure dosages (Tukey's test, α=0.05).

5.3.4 Reducing variation by adding a water evaporation control

In GBV toxicity screening experiments using the original layout (**Scheme 5.1(b)**), it became obvious that the viabilities calculated for negative control samples were often

greater than 1 when the distribution of measured viability for negative control should be centered at 1. **Figure 5.5(a)** shows that the log-transformed viability values for negative controls from the original layout were significantly different from zero (log(1)). Such bias was suspected to be due to systematic errors.

Performing standard plate control experiments aimed to identify any systematic instrumental imperfection, such as non-uniform heating. Results showed that in both trials, smaller Ct values were observed at the left side of the plate, while larger Ct numbers were detected for wells in Row A and Column 12 (**Figure A.4.5(a)**). A randomized layout was implemented to minimize the impact of different positions on the plate (**Scheme A.4.1**). **Figure 5.5(a)** shows that the randomized layout decreased the bias, although not statistically significant, compared to the original layout.

Water evaporation in edge wells (Rows A and H, Columns 1 and 12) was suspected to affect the Ct determination by altering the optical densities and nutrient concentrations in wells. Analysis of Ct values from standard plates (whole plate) shows that, if we exclude the edge wells in data analysis, the range of all Ct values across the plate decreases, yielding an improved coefficient of variation (CV %) (**Table A.4.2**). A control experiment demonstrates that water evaporation is most significant in the edge wells (**Figure A.4.6**). Thus, a water evaporation control, where the edge wells were filled with water, was implemented to reduce such variation (**Scheme A.4.2**). While the reduction in number of wells for experimental conditions (from 96 to 60 wells available) is not ideal, results show that the water evaporation control efficiently reduces the variations of Ct values on the standard plates (**Table A.4.2**) and brings the log-transformed viability of negative control samples closer to zero (**Figure 5.5(a)**). Despite this improvement, the log-transformed viability of negative controls in water evaporation control still shows a statistically significant difference from zero (One-sample t test, $p < 0.05$), indicating room for further improvement. Additional control

experiments show that the order when transferring and diluting bacterial suspension to nutrient-rich medium could affect the intercept of calibration curves (**Figure A.4.7**), indicating that it might be helpful to randomize the order of liquid transfer to further improve the accuracy.

Figure 5.5(b) shows the kanamycin dose-response curves for *S. oneidensis* MR-1 determined from three different experimental layouts. Data points are fitted into sigmoid dose-response curves, and IC_{50} values are determined to be 3.44, 3.13, and 1.97 mg/L for toxicity screening with original, randomized, and water evaporation control layouts, respectively. The dose-response curve from the water evaporation control is also plotted with that from plate colony counting method (**Figure 5.3(b)**). The results show that the IC_{50} values from the three dose-response curves are significantly different from each other (Extra sum-of-square F test, $p < 0.05$). The dose-response curve from the layout accounting for water evaporation is the closest to that determined using the traditional plate colony counting assay (**Figure 5.3(b)**). In addition, no viability larger than 1 was measured when using the layout with the water evaporation control. Thus, the layout with the water evaporation control is considered to be the best layout.

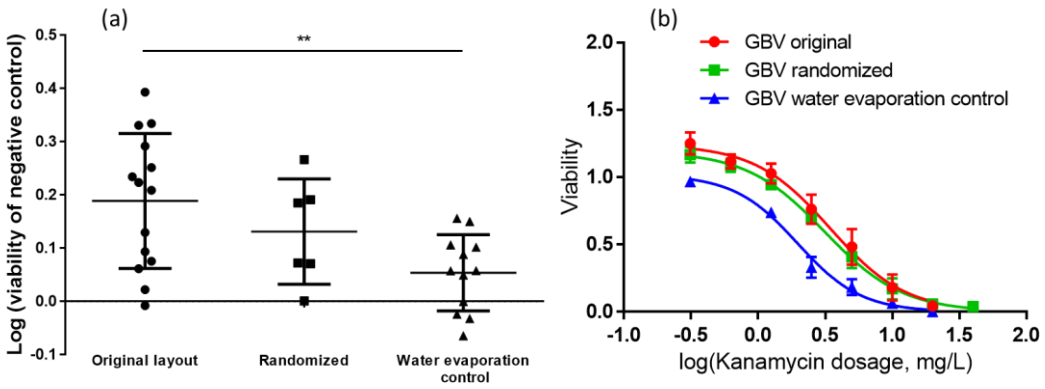

Figure 5. 5 Effects of randomized layout and water evaporation controls on the GBV assay compared to the original layout. (a) A summary of log-transformed viability calculations of negative controls on each plate from various setups. The water evaporation control resulted in an average value that has a statistically significant difference compared to the original layout (Tukey's multiple comparison test, $p < 0.05$). Individual data points are plotted with standard deviations. (b) Kanamycin dose-

response curves resulting from the three different experimental layouts with sigmoid fittings. Solid lines indicate the sigmoid fitting, and error bars indicate standard error of the mean.

5.3.5 Fast and robust automated data analysis for Ct determination

The manual data analysis, as stated in Experimental section, is time-consuming. Moreover, as the linear range of log-transformed growth curve and the threshold values are visually observed and manually selected, the manual data analysis is subject to user bias. To achieve faster and more robust data analysis, computer algorithms were developed in this work by exploiting the similarity between bacterial replication and nucleic acid amplification. Analysis of DNA amplification curves in qPCR has been extensively explored and optimized.[25-27] In a qPCR reaction, a DNA template doubles after one amplification cycle, and analogously, in bacterial exponential growth, a bacterium splits into two after its doubling time. The similarity between these two processes allows adaptation of algorithms from qPCR data analysis to analyze bacterial growth curves quantitatively (see Appendix A.4.12 for more details).

Results from automated and manual data analysis are compared by plotting calibration curves for the same data set (**Figure 5.6(a)**). In our algorithms, thresholds were determined by three different methods, referred to as secondary derivative maximum (SDM), mid-point, and fit-point methods. The slopes determined from manual analysis and automated analysis with 3 different thresholding methods were compared, and they are not significantly different from each other (Extra sum-of-squares F test, p as 0.05), indicating automated data analysis, which takes less than 1 minute in the R program (see R codes in Appendix A.4.13), agrees well with results from manual fitting; this is true for both Gram-negative and Gram-positive bacteria.

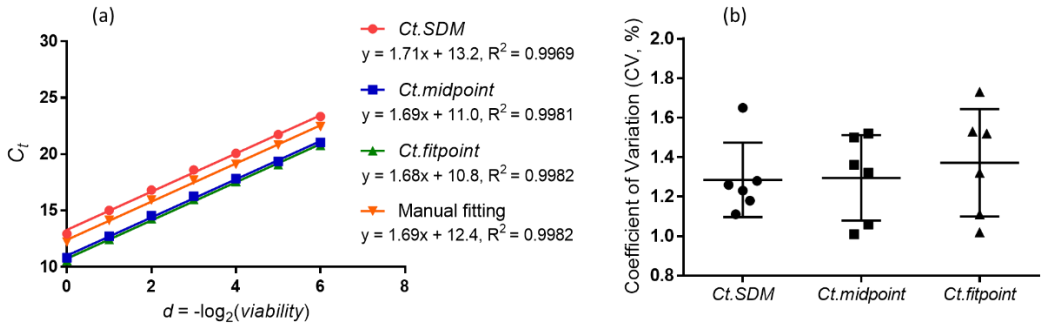

Figure 5.6. Comparing results from three different thresholding methods in automated data analysis. (a) A representative demonstration of calibration curves determined using manual fitting and different threshold methods in automatic analysis. Slopes are not different from each other in any of the four fittings. (b) No difference between the variation of Ct values is determined between three different threshold methods on standard plates. Data points are from standard plate with water evaporation control and standard plates (whole plate) with edge wells excluded in data analysis.

Variation of Ct values on standard plates determined from the three different thresholding methods is also compared (**Figure 5.6(b)**), and no difference is observed (Tukey's multiple comparison test, p as 0.05). Combined with the analysis of calibration curves (**Figure 5.6(a)**), it is clear that all three thresholding methods in this automated data analysis can be used. Since the fit-point thresholding method requires a stable baseline with at least 3 data points to calculate a standard deviation, and the SDM thresholding method results in a threshold at the edge of the exponential growth, which sometimes leads to a crossing point beyond the linear range of exponential window, the mid-point thresholding method is recommended for future use.

5.4 Conclusion

The results presented herein show that by greatly diluting exposed bacterial cells into fresh growth medium and analyzing the subsequent growth profile of remaining viable cells, we can quantitatively correlate cell viability to the delay of bacterial growth after dilution. The large dilution ensures minimal optical interference and toxic effect from nanomaterials in the exposure mixture. The delay in the bacterial growth curve was quantified by measuring the point at which a growth curve surpasses a threshold value.

Data analysis of growth curves was inspired by qPCR, due to the similarity between bacteria replication and DNA amplification. Automated data analysis was achieved by developing algorithms in R code and showed fast and robust determination of antibiotic or NP impact on bacteria. Excitingly, this assay is confirmed to work in 2 different strains plus 2 mutants, including Gram-negative and Gram-positive bacteria, and various materials ranging from molecular antibiotics to ligand-stabilized colloids to complex metal oxide NPs. The main potential challenge in adapting this method to studies with other microorganisms lies in organism replication patterns; for example, if an organism replicates using a method other than simple binary splitting or exhibits extremely slow growth, this assay would have to be adapted. Nonetheless, this assay shows great potential to be applied to all culturable bacteria and a wide range of potential toxicants for high-throughput and fast toxicity assessment.

Chapter 6

DNA damage as a toxicity mechanism of NMC ($Li_xNi_{1/3}Mn_{1/3}Co_{1/3}O_2$) nanomaterial to bacterium *Shewanella oneidensis* MR-1

Adapted from:

Qiu, T. A., Guidolin, V., Hoang, K. N., Pho, T., Carrà, A., Lynn, T. G., Villalta, P. W., Feng, Z. V., Balbo, S., Haynes, C. L., DNA damage as a toxicity mechanism of NMC ($Li_xNi_{1/3}Mn_{1/3}Co_{1/3}O_2$) nanomaterial to bacteria *Shewanella oneidensis* MR-1 and *Bacillus subtilis*, 2018, in preparation.

6.1 Introduction

Lithium-ion batteries (LIB) have been a focus as a promising high-density energy storage solution for electrical devices and vehicles in the last decades. One key component determining the capacity of LIBs is the cathode material. Compared to conventional $LiCoO_2$, layered nickel-rich lithium transition-metal oxides, $LiNi_{1-x}M_xO_2$ (M as transition metals), have attracted attention as a high energy density cathode material.[1] Lithium nickel manganese cobalt oxide ($Li_xNi_yMn_zCo_{1-y-z}O_2$, NMC) represents a class of lithium transition-metal oxide materials with high power performance that is being used at large scale in hybrid electric vehicles.[2-4] By replacing cobalt in $LiCoO_2$ with nickel and manganese, NMC materials are shown to deliver a high discharge capacity of more than 200 mAh/g with great stability, exceeding requirements needed for hybrid electric vehicle batteries.[2] The size scale of NMC ranges from nanometers to micrometers and can transform between these scales via aggregation or stress-induced fracture;[5] nanoscale battery materials are expected to have improved performance due to shortened diffusion paths and increased surface areas.[6]

As the high energy density makes them suitable for large-scale applications such as electrical vehicles and energy storage systems, waste from LIBs is not well--managed due to lack of motivation and infrastructure for recycling.[7] With projected electric vehicle use and sales, the amount of LIB waste is expected to increase, but only 42% of the waste can be properly recycled using current technology.[8] While an economically sound battery recycling strategy needs to be developed,[9,10] it is also urgent to evaluate the risk of these metal-containing battery materials being released into environment in a proactive manner. As an example, leaching of metals was found from spent LIBs, potentially being a source of toxicity towards environmental organisms.[11] In contrast to the urgent need, very limited information is available on the potential health and environmental effects of battery materials. Our recent studies have shown adverse

biological effects from exposure of nanoscale NMC materials, including inhibition of bacterial growth of *Shewanella oneidensis* MR-1, an environmentally relevant bacterium that was introduced in Chapter 2-4,[5,12] and impacts on survival, reproduction and gene expression in *Daphnia magna*, an aquatic invertebrate introduced in Chapter 3.[13] The toxicity mechanism of nanoscale NMC on bacterial growth inhibition was determined to be mainly dissolution to toxic nickel and cobalt ions, while *Daphnia magna* experienced disruption that couldn't be totally attributed to dissolved ions.

Genotoxicity, a mode of toxicity on the DNA level, is shown to be induced by NP exposure in various cell lines and organisms such as bacteria, human cells, fish and plants.[14-18] Mechanisms of genotoxicity induced by nanoparticles (NPs) vary case-by-case, including DNA methylation variations,[19] oxidative DNA adduct formation,[20] DNA strand breakage,[21] and occasionally mutagenesis.[22] These mechanisms can happen via direct interaction of DNA with NPs taken up by cells or indirect mechanisms without direct DNA-NP physical interaction, such as generation of free radicals and dissolution to ions. In fact, Bhabra et al. showed that even in the presence of a barrier composed of a human carcinoma cell line, cobalt-chromium NPs were able to cause DNA damage in human fibroblast cells across the cellular barrier through intercellular communications and transport of dissolved metal ions.[23] In our previous studies, time-dependent dissolution of nickel and cobalt ions from nanoscale NMC was determined in bacterial culture media.[5] As nickel and cobalt appear to induce genotoxicity,[24-26] combined with the observation of bacterial phenotype change upon continuous nano-NMC exposure (unpublished data), we postulate that the inhibition of bacterial growth upon nanoscale NMC exposure is mediated via damage to bacterial DNA induced by dissolved nickel and cobalt ions.

In this study, we investigated bacterial DNA damage upon NMC exposure using an adapted alkaline Comet assay for bacterial DNA strand breakage[27] and a high-resolution

mass spectrometry-based DNA adductomics approach.[28] The Comet assay visualizes the "tails" of stained DNA molecules from each single cell, where longer tails indicate higher levels of DNA strand breakage. A sensitive and rapid tool to assess DNA damage, the Comet assay has been applied widely to study strand breakage induced by NPs.[29] Here we expanded the use of Comet assays to measure bacterial cell response to NP exposure. DNA adducts are chemical modifications, including redox reaction or fusion of molecular species onto DNA molecules, that have been informative for risk assessment of carcinogens.[30,31] Many studies have used DNA adduct formation in the bacterium *Salmonella typhimurium* to study mutagenesis mechanisms and evaluate the risk of chemical mutagenicity,[32-34] with studies of similar purpose expanding to other microbial species, such as *Escherichia coli*.[35,36] However, the implication of DNA adduct formation in ecologically relevant organisms, including environmental microbes,[37] is studied to a much smaller extent compared to studies concerning human health. Herein we aimed to measure DNA adduct formation in the ecologically relevant bacterium, *Shewanella oneidensis* MR-1, to explore the impact of nanoscale NMC exposure to bacterial DNA and its environmental implications.

Currently, the limited pool of DNA adduct studies in nanotoxicology have focused on detecting a single DNA modification, 8-hydroxy-2' -deoxyguanosine (8-OHdG, sometimes referred as 8-oxo-dG), which is indicative of oxidative stress.[38-40] Recently developed DNA adductomic approaches provide possibilities to detect other DNA modifications beyond 8-OHdG and reveal unique molecular mechanisms beyond oxidative stress.[30] Although limited, studies have used DNA adductomics to investigate modes of genotoxicity in mice upon iron oxide NP exposure,[41,42] and adductomics were also applied on a soil bacterium.[37] To our knowledge, the study presented herein is the first one that applies DNA adductomics on bacterial species upon NP exposure. We applied a high-resolution DNA adductomic approach using tandem mass spectrometry, where the neutral loss of deoxyribose from single modified nucleosides triggered the

next level of fragmentation to identify the structural identity of DNA adducts.[28] Successful application of DNA adductomic approaches was confirmed on bacterial DNA. Combined with assays on reactive oxygen species (ROS), Ni/Co metal ion uptake, and NMC toxicity, we determined that DNA damage appeared in the form of DNA double-strand breakage but not DNA adduct formation, and the observed genotoxicity is possibly through indirect mechanism of metal ion uptake into cells, but less likely through generation of intracellular ROS.

6.2 Experimental

6.2.1 Materials

Nanoscale NMC materials were provided by the Hamers lab at University of Wisconsin, Madison. Difco™ LB broth (Miller) and Difco™ agar (granulated) were purchased from Becton, Dickinson, and Company. 2′,7′-Dichlorofluorescin diacetate ($DCFH_2$-DA) was purchased from both Sigma Aldrich (Cat. No.: D6883) and ThermoFisher Scientific (Cat. No.: D399). Newport Green DCF diacetate was purchased from ThermoFisher Scientific (Cat. No.: N7991). $NiSO_4 \cdot 6H_2O$ was purchased from Acros Organics (Cat. No.: B00875). $CoCl_2 \cdot 6H_2O$ was purchased from Mallinckrodt (Cat. No.: B00791). Anhydrous DMSO was purchased from ThermoFisher Scientific (Cat. No.: D12345). Hydrogen peroxide (30% w/w) was purchased from Fisher Scientific (Cat. No.: H325-100). Dulbecco's phosphate-buffered saline (DPBS) was purchased from Mediatech, Inc. All Milli-Q water used had a resistance around 18.0 MΩ·cm. Tris-EDTA (TE) buffer was composed of 10 mM Tris, 1 mM EDTA, brought to pH 8.0 with HCl. Lysozyme was purchased from Sigma Aldrich (Cat. No.: L6876). Isopropanol (IPA) was purchased from ThermoFisher Scientific. Tris-$MgCl_2$ buffer was composed of 10 mM Tris, 5 mM $MgCl_2$, brought to pH of 7.

6.2.2 Medium preparation

LB broth: 25 grams of pre-mixed Difco LB power was dissolved in 1 liter of Milli-Q water and autoclaved. Minimal medium with sodium lactate (MM with lactate): Each liter of minimal medium contains 0.68 g NaCl, 0.3 g KCl, 0.285 g $MgCl_2 \cdot 6H_2O$, 0.3975 g Na_2SO_4, 0.15 g NH_4Cl, 2.383 g HEPES, 0.0125 g Na_2HPO_4 and 0.0056 g $CaCl_2$. Part I stock contains 20x concentration of NaCl, KCl, $MgCl_2 \cdot 6H_2O$, Na_2SO_4, NH_4Cl, and HEPES. Part II stock contains 100x concentration of Na_2HPO_4 and Part III stock contains $CaCl_2$, both sterile filtered. To make 1 liter of 1x minimal medium solution, 50 mL Part I stock was mixed with 930 mL Milli-Q water, and pH was adjusted to 7.2~7.3 using HCl and NaOH solutions. The solution was autoclaved and cooled down to room temperature, and 10 mL of both Part II and Part III stock was added; this solution is called minimal medium (MM) in this study. Immediately before use, 14 mL of sodium DL-lactate syrup 60% w/w aq. soln was mixed with the minimal medium to make a total volume of 1000 mL, referred to as MM with lactate.

6.2.3 Bacterial culture

Shewanella oneidensis MR-1 BAA-1096 (*S. oneidensis*) was purchased from ATCC. Frozen stocks of bacterial cells were prepared by 1:1 mixing mid-log phase bacterial suspension in LB with 50% w/w sterile glycerol stored in a -80 °C freezer. *S. oneidensis* was plated from a frozen stock onto an 15% w/w agar plate and incubated at 30-32 °C overnight, and the formed colonies were used for subsequent bacterial experiments.

6.2.4 Abiotic ROS generation from NMC

$DCFH_2$-DA from Sigma Aldrich was dissolved in anhydrous DMSO to a concentration of 20 mM, divided into 100 µL aliquots and stored at -20 °C in a desiccator. Upon usage, $DCFH_2$-DA DMSO stock was thawed and diluted 1000-fold into MM with lactate. NMC was weighed and dissolved in freshly prepared MM with sodium lactate with a stock concentration of 4 mg/mL. The prepared NMC suspension was aged for 10 days on a bench, and part of the NMC stock suspension was diluted 10-fold using fresh MM

with lactate. On a black wall clear bottom 96-well assay plate, 195 µL of diluted $DCFH_2$-DA solution was added into all 96 wells. At time zero (t = 0), 5 µL of NMC suspensions of two concentrations plus negative control (MM with lactate) and positive control (30% w/w hydrogen peroxide solution) were quickly added in triplicate to the first row of wells that already contained diluted $DCFH_2$-DA, and the plate was immediately sent for fluorescence reading at excitation/emission (Ex/Em) of 485/525 nm on a Synergy 2 Multi-Mode Microplate Reader (BioTek, VT). Every 30 minutes, the same blank, NMC suspension, and hydrogen peroxide solution were added to a new row and immediately sent for fluorescence reading.

6.2.5 Intracellular ROS detection with $DCFH_2$-DA

Bacterial colonies from an agar plate incubated overnight were inoculated into 10 mL fresh LB broth. After 4-5 hours, bacterial suspension at mid- or late-log phase was centrifuged at 2,000 × g for 5 minutes. After removing supernatant, the cell pellet was re-suspended in DPBS buffer. DMSO stock of $DCFH_2$-DA from ThermoFisher Scientific was thawed at room temperature and diluted 1000-fold into bacterial suspension in DPBS buffer, resulting in a final concentration of 20 µM $DCFH_2$-DA. The bacterial suspension containing $DCFH_2$-DA was wrapped in aluminum foil and incubated in a 32 °C shaker for 1 hour. After dye loading, the bacterial suspension was centrifuged at 3,000 × g for 10 minutes, and the pellet was re-suspended in an equal volume of MM with lactate, followed by a second round of centrifugation for a second washing. After the second round of centrifugation, the bacterial suspension was re-suspended again in an equal volume of MM with lactate. About 72-hours prior to exposure, NMC was weighed and suspended in fresh MM with lactate, sonicated in a bath sonicator for 15 minutes, and sat on a bench in the dark at ambient conditions until use. Dye-loaded cells were then 9:1 mixed with NMC suspension plus negative control (MM with lactate) and positive control (hydrogen peroxide) for a 15-min exposure in triplicate with a total volume of 1 mL. After exposure, the mixture was centrifuged at

10,000 × g for 5 minutes in a microcentrifuge, and the resulting pellet was re-suspended in 1 mL MM with lactate. A second round of centrifugation was done, followed by final re-suspension of pellets into 200 µL MM with lactate. The resulted suspensions were transferred to a 96-well assay plate to read both optical density absorbance at 600 nm and fluorescence at Ex/Em = 493/522 nm on a Synergy H1 Hybrid Multi-Mode Microplate Reader (BioTek, VT).

6.2.6 Intracellular metal ion uptake detection with Newport Green DCF diacetate

Newport Green DCF diacetate (NPG-Ac) was dissolved in anhydrous DMSO to make a 2 mM stock. Bacterial preparation for NPG-Ac dye loading was the same as dye loading of $DCFH_2$-DA, except for the dilution fold of the dye stock into bacterial suspension; after a 400-fold dilution, the final concentration for NPG-Ac dye loading was 5 µM. Dye-loaded bacterial suspension was mixed with 72-hour aged NMC suspension or varying concentrations of $NiSO_4$ or $CoCl_2$ plus negative control (MM with lactate) for a 30-min exposure in triplicate with a total volume of 1 mL. The washing steps were also the same as those used in the intracellular ROS experiments. The resulting suspensions were transferred to a 96-well plate to read both optical density at 600 nm (OD_{600}) and fluorescence at Ex/Em = 505/535 nm on a Synergy H1 Hybrid Multi-Mode Microplate Reader (BioTek, VT).

6.2.7 Bacterial growth inhibition and viability test upon NMC exposure

Various concentrations of NMC were exposed to bacterial cells grown in MM with lactate at mid-log phase. Bacterial colonies from an agar plate incubated overnight were inoculated into 10 mL fresh LB broth and harvested after 4-5 hours at mid- or late-log phase by centrifugation at 2,000 × g for 10 minutes. The pellet was re-suspended in fresh MM with lactate, and the OD_{600} of the cell suspension was measured using a Spectronic 20 Spectrophotometer. Cells were then diluted into a large volume of MM

with lactate in a 500 mL Erlenmeyer flask with calculated optical density of 0.01, and the optical density of the diluted cell suspension was measured by transferring 200 µL into a 96-well plate and reading absorbance at 600 nm on a Synergy H1 Hybrid Multi-Mode Microplate Reader (BioTek, VT). Diluted bacterial suspension was shaken at 300 rpm in a 32 °C orbital shaker overnight until the raw optical density reading reached ~0.12, indicating that the bacterial population was approximately halfway through the exponential growth phase. At this point, NMC was weighed and suspended in MM with lactate and sonicated in a bath sonicator for 15 minutes. While waiting for sonication to be done, the bacterial suspension was divided into aliquots of 7.8 mL in glass culture tubes. NMC suspensions of varying concentrations were then spiked into culture tubes for exposure. Exposure was done in triplicate, and the positions of different conditions were randomized on the tube rack. To monitor growth, 200 µL from each tube was transferred onto a 96-well plate at different time points; the tubes were vortexed for several seconds and vigorously shaken prior to liquid transfer to ensure even suspension of NMC and cells. The transferred aliquots were immediately taken to a Synergy H1 Hybrid Multi-Mode Microplate Reader (BioTek, VT) to read OD_{600}. Coupled with the growth inhibition test, a growth-based viability test was performed as described in Chapter 5.[43] Both at 1-hour and 8-hour after adding NMC, 200 µL of bacterial suspension was transferred to a clear sterile transparent 96-well plate with a lid for the growth-based viability assay. Negative control groups were used as 100% reference in building calibration curves, and MM with lactate was used to test contamination. A water evaporation control was implemented by surrounding re-growth area with wells filled with liquid, and positions were randomized. Data were analyzed using the R code published in the previous study, as presented in Appendix A.4.13 in this thesis.

6.2.8 Comet assay for DNA strand breakage

Single cell gel electrophoresis on NMC-treated *S. oneidensis* was conducted following published protocols with minor changes.[44,45] Ten microliters of the NMC-treated cell

suspension was mixed in 100 µL of 0.5% low-melting agarose (LMA) solution. Forty µL of the suspension was pipetted onto a Comet assay microscope slide (Travigen®) and spread evenly in a well. Once solidified at 4 °C, a 0.5% lysozyme-LMA layer was placed on top of the gel and solidified. The assembled slide was then incubated at 30 °C for 30 minutes. The slide was then sequentially immersed in a lysing solution (2.5 M NaCl, 100.0 mM EDTA, 10.0 mM Tris -HCl, 1% sodium N-lauryl sarcosine, 0.6% Triton® X-100, pH 10.0) for 1 hour in the dark, and an enzyme digestion solution (2.5 M NaCl, 10.0 mM EDTA, 10.0 mM Tris-HCl, and 0.5 mg/mL proteinase K, pH 7.4) at 37 °C for 2 hours. Electrophoresis was performed in an electrophoresis buffer (sodium acetate and Tris at pH 9.0) at 12 V for 30 minutes while being chilled. The slide was then washed and dehydrated with 1.0 M ammonium acetate in ethanol, then absolute ethanol, and was left at room temperature to dry in the dark. The samples were then rehydrated in freshly prepared 5% DMSO in10 mM NaH_2PO_4 solution and stained with 50.0 µL of 1.0 µM YOYO-1 in 5% DMSO. After air-drying in the dark for 5 minutes, the stack of microgel was imaged with a fluorescent microscope (100x, Ex/Em = 491/509 nm). ImageJ was used to analyze the DNA tail lengths.

6.2.9 DNA extraction from *S. oneidensis* cells

DNA extraction was done using Gentra Puregene Yeast/Bacteria Kit (Qiagen), and the protocol was optimized to extract bacterial DNA with high yield for the adductomics study. Bacterial cells were harvested via centrifugation. The resulting pellets were suspended in 20 mg/mL lysozyme solution in TE buffer (approximately 300 µL per 1 x 10^9 cells) and incubated at room temperature (RT) for 10 minutes while shaking. Lysozyme-treated cells were pelleted via centrifugation for 1 min at 16,000 × g at 4 °C, followed by careful removal of supernatant with a micropipet. 300 µL of Cell Lysis Solution was added per pellet and mixed with cells by pipetting up and down. The mixture quickly became sticky, and the pellet was partially resuspended. After 5 minutes of rest at RT, 1.5 µL RNase A Solution from the kit was added and mixed by

inverting the tubes 25 times. The mixtures were incubated at RT for 2 hours without shaking. Samples were then quickly cooled down on ice for 1 minute, followed by addition of 100 µL Protein Precipitation Solution and vigorous vortexing for 20 seconds at high speed. The samples were then incubated on ice for 10 minutes and centrifuged for 3 minutes at 16,000 × g at 4 °C. In new, clean 1.5 mL microcentrifuge tubes, the supernatant was carefully poured into 300 µL isopropanol (IPA), and the resulting solution was gently mixed by slowly inverting tubes 50 times. White floating substances, the DNA, started to appear during mixing. To collect precipitated DNA, the mixture was centrifuged for 1 min at 16,000 × g at 4 °C, followed by two washing steps using 300 µL of 70% and 100% IPA. After careful removal of supernatant, tubes containing DNA at bottom were drained on a clean piece of absorbent paper and allowed to air dry. To measure concentration, DNA pellets were dissolved in Tris-$MgCl_2$ buffer overnight in a 4 °C fridge, and the concentration was measured using a NanoDrop One spectrometer with a standard of A260/A280 ~1.8.

6.2.10 Direct exposure of NMC to extracted bacterial DNA

Bacteria were grown in LB broth until mid-log phase and harvested by centrifugation for 30 seconds at 16,000 × g at 4 °C, followed by DNA extraction as described above. NMC was weighed and suspended in Tris-$MgCl_2$ buffer and sonicated in a bath sonicator for 15 minutes. The total DNA amount in each sample was adjusted to ~50 µg, and DNA was mixed with freshly prepared NMC suspension for a final NMC concentration of 50 mg/L, followed by incubation at 4 °C for 48 hours. One replicate was done in the direct exposure. The resulting mixture after exposure was used for DNA adductomic sample preparation.

6.2.11 NMC exposure to bacterial cells for DNA adductomics

The exposure was done similar to that in the bacterial growth inhibition assay. Instead of using varying concentrations of NMC, only the selected 5 mg/L exposure

concentration was used in addition to the negative control. Three replicates were used in the experiment. After being grown in large volume in flask to mid-log phase, 21.9 mL bacterial suspension was aliquoted into 50 mL sterile conical tubes, followed by addition of freshly prepared NMC suspension. Bacterial growth was monitored over time by transferring 200 µL aliquots and measuring OD_{600}. At 8-hour post-exposure, an additional 200 µL aliquot was used for a growth-based viability assay, and the rest of bacterial suspensions were centrifuged at 4,000 × g for 20 minutes. Cell pellets were saved at -80 °C until being thawed for DNA extraction, followed by sample preparation for DNA adductomics.

6.2.12 Sample preparation for DNA adductomics

DNA digestion. Concentration of DNA dissolved in Tris-$MgCl_2$ buffer was quantified using a UV/vis spectrophotometer. A two-step DNA digestion was performed to digest macromolecules into single nucleosides using DNase (from *E. coli*, Aldrich), phospodiesterase-1 (PDE-1) (from *Crotalus adamanteus*, Aldrich) and alkaline phosphatase (ALP) (from *Pichia pastoris*, Aldrich). All the enzymes were purified by using a double filtration membrane Amico Ultra (0.5 mL, cutoff 10 k Da) prior to use. The first step of hydrolysis was done using only DNase, followed by a second step using the full enzyme mixture. Both steps incubated samples for 24 hours at RT. Per 1 µg of DNA, 0.5 Units of DNase was used in the first step, and the second step used 0.5 U, 0.2 U and 0.02 mU of DNase, ALP and PDE-1, respectively. After the two-step hydrolysis, enzymes were removed from the mixture by using an Amicon Microcone single filtration membrane (0.5 mL, cutoff 10 kDa). The digestion yield was assessed by measuring the concentration of dG via an LC/UV measurement.

dG quantitation. An HPLC Ultimate 3000 equipped with a reverse phase column, Luna C18 (250x0.5 mm, 5 µm, 100 Å) was used to separate the four 2'-deoxyribonucleosides (dC, dG, dT, dA) and quantify the amount of dG. A gradient of two mobile phase, H_2O

(A) and methanol (MeOH, B), was used. Operated at 40 °C with a flow rate of 15 µL·min-1, the system started elution with an isocratic step at 5% B for 3 minutes, followed by a first linear gradient of 0.58 % B·min^{-1} (12 min), a second linear gradient of 27.67 % B·min^{-1} (3 min) and it concluded with a second isocratic step at 95 % B (3 min). The column was re-equilibrated for 9 minutes using 5% B. Absorbance at 254 nm was used to monitor elution. Using a calibration curve consisting of eight standard concentrations (0.0625, 0.125, 0.25, 0.50, 1.00, 2.00, 4.0, 8.0 ng/µL pf dG), the amount of dG in digested DNA samples was quantified.

Hydrophobic reversed phase fraction collection. To exclude signals from unmodified deoxyribonucleosides (dC, dG, dT, dA) and enrich analytes of interest (i. e. DNA adducts) for the followed LC/MS^3 measurement, separation and fraction collection using chromatography was performed, followed by sample concentration and reconstitution. An HPLC (Ultimate 3000, Thermo Scientific, Waltham, MA) equipped with a C18-Column (4.6 x 250 mm, 100Å, 5µm Luna-Phenomenex, Torrace, CA) was used for fraction collection, using mobile phase H_2O (A) and MeOH (B) and operating at two different scenarios, I and II, for DNA from direct NMC exposure and DNA extracted from NMC-exposed cells, respectively. Scenario I ran at 25°C with a flow rate of 1.0 mL·min^{-1}. The elution program involved an isocratic step at 2% of B (5 min), followed by a linear gradient of 0.7 %B·min^{-1} (25 min) and a second isocratic step at 100% of B (15 min). At the end of the elution, the LC-system was equilibrated in isocratic condition (2% of B) for 20 min. Scenario II ran at 4°C with a flow rate of 1.0 mL·min^{-1}.The elution program involved an isocratic step at 2% of B (5 min), followed by a series of linear gradients of 0.86% B·min^{-1} (6 min), 0.14% B·min^{-1} (28 min), 4.6% B·min^{-1} (5 min), 13% B·min^{-1} (5 min), and an isocratic step at 100% of B (5 min). At the end of the elution, the LC-system was equilibrated in isocratic conditions (2% of B) for 20 min. Two different wavelengths (190 nm and 254 nm) were used to monitor elution. In Scenario I, eluted fractions after the last nucleoside peak (dA) were collected.

In Scenario II, fraction collection started at 10 min and ended at 60 min of the program, and only fractions between nucleoside peaks were collected. Collected fractions from one sample were combined, dried in a SpeedVac concentrator, and stored at -20 °C until LC/MS^3 adductomic analysis. Two isotopic standards, ^{15}N-N^6-Me-dA and ^{15}N-N^2-Et-dG, were added during DNA digestion and sample concentration for the purpose of quality control. For DNA from direct NMC exposure, two additional isotopic standards, D_4-POB-dT and D_4-POB-dG were also used.[28]

6.2.13 LC/MS3 adductomic analysis

The dried DNA samples were reconstituted in 20 µL of LC-MS water (LCMS grade, Fluka) and then analyzed with a NanoUPLC system (Ultimate 3000, Thermo Scientific, Waltham, MA) coupled to an Orbitrap mass detector (Fusion-Thermo Scientific, Waltham, MA). The UPLC system operated with a 5-µL loop. The chromatographic separation was performed with an RP-column created by hand packing a commercially available fused-silica emitter (230x0.075mm, 15 µm orifice, New Objective, Woburn MA) with C18 stationary phase (5 µm, 100Å, Luna-Phenomenex, Torrace, CA). The mobile phase consists of formic acid (0.05 %v/v in H_2O, phase-A) and acetonitrile (100%v/v, phase-B). The elution program involved an isocratic step (2 % of B for 5 min at 1µL·min^{-1}), followed by a linear gradient of B (1.5 %·min^{-1} for 25 min at 0.3 µL·min^{-1}), and it concluded with a washing isocratic step, performed at 98% of B for 5 min at 0.3µL·min^{-1}. At the end of the elution program, the LC-system was equilibrated for 5 min in isocratic conditions (2% of B, 1 µL·min^{-1}). In the course of the LC run, the injection valve switched at 6 min, excluding the sample loop from hydraulic path. This operation allowed performance of several washes of the injection system, avoiding carryover and preventing memory effects. The LC system was interfaced to the MS-detector using a Nanoflex ESI ion source (Nanoflex Thermo Scientific, Waltham, MA). The source operated in positive ion mode at RT conditions. The electrospray voltage was set at 2.5 kV and the temperature of the ion tube was set up at 350 °C. The overall

ion optics were optimized monitoring the background signal 371.1012 m/z (oligosilorxane, $[C_2H_6SiO]_5$).

The MS-analyses consist of three detection events: full scan, untargeted data dependent MS^2-acquisition (dd-MS^2) and a neutral loss MS^3-data acquisition (NL-MS^3). The full scan (100-1000 m/z) was performed using the front quadrupole to fill up the C-Trap, which worked with a maximum injection time of 50 ms and automatic gain control (AGC) of 5.104. The MS-spectra were acquired by the Orbitrap at resolution of 60000 (ref. 400 m/z). The five most abundant ions detected during each full scan event were picked to trigger the dd-MS^2 fragmentation events. The mass tolerance required to trigger the MS^2 data acquisition was set at 5 ppm. A dynamic exclusion of 20s, and an intensity threshold of 104 counts were introduced to better manage the instrumental dwell time. In the course of the dd-MS^2 acquisitions, the front quadrupole was used to isolate each individual top 5 precursor ions (isolation width ± 1.5 m/z). The fragmentations were performed in the high-pressure stage of the linear ion trap (LIT), which operated with a normalized collision energy of 30 % CID and an activation time of 10 ms. In order to measure the accurate mass of the fragment ions, the MS^2 spectra were recorded with the Orbitrap detector, which operated with a resolution of 15000 (ref. 400 m/z) and a max injection time of 200 ms. During the course of the NL-MS^3 data acquisitions, the ion trap was used to isolate the three most abundant MS^2-fragment ions (isolation width of ±3.0 m/z), which gave the neutral loss signal comparable to the release of the deoxyribose moiety (-dR; 116.0474 ± 0.0006 m/z, 5ppm). The MS^3-fragmentations were performed with the ion routing multipole, which operated with a normalized collision energy of 50% HCD. The MS^3-spectra were recorded with the Orbitrap, which performed a single microscan with a resolution of 15000 (ref. 400 m/z) and operated with injection time of 300 ms.

6.2.14 Adductomic data analysis

Data on putative DNA adducts were extracted from spectra acquired from LC/MS^3 using Xcalibur Qual Browser. Generally, three levels of evidence were acquired to confirm a putative DNA adduct: the m/z values of precursor ($[M+H]^+$) in full scan, fragment after neutral loss in the precursor ion ($[MH-dR]^+$) in MS^2, and other detected fragments in MS^3 that are signatures for the fragment detected in MS^2, and ideally the retention time should make sense as well considering the polarity of the putative DNA adducts. For semi-quantification of a putative DNA adduct in a specific sample, the ion count intensity of the m/z of interest in full scan with a mass range of 5 ppm was used, and the intensity was further normalized using the amount of dG determined in that specific sample. In analysis of adductomic data from single replicate (DNA directly exposed to NMC), all three levels of evidence from tandem mass spectrometry were applied to determine the existence of putative DNA adducts. To analyze data acquired from triplicates (DNA extracted from exposed bacterial cells), putative DNA adducts confirmed by three levels of MS (full scan/MS^2/MS^3) were first summarized. If a putative adduct appeared in more than two of the three replicates in either control or exposed groups, new searches on signature fragments in MS^2 of the rest of replicates that did not show MS^3 spectra were further done to support the confirmation of that putative adduct. If signature fragments were found in MS^2, the putative DNA adduct was regarded as confirmed; if not, the data point was regarded as "not found" and not included in calculating the average for triplicates. In plotting triplicate data, individual data points plus average were plotted versus both retention time (min) and the m/z values of precursor ions.

6.3 Results and discussion

6.3.1 NMC induced ROS generation abiotically

Intracellular ROS detection with 2',7'-dichlorodihydrofluorescein diacetate ($DCFH_2$-DA, also known as 2′,7′-dichlorofluorescin diacetate) is widely applied. The two

acetate groups, which makes the molecule cell-permeant, are expected to be hydrolyzed by esterase in cell plasma. The resultant 2',7'-dichlorodihydrofluorescein ($DCFH_2$) is non-fluorescent until being oxidized by various ROS when it is converted into highly fluorescent 2',7'-dichlorofluorescein (DCF).[46] This reaction is depicted in **Figure 6.1(a)**. Ideally, the reactions should only happen in cell plasma. However, it has been shown that this reaction can happen spontaneously in aqueous solution;[47,48] in fact, the probe was initially developed to measure H_2O_2 in cell-free systems.[47] **Figure 6.1(b)** describes ROS generation in MM with lactate without the presence of cells. Compared to H_2O_2-treated $DCFH_2$-DA in solution, NMC-treated samples showed relatively slow but steady increase in fluorescence intensity, indicating formation of the fluorescent product DCF. We suspect that the continuous oxidation of $DCFH_2$ with H_2O_2/NMC treatment kept moving the reaction equilibrium to the right side, forming more reactive $DCFH_2$ and thus more DCF over time. It is worth noting that the shapes of fluorescence intensity increase for H_2O_2 and NMC were quite different. This might indicate that, different from direct oxidation of $DCFH_2$ by H_2O_2, NMC induced oxidation in an indirect manner, possibly through generation of ROS via reactions between aqueous media and NMC surfaces or released metal ions.[5]

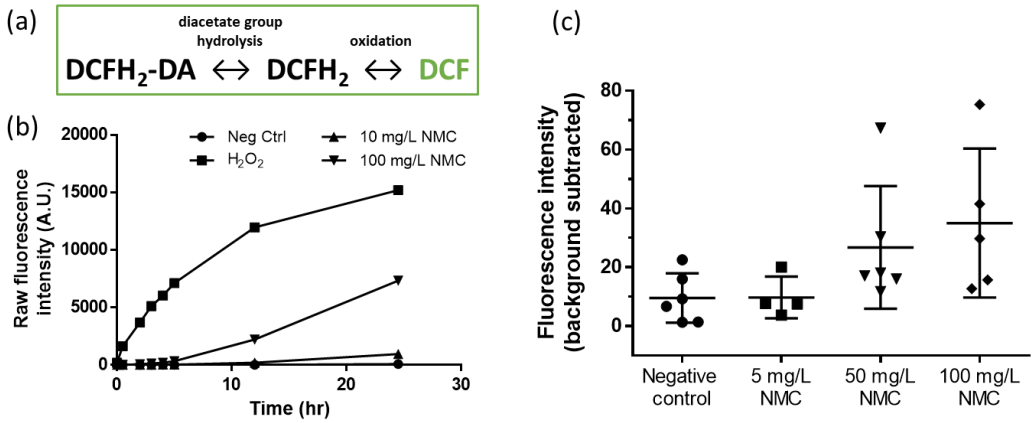

Figure 6. 1 (a) Reaction for $DCFH_2$-DA hydrolysis and oxidation into fluorescent DCF product. (b) Fluorescence intensity over time for 20 µM $DCFH_2$-DA in MM with lactate upon adding different reagents; for clarity, only average values were plotted (n=3). (c) Fluorescence intensity of $DCFH_2$-DA-loaded bacterial cells after incubating with NMC (positive controls were not shown); each data point represents an average value from

an individual experiment. No statistical significance was determined (one-way ANOVA, post-hoc Dunnett's multiple comparison, α=0.05; H_2O_2 positive controls were not included in the statistical tests)

Using the same dye, $DCFH_2$-DA, intracellular ROS generation induced by treatment with NMC was measured. Since the dye can react with ROS without cells, extensive washing was implemented to exclude fluorescence signals outside cells. As described in the Experimental section, bacterial cells were loaded with $DCFH_2$-DA prior to exposure to capture the generation of transient ROS during exposure. Positive control groups treated with H_2O_2 showed increased fluorescence, indicating that the dye was successfully taken up into cells (data not shown). It is worth mentioning that among all experimental trials, not all trials showed successful dye loading, and thus only trials in which positive control groups showed significant increase in fluorescence were used for plotting and statistical tests (**Figure 6.1(c)**). While exposure to 5 mg/L 72-hour aged NMC for a short time (15-min) did not show response in ROS generation, NMC exposure to 50 mg/L or greater doses appeared to increase the average fluorescence intensity compared to control groups in a dose-dependent manner (**Figure 6.1(c)**). However, the increase was not statistically significant, which might be attributed to the short-term exposure (15-min). Thus, it is not conclusive from the $DCFH_2$-DA test whether NMC caused oxidative stress in bacterial cells. Overall, ROS detection using $DCFH_2$-DA clearly showed NMC-generated ROS in bacterial media, but not necessarily increase the level of intracellular ROS in bacterial cells.

6.3.2 Intracellular Ni/Co ions were detected upon exposure

Newport Green DCF diacetate (NPG-Ac) is a cell permeable, Zn^{2+}- (but not Ca^{2+}-) sensitive probe, making it ideal to monitor Zn^{2+} influx into neurons.[49] Similar to $DCFH_2$-DA, upon entering cells, the diacetate groups on NPG-Ac are cleaved by cellular esterases, and binding of metal ions with the cleaved dye turns on fluorescence that can be detected. Besides Zn^{2+}, the Newport Green dye was also found to respond

to transition metal ions, including Cu(I), Ni(II), Cd(II), Co(II), and Fe(II) but not Mn(II) or Fe(III).[50] This makes NPG-Ac an excellent choice to monitor metal ion uptake induced by NMC, whose toxicity to *S. oneidensis* was identified as attributable to the release of nickel and cobalt, but not manganese, ions.[5] In fact, the NPG-Ac dye has been used previously to detect transition metal ion uptake in neurons.[51]

To validate the assay, we first exposed bacterial cells pre-loaded with dye with gradients of aqueous Ni(II) or Co(II) (**Figure 6.2(a)**). The NPG dye showed dose-dependent fluorescence response to the exposure to both metal ions, and at the same concentrations, Ni(II) ions induced higher response than Co(II) ions. The higher sensitivity towards Ni(II) could be due to the higher sensitivity of the NPG dye when responding to Ni(II) abiotically,[50] potentially differential uptake of the two ions into bacterial cells, or a mixed effect. We then followed the same protocol to load dye and expose to a gradient of concentrations of nanoscale NMC. As expected, results showed an NMC dose-dependent fluorescence response, indicating uptake of Ni(II) and/or Co(II) ions (**Figure 6.2(b)**). It should be noted that the NPG-Ac dye is not able to differentiate between Ni(II) and Co(II) ions, but only a mixed effect; neither is it quantitative. ICP-MS is a technique capable of quantitatively determining a mixture of ions, but we did not choose this technique because ICP-MS cannot differentiate among metals inside or outside cells because it is almost impossible to separate cells from NMC materials.

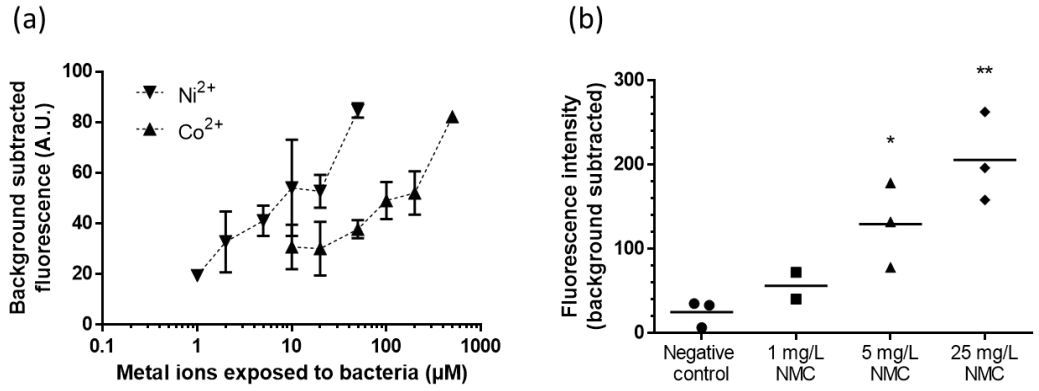

Figure 6. 2 Fluorescence intensity of NPG-Ac-loaded bacterial cells after incubating with different concentrations of (a) Ni/Co ions or (b) NMC. In (a), standard deviation was plotted from the triplicates in one experimental run. In (b), each data point represents an average value of the triplicates in an individual experimental run, and the average of multiple experiments is shown. Stars denote statistical significance (one-way ANOVA, post-hoc Dunnett's multiple comparison, α=0.05).

6.3.3 NMC exposure caused dose-dependent growth inhibition

We started nanoscale NMC exposure at the mid-log phase of bacterial growth instead of at the beginning as bacterial cells actively replicate during exponential growth; thus, the impact on DNA during log phase would have a high possibility to lead to detrimental consequences. After spiking NMC into bacterial suspension, a dose-dependent growth inhibition was observed (**Figure 6.3(a)(b)**). A growth-based viability assay was coupled at different time points post-exposure to complement optical density measurements, as optical density detects intact cells but cannot differentiate viable from non-viable cells (**Figure 6.3(c)**). After 1-hour exposure, both normalized optical density and bacterial viability showed no effect from NMC exposure. However, 8 hours post-exposure, dose-dependent effects were observed for both bacterial growth and viability, indicating NMC toxicity developed over time. Interestingly, while the optical density at 8-hour 50 mg/L post-exposure indicated about half the number of cells present compared to the control, the viability test showed only about 10% of viable cell numbers compared to control. The discrepancy showed that not all cells present at 8-hour 50 mg/L post-exposure were viable, and, as detailed in Chapter 1, it is important to have two

measurements to complement each other to reveal toxicity.

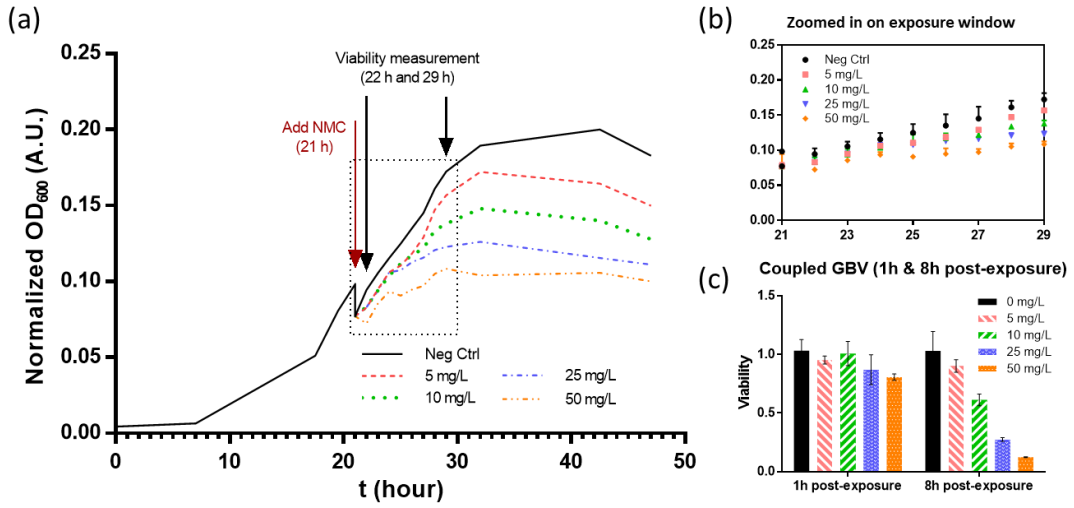

Figure 6. 3 (a) Dosing NMC at mid-log phase of bacterial growth, showing normalized optical density over time before and after adding NMC. For clarity, individual data points and errors of triplicates are not shown. (b) A magnification of the exposure window. (c) Viability of bacterial populations compared to control at different time points post-exposure. Standard deviations are shown in (b) and (c) (n=3).

6.3.4 NMC exposure induced DNA double-strand breakage but no change in adduct formation

From the growth inhibition and viability assay, 5 mg/L was determined to be a sub-lethal dosage used for DNA damage assays, and the exposure for the DNA damage assay was done following the same procedure outlined for the aforementioned toxicity assays. DNA strand breakage was measured using the Comet assay, a single-cell electrophoresis technique that has been used to assess nanoparticle genotoxicity.[52] For the Comet assay on mammalian cells, the shape of stained DNA molecules looks like a comet, giving the assay its name. Different from mammalian cells, during electrophoresis, bacterial DNA molecules will migrate and stretch, forming "tails" instead of "comets", and the tail lengths of these stretched DNA molecules represent the extend of DNA strand breakage.[27] Representative images of undamaged (**Figure**

6.4(a)) and damaged bacterial DNA (**Figure 6.4(b)(c)**) upon NMC exposure are shown. To quantify DNA strand breakage, the lengths of migrated or stretched DNA molecules upon electrophoresis were measured, and the average tail length of NMC-treated groups was compared to that of control groups. **Figure 6.4(d)** shows that, compared to control groups, longer DNA tails were observed in bacterial cells exposed to both 5 and 50 mg/L NMC for 8 hours, indicating DNA strand breakage. Interestingly, there was no significant difference between tail length for 5 and 50 mg/L NMC-exposed cells.

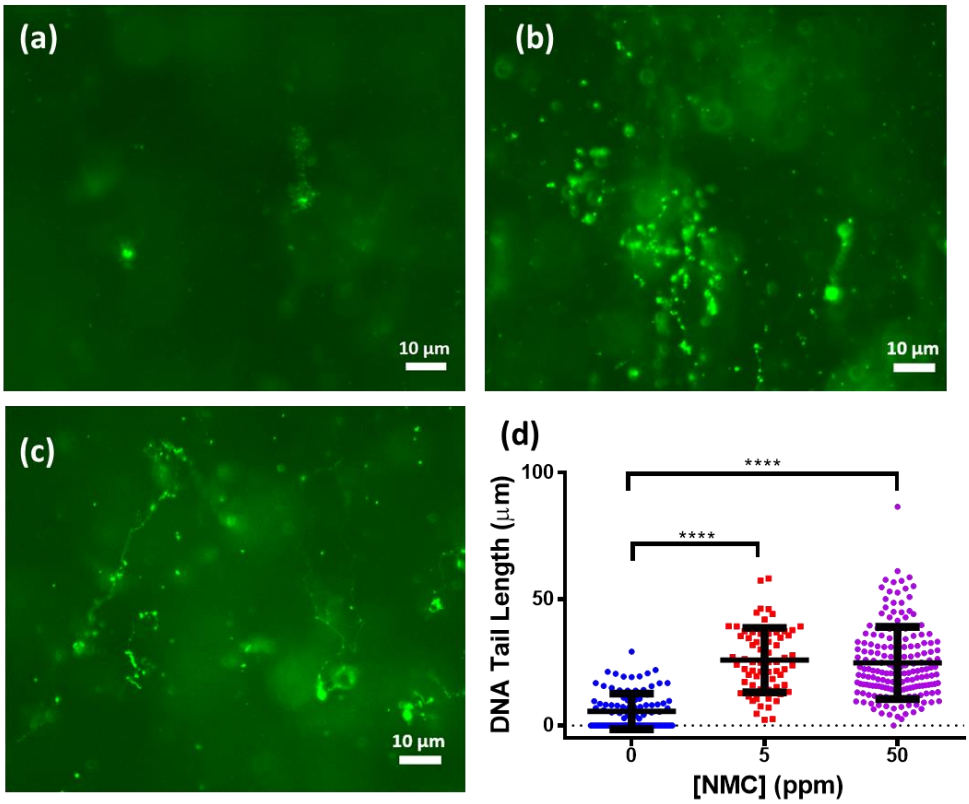

Figure 6. 4 Representative images from the Comet assay of bacterial cells exposed to (a) negative control, (b) 5 mg/L NMC, or (c) 50 mg/L NMC for 8 hours. DNA tail lengths counted from images were combined and compared in (d), showing statistically significant increases ($p<0.0001$) in DNA tail length upon NMC exposure.

DNA adducts refer to chemical modifications of DNA molecules, formed via redox reaction or fusion of molecular species. DNA adduct formation is informative of DNA damage mechanisms, and specific DNA adducts have been used as biomarkers in

molecular epidemiology and cancer studies.[30] We used a high-resolution mass spectrometry-based DNA adductomics approach to measure the formation of DNA adducts in bacteria. For the targeted approach, a list of endogenous DNA adducts was used in mass spectrometry screening. For untargeted screening, all ions resulting from a neutral loss of deoxyribose were further fragmented and recorded. To validate the method and detect potentially maximized effects on DNA upon NMC exposure, direct exposure of extracted DNA to NMC was performed. **Figure 6.5** shows normalized intensity of each putative DNA adduct detected in DNA directly exposed to NMC versus the m/z values of precursor ions, while precursor ions detected with the same m/z but different retention times were plotted together. The targeted approach with an inclusion list showed detection of multiple putative adducts in one run. Three out of four isotopic standards were confirmed. High levels of N^6-Me-dA were shown in both control and exposed samples, consistent with previous literature on bacterial DNA methylation.[53] Generally, we determined that this adductomics approach worked on bacterial DNA. No notable changes were observed between control and exposed bacterial DNA, indicating that direct exposure of NMC, even for a long period of 48 hours at a high concentration of 50 mg/L, did not elicit changes in DNA adduct formation. This is contradictory to the earlier observation that NMC will cause oxidative stress via generation of ROS. As only fractions after the eluted dA peak were collected, it was possible that we did not fully collect oxidative stress-related DNA adducts, as they are likely to be more hydrophilic than dA and thus eluted earlier than the dA peak.

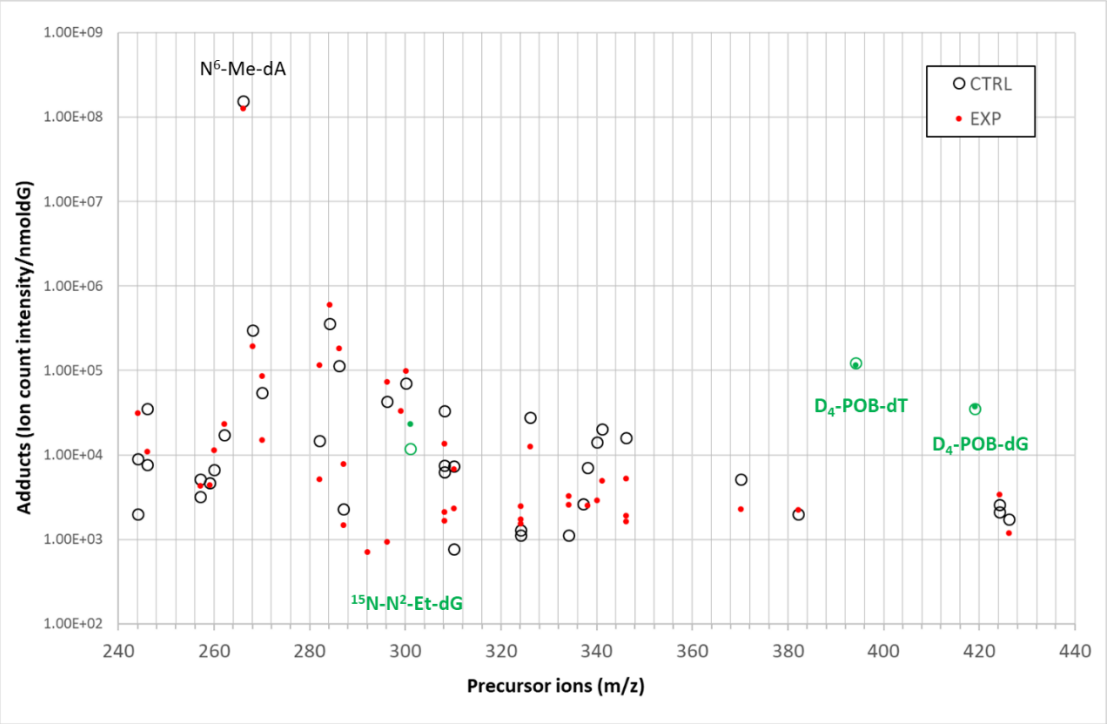

Figure 6. 5 Putative DNA adducts identified using LC/MS^3 adductomics in bacterial DNA directly exposed to nanoscale NMC. Green dots are internal standards detected. Red solid dots refer to putative adducts detected in NMC-exposed DNA and black hollow dots indicates adducts in unexposed DNA. One replicate was used in the direct exposure.

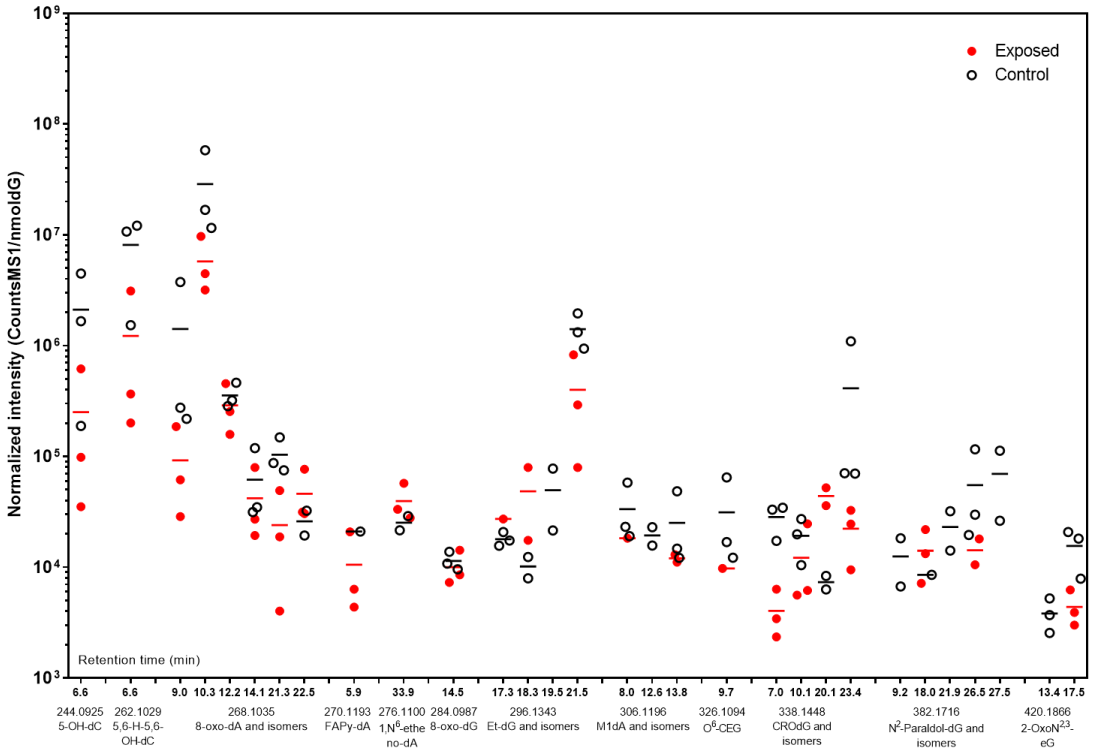

Figure 6. 6 Putative DNA adducts identified using LC/MS^3 adductomics in DNA extracted from NMC-exposed bacterial cells. Retention times are indicated on the x-axis, and the m/z and names of putative DNA adducts are marked at x-axis as well. Red solid dots refer to putative adducts detected in DNA samples extracted from NMC-exposed bacteria, and black hollow dots show adducts from DNA extracted from unexposed bacteria. The exposure was done in triplicate, and the average of the triplicates are shown in red (exposed) and black (control) lines.

We then exposed NMC to bacterial cells at mid-log phase and harvested cells before they fully entered stationary phase. A "sub-lethal" concentration, 5 mg/L, that showed neither inhibition of bacterial growth nor decreased viability was chosen as we preferred to avoid collecting DNA from dead cells, plus the fact that DNA strand breakage was already shown in the Comet assay at this concentration. We also collected all fractions in between peaks of the four 2'-deoxyribonucleosides (dC, dG, dT, dA) so that hydrophilic adducts could be collected as well. Shown in **Figure 6.6**, again, no significant changes were observed in levels of various DNA adducts upon NMC exposure, including oxidative stress-related ones. Adding together, the results from two different DNA adductomic experiments showed that DNA adduct formation was not

likely to be the mechanism contributing to DNA strand breakage observed in the Comet assay. To further explore potential DNA damage mechanisms that might lead to strand breakage, such as inhibition of DNA repair and disruption of transcription,[54] gene expression level changes on DNA repair-related proteins will be studied.

6.4 Conclusion

The potential wide application of nanoscale lithium nickel manganese cobalt oxide ($Li_xNi_yMn_zCo_{1-y-z}O_2$, NMC) as a cathode material in lithium-ion batteries calls for evaluation of its risk when being released into the environment. Previous studies showed that NMC induced inhibition of bacterial growth of an ecologically beneficial bacterium, *Shewanella oneidensis* MR-1, via dissolution of nickel and cobalt ions. Considering the genotoxic effects of nickel and cobalt, we evaluated bacterial DNA damage upon NMC exposure as a potential toxicity mechanism. We found DNA strand breakage via the Comet assay, and successfully applied, for the first time, a high-resolution mass spectrometry-based DNA adductomics approach to study bacterial DNA adducts upon NP exposure. Results showed that sub-lethal concentrations of NMC exposure induced DNA strand breakage, but no significant changes were observed in levels of various DNA adducts. Combined with evidence that clearly indicated Ni/Co metal ion uptake but less evidently inferred oxidative stress, we concluded DNA damage as a toxicity mechanism of NMC exposure to bacterial cells possibly via transition metal ion uptake and potentially ROS.

Chapter 7

Conclusion and outlook

7.1 Conclusion and outlook

Decades ago, DDT, a famous pesticide that was later found to be a persistent toxic pollutant, harmed our environment because of its extensive use without careful evaluation of its potential ecological risk. As materials with novel properties and activities, nanoscale materials and nano-enabled products have been under explosive development in the past decades, and thus, their environmental risks need to be proactively evaluated before wide application. Compared to performing toxicity assays on every nanomaterial that is being produced, a predictive model that links nanomaterial properties to the outcome of biological exposure can guide safer nanoparticle design in a more efficient manner. This thesis contributed to the establishment of predictive models by developing high-throughput toxicity screening assays that can avoid nanomaterial interference and investigating biological response on molecular levels, including biochemical processes, gene expression and DNA damage, upon various nanomaterial exposure using an ecologically relevant bacterial model, *Shewanella oneidensis* MR-1. Combining thorough NP characterization and biological measurement, we concluded that the response of bacterial cells on the molecular level can be dominated by surface modification (surface charge), environmental conditions such as surrounding medium and light, purification strategy, ion release, and the intrinsic properties of NP core composition. Analytical techniques from simple optical assays (fluorescence/colorimetric/absorbance) to complex -omics measurements were combined to obtain a comprehensive understanding of nanotoxicity at the molecular level.

Looking forward, we believe that the field of nanotoxicology is entering a new era. Cutting-edge bioanalytical techniques, such as sub-diffraction microscopy and -omics, are being used to reveal unprecedent details about nanoparticle characterization, nano-bio interactions, and biological responses, and more analytical assays are being adapted

and developed to overcome NP interference and improve toxicity assessment. Studies are more focused on molecular mechanisms underlying nanotoxicity instead of conventional toxicity endpoint assays to understand the causal relationship among NP properties, surrounding environment, and the biological organism of interest. Interdisciplinary collaboration among materials scientists, chemists, biologists, computational and theoretical scientists, and bioinformatic scientists will keep paving the way to a comprehensive picture of nano-bio interactions and the establishment of predictive models among NP properties, biological consequences, and environmental implications. In this thesis, we also provided our perspectives as analytical chemists on the challenges in the field of nanotoxicology for the next decade. We look forward to the next decade of nanotoxicology and believe that this thesis has contributed to solving the grand challenge of understanding nano-bio interactions.

Bibliography

Chapter 1

(1) Roco, M. C.; Tech, N. S. E. *AIChE J.* **2004**, *50*, 890-897.

(2) Roco, M. C.; Mirkin, C. A.; Hersam, M. C. *J. Nanopart. Res.* **2011**, *13*, 897-919.

(3) Liu, Y. Y.; Zhou, G. M.; Liu, K.; Cui, Y. *Acc. Chem. Res.* **2017**, *50*, 2895-2905.

(4) Wolfram, J.; Zhu, M. T.; Yang, Y.; Shen, J. L.; Gentile, E.; Paolino, D.; Fresta, M.; Nie, G. J.; Chen, C. Y.; Shen, H. F.; Ferrari, M.; Zhao, Y. L. *Curr. Drug. Targets* **2015**, *16*, 1671-1681.

(5) Vance, M. E.; Kuiken, T.; Vejerano, E. P.; McGinnis, S. P.; Hochella, M. F.; Rejeski, D.; Hull, M. S. *Beilstein J. Nanotech.* **2015**, *6*, 1769-1780.

(6) Stark, W. J.; Stoessel, P. R.; Wohlleben, W.; Hafner, A. *Chem. Soc. Rev.* **2015**, *44*, 5793-5805.

(7) http://nanodb.dk/en/

(8) http://www.nanotechproject.org/cpi/products/

(9) Nel, A.; Xia, T.; Madler, L.; Li, N. *Science* **2006**, *311*, 622-627.

(10) Oberdorster, G.; Oberdorster, E.; Oberdorster, J. *Environ. Health Perspect.* **2005**, *113*, 823-839.

(11) Oberdörster, G.; Maynard, A.; Donaldson, K.; Castranova, V.; Fitzpatrick, J.; Ausman, K.; Carter, J.; Karn, B.; Kreyling, W.; Lai, D.; Olin, S.; Monteiro-Riviere, N.; Warheit, D.; Yang, H. *Part. Fibre Toxicol.* **2005**, *2*, 8.

(12) Kong, B.; Seog, J. H.; Graham, L. M.; Lee, S. B. *Nanomedicine-UK* **2011**, *6*, 929-941.

(13) Ong, K. J.; MacCormack, T. J.; Clark, R. J.; Ede, J. D.; Ortega, V. A.; Felix, L. C.; Dang, M. K. M.; Ma, G. B.; Fenniri, H.; Veinot, J. G. C.; Goss, G. G. *PloS One* **2014**, *9*.

(14) Alkilany, A. M.; Lohse, S. E.; Murphy, C. J. *Acc. Chem. Res.* **2013**, *46*, 650-661.

(15) Nel, A.; Xia, T.; Meng, H.; Wang, X.; Lin, S. J.; Ji, Z. X.; Zhang, H. Y. *Acc. Chem. Res.* **2013**, *46*, 607-621.

(16) Bour, A.; Mouchet, F.; Silvestre, J.; Gauthier, L.; Pinelli, E. *J. Hazard. Mater.* **2015**, *283*, 764-777.

(17) Drasler, B.; Sayre, P.; Steinhauser, K. G.; Petri-Fink, A.; Rothen-Rutishauser, B. *NanoImpact* **2017**, *8*, 99-116.

(18) Dusinska, M.; Boland, S.; Saunders, M.; Juillerat-Jeanneret, L.; Tran, L.; Pojana, G.; Marcomini, A.; Volkovova, K.; Tulinska, J.; Knudsen, L. E.; Gombau, L.; Whelan, M.; Collins, A. R.; Marano, F.; Housiadas, C.; Bilanicova, D.; Kenzaoui, B. H.; Carreira, S. C.; Magdolenova, Z.; Fjellsbo, L. M.; Huk, A.; Handy, R.; Walker, L.; Barancokova, M.; Bartonova, A.; Burello, E.; Castell, J.; Cowie, H.; Drlickova, M.; Guadagnini, R.; Harris, G.; Harju, M.; Heimstad, E. S.; Hurbankova, M.; Kazimirova, A.; Kovacikova, Z.; Kuricova, M.; Liskova, A.; Milcamps, A.; Neubauerova, E.; Palosaari, T.; Papazafiri, P.; Pilou, M.; Poulsen, M. S.; Ross, B.; Runden-Pran, E.; Sebekova, K.; Staruchova, M.; Vallotto, D.; Worth, A. *Nanotoxicology* **2015**, *9*, 118-132.

(19) Nel, A. E.; Madler, L.; Velegol, D.; Xia, T.; Hoek, E. M. V.; Somasundaran, P.; Klaessig, F.; Castranova, V.; Thompson, M. *Nat. Mater.* **2009**, *8*, 543-557.

(20) Qiu, T. A.; Nguyen, T. H.; Hudson-Smith, N. V.; Clement, P. L.; Forester, D. C.; Frew, H.; Hang, M. N.; Murphy, C. J.; Hamers, R. J.; Feng, Z. V.; Haynes, C. L. *Anal. Chem.* **2017**, *89*, 2057-2064.
(21) Ivask, A.; Mitchell, A. J.; Malysheva, A.; Voelcker, N. H.; Lombi, E. *Wiley Interdisciplinary Reviews: Nanomedicine and NanobioTechnol.* **2017**, e1486-n/a.
(22) Liao, K. H.; Lin, Y. S.; Macosko, C. W.; Haynes, C. L. *ACS Appl. Mater. Inter.* **2011**, *3*, 2607-2615.
(23) Lin, Y. S.; Abadeer, N.; Haynes, C. L. *Chem. Comm.* **2011**, *47*, 532-534.
(24) Rivera-Gil, P.; De Aberasturi, D. J.; Wulf, V.; Pelaz, B.; Del Pino, P.; Zhao, Y. Y.; De La Fuente, J. M.; De Larramendi, I. R.; Rojo, T.; Liang, X. J.; Parak, W. J. *Acc. Chem. Res.* **2013**, *46*, 743-749.
(25) Zhang, H. Y.; Ji, Z. X.; Xia, T.; Meng, H.; Low-Kam, C.; Liu, R.; Pokhrel, S.; Lin, S. J.; Wang, X.; Liao, Y. P.; Wang, M. Y.; Li, L. J.; Rallo, R.; Damoiseaux, R.; Telesca, D.; Madler, L.; Cohen, Y.; Zink, J. I.; Nel, A. E. *ACS Nano* **2012**, *6*, 4349-4368.
(26) Tang, J.; Baxter, S.; Menon, A.; Alaarg, A.; Sanchez-Gaytan, B. L.; Fay, F.; Zhao, Y. M.; Ouimet, M.; Braza, M. S.; Longo, V. A.; Abdel-Atti, D.; Duivenvoorden, R.; Calcagno, C.; Storm, G.; Tsimikas, S.; Moore, K. J.; Swirski, F. K.; Nahrendorf, M.; Fisher, E. A.; Perez-Medina, C.; Fayad, Z. A.; Reiner, T.; Mulder, W. J. M. *P. Natl. Acad. Sci. USA* **2016**, *113*, E6731-E6740.
(27) Fadeel, B.; Fornara, A.; Toprak, M. S.; Bhattacharya, K. *Biochem. Bioph. Res. Co.* **2015**, *468*, 498-503.
(28) Burello, E.; Worth, A. P. *Wires Nanomed. Nanobi.* **2011**, *3*, 298-306.
(29) Singh, K. P.; Gupta, S. *RSC Adv.* **2014**, *4*, 13215-13230.
(30) Lynch, I.; Weiss, C.; Valsami-Jones, E. *Nano Today* **2014**, *9*, 266-270.
(31) Sturla, S. J.; Boobis, A. R.; FitzGerald, R. E.; Hoeng, J.; Kavlock, R. J.; Schirmer, K.; Whelan, M.; Wilks, M. F.; Peitsch, M. C. *Chem. Res. Toxicol.* **2014**, *27*, 314-329.
(32) Gunsolus, I. L.; Haynes, C. L. *Anal. Chem.* **2016**, *88*, 451-479.
(33) Costa, P. M.; Fadeel, B. *Toxicol. Appl. Pharmacol.* **2016**, *299*, 101-111.
(34) Caballero-Diaz, E.; Cases, M. V. *Trac-Trend Anal. Chem.* **2016**, *84*, 160-171.
(35) Frohlich, E. *J. Nanobiotechnol.* **2017**, *15*.
(36) Schnackenberg, L. K.; Sun, J.; Beger, R. D. In *Nanotoxicity: Methods and Protocols*, Reineke, J., Ed.; Humana Press: Totowa, NJ, 2012, pp 141-156.
(37) Matysiak, M.; Kapka-Skrzypczak, L.; Brzoska, K.; Gutleb, A. C.; Kruszewski, M. *J. Proteomics* **2016**, *137*, 35-44.
(38) Revel, M.; Chatel, A.; Mouneyrac, C. *Aquat. Toxicol.* **2017**, *193*, 72-85.
(39) Pillai, S.; Behra, R.; Nestler, H.; Suter, M. J. F.; Sigg, L.; Schirmer, K. *P. Natl. Acad. Sci. USA* **2014**, *111*, 3490-3495.
(40) Shin, T. H.; Lee, D. Y.; Lee, H. S.; Park, H. J.; Jin, M. S.; Paik, M. J.; Manavalan, B.; Mo, J. S.; Lee, G. *BMB Rep.* **2018**, *51*, 14-20.
(41) Ankley, G. T.; Bennett, R. S.; Erickson, R. J.; Hoff, D. J.; Hornung, M. W.; Johnson, R. D.; Mount, D. R.; Nichols, J. W.; Russom, C. L.; Schmieder, P. K.; Serrrano, J. A.; Tietge, J. E.; Villeneuve, D. L. *Environ. Toxicol. Chem.* **2010**, *29*, 730-741.
(42) Garcia-Reyero, N. *Environ. Sci. Technol.* **2015**, *49*, 3-9.

(43) Vietti, G.; Lison, D.; van den Brule, S. *Part Fibre. Toxicol.* **2016**, *13*.
(44) Labib, S.; Williams, A.; Yauk, C. L.; Nikota, J. K.; Wallin, H.; Vogel, U.; Halappanavar, S. *Part Fibre. Toxicol.* **2016**, *13*.
(45) Gerloff, K.; Landesmann, B.; Worth, A.; Munn, S.; Palosaari, T.; Whelan, M. *Comput. Toxicol.* **2017**, *1*, 3-11.
(46) Kaweeteerawat, C.; Ivask, A.; Liu, R.; Zhang, H. Y.; Chang, C. H.; Low-Kam, C.; Fischer, H.; Ji, Z. X.; Pokhrel, S.; Cohen, Y.; Telesca, D.; Zink, J.; Madler, L.; Holden, P. A.; Nel, A.; Godwin, H. *Environ. Sci. Technol.* **2015**, *49*, 1105-1112.
(47) Burello, E.; Worth, A. P. *Nanotoxicology* **2015**, *9*, 116-117.
(48) Burello, E.; Worth, A. P. *Nanotoxicology* **2011**, *5*, 228-235.
(49) Hellack, B.; Nickel, C.; Albrecht, C.; Kuhlbusch, T. A. J.; Boland, S.; Baeza-Squiban, A.; Wohlleben, W.; Schins, R. P. F. *Environ. Sci. Nano* **2017**, *4*, 1920-1934.
(50) Jacobson, K. H.; Gunsolus, I. L.; Kuech, T. R.; Troiano, J. M.; Melby, E. S.; Lohse, S. E.; Hu, D.; Chrisler, W. B.; Murphy, C. J.; Orr, G.; Geiger, F. M.; Haynes, C. L.; Pedersen, J. A. *Environ. Sci. Technol.* **2015**, *49*, 10642-10650.
(51) Reyes, V. C.; Li, M. H.; Hoek, E. M. V.; Mahendra, S.; Damoiseaux, R. *Acs Nano* **2012**, *6*, 9402-9415.
(52) Ivask, A.; Suarez, E.; Patel, T.; Boren, D.; Ji, Z. X.; Holden, P.; Telesca, D.; Damoiseaux, R.; Bradley, K. A.; Godwin, H. *Environ. Sci. Technol.* **2012**, *46*, 2398-2405.
(53) Worle-Knirsch, J. M.; Pulskamp, K.; Krug, H. F. *Nano Lett.* **2006**, *6*, 1261-1268.
(54) Kampfer, A.; La Spina, R.; Gilliland, D.; Valzacchi, S.; Asturiol, D.; Stone, V.; Kinsner-Ovaskainen, A. *Chem. Res. Toxicol.* **2017**, *30*, 1030-1037.
(55) Semisch, A.; Hartwig, A. *Chem. Res. Toxicol.* **2014**, *27*, 169-171.
(56) Stone, V.; Johnston, H.; Schins, R. P. F. *Critical Rev. Toxicol.* **2009**, *39*, 613-626.
(57) Schultz, A. G.; Boyle, D.; Chamot, D.; Ong, K. J.; Wilkinson, K. J.; McGeer, J. C.; Sunahara, G.; Goss, G. G. *Environ. Chem.* **2014**, *11*, 207-226.
(58) Ribeiro, A. R.; Leite, P. E.; Falagan-Lotsch, P.; Benetti, F.; Micheletti, C.; Budtz, H. C.; Jacobsen, N. R.; Lisboa, P. N.; Rocha, L. A.; Kuhnel, D.; Hristozov, D.; Granjeiro, J. M. *NanoImpact* **2017**, *8*, 59-72.
(59) Guadagnini, R.; Kenzaoui, B. H.; Walker, L.; Pojana, G.; Magdolenova, Z.; Bilanicova, D.; Saunders, M.; Juillerat-Jeanneret, L.; Marcomini, A.; Huk, A.; Dusinska, M.; Fjellsbo, L. M.; Marano, F.; Boland, S. *Nanotoxicology* **2015**, *9*, 13-24.
(60) Farcal, L.; Andon, F. T.; Di Cristo, L.; Rotoli, B. M.; Bussolati, O.; Bergamaschi, E.; Mech, A.; Hartmann, N. B.; Rasmussen, K.; Riego-Sintes, J.; Ponti, J.; Kinsner-Ovaskainen, A.; Rossi, F.; Oomen, A.; Bos, P.; Chen, R.; Bai, R.; Chen, C. Y.; Rocks, L.; Fulton, N.; Ross, B.; Hutchison, G.; Tran, L.; Mues, S.; Ossig, R.; Schnekenburger, J.; Campagnolo, L.; Vecchione, L.; Pietroiusti, A.; Fadeel, B. *PloS One* **2015**, *10*.
(61) Catalan, J.; Ilves, M.; Jarventaus, H.; Hannukainen, K. S.; Kontturi, E.; Vanhala, E.; Alenius, H.; Savolainen, K. M.; Norppa, H. *Environ. Mol. Mutagen.* **2015**, *56*, 171-182.
(62) Bermejo-Nogales, A.; Connolly, M.; Rosenkranz, P.; Fernandez-Cruz, M. L.; Navas, J. M. *Ecotoxicol. and Environ. Safety* **2017**, *138*, 309-319.
(63) Mottas, I.; Milosevic, A.; Petri-Fink, A.; Rothen-Rutishauser, B.; Bourquin, C. *Nanoscale* **2017**, *9*, 2492-2504.

(64) Lammel, T.; Sturve, J. *NanoImpact* **2018**, *11*, 1-19.
(65) Karlsson, H. L.; Di Bucchianico, S.; Collins, A. R.; Dusinska, M. *Environ. Mol. Mutagen.* **2015**, *56*, 82-96.
(66) Kroll, A.; Pillukat, M. H.; Hahn, D.; Schnekenburger, J. *Arch. Toxicol.* **2012**, *86*, 1123-1136.
(67) Rosslein, M.; Elliott, J. T.; Salit, M.; Petersen, E. J.; Hirsch, C.; Krug, H. F.; Wick, P. *Chem. Res. Toxicol.* **2015**, *28*, 21-30.
(68) Alkilany, A. M.; Nagaria, P. K.; Hexel, C. R.; Shaw, T. J.; Murphy, C. J.; Wyatt, M. D. *Small* **2009**, *5*, 701-708.
(69) Harper, B.; Sinche, F.; Wu, R. H.; Gowrishankar, M.; Marquart, G.; Mackiewicz, M.; Harper, S. L. *Nanomaterials-Basel* **2014**, *4*, 355-371.
(70) Qiu, T. A.; Torelli, M. D.; Vartanian, A. M.; Rackstraw, N. B.; Buchman, J. T.; Jacob, L. M.; Murphy, C. J.; Hamers, R. J.; Haynes, C. L. *Anal. Chem.* **2017**, *89*, 1823-1830.
(71) Feng, Z. V.; Gunsolus, I. L.; Qiu, T. A.; Hurley, K. R.; Nyberg, L. H.; Frew, H.; Johnson, K. P.; Vartanian, A. M.; Jacob, L. M.; Lohse, S. E.; Torelli, M. D.; Hamers, R. J.; Murphy, C. J.; Haynes, C. L. *Chem. Sci.* **2015**, *6*, 5186-5196.
(72) Qiu, T. A.; Bozich, J. S.; Lohse, S. E.; Vartanian, A. M.; Jacob, L. M.; Meyer, B. M.; Gunsolus, I. L.; Niemuth, N. J.; Murphy, C. J.; Haynes, C. L.; Klaper, R. D. *Environ. Sci. Nano* **2015**, *2*, 615-629.
(73) Ozel, R. E.; Liu, X. B.; Alkasir, R. S. J.; Andreescu, S. *Trac-Trend Anal. Chem.* **2014**, *59*, 112-120.
(74) Hondroulis, E.; Liu, C.; Li, C. Z. *Nanotechnology* **2010**, *21*.
(75) Shah, P.; Zhu, X. N.; Zhang, X. J.; He, J.; Li, C. Z. *Acs Appl. Mater. Inter.* **2016**, *8*, 5804-5812.
(76) Otero-Gonzalez, L.; Sierra-Alvarez, R.; Boitano, S.; Field, J. A. *Environ. Sci. Technol.* **2012**, *46*, 10271-10278.
(77) Timbrell, J. A. *Toxicology* **1998**, *129*, 1-12.
(78) Gonzalez, L.; Kirsch-Volders, M. *Mutat. Res. Rev. Mutat.* **2016**, *770*, 204-216.
(79) Kain, J.; Karlsson, H. L.; Moller, L. *Mutagenesis* **2012**, *27*, 491-500.
(80) Magdolenova, Z.; Bilanicova, D.; Pojana, G.; Fjellsbo, L. M.; Hudecova, A.; Hasplova, K.; Marcomini, A.; Dusinska, M. *J. Environ. Monitor.* **2012**, *14*, 455-464.
(81) Azqueta, A.; Dusinska, M. *Frontiers in Genetics* **2015**, *6*.
(82) Huk, A.; Collins, A. R.; El Yamani, N.; Porredon, C.; Azqueta, A.; de Lapuente, J.; Dusinska, M. *Mutagenesis* **2015**, *30*, 85-88.
(83) Catalán, J.; Suhonen, S.; Huk, A.; Dusinska, M. In *Genotoxicity and DNA Repair: A Practical Approach*, Sierra, L. M.; Gaivão, I., Eds.; Springer New York: New York, NY, 2014, pp 241-268.
(84) Li, Y.; Doak, S. H.; Yan, J.; Chen, D. H.; Zhou, M.; Mittelstaedt, R. A.; Chen, Y.; Li, C.; Chen, T. *Mutagenesis* **2017**, *32*, 151-159.
(85) George, J. M.; Magogotya, M.; Vetten, M. A.; Buys, A. V.; Gulumian, M. *Toxicol. Sci.* **2017**, *156*, 149-166.
(86) Dusinska, M.; Tulinska, J.; El Yamani, N.; Kuricova, M.; Liskova, A.; Rollerova, E.; Runden-Pran, E.; Smolkova, B. *Food Chem. Toxicol.* **2017**, *109*, 797-811.

(87) Qiu, T. A.; Meyer, B. M.; Christenson, K. G.; Klaper, R. D.; Haynes, C. L. *Chemosphere* **2017**, *168*, 1158-1168.
(88) Piret, J. P.; Bondarenko, O. M.; Boyles, M. S. P.; Himly, M.; Ribeiro, A. R.; Benetti, F.; Smal, C.; Lima, B.; Potthoff, A.; Simion, M.; Dumortier, E.; Leite, P. E. C.; Balottin, L. B.; Granjeiro, J. M.; Ivask, A.; Kahru, A.; Radauer-Preiml, I.; Tischler, U.; Duschl, A.; Saout, C.; Anguissola, S.; Haase, A.; Jacobs, A.; Nelissen, I.; Misra, S. K.; Toussaint, O. *Arch. Toxicol.* **2017**, *91*, 2315-2330.
(89) Xia, X.; Owen, M. S.; Lee, R. E. C.; Gaudet, S. *Cell Death & Disease* **2014**, *5*.
(90) Ruan, G.; Agrawal, A.; Marcus, A. I.; Nie, S. *J. Am. Chem. Soc.* **2007**, *129*, 14759-14766.
(91) Fernando, L. P.; Kandel, P. K.; Yu, J. B.; McNeill, J.; Ackroyd, P. C.; Christensen, K. A. *Biomacromolecules* **2010**, *11*, 2675-2682.
(92) Michalet, X.; Pinaud, F. F.; Bentolila, L. A.; Tsay, J. M.; Doose, S.; Li, J. J.; Sundaresan, G.; Wu, A. M.; Gambhir, S. S.; Weiss, S. *Science* **2005**, *307*, 538-544.
(93) Cognet, L.; Leduc, C.; Lounis, B. *Curr. Opin. Chem. Biol.* **2014**, *20*, 78-85.
(94) Wang, W.; Tao, N. J. *Anal. Chem.* **2014**, *86*, 2-14.
(95) Manshian, B. B.; Munck, S.; Agostinis, P.; Himmelreich, U.; Soenen, S. J. *Sci. Rep.-UK* **2015**, *5*.
(96) Zanella, F.; Lorens, J. B.; Link, W. *Trends Biotechnol.* **2010**, *28*, 237-245.
(97) Jan, E.; Byrne, S. J.; Cuddihy, M.; Davies, A. M.; Volkov, Y.; Gun'ko, Y. K.; Kotov, N. A. *ACS Nano* **2008**, *2*, 928-938.
(98) Lin, S. J.; Zhao, Y.; Xia, T.; Meng, H.; Ji, Z. X.; Liu, R.; George, S.; Xiong, S. J.; Wang, X.; Zhang, H. Y.; Pokhrel, S.; Madler, L.; Damoiseaux, R.; Lin, S.; Nel, A. E. *ACS Nano* **2011**, *5*, 7284-7295.
(99) Harris, G.; Palosaari, T.; Magdolenova, Z.; Mennecozzi, M.; Gineste, J. M.; Saavedra, L.; Milcamps, A.; Huk, A.; Collins, A. R.; Dusinska, M.; Whelan, M. *Nanotoxicology* **2015**, *9*, 87-94.
(100) Anguissola, S.; Garry, D.; Salvati, A.; O'Brien, P. J.; Dawson, K. A. *PloS One* **2014**, *9*.
(101) Vanhecke, D.; Rodriguez-Lorenzo, L.; Clift, M. J. D.; Blank, F.; Petri-Fink, A.; Rothen-Rutishauser, B. *Nanomedicine-UK* **2014**, *9*, 1885-1900.
(102) Gunsolus, I. L.; Mousavi, M. P. S.; Hussein, K.; Buhlmann, P.; Haynes, C. L. *Environ. Sci. Technol.* **2015**, *49*, 8078-8086.
(103) SoRelle, E. D.; Liba, O.; Campbell, J. L.; Dalal, R.; Zavaleta, C. L.; de la Zerda, A. *ELife* **2016**, *5*.
(104) Estrela-Lopis, I.; Romero, G.; Rojas, E.; Moya, S. E.; Donath, E. *Journal of Physics: Conference Series* **2011**, *304*, 012017.
(105) Kann, B.; Offerhaus, H. L.; Windbergs, M.; Otto, C. *Adv. Drug. Deliver. Rev.* **2015**, *89*, 71-90.
(106) Lasne, D.; Blab, G. A.; Berciaud, S.; Heine, M.; Groc, L.; Choquet, D.; Cognet, L.; Lounis, B. *Biophys. J.* **2006**, *91*, 4598-4604.
(107) Park, J.; Park, H.; Ercius, P.; Pegoraro, A. F.; Xu, C.; Kim, J. W.; Han, S. H.; Weitz, D. A. *Nano Lett.* **2015**, 15, 4737-4744.
(108) Djurisic, A. B.; Leung, Y. H.; Ng, A. M. C.; Xu, X. Y.; Lee, P. K. H.; Degger, N.; Wu, R. S. S. *Small* **2015**, *11*, 26-44.

(109) Klein, N. D.; Hurley, K. R.; Feng, Z. V.; Haynes, C. L. *Anal. Chem.* **2015**, *87*, 4356-4362.
(110) van der Zwaag, D.; Vanparijs, N.; Wijnands, S.; De Rycke, R.; De Geest, B. G.; Albertazzi, L. *ACS Appl. Mater. Inter.* **2016**, *8*, 6391-6399.
(111) Gunsolus, I. L.; Hu, D. H.; Mihai, C.; Lohse, S. E.; Lee, C. S.; Torelli, M. D.; Hamers, R. J.; Murhpy, C. J.; Orr, G.; Haynes, C. L. *Analyst* **2014**, *139*, 3174-3178.
(112) Becker, J. S.; Zoriy, M.; Matusch, A.; Wu, B.; Salber, D.; Palm, C.; Becker, J. S. *Mass Spectrom. Rev.* **2010**, 29, 156-175.
(113) Elci, S. G.; Jiang, Y.; Yan, B.; Kim, S. T.; Saha, K.; Moyano, D. F.; Tonga, G. Y.; Jackson, L. C.; Rotello, V. M.; Vachet, R. W. *ACS Nano* **2016**, *10*, 5536-5542.
(114) Chughtai, K.; Heeren, R. M. A. *Chem. Rev.* **2010**, 110, 3237-3277.
(115) Chen, S. M.; Xiong, C. Q.; Liu, H. H.; Wan, Q. Q.; Hou, J.; He, Q.; Badu-Tawiah, A.; Nie, Z. X. *Nature Nanotech.* **2015**, *10*, 176-182.
(116) Hou, S.; Sikora, K. N.; Tang, R.; Liu, Y. C.; Lee, Y. W.; Kim, S. T.; Jiang, Z. W.; Vachet, R. W.; Rotello, V. M. *ACS Nano* **2016**, *10*, 6731-6736.
(117) Passarelli, M. K.; Newman, C. F.; Marshall, P. S.; West, A.; Gilmore, I. S.; Bunch, J.; Alexander, M. R.; Dollery, C. T. *Anal. Chem.* **2015**, *87*, 6696-6702.
(118) Hua, X.; Szymanski, C.; Wang, Z. Y.; Zhou, Y. F.; Ma, X.; Yu, J. C.; Evans, J.; Orr, G.; Liu, S. Q.; Zhu, Z. H.; Yu, X. Y. *Integr. Biol.-UK* **2016**, *8*, 635-644.
(119) Hua, X.; Li, H. W.; Long, Y. T. *Anal. Chem.* **2018**, *90*, 1072-1076.
(120) Veith, L.; Vennemann, A.; Breitenstein, D.; Engelhard, C.; Wiemann, M.; Hagenhoff, B. *Analyst* **2017**, *142*, 2631-2639.
(121) Le Trequesser, Q.; Deves, G.; Saez, G.; Daudin, L.; Barberet, P.; Michelet, C.; Delville, M. H.; Seznec, H. *Anal. Chem.* **2014**, *86*, 7311-7319.
(122) James, S. A.; Feltis, B. N.; de Jonge, M. D.; Sridhar, M.; Kimpton, J. A.; Altissimo, M.; Mayo, S.; Zheng, C. X.; Hastings, A.; Howard, D. L.; Paterson, D. J.; Wright, P. F. A.; Moorhead, G. F.; Turney, T. W.; Fu, J. *ACS Nano* **2013**, *7*, 10621-10635.
(123) Liu, Y. X.; Karsai, A.; Anderson, D. S.; Silva, R. M.; Uyeminami, D. L.; Van Winkle, L. S.; Pinkerton, K. E.; Liu, G. Y. *J. Phys. Chem. B* **2015**, *119*, 15118-15129.
(124) Marquis, B. J.; McFarland, A. D.; Braun, K. L.; Haynes, C. L. *Anal. Chem.* **2008**, *80*, 3431-3437.
(125) Marquis, B. J.; Maurer-Jones, M. A.; Braun, K. L.; Haynes, C. L. *Analyst* **2009**, *134*, 2293-2300.
(126) Love, S. A.; Haynes, C. L. *Anal. Bioanal. Chem.* **2010**, *398*, 677-688.
(127) Maurer-Jones, M. A.; Lin, Y. S.; Haynes, C. L. *ACS Nano* **2010**, *4*, 3363-3373.
(128) Marquis, B. J.; Liu, Z.; Braun, K. L.; Haynes, C. L. *Analyst* **2011**, 136, 3478-3486.
(129) Röttgermann, P. J. F.; Dawson, K. A.; Rädler, J. O. *Microarrays* **2016**, 5, 8.
(130) Armbrecht, L.; Dittrich, P. S. *Anal. Chem.* **2017**, *89*, 2-21.
(131) Bandura, D. R.; Baranov, V. I.; Ornatsky, O. I.; Antonov, A.; Kinach, R.; Lou, X. D.; Pavlov, S.; Vorobiev, S.; Dick, J. E.; Tanner, S. D. *Anal. Chem.* **2009**, 81, 6813-6822.
(132) Yang, Y. S. S.; Atukorale, P. U.; Moynihan, K. D.; Bekdemir, A.; Rakhra, K.; Tang, L.; Stellacci, F.; Irvine, D. J. *Nat. Commun.* **2017**, 8.
(133) Toduka, Y.; Toyooka, T.; Ibuki, Y. *Environ Sci. Technol.* **2012**, *46*, 7629-7636.
(134) Suzuki, H.; Toyooka, T.; Ibuki, Y. *Environ Sci. Technol.* **2007**, *41*, 3018-3024.

(135) Zucker, R. M.; Massaro, E. J.; Sanders, K. M.; Degn, L. L.; Boyes, W. K. *Cytom. Part A* **2010**, *77A*, 677-685.
(136) Kumar, A.; Pandey, A. K.; Singh, S. S.; Shanker, R.; Dhawan, A. *Cytom. Part A* **2011**, *79A*, 707-712.
(137) Pan, Y.; Neuss, S.; Leifert, A.; Fischler, M.; Wen, F.; Simon, U.; Schmid, G.; Brandau, W.; Jahnen-Dechent, W. *Small* **2007**, *3*, 1941-1949.
(138) Barteneva, N. S.; Fasler-Kan, E.; Vorobjev, I. A. *J. Histochem. Cytochem.* **2012**, *60*, 723-733.
(139) Vranic, S.; Boggetto, N.; Contremoulins, V.; Mornet, S.; Reinhardt, N.; Marano, F.; Baeza-Squiban, A.; Boland, S. *Part. Fibre Toxicol.* **2013**, *10*.
(140) Bonner, W. A.; Sweet, R. G.; Hulett, H. R.; Herzenberg, L. A. *Rev. Sci. Instrum.* **1972**, 43, 404-+.
(141) Mitchell, H. D.; Markillie, L. M.; Chrisler, W. B.; Gaffrey, M. J.; Hu, D. H.; Szymanski, C. J.; Xie, Y. M.; Melby, E. S.; Dohnalkova, A.; Taylors, R. C.; Grate, E. K.; Cooley, S. K.; McDermott, J. E.; Heredia-Langner, A.; Orr, G. *ACS Nano* **2016**, *10*, 10173-10185.
(142) Wang, D. J.; Bodovitz, S. *Trends Biotechnol.* **2010**, *28*, 281-290.
(143) Schwartzman, O.; Tanay, A. *Nat. Rev. Genet.* **2015**, *16*, 716-726.
(144) Monopoli, M. P.; Aberg, C.; Salvati, A.; Dawson, K. A. *Nature Nanotech.* **2012**, *7*, 779-786.
(145) Lowry, G. V.; Gregory, K. B.; Apte, S. C.; Lead, J. R. *Environ. Sci. Technol.* **2012**, *46*, 6893-6899.
(146) Ong, C. B.; Ng, L. Y.; Mohammad, A. W. *Renew. Sust. Energ. Rev.* **2018**, *81*, 536-551.
(147) Linic, S.; Aslam, U.; Boerigter, C.; Morabito, M. *Nat. Mater.* **2015**, *14*, 567-576.
(148) Pulido-Reyes, G.; Leganes, F.; Fernandez-Pinas, F.; Rosal, R. *Environ. Toxicol. Chem.* **2017**, *36*, 3181-3193.
(149) Ke, P. C.; Lin, S.; Parak, W. J.; Davis, T. P.; Caruso, F. *ACS Nano* **2017**, *11*, 11773-11776.
(150) Tenzer, S.; Docter, D.; Kuharev, J.; Musyanovych, A.; Fetz, V.; Hecht, R.; Schlenk, F.; Fischer, D.; Kiouptsi, K.; Reinhardt, C.; Landfester, K.; Schild, H.; Maskos, M.; Knauer, S. K.; Stauber, R. H. *Nature Nanotech.* **2013**, *8*, 772-U1000.
(151) Casals, E.; Pfaller, T.; Duschl, A.; Oostingh, G. J.; Puntes, V. *ACS Nano* **2010**, *4*, 3623-3632.
(152) Eigenheer, R.; Castellanos, E. R.; Nakamoto, M. Y.; Gerner, K. T.; Lampe, A. M.; Wheeler, K. E. *Environ. Sci. Nano* **2014**, 1, 238-247.
(153) Vilanova, O.; Mittag, J. J.; Kelly, P. M.; Milani, S.; Dawson, K. A.; Radler, J. O.; Franzese, G. *ACS Nano* **2016**, *10*, 10842-10850.
(154) Dominguez-Medina, S.; McDonough, S.; Swanglap, P.; Landes, C. F.; Link, S. *Langmuir* **2012**, *28*, 9131-9139.
(155) Cedervall, T.; Lynch, I.; Lindman, S.; Berggard, T.; Thulin, E.; Nilsson, H.; Dawson, K. A.; Linse, S. *P. Natl. Acad. Sci. USA* **2007**, *104*, 2050-2055.
(156) Del Pino, P.; Pelaz, B.; Zhang, Q.; Maffre, P.; Nienhaus, G. U.; Parak, W. J. *Mater. Horizons* **2014**, *1*, 301-313.
(157) Mudunkotuwa, I. A.; Al Minshid, A.; Grassian, V. H. *Analyst* **2014**, *139*, 870-881.

(158) Tsai, D. H.; DelRio, F. W.; Keene, A. M.; Tyner, K. M.; MacCuspie, R. I.; Cho, T. J.; Zachariah, M. R.; Hackley, V. A. *Langmuir* **2011**, *27*, 2464-2477.
(159) Givens, B. E.; Xu, Z. Z.; Fiegel, J.; Grassian, V. H. *J. Coll. Interface Sci.* **2017**, *493*, 334-341.
(160) Lehman, S. E.; Mudunkotuwa, I. A.; Grassian, V. H.; Larsen, S. C. *Langmuir* **2016**, *32*, 731-742.
(161) Shukla, N.; Liu, C.; Jones, P. M.; Weller, D. *J. Magn. Magn. Mater.* **2003**, *266*, 178-184.
(162) Yoon, S. Y.; Lee, C. G.; Park, J. A.; Kim, J. H.; Kim, S. B.; Lee, S. H.; Choi, J. W. *Chem. Eng. J.* **2014**, *236*, 341-347.
(163) Bonifacio, A.; Dalla Marta, S.; Spizzo, R.; Cervo, S.; Steffan, A.; Colombatti, A.; Sergo, V. *Anal. Bioanal. Chem.* **2014**, *406*, 2355-2365.
(164) Treuel, L.; Malissek, M.; Grass, S.; Diendorf, J.; Mahl, D.; Meyer-Zaika, W.; Epple, M. *Journal of Nanoparticle Research* **2012**, *14*.
(165) Bhaumik, A.; Shearin, A. M.; Delong, R.; Wanekaya, A.; Ghosh, K. *J. Phys. Chem. C* **2014**, *118*, 18631-18639.
(166) Smith, A. M.; Marbella, L. E.; Johnston, K. A.; Hartmann, M. J.; Crawford, S. E.; Kozycz, L. M.; Seferos, D. S.; Millstone, J. E. *Anal. Chem.* **2015**, 87, 2771-2778.
(167) Johnston, K. A.; Smith, A. M.; Marbella, L. E.; Millstone, J. E. *Langmuir* **2016**, 32, 3820-3826.
(168) Wang, A. L.; Vangala, K.; Vo, T.; Zhang, D. M.; Fitzkee, N. C. *J. Phys. Chem. C* **2014**, *118*, 8134-8142.
(169) Ceccon, A.; Tugarinov, V.; Box, A.; Clore, G. M. *J. Am. Chem. Soc.* **2016**, *138*, 5789-5792.
(170) Guo, C. C.; Holland, G. P. *J. Phys. Chem. C* **2015**, 119, 25663-25672.
(171) Marbella, L. E.; Crawford, S. E.; Hartmann, M. J.; Millstone, J. E. *Chem. Comm.* **2016**, 52, 9020-9023.
(172) Chan, Y. H. M.; Boxer, S. G. *Curr. Opin. Chem. Biol.* **2007**, *11*, 581-587.
(173) Rascol, E.; Devoisselle, J. M.; Chopineau, J. *Nanoscale* **2016**, *8*, 4780-4798.
(174) Moghadam, B. Y.; Hou, W. C.; Corredor, C.; Westerhoff, P.; Posner, J. D. *Langmuir* **2012**, *28*, 16318-16326.
(175) Van Lehn, R. C.; Atukorale, P. U.; Carney, R. P.; Yang, Y. S.; Stellacci, F.; Irvine, D. J.; Alexander-Katz, A. *Nano Lett.* **2013**, *13*, 4060-4067.
(176) Zheng, Z.; Saar, J.; Zhi, B.; Qiu, T. A.; Gallagher, M. J.; Fairbrother, D. H.; Haynes, C. L.; Lienkamp, K.; Rosenzweig, Z. *Langmuir* **2018**, 34, 4614-4625.
(177) Williams, D. N.; Pramanik, S.; Brown, R. M.; McIntire, E.; Bo, Z.; Haynes, C. L.; Rosenzweig, Z. *Submitted* **2018**.
(178) Carney, R. P.; Astier, Y.; Carney, T. M.; Voitchovsky, K.; Silva, P. H. J.; Stellacci, F. *ACS Nano* **2013**, *7*, 932-942.
(179) Liu, X. T.; Chen, K. L. *Langmuir* **2015**, *31*, 12076-12086.
(180) Bailey, C. M.; Kamaloo, E.; Waterman, K. L.; Wang, K. F.; Nagarajan, R.; Camesano, T. A. *Biophys. Chem.* **2015**, *203*, 51-61.
(181) Melby, E. S.; Mensch, A. C.; Lohse, S. E.; Hu, D. H.; Orr, G.; Murphy, C. J.; Hamers, R. J.; Pedersen, J. A. *Environ. Sci. Nano* **2016**, *3*, 45-55.

(182) Lu, B.; Smith, T.; Schmidt, J. J. *Nanoscale* **2015**, *7*, 7858-7866.
(183) Hu, P. P.; Qian, W.; Liu, B.; Pichan, C.; Chen, Z. *J. Phys. Chem. C* **2016**, *120*, 22718-22729.
(184) Wang, T.; Feng, Z.; Wang, C.; He, N. *Colloids and Surfaces B: Biointerfaces* **2018**, *164*, 70-77.
(185) Troiano, J. M.; Olenick, L. L.; Kuech, T. R.; Melby, E. S.; Hu, D. H.; Lohse, S. E.; Mensch, A. C.; Dogangun, M.; Vartanian, A. M.; Torelli, M. D.; Ehimiaghe, E.; Walter, S. R.; Fu, L.; Anderton, C. R.; Zhu, Z. H.; Wang, H. F.; Orr, G.; Murphy, C. J.; Hamers, R. J.; Pedersen, J. A.; Geiger, F. M. *J. Phys. Chem. C* **2015**, *119*, 534-546.
(186) Wang, T. T.; Bai, J.; Jiang, X.; Nienhaus, G. U. *ACS Nano* **2012**, *6*, 1251-1259.
(187) Van Lehn, R. C.; Ricci, M.; Silva, P. H. J.; Andreozzi, P.; Reguera, J.; Voitchovsky, K.; Stellacci, F.; Alexander-Katz, A. *Nat. Commun.* **2014**, *5*.

Chapter 2

(1) Fu, G. F.; Vary, P. S.; Lin, C. T. *Journal of Physical Chemistry B* **2005**, *109*, 8889-8898.
(2) Perelshtein, I.; Applerot, G.; Perkas, N.; Grinblat, J.; Gedanken, A. *Chem-Eur J* **2012**, *18*, 4575-4582.
(3) Wang, Z. B.; Li, G. C.; Peng, H. R.; Zhang, Z. K.; Wang, X. *J Mater Sci* **2005**, *40*, 6433-6438.
(4) Sharma, V. K. *J Environ Sci Heal A* **2009**, *44*, 1485-1495.
(5) Manzo, S.; Buono, S.; Rametta, G.; Miglietta, M.; Schiavo, S.; Di Francia, G. *Environ Sci Pollut R* **2015**, *22*, 15941-15951.
(6) Ma, H. B.; Brennan, A.; Diamond, S. A. *Environmental Toxicology and Chemistry* **2012**, *31*, 1621-1629.
(7) Bar-Ilan, O.; Louis, K. M.; Yang, S. P.; Pedersen, J. A.; Hamers, R. J.; Peterson, R. E.; Heideman, W. *Nanotoxicology* **2012**, *6*, 670-679.
(8) Kaegi, R.; Ulrich, A.; Sinnet, B.; Vonbank, R.; Wichser, A.; Zuleeg, S.; Simmler, H.; Brunner, S.; Vonmont, H.; Burkhardt, M.; Boller, M. *Environmental pollution* **2008**, *156*, 233-239.
(9) Kiser, M. A.; Westerhoff, P.; Benn, T.; Wang, Y.; Perez-Rivera, J.; Hristovski, K. *Environmental science & technology* **2009**, *43*, 6757-6763.
(10) Menard, A.; Drobne, D.; Jemec, A. *Environmental pollution* **2011**, *159*, 677-684.
(11) Robichaud, C. O.; Uyar, A. E.; Darby, M. R.; Zucker, L. G.; Wiesner, M. R. *Environmental science & technology* **2009**, *43*, 4227-4233.
(12) Wiesner, M. R.; Lowry, G. V.; Alvarez, P.; Dionysiou, D.; Biswas, P. *Environmental science & technology* **2006**, *40*, 4336-4345.
(13) Adam, V.; Loyaux-Lawniczak, S.; Quaranta, G. *Environ Sci Pollut R* **2015**, *22*, 11175-11192.
(14) Semenzin, E.; Lanzellotto, E.; Hristozov, D.; Critto, A.; Zabeo, A.; Giubilato, E.; Marcomini, A. *Environmental Toxicology and Chemistry* **2015**, *34*, 2644-2659.
(15) Tong, T. Z.; Binh, C. T. T.; Kelly, J. J.; Gaillard, J. F.; Gray, K. A. *Water Research* **2013**, *47*, 2352-2362.

(16) Kuhn, K. P.; Chaberny, I. F.; Massholder, K.; Stickler, M.; Benz, V. W.; Sonntag, H. G.; Erdinger, L. *Chemosphere* **2003**, *53*, 71-77.
(17) Kim, S. W.; An, Y. J. *Applied Microbiology and Biotechnology* **2012**, *95*, 243-253.
(18) Li, Y.; Zhang, W.; Niu, J. F.; Chen, Y. S. *Acs Nano* **2012**, *6*, 5164-5173.
(19) Hau, H. H.; Gralnick, J. A. *Annual Review of Microbiology* **2007**, *61*, 237-258.
(20) Heidelberg, J. F.; Paulsen, I. T.; Nelson, K. E.; Gaidos, E. J.; Nelson, W. C.; Read, T. D.; Eisen, J. A.; Seshadri, R.; Ward, N.; Methe, B.; Clayton, R. A.; Meyer, T.; Tsapin, A.; Scott, J.; Beanan, M.; Brinkac, L.; Daugherty, S.; DeBoy, R. T.; Dodson, R. J.; Durkin, A. S.; Haft, D. H.; Kolonay, J. F.; Madupu, R.; Peterson, J. D.; Umayam, L. A.; White, O.; Wolf, A. M.; Vamathevan, J.; Weidman, J.; Impraim, M.; Lee, K.; Berry, K.; Lee, C.; Mueller, J.; Khouri, H.; Gill, J.; Utterback, T. R.; McDonald, L. A.; Feldblyum, T. V.; Smith, H. O.; Venter, J. C.; Nealson, K. H.; Fraser, C. M. *Nature biotechnology* **2002**, *20*, 1118-1123.
(21) Beliaev, A. S.; Thompson, D. K.; Khare, T.; Lim, H.; Brandt, C. C.; Li, G.; Murray, A. E.; Heidelberg, J. F.; Giometti, C. S.; Yates, J., 3rd; Nealson, K. H.; Tiedje, J. M.; Zhoui, J. *Omics : a journal of integrative biology* **2002**, *6*, 39-60.
(22) Bencheikh-Latmani, R.; Williams, S. M.; Haucke, L.; Criddle, C. S.; Wu, L. Y.; Zhou, J. Z.; Tebo, B. M. *Applied and Environmental Microbiology* **2005**, *71*, 7453-7460.
(23) Chourey, K.; Thompson, M. R.; Morrell-Falvey, J.; VerBerkmoes, N. C.; Brown, S. D.; Shah, M.; Zhou, J. Z.; Doktycz, M.; Hettich, R. L.; Thompson, D. K. *Applied and Environmental Microbiology* **2006**, *72*, 6331-6344.
(24) Leaphart, A. B.; Thompson, D. K.; Huang, K.; Alm, E.; Wan, X. F.; Arkin, A.; Brown, S. D.; Wu, L.; Yan, T.; Liu, X.; Wickham, G. S.; Zhou, J. *Journal of bacteriology* **2006**, *188*, 1633-1642.
(25) Maurer-Jones, M. A.; Gunsolus, I. L.; Meyer, B. M.; Christenson, C. J.; Haynes, C. L. *Analytical chemistry* **2013**, *85*, 5810-5818.
(26) Wu, B.; Zhuang, W. Q.; Sahu, M.; Biswas, P.; Tang, Y. J. *The Science of the total environment* **2011**, *409*, 4635-4639.
(27) Wu, B.; Huang, R.; Sahu, M.; Feng, X. Y.; Biswas, P.; Tang, Y. J. *Science of the Total Environment* **2010**, *408*, 1755-1758.
(28) Reeves, J. F.; Davies, S. J.; Dodd, N. J. F.; Jha, A. N. *Mutation Research/Fundamental and Molecular Mechanisms of Mutagenesis* **2008**, *640*, 113-122.
(29) Xue, C.; Wu, J.; Lan, F.; Liu, W.; Yang, X.; Zeng, F.; Xu, H. *J Nanosci Nanotechnol* **2010**, *10*, 8500-8507.
(30) Maurer-Jones, M. A.; Christenson, J. R.; Haynes, C. L. *Journal of Nanoparticle Research* **2012**, *14*.
(31) Chen, X.; Mao, S. S. *Chemical reviews* **2007**, *107*, 2891-2959.
(32) Cabiscol, E.; Tamarit, J.; Ros, J. *International microbiology : the official journal of the Spanish Society for Microbiology* **2000**, *3*, 3-8.
(33) Brutinel, E. D.; Gralnick, J. A. *Applied Microbiology and Biotechnology* **2012**, *93*, 41-48.
(34) Marsili, E.; Baron, D. B.; Shikhare, I. D.; Coursolle, D.; Gralnick, J. A.; Bond, D. R. *P Natl Acad Sci USA* **2008**, *105*, 3968-3973.
(35) Grzelak, A.; Rychlik, B.; Baptosz, G. *Free Radical Bio Med* **2001**, *30*, 1418-1425.

(36) Kubacka, A.; Diez, M. S.; Rojo, D.; Bargiela, R.; Ciordia, S.; Zapico, I.; Albar, J. P.; Barbas, C.; dos Santos, V. A. P. M.; Fernandez-Garcia, M.; Ferrer, M. *Sci Rep-Uk* **2014**, *4*.
(37) Park, H.-G.; Yeo, M.-K. *Mol Cell Toxicol* **2013**, *9*, 129-139.
(38) Rocheleau, S.; Arbour, M.; Elias, M.; Sunahara, G. I.; Masson, L. *Nanotoxicology* **2015**, *9*, 502-512.
(39) Sohm, B.; Immel, F.; Bauda, P.; Pagnout, C. *PROTEOMICS* **2015**, *15*, 98-113.
(40) Klaper, R.; Crago, J.; Barr, J.; Arndt, D.; Setyowati, K.; Chen, J. *Environmental pollution* **2009**, *157*, 1152-1156.
(41) Higashisaka, K.; Yoshioka, Y.; Yamashita, K.; Morishita, Y.; Fujimura, M.; Nabeshi, H.; Nagano, K.; Abe, Y.; Kamada, H.; Tsunoda, S.; Yoshikawa, T.; Itoh, N.; Tsutsumi, Y. *Biomaterials* **2011**, *32*, 3-9.
(42) Choi, O.; Hu, Z. Q. *Environmental science & technology* **2008**, *42*, 4583-4588.
(43) von Moos, N.; Slaveykova, V. I. *Nanotoxicology* **2014**, *8*, 605-630.
(44) Petkovic, J.; Zegura, B.; Stevanovic, M.; Drnovsek, N.; Uskokovic, D.; Novak, S.; Filipic, M. *Nanotoxicology* **2011**, *5*, 341-353.
(45) Qiu, T. A.; Bozich, J. S.; Lohse, S. E.; Vartanian, A. M.; Jacob, L. M.; Meyer, B. M.; Gunsolus, I. L.; Niemuth, N. J.; Murphy, C. J.; Haynes, C. L.; Klaper, R. D. *Environ-Sci Nano* **2015**, *2*, 615-629.
(46) Lee, S. H.; Pie, J. E.; Kim, Y. R.; Lee, H. R.; Son, S. W.; Kim, M. K. *Mol Cell Toxicol* **2012**, *8*, 113-118.
(47) Cui, Y.; Zhao, Y. Y.; Tian, Y.; Zhang, W.; Lu, X. Y.; Jiang, X. Y. *Biomaterials* **2012**, *33*, 2327-2333.
(48) Zhao, S.; Fernald, R. D. *J Comput Biol* **2005**, *12*, 1047-1064.
(49) Schmittgen, T. D.; Livak, K. J. *Nat. Protocols* **2008**, *3*, 1101-1108.
(50) Isley, S. L.; Penn, R. L. *J Phys Chem C* **2008**, *112*, 4469-4474.
(51) French, R. A.; Jacobson, A. R.; Kim, B.; Isley, S. L.; Penn, R. L.; Baveye, P. C. *Environmental science & technology* **2009**, *43*, 1354-1359.
(52) Motulsky, H. J.; Brown, R. E. *Bmc Bioinformatics* **2006**, *7*.
(53) Bilski, P.; Belanger, A. G.; Chignell, C. F. *Free Radical Bio Med* **2002**, *33*, 938-946.
(54) Dias, C. F. B.; Araujo-Chaves, J. C.; Mugnol, K. C. U.; Trindade, F. J.; Alves, O. L.; Caires, A. C. F.; Brochsztain, S.; Crespilho, F. N.; Matos, J. R.; Nascimento, O. R.; Nantes, I. L. *Rsc Adv* **2012**, *2*, 7417-7426.
(55) Ahmad, I.; Fasihullah, Q.; Vaid, F. H. M. *J Photoch Photobio B* **2006**, *82*, 21-27.
(56) de la Rochette, A.; Silva, E.; Birlouez-Aragon, I.; Mancini, M.; Edwards, A. M.; Morliere, P. *Photochemistry and photobiology* **2000**, *72*, 815-820.
(57) Kim, H. J.; Park, H. S.; Hyun, M. S.; Chang, I. S.; Kim, M.; Kim, B. H. *Enzyme and Microbial Technology* **2002**, *30*, 145-152.
(58) Kathiravan, A.; Renganathan, R. *Spectrochimica Acta Part A: Molecular and Biomolecular Spectroscopy* **2008**, *71*, 1080-1083.
(59) Shinohara, H.; Gratzel, M.; Vlachopoulos, N.; Aizawa, M. *Bioelectroch Bioener* **1991**, *26*, 307-320.
(60) Qiu, X. Y.; Sundin, G. W.; Wu, L. Y.; Zhou, J. Z.; Tiedje, J. M. *Journal of bacteriology* **2005**, *187*, 3556-3564.

(61) Jiang, Y. M.; Dong, Y. Y.; Luo, Q. X.; Li, N.; Wu, G. F.; Gao, H. C. *Journal of bacteriology* **2014**, *196*, 445-458.
(62) Farr, S. B.; Kogoma, T. *Microbiol Rev* **1991**, *55*, 561-585.
(63) Thormann, K. M.; Duttler, S.; Saville, R. M.; Hyodo, M.; Shukla, S.; Hayakawa, Y.; Spormann, A. M. *Journal of bacteriology* **2006**, *188*, 2681-2691.
(64) Thormann, K. M.; Saville, R. M.; Shukla, S.; Pelletier, D. A.; Spormann, A. M. *Journal of bacteriology* **2004**, *186*, 8096-8104.
(65) Godeke, J.; Paul, K.; Lassak, J.; Thormann, K. M. *Isme J* **2011**, *5*, 613-626.
(66) Rakshe, S.; Leff, M.; Spormann, A. M. *Appl Environ Microbiol* **2011**, *77*, 2196-2198.
(67) Darwin, A. J. *Molecular microbiology* **2005**, *57*, 621-628.
(68) Weiner, L.; Brissette, J. L.; Model, P. *Genes & Development* **1991**, *5*, 1912-1923.
(69) Maxson, M. E.; Darwin, A. J. *Molecular microbiology* **2006**, *59*, 1610-1623.
(70) Aussel, L.; Barre, F. X.; Aroyo, M.; Stasiak, A.; Stasiak, A. Z.; Sherratt, D. *Cell* **2002**, *108*, 195-205.
(71) Coursolle, D.; Baron, D. B.; Bond, D. R.; Gralnick, J. A. *Journal of bacteriology* **2010**, *192*, 467-474.
(72) Covington, E. D.; Gelbmann, C. B.; Kotloski, N. J.; Gralnick, J. A. *Molecular microbiology* **2010**, *78*, 519-532.
(73) Beliaev, A. S.; Klingeman, D. M.; Klappenbach, J. A.; Wu, L.; Romine, M. F.; Tiedje, J. A.; Nealson, K. H.; Fredrickson, J. K.; Zhou, J. *Journal of bacteriology* **2005**, *187*, 7138-7145.
(74) Steuber, J. *Bba-Bioenergetics* **2001**, *1505*, 45-56.
(75) Horst, A. M.; Ji, Z. X.; Holden, P. A. *Journal of Nanoparticle Research* **2012**, *14*.

Chapter 3

(1) Arico, A. S.; Bruce, P.; Scrosati, B.; Tarascon, J.-M.; van Schalkwijk, W. *Nat Mater* **2005**, *4*, 366-377.
(2) Xie, J.; Liu, G.; Eden, H. S.; Ai, H.; Chen, X. *Accounts of chemical research* **2011**, *44*, 883-892.
(3) Pendergast, M. M.; Hoek, E. M. V. *Energ Environ Sci* **2011**, *4*, 1946-1971.
(4) Nel, A.; Xia, T.; Madler, L.; Li, N. *Science* **2006**, *311*, 622-627.
(5) Pan, Y.; Neuss, S.; Leifert, A.; Fischler, M.; Wen, F.; Simon, U.; Schmid, G.; Brandau, W.; Jahnen-Dechent, W. *Small* **2007**, *3*, 1941-1949.
(6) Albanese, A.; Tang, P. S.; Chan, W. C. *Annual review of biomedical engineering* **2012**, *14*, 1-16.
(7) Arndt, D. A.; Moua, M.; Chen, J.; Klaper, R. D. *Environmental science & technology* **2013**, *47*, 9444-9452.
(8) Klaper, R.; Arndt, D.; Setyowati, K.; Chen, J.; Goetz, F. *Aquatic toxicology* **2010**, *100*, 211-217.
(9) Klaper, R.; Crago, J.; Barr, J.; Arndt, D.; Setyowati, K.; Chen, J. *Environmental Pollution* **2009**, *157*, 1152-1156.
(10) Chithrani, B. D.; Ghazani, A. A.; Chan, W. C. *Nano letters* **2006**, *6*, 662-668.
(11) Yang, H.; Liu, C.; Yang, D.; Zhang, H.; Xi, Z. *Journal of applied Toxicology* **2009**, *29*, 69-78.

(12) Aillon, K. L.; Xie, Y.; El-Gendy, N.; Berkland, C. J.; Forrest, M. L. *Advanced drug delivery reviews* **2009**, *61*, 457-466.
(13) Bozich, J. S.; Lohse, S. E.; Torelli, M. D.; Murphy, C. J.; Hamers, R. J.; Klaper, R. D. *Environmental Science: Nano* **2014**, *1*, 260-270.
(14) El Badawy, A. M.; Silva, R. G.; Morris, B.; Scheckel, K. G.; Suidan, M. T.; Tolaymat, T. M. *Environmental science & technology* **2010**, *45*, 283-287.
(15) He, C.; Hu, Y.; Yin, L.; Tang, C.; Yin, C. *Biomaterials* **2010**, *31*, 3657-3666.
(16) Schaeublin, N. M.; Braydich-Stolle, L. K.; Schrand, A. M.; Miller, J. M.; Hutchison, J.; Schlager, J. J.; Hussain, S. M. *Nanoscale* **2011**, *3*, 410-420.
(17) Verma, A.; Stellacci, F. *Small* **2010**, *6*, 12-21.
(18) Dominguez, G. A.; Lohse, S. E.; Torelli, M. D.; Murphy, C. J.; Hamers, R. J.; Orr, G.; Klaper, R. D. *Aquatic Toxicology* **2015**, *162*, 1-9.
(19) Albanese, A.; Chan, W. C. W. *Acs Nano* **2011**, *5*, 5478-5489.
(20) Lewinski, N.; Colvin, V.; Drezek, R. *small* **2008**, *4*, 26-49.
(21) Khlebtsov, N.; Dykman, L. *Chemical Society Reviews* **2011**, *40*, 1647-1671.
(22) Lam, C.-w.; James, J. T.; McCluskey, R.; Arepalli, S.; Hunter, R. L. *CRC Critical Reviews in Toxicology* **2006**, *36*, 189-217.
(23) Fröhlich, E. *International journal of nanomedicine* **2012**, *7*, 5577.
(24) Sohaebuddin, S. K.; Thevenot, P. T.; Baker, D.; Eaton, J. W.; Tang, L. *Particle and fibre toxicology* **2010**, *7*, 22.
(25) Heinlaan, M.; Ivask, A.; Blinova, I.; Dubourguier, H.-C.; Kahru, A. *Chemosphere* **2008**, *71*, 1308-1316.
(26) Sanderson, H.; Thomsen, M. *Bulletin of environmental contamination and toxicology* **2007**, *79*, 331-335.
(27) Moore, D. R.; Breton, R. L.; MacDonald, D. B. *Environmental Toxicology and chemistry* **2003**, *22*, 1799-1809.
(28) Shvedova, A. A.; Pietroiusti, A.; Fadeel, B.; Kagan, V. E. *Toxicology and applied pharmacology* **2012**, *261*, 121-133.
(29) Marquis, B. J.; Love, S. A.; Braun, K. L.; Haynes, C. L. *Analyst* **2009**, *134*, 425-439.
(30) Manke, A.; Wang, L.; Rojanasakul, Y. *BioMed research international* **2013**, *2013*.
(31) Park, E. J.; Park, K. *Toxicology letters* **2009**, *184*, 18-25.
(32) Klaper, R.; Arndt, D.; Bozich, J.; Dominguez, G. *Analyst* **2014**, *139*, 882-895.
(33) Gottschalk, F.; Sonderer, T.; Scholz, R. W.; Nowack, B. *Environmental science & technology* **2009**, *43*, 9216-9222.
(34) Valavanidis, A.; Vlahogianni, T.; Dassenakis, M.; Scoullos, M. *Ecotoxicology and environmental safety* **2006**, *64*, 178-189.
(35) Franco, R.; Sanchez-Olea, R.; Reyes-Reyes, E. M.; Panayiotidis, M. I. *Mutat Res-Gen Tox En* **2009**, *674*, 3-22.
(36) Finkel, T.; Holbrook, N. J. *Nature* **2000**, *408*, 239-247.
(37) Ryan, J.; Hightower, L. In *Stress-Inducible Cellular Responses*; Springer, 1996, pp 411-424.
(38) Kilty, C. G.; Keenan, J.; Shaw, M. **2007**.
(39) Eason, C.; O'Halloran, K. *Toxicology* **2002**, *181*, 517-521.

(40) Niemuth, N. J.; Jordan, R.; Crago, J.; Blanksma, C.; Johnson, R.; Klaper, R. D. *Environmental Toxicology and Chemistry* **2014**.
(41) Ankley, G. T.; Jensen, K. M.; Kahl, M. D.; Korte, J. J.; Makynen, E. A. *Environmental Toxicology and Chemistry* **2001**, *20*, 1276-1290.
(42) Johns, S. M.; Kane, M. D.; Denslow, N. D.; Watanabe, K. H.; Orlando, E. F.; Villeneuve, D. L.; Ankley, G. T.; Sepúlveda, M. S. *Environmental Toxicology and Chemistry* **2009**, *28*, 873-880.
(43) Garvey, J. S. In *Preprints of Papers Presented at National Meeting, Division of Water, Air and Waste Chemistry, American Chemical Society;(USA)*, 1988.
(44) Fischbach, M.; Sabbioni, E.; Bromley, P. *Cell biology and toxicology* **1993**, *9*, 177-188.
(45) Hau, H. H.; Gralnick, J. A. *Annu. Rev. Microbiol.* **2007**, *61*, 237-258.
(46) Gulati, R. *Hydrobiologia* **1978**, *59*, 101-112.
(47) Jana, N. R.; Gearheart, L.; Murphy, C. J. *Langmuir* **2001**, *17*, 6782-6786.
(48) Sau, T. K.; Murphy, C. J. *Journal of the American Chemical Society* **2004**, *126*, 8648-8649.
(49) Giljohann, D. A.; Seferos, D. S.; Daniel, W. L.; Massich, M. D.; Patel, P. C.; Mirkin, C. A. *Angewandte Chemie International Edition* **2010**, *49*, 3280-3294.
(50) Sweeney, S. F.; Woehrle, G. H.; Hutchison, J. E. *Journal of the American Chemical Society* **2006**, *128*, 3190-3197.
(51) Yang, J. A.; Lohse, S. E.; Murphy, C. J. *Small* **2014**, *10*, 1642-1651.
(52) Ackerson, C. J.; Jadzinsky, P. D.; Kornberg, R. D. *Journal of the American Chemical Society* **2005**, *127*, 6550-6551.
(53) Torelli, M. D.; Putans, R. A.; Tan, Y.; Lohse, S. E.; Murphy, C. J.; Hamers, R. J. *Acs Appl Mater Inter* **2015**, *7*, 1720-1725.
(54) EPA, Standard operating procedure for moderately hard reconstituted water; SoBran: Dayton, OH, USA, 2003.
(55) Zhao, S.; Fernald, R. D. *Journal of computational biology* **2005**, *12*, 1047-1064.
(56) Heckmann, L.-H.; Sorensen, P.; Krogh, P.; Sorensen, J. *BMC Bioinformatics* **2011**, *12*, 250.
(57) Wang, S.; Lu, W.; Tovmachenko, O.; Rai, U. S.; Yu, H.; Ray, P. C. *Chem Phys Lett* **2008**, *463*, 145-149.
(58) Rice, P. A.; Iglewski, B. H. *Rev Infect Dis* **1988**, *10*, S277-S278.
(59) Martínez-Palomo, A. In *International Review of Cytology*, G.H. Bourne, J. F. D.; Jeon, K. W., Eds.; Academic Press, 1970, pp 29-75.
(60) Goodman, C. M.; McCusker, C. D.; Yilmaz, T.; Rotello, V. M. *Bioconjugate Chemistry* **2004**, *15*, 897-900.
(61) Feng, Z. V.; Gunsolus, I. L.; Qiu, T. A.; Hurley, K. R.; Nyberg, L. H.; Frew, H.; Johnson, K. P.; Vartanian, A. M.; Jacob, L. M.; Lohse, S. E. *Chem Sci* **2015**.
(62) Jacobson, K. H.; Gunsolus, I. L.; Kuech, T. R.; Troiano, J. M.; Melby, E. S.; Lohse, S. E.; Hu, D.; Chrisler, W. B.; Murphy, C. J.; Orr, G.; Geiger, F. M.; Haynes, C. L.; Pedersen, J. A. *Environ. Sci. Technol.* **2015**, *49*, 10642-10650.
(63) Zhao, Y. Y.; Tian, Y.; Cui, Y.; Liu, W. W.; Ma, W. S.; Jiang, X. Y. *Journal of the American Chemical Society* **2010**, *132*, 12349-12356.

(64) Dalai, S.; Pakrashi, S.; Kumar, R. S.; Chandrasekaran, N.; Mukherjee, A. *Toxicology Research* **2012**, *1*, 116-130.
(65) Kumar, A.; Pandey, A. K.; Singh, S. S.; Shanker, R.; Dhawan, A. *Chemosphere* **2011**, *83*, 1124-1132.
(66) Schwerin, S.; Zeis, B.; Lamkemeyer, T.; Paul, R. J.; Koch, M.; Madlung, J.; Fladerer, C.; Pirow, R. *BMC physiology* **2009**, *9*, 8.
(67) Ehrenberg, M.; McGrath, J. L. *Acta Biomaterialia* **2005**, *1*, 305-315.
(68) Ruenraroengsak, P.; Florence, A. T. *Journal of drug targeting* **2010**, *18*, 803-811.
(69) Walker, V. G.; Li, Z.; Hulderman, T.; Schwegler-Berry, D.; Kashon, M. L.; Simeonova, P. P. *Toxicology and applied pharmacology* **2009**, *236*, 319-328.
(70) Mironava, T.; Hadjiargyrou, M.; Simon, M.; Jurukovski, V.; Rafailovich, M. H. *Nanotoxicology* **2010**, *4*, 120-137.
(71) Farr, S. B.; Kogoma, T. *Microbiological reviews* **1991**, *55*, 561-585.
(72) Chourey, K.; Thompson, M. R.; Morrell-Falvey, J.; VerBerkmoes, N. C.; Brown, S. D.; Shah, M.; Zhou, J.; Doktycz, M.; Hettich, R. L.; Thompson, D. K. *Applied and environmental microbiology* **2006**, *72*, 6331-6344.
(73) Ivask, A.; Suarez, E.; Patel, T.; Boren, D.; Ji, Z.; Holden, P.; Telesca, D.; Damoiseaux, R.; Bradley, K. A.; Godwin, H. *Environmental science & technology* **2012**, *46*, 2398-2405.
(74) Paul, B. J.; Ross, W.; Gaal, T.; Gourse, R. L. *Annual Review of Genetics* **2004**, *38*, 749-770.
(75) Crawford, D. R.; Wang, Y. H.; Schools, G. P.; Kochheiser, J.; Davies, K. J. A. *Free Radical Bio Med* **1997**, *22*, 551-559.
(76) Basturea, G. N.; Zundel, M. A.; Deutscher, M. P. *RNA* **2011**, *17*, 338-345.
(77) Hsu, D.; Shih, L.-M.; Zee, Y. C. *Journal of bacteriology* **1994**, *176*, 4761-4765.
(78) Deutscher, M. P. *Nucleic Acids Research* **2006**, *34*, 659-666.
(79) Kuwano, M.; Taniguchi, H.; Ono, M.; Endo, H.; Ohnishi, Y. *Biochem Bioph Res Co* **1977**, *75*, 156-162.
(80) Darzynkiewicz, Z.; Bruno, S.; Delbino, G.; Gorczyca, W.; Hotz, M. A.; Lassota, P.; Traganos, F. *Cytometry* **1992**, *13*, 795-808.
(81) Brown, S. D.; Thompson, M. R.; VerBerkmoes, N. C.; Chourey, K.; Shah, M.; Zhou, J. Z.; Hettich, R. L.; Thompson, D. K. *Mol Cell Proteomics* **2006**, *5*, 1054-1071.
(82) Chourey, K.; Thompson, M. R.; Morrell-Falvey, J.; VerBerkmoes, N. C.; Brown, S. D.; Shah, M.; Zhou, J. Z.; Doktycz, M.; Hettich, R. L.; Thompson, D. K. *Applied and Environmental Microbiology* **2006**, *72*, 6331-6344.

Chapter 4

(1) Bruening, M. L.; Dotzauer, D. M.; Jain, P.; Ouyang, L.; Baker, G. L. *Langmuir* **2008**, *24*, 7663-7673.
(2) Gentile, P.; Carmagnola, I.; Nardo, T.; Chiono, V. *Nanotechnology* **2015**, *26*.
(3) Richardson, J. J.; Bjornmalm, M.; Caruso, F. *Science* **2015**, *348*.
(4) Rydzek, G.; Ji, Q. M.; Li, M.; Schaaf, P.; Hill, J. P.; Boulmedais, F.; Ariga, K. *Nano Today* **2015**, *10*, 138-167.

(5) Elbakry, A.; Zaky, A.; Liebkl, R.; Rachel, R.; Goepferich, A.; Breunig, M. *Nano Lett.* **2009**, *9*, 2059-2064.
(6) Sivapalan, S. T.; DeVetter, B. M.; Yang, T. K.; Schulmerich, M. V.; Bhargava, R.; Murphy, C. J. *J. Phys. Chem. C* **2013**, *117*, 10677-10682.
(7) Fujigaya, T.; Kim, C.; Matsumoto, K.; Nakashima, N. *Polym. J. (Tokyo, Jpn.)***2013**, *45*, 326-330.
(8) Gao, H.; Liu, R.; Gao, F. P.; Wang, Y. L.; Jiang, X. L.; Gao, X. Y. *ACS Nano* **2014**, *8*, 7260-7271.
(9) Liu, Y. Y.; Su, G. X.; Zhang, B.; Jiang, G. B.; Yan, B. *Analyst* **2011**, *136*, 872-877.
(10) Alkilany, A. M.; Nagaria, P. K.; Hexel, C. R.; Shaw, T. J.; Murphy, C. J.; Wyatt, M. D. *Small* **2009**, *5*, 701-708.
(11) Harper, B.; Sinche, F.; Wu, R. H.; Gowrishankar, M.; Marquart, G.; Mackiewicz, M.; Harper, S. L. *Nanomaterials* **2014**, *4*, 355-371.
(12) Pierre, M. C. S.; Haes, A. J. *Anal. Chem.* **2012**, *84*, 7906-7911.
(13) Hirsjarvi, S.; Peltonen, L.; Hirvonen, J. *AAPS PharmSciTech* **2009**, *10*, 488-494.
(14) Lohse, S. E.; Eller, J. R.; Sivapalan, S. T.; Plews, M. R.; Murphy, C. J. *ACS Nano* **2013**, *7*, 4135-4150.
(15) Sweeney, S. F.; Woehrle, G. H.; Hutchison, J. E. *J. Am. Chem. Soc.* **2006**, *128*, 3190-3197.
(16) Gilbertson, L. M.; Zimmerman, J. B.; Plata, D. L.; Hutchison, J. E.; Anastas, P. T. *Chem. Soc. Rev.* **2015**, *44*, 5758-5777.
(17) Eby, D. M.; Harbaugh, S.; Tatum, R. N.; Farrington, K. E.; Kelley-Loughnane, N.; Johnson, G. R. *Langmuir* **2012**, *28*, 10521-10527.
(18) Shutava, T. G.; Balkundi, S. S.; Vangala, P.; Steffan, J. J.; Bigelow, R. L.; Cardelli, J. A.; O'Neal, D. P.; Lvov, Y. M. *ACS Nano* **2009**, *3*, 1877-1885.
(19) Beliaev, A. S.; Klingeman, D. M.; Klappenbach, J. A.; Wu, L.; Romine, M. F.; Tiedje, J. A.; Nealson, K. H.; Fredrickson, J. K.; Zhou, J. *J. Bacteriol.* **2005**, *187*, 7138-7145.
(20) Orendorff, C. J.; Murphy, C. J. *J. Phys. Chem. B* **2006**, *110*, 3990-3994.
(21) Herigstad, B.; Hamilton, M.; Heersink, J. *J. Microbiol. Methods* **2001**, *44*, 121-129.
(22) Bantan-Polak, T.; Kassai, M.; Grant, K. B. *Anal. Biochem.* **2001**, *297*, 128-136.
(23) Noble, J. E.; Knight, A. E.; Reason, A. J.; Di Matola, A.; Bailey, M. J. A. *Mol. Biotechnol.* **2007**, *37*, 99-111.
(24) Shapiro, S. S.; Wilk, M. B. *Biometrika* **1965**, *52*, 591-611.
(25) Kreibig, U.; Genzel, L. *Surf. Sci.* **1985**, *156*, 678-700.
(26) Alkilany, A. M.; Murphy, C. J. *J. Nanopart. Res.* **2010**, *12*, 2313-2333.
(27) Marbella, L. E.; Millstone, J. E. *Chem. Mater.* **2015**, *27*, 2721-2739.
(28) Dietrich, P. M.; Graf, N.; Gross, T.; Lippitz, A.; Krakert, S.; Schupbach, B.; Terfort, A.; Unger, W. E. S. *Surf. Interface Anal.* **2010**, *42*, 1184-1187.
(29) Song, X. N.; Ma, Y.; Wang, C. K.; Dietrich, P. M.; Unger, W. E. S.; Luo, Y. *J. Phys. Chem. C* **2012**, *116*, 12649-12654.
(30) Dalwadi, G.; Benson, H. E.; Chen, Y. *Pharm. Res.* **2005**, *22*, 2152-2162.
(31) Choe, T. B.; Masse, P.; Verdier, A.; Clifton, M. J. *J. Membr. Sci.* **1986**, *26*, 17-30.
(32) Armstrong, J. K.; Wenby, R. B.; Meiselman, H. J.; Fisher, T. C. *Biophys. J.* **2004**, *87*, 4259-4270.

(33) Jachimska, B.; Jasinski, T.; Warszynski, P.; Adamczyk, Z. *Colloid Surf. A* **2010**, *355*, 7-15.
(34) Dobrynin, A. V.; Rubinstein, M. *Prog. Polym. Sci.* **2005**, *30*, 1049-1118.
(35) Gittins, D. I.; Caruso, F. *J. Phys. Chem. B* **2001**, *105*, 6846-6852.
(36) Wang, Y.; Angelatos, A. S.; Caruso, F. *Chem. Mater.* **2008**, 20, 848-858.

Chapter 5

(1) Li, Q.; Mahendra, S.; Lyon, D. Y.; Brunet, L.; Liga, M. V.; Li, D.; Alvarez, P. J. J. *Water Res.* **2008**, *42*, 4591-4602.
(2) Akhavan, O.; Ghaderi, E. *ACS Nano* **2010**, *4*, 5731-5736.
(3) Maurer-Jones, M. A.; Gunsolus, I. L.; Murphy, C. J.; Haynes, C. L. *Anal. Chem.* **2013**, *85*, 3036-3049.
(4) Postgate, J. R. In *Methods in Microbiology*, Norris, J. R.; Ribbons, D. W., Eds.; Academic Press, 1969, pp 611-628.
(5) Hammes, F.; Berney, M.; Egli, T. In *High Resolution Microbial Single Cell Analytics*, Müller, S.; Bley, T.; Springer Berlin Heidelberg, 2011, pp 123-150.
(6) Bleve, G.; Rizzotti, L.; Dellaglio, F.; Torriani, S. *Appl. Environ. Microbiol.* **2003**, *69*, 4116-4122.
(7) Damoiseaux, R.; George, S.; Li, M.; Pokhrel, S.; Ji, Z.; France, B.; Xia, T.; Suarez, E.; Rallo, R.; Madler, L.; Cohen, Y.; Hoek, E. M. V.; Nel, A. *Nanoscale* **2011**, *3*, 1345-1360.
(8) Jin, X.; Li, M.; Wang, J.; Marambio-Jones, C.; Peng, F.; Huang, X.; Damoiseaux, R.; Hoek, E. M. *Environ. Sci. Technol.* **2010**, *44*, 7321-7328.
(9) Mortimer, M.; Kasemets, K.; Heinlaan, M.; Kurvet, I.; Kahru, A. *Toxicol. In Vitro* **2008**, *22*, 1412-1417.
(10) Parvez, S.; Venkataraman, C.; Mukherji, S. *Environ. Int.* **2006**, *32*, 265-268.
(11) Kroll, A.; Pillukat, M. H.; Hahn, D.; Schnekenburger, J. *Eur. J. Pharm. Biopharm.* **2009**, *72*, 370-377.
(12) Ong, K. J.; MacCormack, T. J.; Clark, R. J.; Ede, J. D.; Ortega, V. A.; Felix, L. C.; Dang, M. K. M.; Ma, G. B.; Fenniri, H.; Veinot, J. G. C.; Goss, G. G. *Plos One* **2014**, *9*.
(13) Monteiro-Riviere, N. A.; Inman, A. O.; Zhang, L. W. *Toxicol. Appl. Pharmacol.* **2009**, *234*, 222-235.
(14) Wörle-Knirsch, J. M.; Pulskamp, K.; Krug, H. F. *Nano Lett.* **2006**, *6*, 1261-1268.
(15) Guadagnini, R.; Kenzaoui, B. H.; Walker, L.; Pojana, G.; Magdolenova, Z.; Bilanicova, D.; Saunders, M.; Juillerat-Jeanneret, L.; Marcomini, A.; Huk, A.; Dusinska, M.; Fjellsbo, L. M.; Marano, F.; Boland, S. *Nanotoxicology* **2015**, *9*, 13-24.
(16) Horst, A. M.; Vukanti, R.; Priester, J. H.; Holden, P. A. *Small* **2013**, *9*, 1753-1764.
(17) Clarke, M. L.; Burton, R. L.; Hill, A. N.; Litorja, M.; Nahm, M. H.; Hwang, J. *Cytometry, Part A* **2010**, *77A*, 790-797.
(18) Ivask, A.; Suarez, E.; Patel, T.; Boren, D.; Ji, Z. X.; Holden, P.; Telesca, D.; Damoiseaux, R.; Bradley, K. A.; Godwin, H. *Environ. Sci. Technol.* **2012**, *46*, 2398-2405.
(19) Pelletier, D. A.; Suresh, A. K.; Holton, G. A.; McKeown, C. K.; Wang, W.; Gu, B.; Mortensen, N. P.; Allison, D. P.; Joy, D. C.; Allison, M. R.; Brown, S. D.; Phelps, T. J.; Doktycz, M. J. *Appl. Environ. Microbiol.* **2010**, *76*, 7981-7989.

(20) Suresh, A. K.; Pelletier, D. A.; Wang, W.; Moon, J. W.; Gu, B. H.; Mortensen, N. P.; Allison, D. P.; Joy, D. C.; Phelps, T. J.; Doktycz, M. J. *Environ. Sci. Technol.* **2010**, *44*, 5210-5215.
(21) Lok, C. N.; Ho, C. M.; Chen, R.; He, Q. Y.; Yu, W. Y.; Sun, H.; Tam, P. K. H.; Chiu, J. F.; Che, C. M. *J. Biol. Inorg. Chem.* **2007**, *12*, 527-534.
(22) Qiu, T. A.; Torelli, M. D.; Vartanian, A. M.; Rackstraw, N. B.; Buchman, J. T.; Jacob, L. M.; Murphy, C. J.; Hamers, R. J.; Haynes, C. L. *Anal. Chem.* **2016**, DOI: 10.1021/acs.analchem.6b04161.
(23) Gunsolus, I. L.; Hang, M. N.; Hudson-Smith, N. V.; Buchman, J. T.; Bennett, J. W.; Mason, S. E.; Hamers, R. J.; Haynes, C. L. *Unpublished work*, University of Minnesota, **2016**.
(24) Feng, Z. V.; Gunsolus, I. L.; Qiu, T. A.; Hurley, K. R.; Nyberg, L. H.; Frew, H.; Johnson, K. P.; Vartanian, A. M.; Jacob, L. M.; Lohse, S. E.; Torelli, M. D.; Hamers, R. J.; Murphy, C. J.; Haynes, C. L. *Chem. Sci.* **2015**, *6*, 5186-5196.
(25) Heid, C. A.; Stevens, J.; Livak, K. J.; Williams, P. M. *Genome Res.* **1996**, *6*, 986-994.
(26) Tichopad, A.; Dilger, M.; Schwarz, G.; Pfaffl, M. W. *Nucleic Acids Res.* **2003**, *31*.
(27) Zhao, S.; Fernald, R. D. *J. Comput. Biol.* **2005**, *12*, 1047-1064.
(28) Wai, S. N.; Mizunoe, Y.; Takade, A.; Yoshida, S. *Arch. Microbiol.* **2000**, *173*, 307-310.
(29) Cuny, C.; Lesbats, M. N.; Dukan, S. *Appl. Environ. Microbiol.***2007**, *73*, 885-889.

Chapter 6

(1) Liu, W.; Oh, P.; Liu, X.; Lee, M. J.; Cho, W.; Chae, S.; Kim, Y.; Cho, J. *Angew. Chem. Int. Edit.* **2015**, *54*, 4440-4457.
(2) Belharouak, I.; Sun, Y. K.; Liu, J.; Amine, K. *J. Power Sources* **2003**, *123*, 247-252.
(3) Yang, F. F.; Liu, Y. J.; Martha, S. K.; Wu, Z. Y.; Andrews, J. C.; Ice, G. E.; Pianetta, P.; Nanda, J. *Nano Lett.* **2014**, *14*, 4334-4341.
(4) Zheng, F. H.; Yang, C. H.; Xiong, X. H.; Xiong, J. W.; Hu, R. Z.; Chen, Y.; Liu, M. L. *Angew. Chem. Int. Edit.* **2015**, *54*, 13058-13062.
(5) Hang, M. N.; Gunsolus, I. L.; Wayland, H.; Melby, E. S.; Mensch, A. C.; Hurley, K. R.; Pedersen, J. A.; Haynes, C. L.; Hamers, R. J. *Chem. Mater.* **2016**, *28*, 1092-1100.
(6) Song, H. K.; Lee, K. T.; Kim, M. G.; Nazar, L. F.; Cho, J. *Adv. Funct. Mater.* **2010**, *20*, 3818-3834.
(7) Dutta, T.; Kim, K. H.; Deep, A.; Szulejko, J. E.; Vellingiri, K.; Kumar, S.; Kwon, E. E.; Yun, S. T. *Renew. Sust. Energ. Rev.* **2018**, *82*, 3694-3704.
(8) Richa, K.; Babbitt, C. W.; Gaustad, G.; Wang, X. *Resour. Conserv. Recy.* **2014**, *83*, 63-76.
(9) Lain, M. J. *J. Power Sources* **2001**, *97-8*, 736-738.
(10) Castillo, S.; Ansart, F.; Laberty-Robert, C.; Portal, J. *J. Power Sources* **2002**, *112*, 247-254.
(11) Boxall, N. J.; Adamek, N.; Cheng, K. Y.; Haque, N.; Bruckard, W.; Kaksonen, A. H. *Waste Manage.* **2018**, *74*, 435-445.
(12) Gunsolus, I. L.; Hang, M. N.; Hudson-Smith, N. V.; Buchman, J. T.; Bennett, J. W.; Conroy, D.; Mason, S. E.; Hamers, R. J.; Haynes, C. L. *Environ. Sci. Nano* **2017**, *4*, 636-646.
(13) Bozich, J.; Hang, M. M.; Hamers, R.; Klaper, R. *Environ. Toxicol. Chem.* **2017**, *36*, 2493-2502.

(14) Wang, H. H.; Wu, F. C.; Meng, W.; White, J. C.; Holden, P. A.; Xing, B. S. *Environ. Sci. Tech.* **2013**, *47*, 13212-13214.
(15) Magdolenova, Z.; Collins, A.; Kumar, A.; Dhawan, A.; Stone, V.; Dusinska, M. *Nanotoxicology* **2014**, *8*, 233-278.
(16) Ghosh, M.; Bandyopadhyay, M.; Mukherjee, A. *Chemosphere* **2010**, *81*, 1253-1262.
(17) Butler, K. S.; Peeler, D. J.; Casey, B. J.; Dair, B. J.; Elespuru, R. K. *Mutagenesis* **2015**, *30*, 577-591.
(18) Vignardi, C. P.; Hasue, F. M.; Sartorio, P. V.; Cardoso, C. M.; Machado, A. S. D.; Passos, M. J. A. C. R.; Santos, T. C. A.; Nucci, J. M.; Hewer, T. L. R.; Watanabe, I. S.; Gomes, V.; Phan, N. V. *Aquat. Toxicol.* **2015**, *158*, 218-229.
(19) Chen, Y.; Xu, M.; Zhang, J.; Ma, J.; Gao, M.; Zhang, Z. H.; Xu, Y.; Liu, S. J. *Adv. Mater.* **2017**, *29*.
(20) Bhattacharya, K.; Davoren, M.; Boertz, J.; Schins, R. P.; Hoffmann, E.; Dopp, E. *Part. Fibre Toxicol.* **2009**, *6*, 17.
(21) Kyjovska, Z. O.; Jacobsen, N. R.; Saber, A. T.; Bengtson, S.; Jackson, P.; Wallin, H.; Vogel, U. *Environ. Mol. Mutagen.* **2015**, *56*, 41-49.
(22) Jacobsen, N. R.; Saber, A. T.; White, P.; Moller, P.; Pojana, G.; Vogel, U.; Loft, S.; Gingerich, J.; Soper, L.; Douglas, G. R.; Wallin, H. *Environ. Mol. Mutagen.* **2007**, *48*, 451-461.
(23) Bhabra, G.; Sood, A.; Fisher, B.; Cartwright, L.; Saunders, M.; Evans, W. H.; Surprenant, A.; Lopez-Castejon, G.; Mann, S.; Davis, S. A.; Hails, L. A.; Ingham, E.; Verkade, P.; Lane, J.; Heesom, K.; Newson, R.; Case, C. P. *Nat. Nanotech.* **2009**, *4*, 876-883.
(24) De Boeck, M.; Kirsch-Volders, M.; Lison, D. *Mutat. Res., Fundam. Mol. Mech. Mutagen.* **2003**, *533*, 135-152.
(25) Kirkland, D.; Brock, T.; Haddouk, H.; Hargeaves, V.; Lloyd, M.; Mc Garry, S.; Proudlock, R.; Sarlang, S.; Sewald, K.; Sire, G.; Sokolowski, A.; Ziemann, C. *Regul. Toxicol. Pharmacol.* **2015**, *73*, 311-338.
(26) Salnikow, K.; Zhitkovich, A. *Chem. Res. Toxicol.* **2008**, *21*, 28-44.
(27) Singh, N. P.; Stephens, R. E.; Singh, H.; Lai, H. *Mutat. Res., Fundam. Mol. Mech. Mutagen.* **1999**, *429*, 159-168.
(28) Balbo, S.; Hecht, S. S.; Upadhyaya, P.; Villalta, P. W. *Anal. Chem.* **2014**, *86*, 1744-1752.
(29) Azqueta, A.; Dusinska, M. *Frontiers in genetics* **2015**, *6*.
(30) Balbo, S.; Turesky, R. J.; Villalta, P. W. *Chem. Res. Toxicol.* **2014**, *27*, 356-366.
(31) Swenberg, J. A.; Lu, K.; Moeller, B. C.; Gao, L.; Upton, P. B.; Nakamura, J.; Starr, T. B. *Toxicol. Sci.* **2011**, *120 Suppl 1*, S130-145.
(32) Beranek, D. T.; White, G. L.; Heflich, R. H.; Beland, F. A. *P. Natl. Acad. Sci.-Biol.* **1982**, *79*, 5175-5178.
(33) Mermelstein, R.; Kiriazides, D. K.; Butler, M.; Mccoy, E. C.; Rosenkranz, H. S. *Mutat. Res.* **1981**, *89*, 187-196.
(34) Beland, F. A.; Beranek, D. T.; Dooley, K. L.; Heflich, R. H.; Kadlubar, F. F. *Environ. Health Perspect.* **1983**, *49*, 125-134.
(35) VanderVeen, L. A.; Hashim, M. F.; Shyr, Y.; Marnett, L. J. *Proc. Natl. Acad. Sci. USA* **2003**, *100*, 14247-14252.
(36) Fink, S. P.; Reddy, G. R.; Marnett, L. J. *Proc. Natl. Acad. Sci. USA* **1997**, *94*, 8652-8657.

(37) Kanaly, R. A.; Micheletto, R.; Matsuda, T.; Utsuno, Y.; Ozeki, Y.; Hamamura, N. *MicrobiologyOpen* **2015**, *4*, 841-856.
(38) Bar-Ilan, O.; Chuang, C. C.; Schwahn, D. J.; Yang, S.; Joshi, S.; Pedersen, J. A.; Hamers, R. J.; Peterson, R. E.; Heideman, W. *Environ. Sci. Tech.* **2013**, *47*, 4726-4733.
(39) Jin, Y.; Kannan, S.; Wu, M.; Zhao, J. X. *Chem. Res. Toxicol.* **2007**, *20*, 1126-1133.
(40) Papageorgiou, I.; Brown, C.; Schins, R.; Singh, S.; Newson, R.; Davis, S.; Fisher, J.; Ingham, E.; Case, C. P. *Biomaterials* **2007**, *28*, 2946-2958.
(41) Ishino, K.; Kato, T.; Kato, M.; Shibata, T.; Watanabe, M.; Wakabayashi, K.; Nakagama, H.; Totsuka, Y. *Int. J. Mol. Sci.* **2015**, *16*, 3474-3492.
(42) Totsuka, Y.; Ishino, K.; Kato, T.; Goto, S.; Tada, Y.; Nakae, D.; Watanabe, M.; Wakabayashi, K. *Nanomaterials-Basel* **2014**, *4*, 175-188.
(43) Qiu, T. A.; Nguyen, T. H.; Hudson-Smith, N. V.; Clement, P. L.; Forester, D. C.; Frew, H.; Hang, M. N.; Murphy, C. J.; Hamers, R. J.; Feng, Z. V.; Haynes, C. L. *Anal. Chem.* **2017**, *89*, 2057-2064.
(44) Solanky, D.; Haydel, S. E. *J. Microbiol. Meth.* **2012**, *91*, 257-261.
(45) Olive, P. L.; Banath, J. P. *Nat. Protoc.* **2006**, *1*, 23-29.
(46) Chen, X. P.; Zhong, Z. F.; Xu, Z. T.; Chen, L. D.; Wang, Y. T. *Free Radical Res.* **2010**, *44*, 587-604.
(47) Brandt, R.; Keston, A. S. *Anal. Biochem.* **1965**, *11*, 6-&.
(48) Zhou, M. J.; Diwu, Z. J.; PanchukVoloshina, N.; Haugland, R. P. *Anal. Biochem.* **1997**, *253*, 162-168.
(49) Sensi, S. L.; Yin, H. Z.; Carriedo, S. G.; Rao, S. S.; Weiss, J. H. *P. Natl. Acad. Sci. USA* **1999**, *96*, 2414-2419.
(50) Zhao, J. F.; Bertoglio, B. A.; Devinney, M. J.; Dineley, K. E.; Kay, A. R. *Anal. Biochem.* **2009**, *384*, 34-41.
(51) Cadosch, D.; Meagher, J.; Gautschi, O. P.; Filgueira, L. *J. Neurosci. Meth.* **2009**, *178*, 182-187.
(52) Karlsson, H. L.; Di Bucchianico, S.; Collins, A. R.; Dusinska, M. *Environ. Mol. Mutagen.* **2015**, *56*, 82-96.
(53) Sanchez-Romero, M. A.; Cota, I.; Casadesus, J. *Curr. Opin. Microbiol.* **2015**, *25*, 9-16.
(54) Mehta, A.; Haber, J. E. *Cold Spring Harbor Perspect. Biol.* **2014**, *6*.

Appendices

A.1 Chapter 2 Supporting Information

A.1.1 TiO_2 nanoparticle synthesis and characterization

TiO_2 nanoparticles were synthesized using a sol-gel method developed by Isley and Penn (Isley, S. L.; Penn, R. L. *J Phys Chem C* **2008**, *112*, 4469-4474). In an ice bath, 75 mL of isopropyl alcohol (Fisher, HPLC Grade) and 7.5 mL of titanium isopropoxide (Ti-Iso, Aldrich) were added to a 250 mL round bottom flask with stirring. The reaction was then chilled for 30 minutes. A nitric acid solution of pH -0.34 was prepared with 3.790 mL of Milli-Q water and 0.630 mL of 68.0~70.0% nitric acid (BDH, ARISTAR). The acid solution was added dropwise to the isopropyl alcohol/Ti-Iso solution with continuous stirring. After adding all the acid, the reaction vessel was brought to room temperature and then heated to boiling, followed by a 24-hour reflux in an oil bath at 85-90 °C.

The resulting solution was then transferred to a Fisherbrand regenerated cellulose dialysis membrane with a molecular weight cut-off of 12,000-14,000 Da for a ten-day dialysis in Milli-Q water to remove small-molecule reaction by-products and leftover nitric acid. Over ten days, the water was changed at least 15 times. After dialysis, 8 mL of nanoparticle suspension and 15 mL of Milli-Q water were mixed and loaded into the Teflon chamber of a Parr Instrument autoclave bomb for hydrothermal aging. The suspension was aged in an oven at 200°C for 48 hours and then taken out to cool down to room temperature. A nanoparticle powder was obtained after all the water in the suspension was evaporated. A pre-weighed amount was suspended in, and then sonicated at room temperature for 3.5 hours to obtain a TiO_2 nanoparticle suspension stock with a concentration of 5 mg/mL.

A.1.2 Actinometry of UV illumination

The UV lamp used in all UV exposure experiments was a 150 W 10,000 K Aqualite™ metal halide lamp from Ushino America, Inc. It has a broad emission spectrum simulating the appearance of sunlight near the equator in ocean depths of approximately 5 meters. A potassium ferrioxalate actinometer was applied to monitor the photon flux of the UV lamp. The procedure was adapted from the IUPAC Technical Report (Kuhn, H. J.; Braslavsky, S. E.; Schmidt, R. *Pure Appl Chem* **2004**, *76*, 2105-2146). $K_3[Fe(C_2O_4)_3] \cdot 3H_2O$ crystals were firstly synthesized in house. 180 mL of 1.5 M

$K_2C_2O_4$ solution and 60 mL of 1.5 M $FeCl_3$ solution were mixed together, and crystals were recrystallized three times from the mixture with warm water, dried at 45 °C and kept in the dark. The resultant crystals were green in color. A 0.1% 1, 10-phenanthroline solution (stored in the dark) was prepared along with a 100 mL acidic buffer containing 8.2 g CH_3COONa and 1 mL concentrated H_2SO_4. 2.947 grams of $K_3[Fe(C_2O_4)_3] \cdot 3H_2O$ crystals were dissolved in 100 mL of 0.5 M H_2SO_4 and diluted to 1 L to create a 0.006 M solution. The absorption spectrum of the solution from 300 to 900 nm was obtained using a DH-2000 Mikropack spectrometer with deuterium and halogen light source. 3 mL (V_1) of the solution was irradiated by the UV lamp for about 6 minutes (t) under sufficient stirring. 4 mL of the 0.1% 1, 10-phenanthroline solution and 0.5 mL of the acidic buffer were mixed in a 10 mL (V_3) volumetric flask, followed by the addition of 1 mL (V_2) of the irradiated solution. This procedure was repeated for the dark reference, the same solution without irradiation. After diluting the solution to 10 mL (V_3), the mixture was incubated in the dark for one hour until full color development was achieved, and the absorbance spectra of both the dark reference and the irradiated samples were measured. This experiment was done in triplicate with all steps performed under dark red light. All water used in this procedure refers to DI water.

Photon flux (I) was calculated using the equations below:

$$I = \frac{\Delta n}{10^{-3} \cdot \Phi \cdot V_1 \cdot t}$$

$$\Delta n = \frac{10^{-3} \cdot V_1 \cdot V_3 \cdot C_t}{V_2}$$

$$C_t = \frac{Absorbance(510\ nm)}{\varepsilon(510\ nm) \cdot l}$$

Φ: quantum yield was chosen to be 1.16 as our lamp centers at 380-405 nm according to the product specification; t: irradiation time, 360 seconds; l: length of the cuvette, 1 cm; $\varepsilon(510\ nm)$: 11100 $dm^3 \cdot mol^{-1} \cdot cm^{-1}$. The average solution absorbance at 510 nm was applied in this calculation; C_t: concentration of ferrous iron after dilution in molarity ($mol \cdot dm^{-3}$); Δn: ferrous ion photo-generated in moles (mol).

The final intensity I was calculated to be $2.54 \times 10^{-6}\ Einstein \cdot L^{-1} \cdot s^{-1}$. Considering the irradiated volume to be 3 mL and the wavelength as 400 nm, the energy of photon flux was calculated to be $0.23\ J \cdot s^{-1}$. The solar irradiation on earth surface is approximately $1.4\ W/m^2$. Assuming the irradiation area to be $1\ cm^2$ (approximately the irradiated area of the test tubes in this study), the solar energy is estimated to be $0.00014\ J \cdot s^{-1}$. Thus, our irradiation intensity in this experiment is much higher than the average solar energy.

A.1.3 Hyperspectral imaging of TiO_2 NP-exposed bacterial cells

Hyperspectral microscopy instrumentation from CytoViva, Inc. provides dark field hyperspectral imaging capability, which can provide full spectra from every pixel in a 2D image, enabling comparison of spectral differences across pixels within a field of view with a spectral resolution of 2 nm. Nanoparticles can be identified via their unique spectral response based on the materials that they are composed of, as different materials have different spectral characteristics. This technique does not require any staining or tagging.

TiO_2 nanoparticles were re-suspended in LB medium to reach a final concentration of 100 mg/L. Bacterial suspensions were grown overnight to stationary phase and diluted 10-fold into the TiO_2 NP suspension of LB broth. After sufficient mixing, about 3 µL of either the TiO_2 suspension in LB broth or the TiO_2 NP-exposed bacterial suspension were dropped onto a glass slide, covered with cover slips, and sealed using nail polishing to avoid water evaporation. These samples were then brought to the hyperspectral microscope. A library of TiO_2 NP spectra was created as a reference. Then, hyperspectral images of bacteria with added TiO_2 suspension was created as shown in Figure S2(a), wherein each pixel was compared with the TiO_2 NP spectra library with a certain threshold. Pixels that had high similarity with the reference spectrum were highlighted as shown in Figure S2(b). The large aggregate has a good spectral match to known TiO_2 NP aggregates, while bacterial cells only attached to the edge of the huge aggregate.

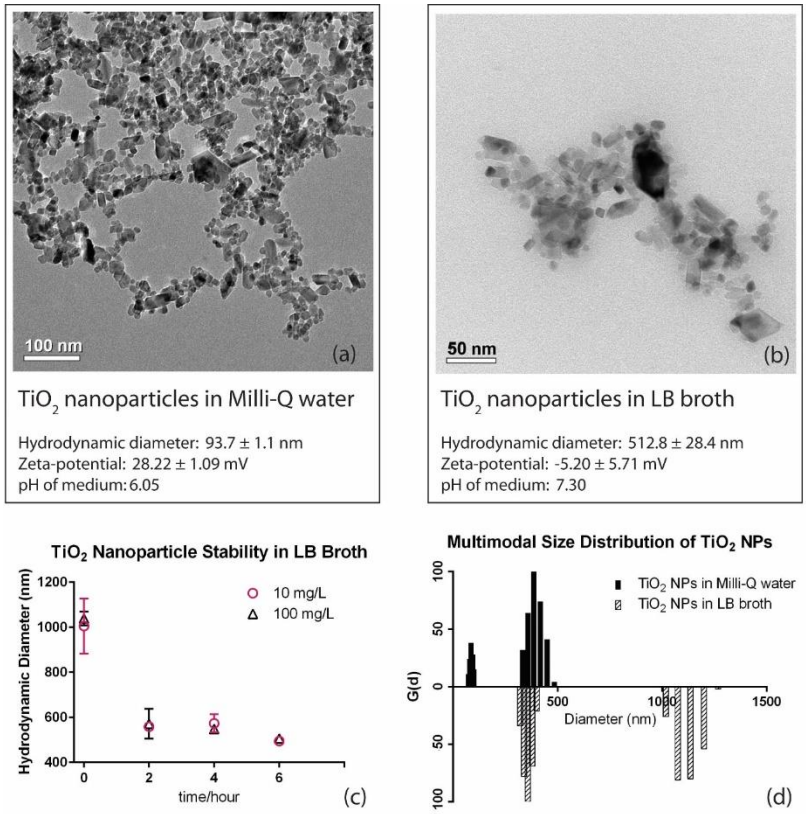

Figure A.1.1. TEM images of TiO_2 nanoparticles in (a) Milli-Q water and (b) LB broth. (c) The hydrodynamic diameters of nanoparticles are stable with time. Error bars show the standard deviation of material replicates (n=3). (d) Multimodal size distribution of TiO_2 nanoparticles in Milli-Q water and LB broth shows that a portion of TiO_2 nanoparticles aggregate in LB broth.

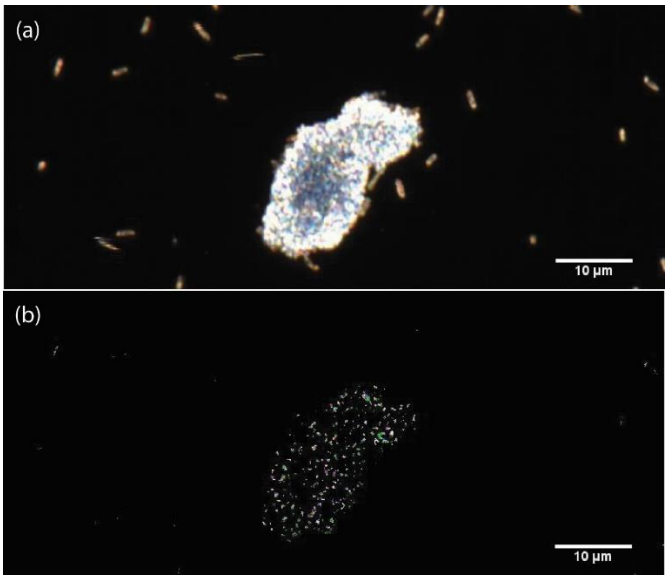

Figure A.1.2. TiO_2 NPs aggregate in LB broth and bacterial cells attach to the edge of the TiO_2 aggregate. (a) Dark field image of TiO_2 NP-exposed cells in LB broth (full

hyperspectral spectrum available but not shown for each pixel); (b) Highlighted area indicating pixels with high spectral similarity to the reference TiO_2 NP spectrum.

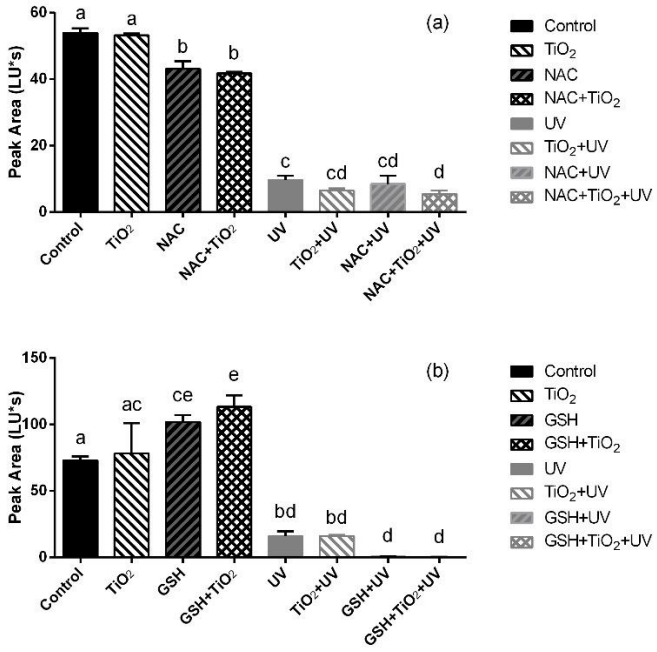

Figure A.1.3. Riboflavin levels upon 100 mg/L TiO_2 NP and/or UV light exposure with the presence of antioxidant (a) N-acetylcysteine (NAC) for 1 hour or (b) glutathione (GSH) for 6 hours. Adding antioxidant did not recover the riboflavin levels influenced by UV illumination. Different letter designations denote statistically significant differences between groups (one-way ANOVA followed by a post-hoc Tukey's test, $p<0.05$).

A.2 Chapter 3 Supporting Information

A.2.1 Ligand control estimation: PAH-AuNPs

Ahead of organism exposure, PAH-AuNPs were purified by centrifugation, making it possible for PAH free ligand to be left over in the PAH-AuNP suspension. To estimate the presence of free PAH ligand in the nanoparticle suspension, a fluorescence quantification method was used to determine primary amine content (Bantan-Polak, T.; Kassai, M.; Grant, K. B. *Anal Biochem* **2001**, *297*, 128-136).

In this procedure, 0.01 g fluorescamine (Sigma-Aldrich) was dissolved in 10 mL acetonitrile to reach a concentration of 0.1% (w/v). 0.05 M sodium borate buffer was prepared by dissolving 5.03 g $Na_2B_4O_7$ in 500 mL MilliQ water followed by the adjustment of pH to approximately 8 using 12 M HCl. PAH-AuNP suspension was

centrifuged at 66,000 g for 45 minutes at 4 °C to pellet all AuNPs, and the clear supernatant was removed from the centrifugation tubes. 120 L samples were mixed with 20 µL of borate buffer on a 96-well plate, and 60 µL of fluorescamine solution was lastly added to the mixture. The reaction was incubated at room temperature for 5 minutes, and the fluorescence intensity was measured by plate reader with E_{ex}/E_{em} = 425 nm/480 nm. A calibration curve using a series of PAH solutions of known concentrations was created every time before sample measurement, and the concentration of PAH in samples were calculated based the fitting results from linear regression.

The amount of PAH free ligand in 30 µg/L PAH-AuNP suspension was determined to be 210 (192 to 228) µg/L. In addition, the amount of PAH ligand on NP surface was estimated to be 2.7 µg/L (PAH charge density on AuNP surface: 12.8 charge/nm^2 determined by XPS[2]), based on the same calculation as below for MPA-AuNPs. Thus, a 10-fold PAH free ligand control (300 µg/L PAH free ligand in the case of 30 µg/L PAH-AuNPs) was chosen in this study to represent the effect of PAH free ligand in PAH-AuNP suspension.

A.2.2 Ligand control estimation: MPA-AuNPs

Excessive MPA free ligand from synthesis were expected to be eliminated by diafiltration, and the total MPA ligand present in MPA-AuNP suspension was estimated to be the amount of MPA ligand attached to NP surface. The surface charge density of MPA-AuNPs was determined to be $5.6\ charge \cdot nm^{-2}$ by XPS (Torelli, M. D.; Putans, R. A.; Tan, Y.; Lohse, S. E.; Murphy, C. J.; Hamers, R. J. *Acs Appl Mater Inter* **2015**, *7*, 1720-1725).

Calculating number of AuNPs per liter:

$$AuNP\ diameter \sim 4\ nm$$

$$Volume\ per\ AuNP = \frac{4}{3}\pi(\frac{AuNP\ diameter}{2})^3 = 33.5\ nm^3 = 3.35 \times 10^{-20}\ cm^3$$

$$Mass\ per\ AuNP = Density \times Volume\ per AuNP$$

$$= 19.3\ g \cdot cm^{-3} \times 3.35 \times 10^{-20}\ cm^3 = 6.47 \times 10^{-19}\ g$$

$$N_{MPA-AuNPs} = Number\ of\ MPA - AuNPs\ per\ liter = \frac{5\ mg \cdot L^{-1}}{6.47 \times 10^{-19}\ g}$$

$$= 7.73 \times 10^{15}\ L^{-1}$$

Calculating the mass of total amount of surface ligand:

$$Ligand\ amount\ per\ AuNP = Charge\ density \times Surface\ area$$

$$M_{Ligand} = Total\ ligand\ mass\ on\ NPs$$
$$= \frac{N_{AuNPs} \times Ligand\ amount\ per\ AuNP}{Avogadro\ constant} \times MW_{Ligand\ Unit}$$
$$MPA\ ligand\ per\ AuNP = 5.6\ charge \cdot nm^{-2} \times 4\pi \left(\frac{4\ nm}{2}\right)^2 = 2.8 \times 10^2$$
$$M_{MPA\ ligand} = \frac{2.8 \times 10^2 \times (7.73 \times 10^{15}\ L^{-1})}{6.02 \times 10^{23}\ mol^{-1}} \times 106.14\ g \cdot mol^{-1} = 0.38\ mg \cdot L^{-1}$$
$$< 5\ mg \cdot L^{-1}$$

Based on the calculation above, the equivalent mass concentration of MPA ligand was an excessive estimation of the actual MPA ligand present in the suspension.

A.2.3 Bacterial doubling time estimation

A rough estimation of *S. oneidensis* doubling time in the growth medium used in this study was calculated as below. Assuming that cell oxygen uptake (M) is proportional to the cell number (N), at exponential growth phase:

$$M = M_0 \times 2^{kt} \quad (1)$$
$$N = N_0 \times 2^{kt} \quad (2)$$

k: growth rate at exponential phase (hour^{-1}); t: time (hour); T=1/k: doubling time (hour); N: cell number; N_0: original cell number; M: cell oxygen uptake; M_0: original cell oxygen uptake. Take first derivative of equation (2):

$$N_t' = N_0 \times (kln2) \times 2^{kt} \quad (3)$$

The first derivative was calculated in GraphPad, Prism. Two different time points from exponential phase, t_1 and t_2, and the first derivative at these two time points were substituted into equation (3) to get the ratio:

$$\frac{N_{t1}'}{N_{t2}'} = 2^{k(t1-t2)} \quad (4)$$

The growth rate at exponential phase (k) was calculated from equation (4) followed by the calculation of doubling time (T):

$$T = \frac{1}{k}$$

Plugging values from different traces in various experimental runs yielded bacterial doubling times between 2-3 hours.

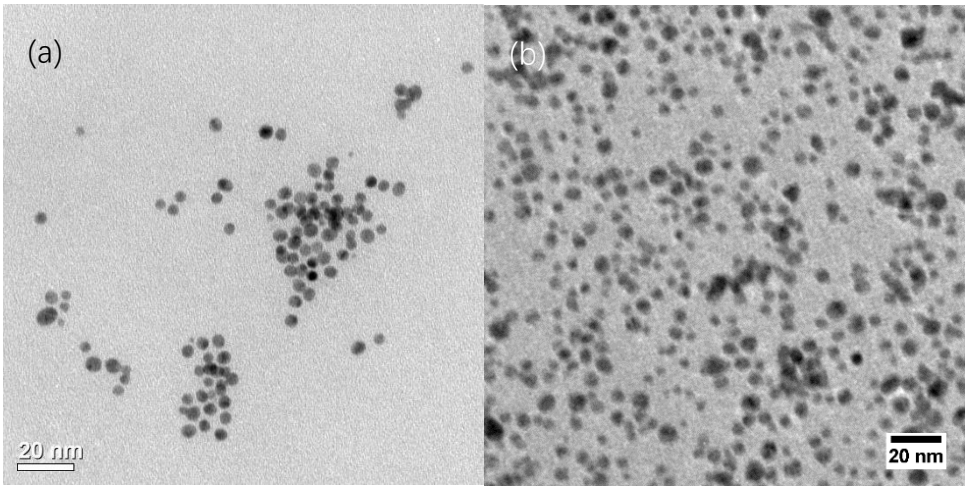

Figure A.2.1. TEM image of (a) PAH-AuNPs and (b) MPA-AuNPs before exposure to either organism.

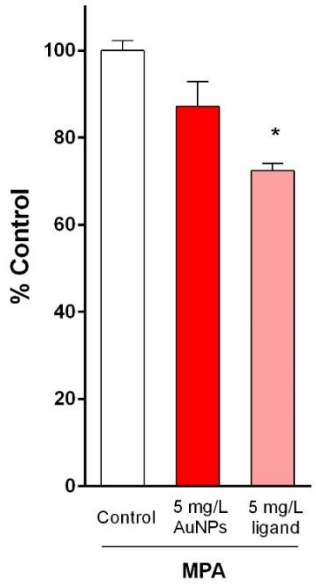

Figure A.2.2. Inhibition on oxygen uptake of *S. oneidensis* upon MPA-AuNP and the respective ligand exposure. Error bars showed standard error of the mean (n=2). Stars indicate significant difference between treated and control groups (unpaired t-test, $p < 0.05$).

A.3 Chapter 4 Supporting Information

A.3.1 Materials

All materials were used as received, unless otherwise indicated. Gold tetrachloroaurate trihydrate ($HAuCl_4 \cdot 3H_2O$), sodium borohydride ($NaBH_4$), and trisodium citrate were

obtained from Sigma Aldrich. Nanoparticle reactions were performed in new polyethylene centrifuge tubes, new glass vials, or glassware cleaned with *aqua regia* (Caution! extremely corrosive, explosion hazard, handle with extreme caution). All water used for NP synthesis was ultrapure deionized water collected from Barnstead NANOPURE water filtration systems (Resistance at least 17.8 MΩ·cm). All water used for nanoparticle characterization and bacterial toxicity assays was Milli-Q water (Resistance 18.2 MΩ·cm) or autoclaved Milli-Q water.

A.3.2 PAH-AuNP synthesis

PAH-AuNPs were synthesized by polyelectrolyte-wrapping of 4-nm-diameter citrate-AuNPs. In a typical flow reactor synthesis as described before (Lohse, S. E.; Eller, J. R.; Sivapalan, S. T.; Plews, M. R.; Murphy, C. J. *ACS Nano* **2013**, *7*, 4135-4150), 20 mL of $HAuCl_4$ (0.01 M) and 6 mL of sodium citrate (0.1 M) were combined in a 2 L Erlenmeyer flask containing 1600 mL of nanopure water. In a second 2 L Erlenmeyer flask, 1614 mL of water was chilled in an ice-water bath. Then, 12 mL of chilled aqueous $NaBH_4$ (0.1 M) was added to the cold flask, which was swirled briefly. A flow line was placed into each 2 L flasks and the flow reactor pump was started at a setting of 40 mL/min. Once the two solutions combined in the flow reactor line, the solution turned a light red-brown and the synthesized particles were collected in a 4 L polyethylene bottle with gentle stirring. The resulting citrate-AuNP solution was then stirred for at least 3 h. The 4-nm-diameter citrate-AuNPs were then wrapped with 15 kDa PAH to prepare 4-nm-diameter PAH-AuNPs. To the approximately 3.2 L of as-synthesized particles, 32.0 mL of NaCl (100 mM) and 100.0 mL of a PAH solution (10 mg/mL in 1 mM NaCl) were added with vigorous stirring. The nanoparticles were then allowed to stir overnight in the wrapping solution.

A.3.3 UV-vis Spectroscopy

The concentration and degree of aggregation of AuNP suspensions were evaluated using UV-vis extinction spectroscopy (Mikropack DH-2000 UV-vis-NIR spectrometer). PAH-AuNP stock suspensions were diluted 20-fold in Milli-Q water for UV-vis measurement. The molar concentration of the AuNP suspensions was calculated by dividing the extinction at 450 nm by the extinction coefficient of 4-nm-diameter AuNPs (7.41×10^7 M^{-1}) (Orendorff, C. J.; Murphy, C. J. *J. Phys. Chem. B* **2006**, *110*, 3990-3994). The mass concentration of AuNP suspension was determined based on the product of molar concentration and the molar mass of 4-nm-diameter AuNP (defined as the mass of 1 mole 4-nm-AuNPs, 3.90×10^5 g/mol). The mass concentration of PAH-AuNPs in this manuscript refers to the mass concentration of gold alone, not including

the mass of surface modification (citrate and PAH).

A.3.4 Transmission Electron Microscopy (TEM)

To prepare the samples for TEM analysis, PAH-AuNP suspensions were diluted in Milli-Q water to approximately 1 mg Au/L and sonicated for 5 minutes. Then, a 2 μL aliquot was drop-cast onto a 200 mesh copper grid with Formvar and carbon supports from Ted Pella, Inc. (Redding, CA). The grid was air-dried near an open 65 °C oven for 5 minutes. An FEI Tecnai T12 transmission electron microscope with an operating voltage of 120 kV was used to acquire images of the samples. To perform size analysis of PAH-AuNPs, the diameters of over 500 nanoparticles were measured from the collected TEM images using ImageJ (National Institutes of Health). The average and standard deviation of these measurements were presented as the nanoparticle diameter (average ± standard deviation).

A.3.5 Dynamic Light Scattering (DLS) and ζ-potential

A Brookhaven ZetaPALS instrument was used for DLS and ζ-potential measurements. PAH-AuNP stock suspensions were diluted 20-fold in Milli-Q water for the measurements. For DLS, the intensity-weighted average diameter was reported as "Z-average", and the mean diameter from the multimodal distribution was also reported. For each specific PAH-AuNP data set, the same AuNP suspension was used across UV-vis, DLS, and ζ-potential measurements.

A.3.6 Drop plate counting for bacterial toxicity assay

An adapted assay from the traditional plate-counting method was used to measure the bacterial toxicity of PAH-AuNPs and PAH polymer (Herigstad, B.; Hamilton, M.; Heersink, J. *J. Microbiol. Methods* **2001**, *44*, 121-129). *Shewanella oneidensis* MR-1 was plated on an agar plate and incubated overnight. A controlled number of bacterial colonies was inoculated into fresh LB (Miller) broth, and the inoculum was agitated on a 32 °C orbital shaker at 300 rpm until mid-log phase (optical density (OD_{600}) between 0.6~1). Bacterial cells were harvested by centrifugation at 750 × g for 10 minutes. The pellet was washed using an equal volume of sterile Dulbecco's phosphate-buffered saline (DPBS) buffer, and centrifuged at 750 × g again for 10 minutes. Cells were finally re-suspended in a 4-(2-hydroxyethyl)-1-piperazineethanesulfonic acid (HEPES) buffer of pH 7.4 containing 2 mM HEPES and 25 mM NaCl. The cell suspension was diluted with HEPES buffer to reach a final optical density of ~0.05 (~10^7 cells/mL). To set up an exposure, a NP suspension at 10 times the intended exposure concentration was mixed 1:9 (v:v) with the OD_{600}~0.05 bacterial suspension in HEPES buffer and

incubated for 15 minutes; autoclaved Milli-Q water was used instead of NP suspension to set up a negative control. A 10-fold serial dilution was then performed to dilute the sample to a proper cell density. In a biosafety cabinet, aliquots of 10 μL diluted samples were dropped onto the surface of a sterile LB agar plate, and the drops were allowed to fully absorb into the agar. At least 3 consecutive dilutions (e.g. the 10^3-, 10^4- and 10^5-fold dilution of the original sample) were plated for each individual sample, and between 4-7 drops were plated for each dilution. Plates were incubated overnight, and then individual colonies were counted for each drop on a plate counter. The dilution that resulted in 3-35 colonies per drop was regarded as the best dilution fold for that specific sample, and the number of colonies for the drop from that dilution was used for further analysis.

A.3.7 Data analysis of drop plate counting

A treated or control sample of bacterial suspension was regarded as a biological replicate. A biological replicate was diluted to the best dilution fold, and all drops pulled from that best dilution from that biological replicate were regarded as technical replicates. The numbers of bacterial colonies from technical replicates were averaged, divided by the volume of the drop (10 μL) and then multiplied by the corresponding dilution factor to obtain the colony-forming unit density (CFUs/mL) of the original biological replicate. To combine data points from different experimental runs, for every individual experimental run, the average colony-forming unit of the biological replicates from the control group was calculated, and the colony-forming unit of every sample in that experimental run was divided by the average of control groups. Normalized CFUs from different experimental runs were then combined and used for further statistical analysis. In most of the cases in this study, at least 7 biological replicates were run for each treatment.

A.3.8 Determining the amount of PAH polymer in the retentate after dialysis

After dialysis of PAH polymers, the concentration of PAH polymer remaining was determined using the aforementioned fluorescamine assay. To make calibration curves, two different PAH polymers (15k from Sigma or 3k from Nittobo) were separately weighed and dissolved in Milli-Q water to make standard solutions of 1 mg/mL. The standard solutions were then diluted in Milli-Q water to make a final concentration of 200 mg/L. Calibration curves were collected for both PAH polymers, and linear regions were located. For each dialyzed sample, different volumes of dialyzed sample ranging from 2 μL to 120 μL was added to react with fluorescamine to collect a fluorescence *vs.* sample volume curve, and the linear region of each curve was located. Only readings

from the linear region of the sample curve and higher than the limit of quantification was used for quantification using the calibration curve. For the dialyzed 15 kDa Sigma PAH sample, 6 readings were used and the average and standard deviation were reported. For the dialyzed 3 kDa Nittobo PAH sample, 2 readings were used and the average and range were reported.

Table A.3.1. The amount of unbound PAH in PAH-AuNP suspensions determined in two different AuNP batches synthesized in different time.

		d-PAH-AuNP	c-PAH-AuNP	cc-PAH-AuNP
Unbound PAH in AuNP suspension (mg/L per mg/L of NPs)	**Batch 16**	469 ± 34	7.65 ± 0.28	0.57 (0.55-0.59) [a)]
	Batch 7 [a)]	559 (529-589)	7.0 (6.4-7.6)	0.46 (0.45-0.47)

a) Range is shown instead of standard deviation as results from less than three replicates were obtained.

A.4 Chapter 5 Supporting Information

A.4.1 Materials and reagents

Difco™ LB broth (Miller) and Difco™ agar (granulated) were purchased from Becton, Dickinson, and Company. Dulbecco's phosphate-buffered saline (DPBS) was purchased from Mediatech, Inc.

A.4.2 Exposure medium used in this study

Sodium chloride (NaCl) and 4-(2-hydroxyethyl)-1-piperazineethanesulfonic acid (HEPES) were purchased from Sigma Aldrich. Magnesium chloride hexhydrate ($MgCl_2 \cdot 6H_2O$), ammonium chloride (NH_4Cl), calcium chloride ($CaCl_2$), and 1 N hydrochloric acid (HCl) were purchased from Fisher Scientific. Potassium chloride (KCl) was purchased from Mallinckrodt Baker Inc. Sodium sulfate (Na_2SO_4) was purchased from Para Scientific Co. Sodium hydroxide (NaOH) pellets were purchased from Macron Fine Chemicals. Dibasic sodium phosphate (Na_2HPO_4) was purchased from Riedel-de Haën. Sodium DL- lactate 60% w/w aqueous solution was purchased from Alfa Aesar. Difco™ Luria-Bertani (LB) broth, Miller and Difco™ agar, granulated were purchased from BD. Sterile Dulbecco's phosphate-buffered saline (DPBS) was purchased from Mediatech, Inc.

HEPES buffer: In MilliQ water, 2 mM HEPES and 25 mM NaCl were dissolved. The solution was adjusted to pH 7.4, followed by filtering with a 0.22 μm cellulose acetate sterile filter (Corning Inc., NY).

Minimal medium with sodium lactate: In 1 liter Milli-Q water, 0.68 g NaCl, 0.3 g KCl, 0.285 g $MgCl_2 \cdot 6H_2O$, 0.3975 g Na_2SO_4, 0.15 g NH_4Cl, 2.383 g HEPES was dissolved, and the pH of the solution was adjusted to 7.2~7.3 using HCl and NaOH solutions. The solution was autoclaved and cooled down, and 0.0125 g Na_2HPO_4 and 0.0056 g $CaCl_2$ were then added; this solution was called minimal medium. Immediately before use, 14 mL of sodium DL-lactate syrup 60% w/w aq. soln was mixed with the minimal medium to make a total volume of 1000 mL, and the minimal medium with sodium lactate was finally used for subsequent studies.

A.4.3 Bacterial culture and preparation

Shewanella oneidensis MR-1 was plated on an agar plate and incubated at 30-32 °C overnight. Bacterial colonies were inoculated into fresh LB (Miller) broth, and the inoculum was agitated on a 30-32 °C orbital shaker at 300 rpm until harvesting. The bacterial suspension was harvested before entering stationary phase (optical density (OD_{600}) between 0.6~1.4), and collected *via* centrifugation at 750 × g for 10 minutes. The pellet was washed using an equal volume of sterile DPBS as the amount of LB and centrifuged at 750 × g for 10 minutes again. The washed cells were finally re-suspended in exposure medium, either HEPES buffer or minimal medium with lactate, and diluted to reach a final optical density of ~0.05 (~10^7 cells/mL), as the prepared bacterial suspension for later use.

While very similar, the preparation of bacterial suspensions had slight difference for different exposure conditions. *S. oneidensis* MR-1 were grown in LB broth as described in the main text. Before the bacterial suspension entered the stationary phase, 10 mL of bacterial suspension in LB broth was centrifuged at 2000 rpm (931 × g) for 10 minutes, and the supernatant was removed. The bacterial pellet was re-dispersed in 10 mL of 0.85% (w/w) NaCl in autoclaved Milli-Q water and centrifuged down again. The supernatant was removed, the bacterial pellet was re-suspended in minimal medium with sodium lactate, and the optical density was adjusted to about 0.1 for exposure. NMC nanomaterials were weighed, re-dispersed in autoclaved water, followed by 10-min sonication immediately before use. During 3-hour exposure, bacterial suspensions were left at room temperature.

Bacillus subtilis SB491 (wild type), *Bacillus subtilis* Δ*dltA* (mutant strain), and *Bacillus subtilis* Δ*tagE* (mutant strain), were plated on agar plates to grow at 37 °C overnight. Bacterial colonies were inoculated into fresh LB (Miller) broth to grow for 12-18 hours at 37°C and 300 rpm agitation. The bacterial suspensions were harvested before entering stationary phase (optical density (OD_{600})) between 0.2~0.8, and followed the same steps as for *S. oneidensis* MR-1 for washing and re-suspension before nanoparticle exposures.

A.4.4 Plate colony counting assay

A traditional plate counting assay was performed to measure the toxicity response of *S. oneidensis* MR-1 exposed to kanamycin or PAH-AuNPs; results were used to compare with those from the growth-based viability assay. A drop plate assay adapted from a traditional plate counting method was used for *S. oneidensis* MR-1.[1] Bacteria were cultured, harvested, re-suspended in HEPES buffer with OD ~ 0.05, and subjected to either antiobiotic or NPs. The *S. oneidensis* MR-1 suspension was exposed to 0.25, 1, 5, and 10 mg/L kanamycin or 0, 30, 78.6, 131, 250, 300 or 600 μg Au/L PAH-AuNPs. Results were analyzed as described in previous work (Qiu, T. A.; Torelli, M. D.; Vartanian, A. M.; Rackstraw, N. B.; Buchman, J. T.; Jacob, L. M.; Murphy, C. J.; Hamers, R. J.; Haynes, C. L. *Anal. Chem.* **2016**, DOI: 10.1021/acs.analchem.6b04161).

A.4.5 Randomized experimental layout

To reduce variation from any instrumental errors, such as transfer errors from multi-channel pipets and possible inconsistent conditions at different positions in the plate reader, a randomized experimental layout was implemented (**Scheme A.4.1**). In this work, random sequences were generated using the `sample` function in R (statistical modeling and analysis software), and assigned to the wells and columns. The numbers in each sequence indicated the order of serial dilution or large dilution into LB broth. As the order of serial dilution and growth wells were randomized, the experimental procedure was kept the same as the original experimental layout described in **Scheme 5.1b**.

	1	2	3	4	5	6	7	8	9	10	11	12
	Screening		Calibration curve	Residue Control		Growth						
	10X working solution (WS)	Exposure	Bacteria serial dilution	NP WS	Bacteria	6	5	3	4	7	2	1
A	1 (WS)	All wells: • 180 µL bacteria • 20 µL 10X working solution parallel transferred from Column 1	8 (HEPES)	5 (WS+H_2O)	All wells: • 180 µL bacteria • 20 µL ddH_2O							
B	7 (WS+H_2O)		3 (Cell+HEPES)	8 (H_2O)								
C	3 (WS+H_2O)		7 (Cell+HEPES)	7 (WS+H_2O)								
D	4 (WS+H_2O)		6 (Cell+HEPES)	1 (WS+H_2O)								
E	8 (H_2O)		2 (Cell+HEPES)	6 (WS+H_2O)								
F	6 (WS+H_2O)		5 (Cell+HEPES)	3 (WS+H_2O)								
G	5 (WS+H_2O)		1 (Cell+H_2O)	4 (WS+H_2O)								
H	2 (WS+H_2O)		4 (Cell+HEPES)	2 (WS+H_2O)								

Scheme A.4.1. An example of the randomized layout for high-throughput screening.

A.4.6 Water evaporation control

To correct for the loss of water in the wells on the edge of the plate, a water evaporation control was implemented. In experiments with the water evaporation control, the wells on the edge were supplied with 200 µL of autoclaved water, instead of being used for bacterial growth. The remaining wells were used for exposure and bacterial growth, and the edges of the plate were parafilmed before being positioned on the plate reader stage. A detailed experimental layout can be found in **Scheme A.4.2**.

	Calibration curve			Screening				Residue control				
	1	2	3	4	5	6	7	8	9	10	11	12
	Bacteria serial dilution	Growth		10X working solution (WS)	Exposure	Growth		Diluted working solution	Bacteria	Growth		
A												
B	• 180 µL bacteria • 20 µL ddH_2O	All wells: • 190/195 µL LB • 10/5 µL diluted bacteria series parallel transferred from Column 1		Working solution with the highest concentration	All wells: • 180 µL bacteria • 20 µL 10X working solution parallel transferred from Column 5	All wells: • 190/195 µL LB • 10/5 µL exposed bacteria parallel transferred from Column 6		• 180 µL ddH_2O • 20 µL A5	All wells: • 180 µL bacteria • 20 µL ddH_2O	All wells: • 180/190 µL LB • 10/5 µL diluted working solution parallel transferred from Column 9 • 10/5 µL bacteria parallel transferred from Column 10		
C												
D	1:1 serial dilution from the well above using exposure buffer			1:1 serial dilution from the well above using ddH_2O				1:1 serial dilution from the well above using ddH_2O				
E												
F												
G	Exposure buffer only			ddH_2O only				ddH_2O only				
H												

Scheme A.4.2. An experimental layout with water evaporation control. Grey wells are filled with 200 µL autoclaved water for use as evaporation control. Column 1 was first used for bacterial serial dilution. After bacterial suspensions were transferred to growth columns on the well plate (Column 2-3), autoclaved water was added to make up to a volume of 200 µL.

A.4.7 Standard plate

Standard plates were used to examine variations in bacterial growth across all wells on a 96-well plate. In wells to be tested, equal volumes of prepared bacterial suspension, either 5 or 10 µL, were diluted into fresh LB medium to make up a total volume of 200 µL. Two kinds of standard plate were used in this study: whole plate (all 96 wells are used), and standard plate with evaporation control (36 of edge wells filled with water, 60 of inner wells used to growth bacteria).

A.4.8 Testing bacteria harvested at different growth stages

S. oneidensis MR-1 was plated on a solid agar plate and inoculated into fresh LB medium at different time points. Two inocula in different tubes were agitated in the orbital shaker overnight or several hours and harvested at the same time when they each reached stationary phase or mid-log phase, respectively. Both harvested bacterial suspensions were washed in sterile Dulbecco's phosphate-buffered saline (DPBS) and re-suspended in HEPES buffer, and the optical density for the final bacterial suspension for exposure were both adjusted to ~0.05. Prepared bacterial suspensions were then used to generate the calibration curve for the GBV assay.

A.4.9 Measuring water loss on plate

To each well of a 96-well plate, 200 µL of Milli-Q water was added. The plate was covered with a lid and incubated in the plate reader at 37 °C for 20 hours. After 20 hours, the plate was removed, and each well was sequentially dried using a piece of KimWipe. The of mass of the plate was recorded after each well was dried, and the result is shown in **Figure A.4.6**.

A.4.10 Orthogonal residue control

The *residue control* stated in the Experimental section only tests the effect of residues on bacterial suspensions at 100% viability. However, it is possible that the same amount of residue that do not affect bacterial growth starting at 100% viability can affect the growth curve starting with less number of cells. In this case, a “bended” calibration curve at the lower viability end is expected, when all wells containing different number of bacterial cells in calibration curve are tested with the same amount of residue added. An orthogonal residue control was designed to address such concern (**Scheme A.4.3**) and tested for kanamycin exposure. In the layout, Row A was used for serial dilution of kanamycin solution, and Column 1 was used to perform serial dilution of bacterial suspension, as in calibration curve section. In the rest of wells, a portion from Row A was transferred to other rows, and the same volume from Column 1 was transferred to

other columns, generating calibration curves that resulted from treatment with residues.

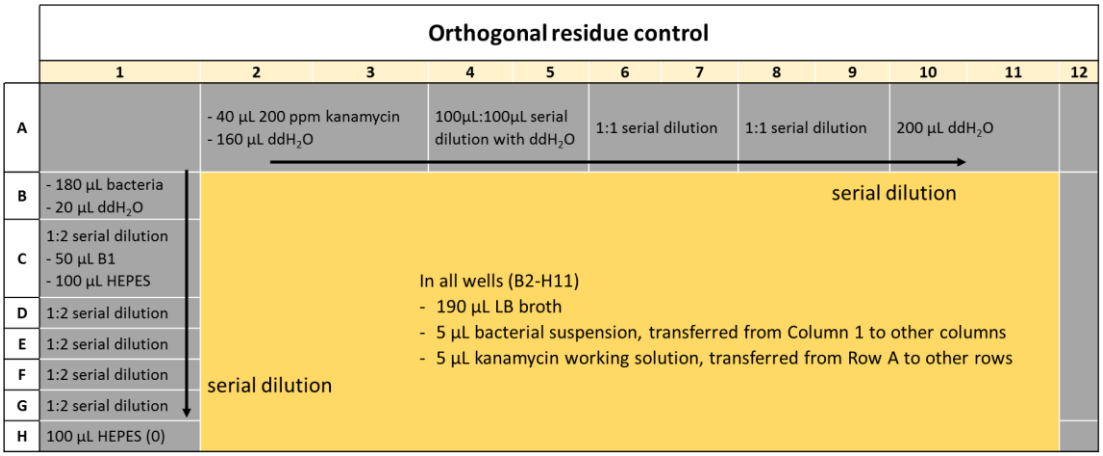

Scheme A.4.3: Plate layout of a stricter residue control, referred as "orthogonal residue control". This layout shows an example layout to test if the residue of kanamycin will affect the growth starting with different amount of cells.

A.4.11 Mathematical modeling of bacterial exponential phase

Variables in this modeling are defined as: t: time lapsed in bacterial growth; N_0: number of cells at t=0; $N(t)$: number of cells at time t; E: bacterial replication efficiency; k: bacterial population growth rate at exponential growth; L: length of lag phase (same unit as t)

Bacterial lag phase and exponential phase growth model:

$$N(t) = \begin{cases} N_0 \cdot (1+E)^{k(t-L)}, & t \geq L \\ N_0, & 0 \leq t < L \end{cases}$$

Set a threshold for cell numbers, T_N. Let

$$T_N = \log[N(C_t)]$$

C_t refers to the "fractional cycle number at threshold" when the cell numbers reach T_N. Here, "cycle number" is a user-defined unit to replace unit "time" and simplify data analysis. For example, in our study, since the plate reads optical density every 20 minutes, 1 cycle number is equivalent to 20 minutes. During the exponential growth phase, $t \geq L$, and C_t is calculated as:

$$T_N = \log N(C_t) = \log[N_0 \cdot (1+E)^{k(C_t - L)}]$$

$$\therefore C_t = \frac{T_N - \log(N_0)}{k \cdot \log(1+E)} + L$$

Viability refers to the percentage of bacterial cell amount ($N_{0,i}$) at $t = 0$ compared to the 100% viability reference ($N_{0,0}$) at $t = 0$, so viability of a specific sample i can be defined as: $v_i = \frac{N_{0,i}}{N_{0,0}}$ $(v_0 = 1)$.

$$\therefore C_{t,i} = \frac{T_N - \log(N_{0,i})}{k_i \cdot \log(1+E_i)} + L_i$$

$$\therefore C_{t,i} = \frac{T_N - \log(N_{0,0} \times v_i)}{k_i \cdot \log(1+E_i)} + L_i$$

$$= \left[-\frac{1}{k_i \cdot \log(1+E_i)}\right] \cdot \log v_i + \left[\frac{T_N - \log(N_{0,0})}{k_i \cdot \log(1+E_i)} + L_i\right]$$

Let $v_i = 2^{-d_i}$

$$\therefore C_{t,i} = \left[\frac{\log(2)}{k_i \cdot \log(1+E_i)}\right] \cdot d_i + \left[\frac{T_N - \log(N_{0,0})}{k_i \cdot \log(1+E_i)} + L_i\right] \quad (*)$$

Assumption 1: In the same medium, the same bacterial strain will have a similar growth rate during the exponential growth phase ($k_i \cong k$).

Assumption 2: During the exponential growth phase, all bacterial cells in the suspension will replicate ($E \cong 1$).

Assumption 3: In one experimental run (on the same plate), the length of lag phase for the same bacterial strain will be the same ($L_i \cong L$).

Based on these 3 assumptions above, equation (*) can be approximated as:

$$C_{t,i} = \frac{1}{k} \cdot d_i + \left[\frac{T_N - \log(N_{0,0})}{k \cdot \log(2)} + L\right]$$

To transform cell number (N) to measurable parameters, another assumption is made:

Assumption 4: The optical density reading at 600 nm (OD_{600}, simplified as OD) is proportional to the density of cell numbers in a bacterial cell suspension ($OD(t) = P \cdot N(t)$, P is a correcting factor).

Make threshold of OD reading

$$T_{OD} = \log OD(C_t)$$

$$\therefore T_N = \log N(C_t) = \log \frac{OD(C_t)}{P} = T_{OD} - \log(P)$$

$$C_{t,i} = \frac{1}{k} \cdot d_i + \left[\frac{T_{OD} - \log(P) - \log(N_{0,0})}{k \cdot \log(2)} + L\right]$$

In data analysis, T_{OD} is set as a constant for every plate, P and $N_{0,0}$ are unknown but are also constants for the same plate. By using a calibration curve on every plate, the linear regression between $C_{t,i}$ $versus$ d_i can be obtained, and the d_i value of a certain treatment *i* could be extrapolated by calculating $C_{t,i}$ of that treatment.

A.4.12 Algorithms for Ct determination of individual growth curves

Inspired by the data analysis on qPCR amplification plot, algorithms were developed for Ct determination, consisting of (1) determining the starting point of exponential

phase (SPE), (2) determining the end point of exponential phase (EPE), (3) linear regression of the log-transformed exponential growth window, and (4) determining threshold values (*th*) for the plate. The algorithms were written in R for this manuscript, and a detailed tutorial for using these R codes was also written (see original R codes).

Determining the Starting Point of Exponential phase (SPE). In our study, a statistical estimation of SPE is achieved by inspecting externally studentized residuals in the linear regression of data points at the beginning of bacterial growth (Tichopad, A.; Dilger, M.; Schwarz, G.; Pfaffl, M. W. *Nucleic Acids Res.* **2003**, *31*). Raw data for optical density readings are used. After excluding the first reading, which is usually above the baseline, the linear regression is first performed on the first three observations. An outlier of such fitting is identified by comparing the externally studentized residuals with the Student t Distribution. If the last data point is not an outlier, the next observation is added for the next round of linear regression and outlier identification. When two consecutive outliers are identified, the latter outlier is then identified as the SPE data point, and the cycle number of this data point is returned as the SPE value. In the R code attached, the algorithm is carried out in two functions: FindInfluentialDataPoint(x,y) and FindSPE_v2(x,y).

Determine the End Point of Exponential phase (EPE). The EPE is calculated by finding the secondary derivative maximum (SDM) of the growth curve (Zhao, S.; Fernald, R. D. *J. Comput. Biol.* **2005**, *12*, 1047-1064). Since the data points are discrete in growth curves and efforts failed to fit the growth curve with a traditional sigmoid, a finite difference approximation for discrete plots is used to calculate the standard second order centered approximation (LeVeque, R. *Finite Difference Methods for Ordinary and Partial Differential Equations*; Society for Industrial and Applied Mathematics, 2007):

$$D^2u(\bar{x}) = \frac{1}{h}\left(\left(\frac{u(\bar{x}+h)-u(\bar{x})}{h}\right)-\left(\frac{u(\bar{x})-u(\bar{x}-h)}{h}\right)\right)$$

$u(\bar{x})$ refers to the measured value at variable $\bar{x}$, and *h* refers to the step length. Here, the step length is 1 as cycle numbers, which are integers, are used as variables. Thus, the equation is simplified as:

$$SD_n = D^2u(n) = u(n+1) - 2 \times u(n) + u(n-1)$$

SD_n refers to the second order centered approximation. To find the maximum and eliminate the fluctuations near the baseline, a box-car smoothing with 5 nearby data points is applied:

$$SD_{n,smooth} = (SD_{n-2} + SD_{n-1} + SD_n + SD_{n+1} + SD_{n+2})/5$$

After smoothing, the cycle number where $SD_{n,smoothed}$ reaches the maximum is returned as SDM, which is regarded as EPE in the algorithm. In the R code attached, this algorithm is carried out in function FindSDM_v3(x,y).

Linear regression of the log-transformed exponential growth window. An original exponential growth window is located from the SPE to the EPE values determined earlier. After log2 transformation of background-subtracted optical density readings, adjustment of the exponential window is made based on user-set fine-tuning parameters and the attempt to not include invalid values due to the log2 transformation (See tutorial and R code for more information). Linear regression is performed and evaluated on the log2-transformed exponential window. A manual fitting, where observations in between a pre-set window are used instead of the algorithm-determined window for linear regression, is triggered if the length of exponential window is less than 3 data points or the r square value of the linear regression is less than 0.99. A series of output values, including slope and intercept of the linear regressions, are recorded for the following Ct determination. In the R code attached, this algorithm is carried out in function LinearFitting_v2(x,y,name).

Determining threshold values (th). Three different strategies are used to determine the threshold value for the whole plate: SDM, mid-point, and fit-point (Heid, C. A.; Stevens, J.; Livak, K. J.; Williams, P. M. *Genome Res.* **1996**, *6*, 986-994). The threshold values, referred as *th.SDM*, *th.midpoint* and *th.fitpoint*, are calculated as equations below.

$$th.SDM = \frac{\sum_1^n \log(OD_{normalized}\ at\ SDM)}{n}$$

$$th.midpoint = \frac{\sum_1^n [\log(OD_{normalized}\ at\ SPE) + log(OD_{normalized}\ at\ SDM)]/2}{n}$$

$$th.fitpoint = \frac{\sum_1^n \log_{10}(10 \times standard\ deviation\ of\ baseline)}{n}$$

Briefly, with cycle numbers of SPE and SDM determined and adjusted earlier, threshold of SDM is determined as the average of all log-transformed normalized OD reading ($OD_{normalized}$) at their own SDM cycle number. For the threshold of mid-point, log-transformed normalized OD readings at SPE and SDM are averaged first to get a mid-point value, and all mid-point values across the plate are averaged to get the threshold of midpoint. It should be noted that the growth curves which are manually fitted are not used for threshold calculation. For the threshold of fit-point, the average of log10-transformed ten times standard deviation of baseline, which is defined from the second data point to SPE, is calculated.

Ct determination. Ct values from three different threshold values were determined, referred to as *ct.SDM*, *ct.midpoint* and *ct.fitpoint* in the R code. For each growth curve, threshold values are plugged in the linear regression, and Ct values corresponding to different threshold values are determined at the crossing point of threshold and linear fitting of the exponential growth window. Determination of thresholds and Ct values are carried out in function GBV(data) in the R code attached.

Table A.4.1. Nanoparticle characterization of gold nanoparticles used in this study.

Material	Core size (nm)*	Z-average (nm)**	ζ-potential (mV)***	Absorption peak wavelength (nm)	Color of colloid	Reference
PAH-AuNPs (a)	4.5 ± 1.2 (N=557)	197 ± 4	+66 ± 2	535	Deep purple	1
MPNH$_2$-AuNPs (b)	8.9 ± 3.0 (N ≥ 250)	38.4 ± 0.6	+27 ± 7	521	Navy blue	(c)

a) Poly(allylamine hydrochloride)-wrapped gold NPs; (b) Mercaptopropylamine-capped gold NPs. *Determined by TEM. **Hydrodynamic diameter in MilliQ water determined by dynamic light scattering. ***In MilliQ water.

(c) Feng, Z. V.; Gunsolus, I. L.; Qiu, T. A.; Hurley, K. R.; Nyberg, L. H.; Frew, H.; Johnson, K. P.; Vartanian, A. M.; Jacob, L. M.; Lohse, S. E.; Torelli, M. D.; Hamers, R. J.; Murphy, C. J.; Haynes, C. L. *Chem. Sci.* **2015**, *6*, 5186-5196

Table A.4.2. Water evaporation control reduces the variation among wells on standard plates. All numbers are Ct values except for percentage coefficient of variation (CV %).

		Ct_{max} -Ct_{min}	Standard Deviation	CV %		Ct_{max} -Ct_{min}	Standard Deviation	CV %
Standard plate (Whole plate)	Trial 1	1.131	0.224	1.94	**Exclude wells at edges**	0.735	0.152	1.32
	Trial 2	1.268	0.216	1.63		0.639	0.133	1.01
Standard plate with water evaporation control	Trial 1	--	--	--		0.874	0.169	1.36
	Trial 2	--	--	--		0.607	0.129	1.06
	Trial 3	--	--	--		0.944	0.169	1.52
	Trial 4	--	--	--		0.841	0.166	1.50

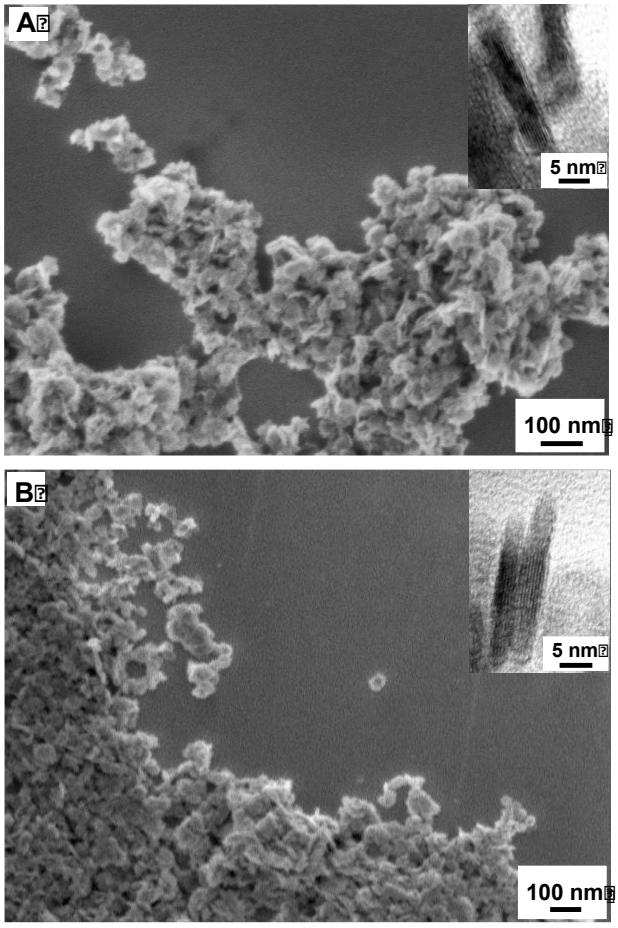

Figure A.4.1. Analysis of NMC nano-sheets using scanning electron microscopy (SEM) images and transmission electron microscopy (TEM) images in the inset for a.) $Li_{0.61}Ni_{0.23}Mn_{0.55}Co_{0.22}O_2$, b.) $Li_{0.52}Ni_{0.14}Mn_{0.72}Co_{0.14}O_2$.

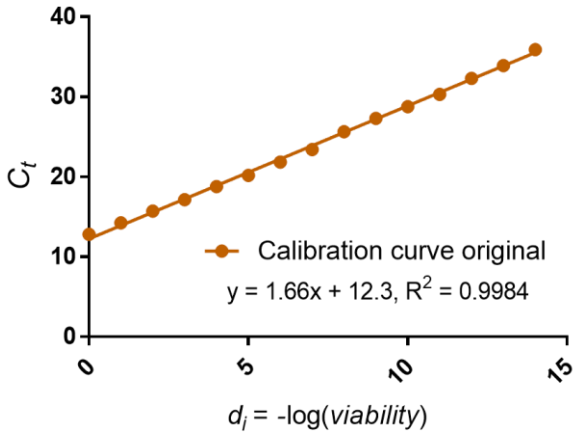

Figure A.4.2. Testing the linear range of the calibration curve for *S. oneidensis* MR-1.

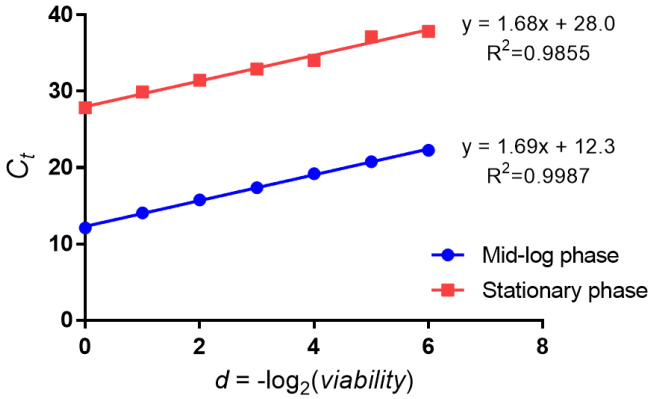

Figure A.4.3. Comparison of calibration curves from *S. oneidensis* MR-1 harvested at mid-log phase and stationary phase.

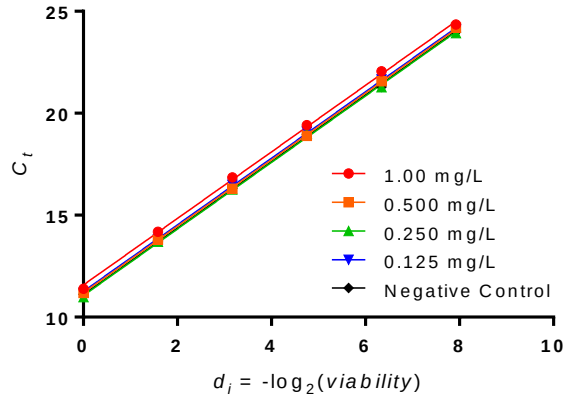

Figure A.4.4. Calibration curves from the orthogonal residue control show that the existence of residues does not affect calibration curve. All linear regressions show $R^2 >$ 0.99. Concentrations in legends refer to the amount of kanamycin residue accompanying bacterial growth.

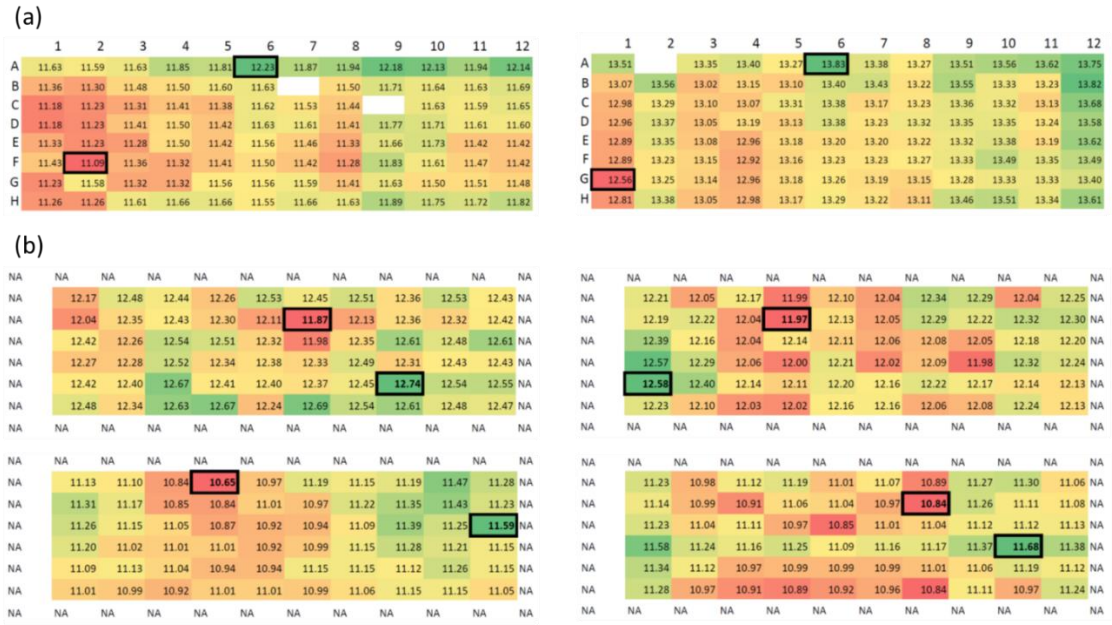

Figure A.4.5. Heat maps of standard plates (a) without or (b) with water evaporation control. The minimal and maximal value on each plate was marked with black bold frames.

	1	2	3	4	5	6	7	8	9	10	11	12
A	0.71	0.89	0.88	0.84	0.87	0.85	0.85	0.85	0.88	0.84	0.84	0.73
B	1.08	1.01	0.98	1.01	0.97	0.96	0.95	0.86	0.96	0.96	0.95	0.84
C	0.88	1.01	0.96	0.99	1.00	1.01	0.96	0.99	0.93	0.98	0.96	0.85
D	0.80	1.00	0.99	1.01	0.99	0.99	0.99	1.02	0.94	0.99	1.00	0.85
E	0.91	1.01	0.99	0.99	0.99	0.99	0.99	1.00	0.99	1.27*	0.68*	0.86
F	0.90	1.01	0.99	0.99	0.98	0.99	1.04	0.98	0.96	0.99	0.95	0.80
G	0.84	0.97	1.00	0.99	0.99	0.96	0.93	0.99	1.00	0.95	0.95	0.87
H	0.72	0.87	0.89	0.89	0.88	0.88	0.85	0.87	0.88	0.83	0.83	0.74

* Maximum and minimum values are excluded in heatmap.

Figure A.4.6. Percentage of water mass left after the plate was incubated at 37 °C for 21 hours.

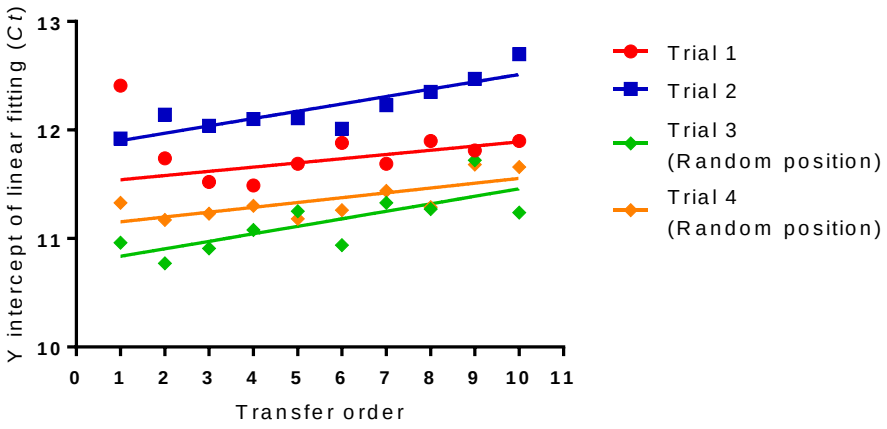

Figure A.4.7. Calibration curves were obtained from the same plate with water evaporation control, and the y-intercepts from linear fitting were plotted versus the transfer order during experiment. In trial 1 and 2, the transferring order was from Column 2 to 11, left to right, and the position for each transfer in trial 3 and 4 was randomized to eliminate the effect of different positions on plate. Linear regression with outlier elimination of y-intercept versus transfer order reveals slopes that are significantly different zero for all four trials (Extra sum-of-squares F test, $p < 0.05$). This indicate that the transferring order in GBV assay can affect the final Ct determination.

A.4.13 R codes for automated data analysis

R code: function FindInfluentialDataPoint(x,y)

```
FindInfluentialDataPoint <- function(x,y) {
    if (!length(x)==length(y)) {
        message("x and y have different sizes")
        break
    }
    n <- length(x)
    lm.out <- lm(y~x) ## Linear regression
    stu.del.res <- rstudent(lm.out) ## Find externally studentized residues, aka student deleted residues
    #print(stu.del.res)
    p.values <- 2*pt(-abs(stu.del.res),df=n-2) ## pt is the cumulative t distribution (df=n-1-p, p=1)
    return(p.values<0.05)
}
```

R code: function FindSPE.v2(x,y)

```
FindSPE.v2 <- function(x,y) {    ## Find the starting point of exponential (SPE) phase
    ## x: cycle numbers
    ## y: raw optical density readings
    ## Source the function to determine influential data point
    source("FindInfluentialDataPoint.r")
    ## Get number of data points for each sample (the number of observations)
    n <- length(x)
    ## Find SPE
    SPE.index <- 0
    outlier <- c(rep(FALSE, n)) ## the string to temporarily save outlier results
    for (j in c(3:n)) {
        outlier[j] <- FindInfluentialDataPoint(x[2:j],y[2:j])[j-1]
        ## It would return NA sometimes when an infinite p value is calculated.
        if (is.na(outlier[j])) { outlier[j] <- FALSE }
        if (outlier[j]==TRUE) {
            if (outlier[j-1]==TRUE && y[j]>0) {
                SPE.index <- j    ## SPE found
                break
            }
        }
        if (j == n) {
            SPE.index <- NA
        }
    }
```

```
    ## Return the index of SPE value
    return(SPE.index)
}
```

R code: function FindSDM.v3(x,y)

```
FindSDM.v3 <- function(x,y) {
    ## Find the Second Derivative Maximum (SDM) using finite difference approximation
    ## x: cycle numbers
    ## y: raw optical density readings
    ## Get number of data points for each sample (the number of observations)
    n <- length(x)
    ## Calculate standard second order centered approximation
    ## SD[1], SD[2] and SD[n] will always be 0 (not calculated)
    SD <- c(rep(0,n))
    SD.boxcar <- c(rep(0,n))
    for (j in c(3:(n-1))) { SD[j] = y[j-1] - 2*y[j] + y[j+1] } ## Calculate standard second order centered approximation
    ## Box-car smoothing
    for (i in c(3:(n-2))) { SD.boxcar[i] = mean(SD[(i-2):(i+2)])}
    SDM.index <- which(SD.boxcar==max(SD.boxcar))[1] #+ 1
    ## Return the index of SDM
    return(SDM.index)
}
```

R code: function LinearFitting.v2(x,y,name)

```
LinearFitting.v2 <- function(x,y,name) {  ## Linear fitting of exponential growth window
    ## x: cycle numbers
    ## y: raw optical density readings
    ## You can set your working directory at the beginning of the function
    #setwd("your path")
    ## Get number of data points for each sample (the number of observations)
    n <- length(x)
    ## Source functions to calculate SPE and SDM
    source("FindInfluentialDataPoint.r")
    source("FindSPE_v2.r")
    source("FindSDM_v3.r")
    ## Fine tuning parameters
    background <- c(2:4)
    pre.set.window.len <- 5
    manual.window.upper <- -1.5
```

```
manual.window.lower <- -2.5
unstable.baseline <- c(1)
expand.SDM <- 0

## Determine if there is a growth
growth <- TRUE
raw.slope <- summary(lm(y~x))$coefficients[2,1]
raw.Pr <- summary(lm(y~x))$coefficients[2,4]
if ( raw.slope<=0 || raw.Pr>=0.05) { growth <- FALSE }

## Find SPE, SDM, and exponential growth window (from SPE to SDM)
SPE <- FindSPE.v2(x,y)
SDM <- FindSDM.v3(x,y)
exp.window <- SDM - SPE + 1

## If the SPE is NA, then the exp.window is NA, there is no growth
if ( is.na(exp.window) ) { growth <- FALSE }

## If there is no growth, return everything as NA, and leave the function
if ( !growth ) {
    results <- list(SPE=NA, SDM=NA, exp.window=NA, SPE.adj=NA, SDM.adj=NA,
                    exp.window.adj=NA, slope=NA, intercept=NA, r.square=NA, bad.fit=NA,
                    bg.sd=NA, manual.fit=NA)
    return(as.data.frame(results))
}

## Initialize .adjs & linear regression parameters
SPE.adj <- SPE # not NA at this point
SDM.adj <- SDM # not NA at this point
exp.window.adj <- exp.window # not NA at this point
lm.temp <- NA
slope <- NA
intercept <- NA
r.square <- NA
bad.fit <- NA
## For bad.fit: FALSE for a real fit with r2>0.99. NA for "no-growth".
manual.fit <- 0
## For manual.fit: 0 represents FALSE (original SPE&SDM used), 1 represents expanded window,
    ## 2 represents SPE adjusted based on NA/Inf values, 3 represents manual fit using a pre-set window
```

```
## Normalize
y.n <- y - mean(y[background]) # Background was set as the average of raw OD readings at user-defined baseline.

## Logarithmic
y.log <- log(y.n, base=10)

## Adjust exponentila growth window if it is less than a pre-set number.
if ( exp.window > 0 && exp.window < pre.set.window.len) {
    SDM.adj <- SDM + expand.SDM
    SPE.adj <- SPE - ( ( pre.set.window.len - expand.SDM ) - exp.window )
    exp.window.adj <- pre.set.window.len
    manual.fit <- 1
}

## Adjust SPE so that it doesn't have NA or Inf after it.
y.log.na.index <- which(is.na(y.log))
y.log.inf.index <- which(is.infinite(y.log))
if ( length(y.log.na.index)>0 || length(y.log.inf.index)>0 ) {
    last.na.or.inf <- max(y.log.na.index, y.log.inf.index)
} else {
    last.na.or.inf <- 0
}
if ( SPE.adj <= last.na.or.inf ) {
    SPE.adj <- last.na.or.inf + 1
    exp.window.adj <- SDM.adj - SPE.adj + 1
    manual.fit <- 2
}

## Calculate the standard deviation of baseline (for fit point threshold calculation)
if ( sum(!complete.cases(y[2:(SPE.adj-1)]))==0 ) { bg.sd <- sd(y[2:(SPE.adj-1)]) }
else { bg.sd <- NA }

## Locate exponential growth window
#growth.1 <- !is.na(SPE.adj) && !is.na(SDM.adj) && (exp.window.adj>=3)
small.window <- FALSE
if ( exp.window.adj>=3 ) { # Linear regression doesn't happen if it's a small window (<=3)
    y.l <- y.log[SPE.adj:SDM.adj]
    x.l <- x[SPE.adj:SDM.adj]
    #growth.2 <- (sum(is.na(y.l))==0) && (sum(is.infinite(y.l))==0)
    lm.temp <- lm(y.l~x.l)
```

```
            if ( !is.na(summary(lm.temp)$r.squared) ) {
                if ( summary(lm.temp)$r.squared<0.99 ) { bad.fit <- TRUE } else
{ bad.fit <- FALSE}
            } else {
                bad.fit <- TRUE
            }

        } else {
            small.window <- TRUE
        }

        ## Manual fit triggerred if it is a bad fit or if exponential window <3.
        if ( bad.fit==TRUE || small.window==TRUE) {
            manual.window <- which(y.log[-
(unstable.baseline)]<=manual.window.upper & y.log[-
(unstable.baseline)]>=manual.window.lower)+length(unstable.baseline)
            ## Manually set up the window. CAUTION! Always needs to be tuned.
            #print(manual.window)
            if ( length(manual.window)>=3 ) { # Linear regression doesn't happen if it's
a small window (<=3)
                y.l <- y.log[manual.window]
                x.l <- x[manual.window]
                SPE.adj <- manual.window[1]
                SDM.adj <- manual.window[length(manual.window)]
                exp.window.adj <- length(manual.window)
                manual.fit <- 3
                lm.temp <- lm(y.l~x.l)
                if ( summary(lm.temp)$r.squared < 0.99 ) { bad.fit <- TRUE } else
{ bad.fit <- FALSE}
            }
        }

        ## Outputs
        if ( !class(lm.temp)=="lm" ) { # which means the linear fitting never happened,
probably because the window is <=0.
            slope <- NA
            intercept <- NA
            r.square <- NA
            bad.fit <- NA
        } else {
            slope <- coefficients(lm.temp)[2]
            names(slope) <- NULL
            intercept <- coefficients(lm.temp)[1]
```

```
            names(intercept) <- NULL
            r.square <- summary(lm.temp)$r.squared
            ## If the adjusted exponential window is too small for a linear regression, it's
a bad fit.
            #if ( r.square < 0.99 || exp.window.adj <=2 ) { bad.fit <- TRUE } else { bad.fit
<- FALSE }
            ## Plot final figures
            plot(y.log~x)
            abline(lm.temp)
            abline(v=c(SPE.adj,SDM.adj))
            abline(v=c(SPE, SDM), col="red")
            text(n,-2,name)
      }

      ## Put results together and return a data frame
      results <- list(SPE=SPE, SDM=SDM, exp.window=exp.window,
SPE.adj=SPE.adj, SDM.adj=SDM.adj,
                        exp.window.adj=exp.window.adj, slope=slope,
intercept=intercept, r.square=r.square, bad.fit=bad.fit,
                        bg.sd=bg.sd, manual.fit=manual.fit)
      #print(results)
      return(as.data.frame(results))
}
```

R code: function GBV(data)

```
GBV <- function(data) {    ## Find threshold and determine Ct
      ## data: the input dataframe of Cycle vs. raw OD reading

      ## Working directory -- needs to be reset if switch computer/folder.
      #setwd("your path")

      #dir.create(paste(getwd(),"/Plots", sep=""))
      source("LinearFitting_v2.r")

      sample_num <- ncol(data) - 1        ## number of samples in this dataframe
      if ( colnames(data)[1] != "Cycle") {
            colnames(data)[1] <- "Cycle"
            message("First column renamed as 'Cycle'.")
      }

      x <- data$Cycle      ## x is the vector for cycle numbers
      n <- length(x)    ## n is the number of data points for each sample (the number of
observations)
```

```
    if (n < 10) {
        message("Not enough data point (n < 10). Program terminated.")
        break
    }

    ## Acquire SPE, SDM, and linear fitting of individual data points
    output <- NA
    for (i in c(1:sample_num)) {
        y <- data[[i+1]]
        plot(y~x)
        text(n,range(y)[1], colnames(data)[i+1])
        sample.name <- colnames(data)[i+1]
        results <- data.frame(Name=sample.name,
LinearFitting.v2(x,y,sample.name))
        ## Print names of each sample. The position of labels can be adjusted.
        #if (!is.na(results$slope)) { text(n,-2,colnames(data)[i+1]) }
        output <- rbind(output, results)
        if (i == 1) { output <- output[-1,]}
        rownames(output)[i] <- colnames(data)[i+1]
    }
    #print(output)

    ## Calculate individual threshold values (only the ones with a good fit (r2>0.99))
to acquire average threshold across plate.
    fun.lm <- function(slope, x, intercept, bad.fit) {
        if ( !is.na(bad.fit) ) {
            if ( !bad.fit ) { return(slope*x+intercept) }
            else { return(NA) }
        }
        else { return(NA) }
    }
    th.SPE <- mapply(fun.lm, output$slope, output$SPE.adj, output$intercept,
output$bad.fit, SIMPLIFY=TRUE)
    th.SDM <- mapply(fun.lm, output$slope, output$SDM.adj, output$intercept,
output$bad.fit, SIMPLIFY=TRUE)
    th.midpoint <- mapply(function(x,y){return((x+y)/2)}, th.SPE, th.SDM,
SIMPLIFY=TRUE)
    fun.fitpoint <- function(sd, manual.fit) {
        if ( !is.na(sd) && !is.na(manual.fit)) {
            if ( manual.fit<=2 && !(sd==0) ) { return(log(10*sd, base=10)) }
            else { return(NA) }
        }
        else { return(NA) }
```

```
    }
    th.fitpoint <- mapply(fun.fitpoint, output$bg.sd, output$manual.fit,
SIMPLIFY=TRUE)

    ## Calculate threshold values for three different methods
    th.ave.SDM <- mean(th.SDM, na.rm=TRUE)
    th.ave.midpoint <- mean(th.midpoint, na.rm=TRUE)
    th.ave.fitpoint <- mean(th.fitpoint, na.rm=TRUE)

    ## The percentage of data points used to calculate threshold values
    effective.points.th <-
sum(complete.cases(th.SDM))/sum(complete.cases(output$slope))

    ## The percentage of total manual fit to all linear fitting that happened with a
slope>0
    total.manual.fit <-
length(which(output$manual.fit==3))/length(which(output$slope>0))

    ## Determine Ct based on threshold
    fun.ct <- function(y, intercept, slope) {
        if ( !is.na(slope) ) {
            if ( slope>0 ) { return((y-intercept)/slope) }
            else { return(NA) }
        } else { return(NA) }
    }
    ct.SDM <- mapply(fun.ct, th.ave.SDM, output$intercept, output$slope,
SIMPLIFY=TRUE)
    ct.midpoint <- mapply(fun.ct, th.ave.midpoint, output$intercept, output$slope,
SIMPLIFY=TRUE)
    ct.fitpoint <- mapply(fun.ct, th.ave.fitpoint, output$intercept, output$slope,
SIMPLIFY=TRUE)

    ## Put output together and write in "Results.csv"
    output <- data.frame(output, th.SDM, th.midpoint, th.fitpoint, ct.SDM,
ct.midpoint, ct.fitpoint)
    final.output <- list(output, th.ave.SDM=th.ave.SDM,
th.ave.midpoint=th.ave.midpoint,
                         th.ave.fitpoint=th.ave.fitpoint,
effective.points.th=effective.points.th, total.manual.fit=total.manual.fit)
    write.csv(final.output, "Results.csv", row.names =FALSE)
    return(final.output)
}
```

Curriculum Vitae

Tian (Autumn) Qiu

University of Minnesota, Twin Cities
207 Pleasant Street SE | *425 13th Ave SE*
Smith 139, Box K-11 | *Apt. 1506*
Minneapolis, MN 55455 | *Minneapolis, 55414*
Phone: 612-626-5282 | *Email: qiuxx152@umn.edu*

EDUCATION

Candidate for Doctor of Philosophy in Chemistry *2014-2018 (expected)*
Department of Chemistry, University of Minnesota, Twin Cities
Advisor: Dr. Christy Haynes
Thesis title: Bacterial response to nanoparticles on molecular levels

Master of Science in Chemistry *2012-2014*
Department of Chemistry, University of Minnesota, Twin Cities
Cumulative GPA: **3.89/4.00**
Advisor: Dr. Christy Haynes

Bachelor of Science in Chemistry *2008-2012*
College of Chemistry and Molecular Engineering, Peking University, China
Overall GPA: **3.52/4.00** (86/100)
Advisor: Dr. Yanyi Huang

RESEARCH EXPERIENCE

Research Assistant, Department of Chemistry, University of Minnesota *May 2013 – Present*
Research Advisor: Dr. Christy Haynes, Department of Chemistry
Study the mechanisms of nanoparticle-cell interactions using various bioanalytical tools, aiming to link nanoparticle properties to the consequences of nanoparticle exposure.

- Investigation of bacterial response to various nanomaterials, including TiO_2, functionalized gold nanoparticles, and next-generation nano-scale battery materials;
- Exploration of cellular response at the molecular level from DNA damage, RNA expression to metabolite secretion using various bioanalytical tools;
- Development of a high-throughput assay for interference-free bacterial nanotoxicity screening along with programmed data interpretation using R language;
- **Skills**: bacterial cell culture, colony counting, fluorescence/colorimetric assays, bacterial respirometry, RNA/DNA isolation, RT-qPCR, HPLC, fluorescence/confocal microscopy, CytoViva microscopy with hyperspectral imaging, data analysis, programming

Undergraduate Research Assistant, Peking University *Apr. 2011 – Jun. 2012*
Research Advisor: Dr. Yanyi Huang, College of Engineering
Designed and fabricated microfluidic devices for water-in-oil microdroplet generation to apply the device for *in vitro* directed evolution.

- **Skills**: design, fabrication and operation of PDMS microfluidic chips, *in vitro* protein expression

Summer REU Program, University of Michigan, Ann Arbor *Jul. 2010 - Aug.2010*
Research Advisor: Dr. Carol Fierke, Department of Chemistry
Constructed plasmid for the expression of iron-binding proteins in *E. coli*.

- **Skills**: mammalian cell culture

Undergraduate Research Assistant, Peking University *Oct. 2009 -Mar.2011*
Research Advisor: Dr. Peng R. Chen**,** Department of Chemical Biology
Developed a standard protocol for the expression of ZitR, a zinc-binding protein, in *Escherichia coli* and its purification using fast protein liquid chromatography (FPLC).

- **Skills**: recombinant protein production (plasmid construction and transformation, protein expression and purification using FPLC), plasmid extraction, DNA gel electrophoresis, SDS-PAGE, PCR, western blotting

PUBLICATIONS

In Preparation:

Qiu, T. A., Clement, P. L., Haynes, C. L., Linking nanomaterial properties to biological outcomes: analytical challenges in nanotoxicology for the next decade, 2018, *in preparation*.

Qiu, T. A., Guidolin, V., Hoang, K. N., Pho, T., Carrà, A., Lynn, T. G., Villalta, P. W., Feng, Z. V., Balbo, S., Haynes, C. L., DNA damage as a toxicity mechanism of NMC ($Li_xNi_{1/3}Mn_{1/3}Co_{1/3}O_2$) nanomaterial to bacteria *Shewanella oneidensis* MR-1 and *Bacillus subtilis*, 2018, *in preparation*.

Submitted and In Revision:

Gallagher, M. J., Buchman, J. T., **Qiu, T. A.**, Zhi, B., Lyons, T. Y., Rosenzweig, Z., Haynes, C. L., Fairbrother, D. H., Release, detection and toxicity of fragments generated during artificial accelerated weathering of CdSe/ZnS and CdSe quantum dot polymer composites, ***Environmental Science: Nano***, 2018, *in revision*.

Olenick, L. L., Troiano, J. M., Vartanian, A. M., Melby, E. S., Zhang, L., **Qiu, T. A.**, Lohse, S. E., Zhang, Xi., Kuech, T. R., Gunsolus, I. L., McGeachy, A., Doğangün, M, Hu, D., Walter, S. R., Lovern, S., Owen, H., Hang, M. N., Torelli, M. D., Feng, Z. V., Hurley, K. R., Dalluge, J., Haynes, C. L., Hamers, R. J., Pedersen, J. A., Cui, Q., Orr, G., Murphy, C. J., Geiger, F. M., Lipid corona formation from nanoparticle interactions with membranes, ***Chem***, 2018, *submitted*.

Peer-reviewed Publication:

Zheng, Z., Saar, J., Zhi, B., **Qiu, T. A.**, Gallagher, M. J., Fairbrother, D. H., Haynes, C. L., Lienkamp,

K., Rosenzweig, Z., Structure-property relationships of amine-rich and membrane-disruptive poly(oxonorbornene)-coated gold nanoparticles, ***Langmuir***, 2018, **34**(15), 4614-4625.

Zhi, B., Gallagher, M. J., Frank, B. P., Lyons, T. Y., **Qiu, T. A.**, Da, J., Mensch, A. C., Hamers, R. J., Rosenzweig, Z., Fairbrother, D. H.; Haynes, C. L., Synthesis and bacterial toxicity of nitrogen and phosphorus co-doped amorphous carbon dots, ***Carbon***, 2017, **129**, 438-449.

Qiu, T. A., Nguyen, T. H. T., Hudson-Smith, N. V., Clement, P. L., Forester, D-C., Frew, H., Hang, M. N., Murphy, C. J., Hamers, R. J., Feng, Z. V., Haynes, C. L., Growth-based bacterial viability assay for interference-free and high-throughput toxicity screening of nanomaterials, ***Analytical Chemistry***, 2017, **89**, 2057–2064.

Qiu, T. A., Torelli, M. D., Vartanian, A. M., Rackstraw, N. B., Buchman, J. T., Jacob, L. M., Murphy, C. J., Hamers, R. J., Haynes, C. L., Quantification of free polyelectrolytes present in colloidal suspension, revealing source of toxic responses for polyelectrolyte-wrapped gold nanoparticles, ***Analytical Chemistry***, 2017, **89**, 1823–1830.

Qiu, T. A., Meyer, B. M., Christenson, K. G., Klaper, R. D., Haynes, C. L., A mechanistic study of TiO_2 nanoparticle toxicity on *Shewanella oneidensis* MR-1 with UV-containing simulated solar irradiation: Bacterial growth, riboflavin secretion, and gene expression, ***Chemosphere***, 2017, **168**, 1158-1168.

Finkenstaedt-Quinn, S. A., **Qiu, T. A.**, Shin K., Haynes, C. L., Super-resolution imaging for monitoring cytoskeleton dynamics, ***Analyst***, 2016, **141**, 5674-5688.

Qiu, T. A.*, Bozich, J. S.*, Lohse,S. E., Vartanian, A. M., Jacob, L. M., Meyer, B. M., Gunsolus, I. L., Niemuth, N. J., Murphy, C. J., Haynes, C. L., Klaper, R. D., Gene expression as an indicator of the molecular response and toxicity in the bacterium *Shewanella oneidensis* and the water flea *Daphnia magna* exposed to functionalized gold nanoparticles, ***Environmental Science: Nano***, 2015, **2**, 615-629. (*These two authors contributed equally to this work.)

Feng, Z. V., Gunsolus, I. L., **Qiu, T. A.,** Hurley, K., Nyberg, L. H., Frew, H., Johnson, K. P., Vartanian, A. M., Jacob, L. M., Lohse, S. E., Torelli, M. D., Hamers, R. J., Murphy, C. J., Haynes, C. L., Impacts of gold nanoparticle charge and ligand type on surface binding and toxicity to Gram-negative and Gram-positive bacteria, ***Chemical Science***, 2015, **6**, 5186-5196

Invited Research Highlights (Not Peer-reviewed):

Allen, C., **Qiu, T. A.**, Pramanik, S., Buchman, J. T., Krause, M. O. P., Murphy, C. J., Research highlights: Investigating the role of nanoparticle surface charge in nano-bio interactions, ***Environmental Science: Nano***, 2017, **4**, 741-746.

Gallagher, M. J., Allen, C., Buchman, J. T., **Qiu, T. A.**, Clement, P. L., Krause, M. O. P., Gilbertson, L. M., Research highlights: applications of life-cycle assessment as a tool for characterizing environmental impacts of engineered nanomaterials, ***Environmental Science: Nano***, 2017, **4**, 276-281.

Qiu, T. A., Gallagher, M. J., Hudson-Smith, N. V., Wu, J., Krause, M. O. P., Fortner, J. D., Haynes, C. L., Research highlights: unveiling the mechanisms underlying nanoparticle-induced ROS generation and oxidative stress, ***Environmental Science: Nano***, 2016, 3, 940-945.

CONFERENCE PRESENTATIONS

Oral presentation, "Growth-based bacterial viability (GBV) assay for interference-free and high-throughput nanotoxicity screening", Society of Environmental Toxicology and Chemistry (SETAC) North America 38th Annual Meeting, Minneapolis, MN, November 13, 2017.

Oral presentation, "Growth-based Bacterial Viability (GBV) assay for interference-free and high-throughput nanotoxicity screening", 253rd ACS National Meeting, San Francisco, CA, April 4, 2017.

Invited oral presentation, "Microbial assays for fast, broad screening of engineered nanoparticle toxicity to bacteria." SciX, Minneapolis, MN, September 20, 2016.

Poster, "A novel growth-based bacterial viability assay for high-throughput nanoparticle toxicity screening." SciX, Minneapolis, MN, September 22, 2016.

Poster, "A novel growth-based bacterial viability assay for high-throughput nanoparticle toxicity screening." International Graduate Student Research Showcase at University of Minnesota, Minneapolis, MN, April 22, 2016.

Poster, "Development of a novel growth-based bacterial viability assay for nanoparticle toxicity screening." Midwest Universities Analytical Chemistry Conference, Minneapolis, MN, November 05, 2015.

Poster, "The impact of nanoparticle purification method on bacterial toxicity using poly(allylamine hydrochloride)-wrapped gold nanoparticles as a model material." Gordon Research Conference, Environmental Nanotechnology, West Dover, VT, June 25, 2015.

Oral presentation, "Gene expression response induced by functionalized gold nanoparticles: comparisons between the Gram-negative bacterium *Shewanella oneidensis* and the microcrustacean *Daphnia magna*." 248th ACS National Meeting, San Francisco, CA, August 13, 2014.

Poster, "Development of a readily exchangeable iron biosensor for intracellular use." Regional Poster Session for Summer Undergraduate Research Students, Hope College, Holland, MI, July 31, 2010.

RESEARCH PROPOSALS

Beckman Postdoctoral Fellowship Proposal, Beckman Institute for Advanced Science and Technology at the University of Illinois, awarded, February 2018.

Student Seed Grant Proposal, Center for Sustainable Nanotechnology, "Identifying DNA damage of *Shewanella oneidensis* MR-1 upon nano-nickel manganese cobalt oxide (NMC) exposure using a high-resolution mass-spectrometry-based DNA adductomics approach", funded, April 2016.

TEACHING EXPERIENCE

Undergraduate Researcher Mentor, Haynes Lab, U of Minnesota *May 2017 – Aug. 2017*
Co-mentor to Anaeli Shockey on characterizing gold nanoparticles interacting with lipids.

Undergraduate Researcher Mentor, Haynes Lab, U of Minnesota *Sep. 2015 – May 2017*
Mentor to Dona-Carla Forester on bacterial toxicity assays and magnetic nanoparticle synthesis.

Undergraduate Researcher Mentor, Haynes Lab *Jun. 2015 – Aug. 2015*
Mentor to Nathan Rackstraw on measuring the toxicity of functionalized gold nanoparticles to *Shewanella oneidensis* using drop plate counting method.

Undergraduate Researcher Mentor, Haynes Lab *Jun. 2014 – Aug. 2014*
Mentor to Ky Christenson on *Shewanella oneidensis* RNA extraction, riboflavin measurement via HPLC, and bacterial biofilm formation.

Teaching Assistant, University of Minnesota *Sep. 2013 – Dec. 2013*
Course: *Modern Instrumental Methods of Chemical Analysis Lecture*
Assisted in an advanced analytical chemistry class. Responsibilities included helping with the maintenance of class website, assisting students with assignments, and grading problem sets, quizzes, and portions of exams.

Teaching Assistant, University of Minnesota *Sep. 2012 – May 2013*
Course: *Organic Chemistry Lab*
Taught a fundamental organic chemistry laboratory for the study, synthesis, isolation, purification and characterization of various organic compounds. Responsibilities included lab tutoring, conducting lab discussion, after-class office hours, and grading lab reports and assignments.

HONORS AND AWARDS

Mary Haga Travel Award, Xi Chapter of Graduate Women in Science *2017*
Agnes Hansen Travel Award, Xi Chapter of Graduate Women in Science *2014*
Graduation with Honors: College Graduation Excellence Award, Beijing *2012*
Graduation with Honors: College Graduation Excellence Award, Peking University *2012*
Wu Si Scholarship, Peking University *2010, 2011*
Summer Research Scholarship, REU Program, University of Michigan *2010*
2nd prize in the Challenge Cup, Wu Si Youth Science Competition, Peking University *2010*
Merit Student, Peking University *2009, 2010*
Founder Scholarship, Peking University *2009*

PROFESSIONAL AFFILIATIONS

American Chemical Society
Society of Environmental Toxicology and Chemistry

OUTREACH AND COMMUNITY SERVICE

Volunteer for the various outreach activities including (but not limited to):

West 7th Community Center Outreach, St Paul *Jul. 2013, 2015, 2016*
Sustainability Action! Open House, University of Minnesota *Aug. 2013, 2014, 2016*

Energy and U, University of Minnesota *May 2014*

Green Chemistry and Green Engineering, Minnesota State Fair *Aug. 2013, 2014*

Math and Science Family Fun Fair, University of Minnesota *Nov. 2012*

ACS Outreach: Chemists-in-the-Library, Minneapolis *Aug. 2012*

Member of Student Board in the Center of Sustainable Nanotechnology *Jun. 2015 – Present*

Lab Safety Officer of the Haynes Lab *Jan. 2015 – Sep. 2016*

Member of the Analysis and Compliance Committee, Joint Safety Team *Sep. 2015 – Sep. 2016*

Blogger for Center of Sustainable Nanotechnology website: *Aug. 2013 – Present*

- *Bacteria in the Shell: A Nano-bio Hybrid for Solar Energy Capture*
- *Using Gene Expression to Learn About Nanoparticle Toxicity (ScienceSeeker Editor's Picks)*
- *Theres plenty of room at the bottom…for ART!*
- *Space Elevator: A Lasting Dream for a Sky-Reaching Tree*
- *Forensic Nanotechnology: a scientific whodunit*

President, Peking University Alumni Association at U of Minnesota *Sep. 2015 – Sep. 2017*

English-to-Chinese translator for a Chinese popular science website *May 2013 – Sep. 2013*